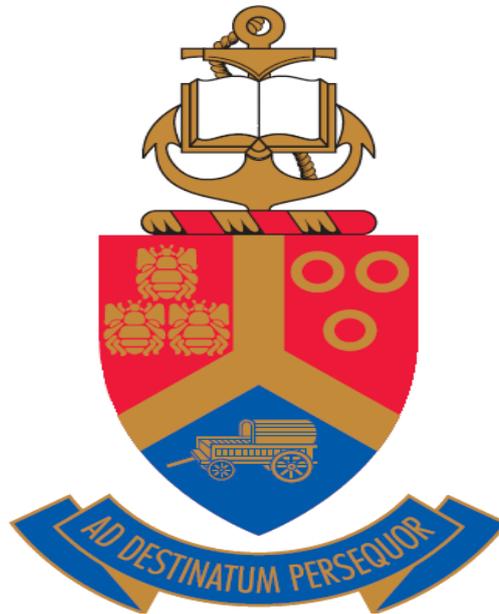# Synthesis and characterization of Co-based hydroxides and metal disulphides with various forms of carbon for supercapacitor applications

by

Tshifhiwa Moureen Masikhwa

A thesis submitted in partial fulfilment of the requirements for the degrees of

DOCTOR OF PHILOSOPHY (Ph.D.) IN PHYSICS

Faculty of Natural and Agricultural Science

UNIVERSITY OF PRETORIA

Hatfield, Pretoria

August 2016

Supervisor: Prof.N.I.Manyala
Co-supervisor: Dr J. K. Dangbegnon

1

Declaration of Originality

© University of Pretoria

I, **Tshifhiwa Moureen Masikhwa** declare that the matter in this thesis, *Synthesis and characterization of Co-based hydroxides and metal disulphides with various forms of carbon for supercapacitor applications,* is the result of investigations carried out by me under the supervision and co-supervision of Prof. NI. Manyala and Dr. JK Dangbegnon respectively, in the Physics department at the University of Pretoria South Africa and that it has not previously been submitted elsewhere for the award of any degree or diploma at this or any other tertiary institution.

Signature...   Date.................................

Dedicated

To my mother: Nyadzanga Annah

Masikhwa

The reason of what I become today.

Thanks for your support, guidance and

continuous care.

Acknowledgements

Firstly, I would like to thank God for guiding me and leading me throughout my studies. I would like to convey my deepest appreciation to my supervisor, Prof. N.Manyala, for his constant encouragement, invaluable guidance, patience and understanding throughout the whole period of my Ph.D. Without his guidance and persistence help this dissertation would not have been possible. I also thank the examiners for their valuable time, recommendation and suggestions.

My special gratitude to Dr. A. Bello and Dr. J. K. Dangbegnon for giving me unending assistances both in the laboratory and making my postgraduate research a success. My special thanks to them for the role they played in working extra hours in ensuring we were able to get good results and finish up my work in record time.

My special thanks to Dr.J. Madito for your kindness, support and valuable friendship, getting to know you is one of the comforts, like having a brother.

I would like to thank the rest of the group members for all the valuable discussions, kind co-operation and assistance during my research.

I would also like to be thankful to the great friends I made here at the Physics Department, fellow students, staff for their motivating discussions and wonderful memories shared, Dr .K. Makgopa, Mr. J. Lekitima, Dr. E. Mapasha, Dr. T.Hlatswayo , Mr. P.Ngoepe and Mr. S.Tunhuma. My life has been so interesting and memorable with you guys.

My sincere thanks to Mrs. Isbe van DerWesthuizen, Mrs. Suzette Seymore and Mrs. E. Meyburgh for their contributions support in procurements and laboratory work. I would like to thank especially Mrs. Antoinette Buys and Andre Botha at the Microscopy Department for their assistance in getting SEM images, Dr. Linda Prinsloo for all the assistance with the Raman measuring equipment and Mrs. Wiebke Grote for XRD analysis.

I would like to confer my appreciation to the Head of the Department Prof.C.C.Theron for some part-time work he offered me within the department which enabled me to supplement my finances. I would like to thank both the University of Pretoria and the South African National research foundation (NRF) for financial support during my studies.

Deep gratitude to be expressed to my family, Mrs. D.E.Maluleke, Mr. T.M.Masikhwa and Mr. M.B. Masikhwa for your love, unconditional support, guidance, prayers and encouragement throughout my life. Also like to thanks my grandmother, my brothers and sister for your prayers, love and support.

Special thanks to my lovely mother (my best friend) for your love, unending calls and constant prayers during my studies. Words cannot express how grateful I am for all your moral support and sacrifices that you have made on my behalf. Your prayers for me were what sustained me thus far. Thank you mom for everything…………….

Abstract

The aim and objectives of this work are to synthesize cobalt-based hydroxides and transition metal disulphides composites with carbon materials such as graphene foam and activated carbon by a facile and environmentally friendly hydrothermal technique for energy storage application. Because faradaic materials suffer from poor electrical conductivity and low electrochemical stability, while carbon materials are known to have good electrical conductivity and electrochemical stability, the combination of the two materials to make hybrid material should be able to improve the electrochemical properties of the composite material. Morphological, structural, surface area and compositions properties of the produced materials were evaluated and characterized using methods such as scanning electron microscopy (SEM), transmission electron microscopy (TEM), X-ray diffraction (XRD), X-ray photoelectron spectroscopy (XPS), N_2 adsorption-desorption isotherm (BET), Fourier transformation infrared spectroscopy (FTIR) and Raman spectroscopy. Electrochemical characterization involved cycling voltammetry (CV), galvanostatic charge-discharge (GCD), electrochemical impedance spectroscopy (EIS) and cycling life were carried out in two (asymmetric device) and three-electrode configurations using 6 M KOH aqueous electrolyte and they all showed excellent electrochemical performance. For instance the asymmetric devices based on CoA-LDH/graphene foam//AEG gave specific capacitance of 101.4 F g^{-1} with a maximum energy density of 28 Wh kg^{-1} and a corresponding power density of 1420 W kg^{-1} at a current density of 0.5 A g^{-1} , VS_2//AC gave specific capacity of 155 F g^{-1} and high energy and power densities of 42 Wh kg^{-1} and 700 W kg^{-1} respectively at current density of 1 A g^{-1} and MoS_2_150 mg GF //AEG gave high specific capacitance of 59 F g^{-1} with maximum energy and power densities of 16 Wh kg^{-1} and 758 W kg^{-1} respectively at a current density of 1 A g^{-1} respectively . All these results showed the great potential of the hybrid materials

6

derived from the incorporation of cobalt based hydroxides and transition metal disulphides with carbon for supercapacitor application.

Table of Contents

9

List of figures

12

List of Equations

13

14

$$C = \frac{1}{2\Pi f m(Z)}$$

$$Re(C) = \frac{-Im(Z)}{\omega|z|^2}$$

$$Im(C) = \frac{Re(Z)}{\omega|z|^2}$$

$$\eta = \frac{t_D}{t_C} \times 100\%$$

$$2d \sin \theta = n\lambda$$

$$KE = hv - E_B$$

List of Tables

Table 2.1: Comparison of capacitor, supercapacitor and battery characteristics [4].

List of Abbreviations and Symbols

ACs	Activated Carbon
AP-CVD	Atmospheric Pressure Chemical Vapour Deposition
Ag/AgCl	Silver-Silver Chloride
BET	Brunauer-Emmett-Taylor
CPs	Conducting Polymers
CV	Cycling Voltrammetry
C_s	Specific Capacitance
°C	Degree Celsius
CDCs	Carbide-Derived Carbons
CNTs	Carbon Nanotubes
DL	Double Layer

DWCNTs	Double –Walled Carbon Nanotubes
EC	Electrochemical Capacitor
EDLC	Electric Double Layer Capacitor
ESR	Equivalent Series Resistance
EG	Expanded Graphite
ESR	Equivalent series Resistance
GCD	Galvanostatic Charge-Discharge
FTIR	Fourier Transform Infrared Spectroscopy
ILs	Ionic Liqiuds
LDH	Layered double Hydroxide
MWCNTs	Multi-walled carbon nanotubes
P_M	Maximum Power Density
NMP	N-Methyl-2-pyrolidone
PTFE	Polytetrafluoroethylene
PVDF	Polyvinylidene Fluoride
R_s	Solution (electrolyte) resistance
SCs	Supercapacitors
SEM	Scanning Electron Microscopy
SSA	Specific Surface Area
tMOs	Transitional –metal oxide
tM-OH	Transitional metal hydroxides
V	Volt
XPS	X-ray photoelectron spectroscopy
XRD	X-ray Diffraction
W	Warburg Impedance

© University of Pretoria

Z´   Real impedance

Z″   Imaginary impedance

CHAPTER 1

1.0 INTRODUCTION

1.1 Background and General Motivation

The high demand for energy is among the problems leading to the rapid depletion of fossil fuels, environmental pollution/deterioration, and global warming. Adequately addressing these problems through the design and development of alternative energy sources coupled to efficient energy storage and conversion devices have encouraged intensive research undertaken by the global scientific community. The latter devices must possess high energy and power densities, great cyclic stability with long operating lifetime for mitigating these serious environmental and energy issues [1]. Some common energy conversion and storage technologies already in use include fuel cells, batteries, and electrolytic capacitors. Batteries are the most widely used in many systems and are known to display high energy density due to the adopted bulk electrode material characterized by high capacity for charge storage. However, the nature of the electrochemical charge storing processes within the bulk of the electrode confines reaction kinetics via electron and ion transportation, thereby reducing the complete power delivery.

Recently, supercapacitors (SCs) also known as electrochemical capacitors (ECs) have been discovered to be more suitable candidates for next-generation energy storage devices due to their moderate specific energy (~10 Wh kg^{-1}), higher power density value (>10 kW kg^{-1}), fast charge-discharge rate, as well as better cycle stability performance as compared to conventional batteries and electrolytic capacitors [2]. Supercapacitors have been employed in a variety of applications such as portable electronics, mobile communications, hybrid electric vehicles, memory backup systems and military devices, where high power density, excellent reversibility and long cycle life are highly required [2]. Nevertheless, the main constraint of

18

the state of art supercapacitor lies in their lower energy density compared with batteries. The capacitance and the cell voltage have the great impact on the energy density of supercapacitor. Although the energy density of supercapacitor is much higher than conventional dielectric capacitors, it is still lower than those of common batteries and fuel cells in use. Most of the commercially available supercapacitors have a specific energy density values less than 10 Wh kg^{-1} [3]. Therefore, there has been an increasing interest in energy storage research aimed at increasing the energy density of supercapacitor to be close to or even higher than that of commercial batteries.

The electrode material plays an important part in improving the overall device performance and this remains a great challenge in finding unique and efficient electrode materials for this purpose. Hence, in order to increase the energy density of supercapacitors, further optimization of the capacitance and operating potential of the individual electrode materials is essential. This optimization lies in thoroughly understanding the basic physics and chemistry of the material electrodes adopted in fabricating the supercapacitor devices.

Based on the mechanism of charge storage, supercapacitors can be divided into three types, namely electrical double-layer capacitors (EDLCs), faradic capacitors and hybrid capacitors. EDLCs store charges electrostatically through the reversible adsorption of the electrolyte ions onto the active materials surface via non-faradaic reactions, whereas faradaic storage mechanism results from the fast reversible redox reactions (reduction-oxidation reactions) at the electrode/electrolyte interface [4]. Hybrid capacitors are obtained from either making composites of the materials with different charge storage mechanism (EDLC- and faradic-type behavior) or fabricating two distinct electrodes as positive and negative electrodes to form an asymmetric cell. For example, the device could be made from an EDLC-type and faradaic-type materials as the negative electrode and positive electrode, respectively. This offers the possibility of synergizing the advantages of both electrodes such as the high

19

electrical conductivity and stability of EDLC materials along with the high specific capacitance of faradic or pseudo-capacitance materials. The properties of the resulting hybrid device span between a supercapacitor and a battery [5].

In general, the main electrode materials for supercapacitors are carbon-based materials, transition metal oxides/hydroxides and metal chalcogenides materials. Carbon materials such as graphene [6], activated carbon [7], carbon nanotubes [8], carbon aerogels [9], carbide-derived carbons (CDCs) [10], onion-like carbons (OLCs) [11] with unchanged physicochemical properties, good conductivity, relatively low cost, and tunable porous network can provide a long cycle life but relatively low energy densities which are detrimental for most EDLCs applications [12]. They can be used as the main materials in device electrode components or as part of a material blend forming composite electrodes in a supercapacitor. Graphene-based composites for example, adopted as possible supercapacitor materials possess a large advantage in supercapacitor applications due to their superior electrical conductivity, large specific surface area and chemical stability [13]. Graphene is a 2-dimensional (2D) sp^2-hybridized carbon sheet with one atom thickness and has attracted increasing attention because of its unique structure. The electrical conductivity of graphene ($\sim$64 m S cm^{-1}), which is linked to the widespread conjugated sp^2-carbon network, is about 60 times greater than that of carbon nanotubes (CNTs) [22] and remains stable over a wide range of temperatures suitable for energy applications. Compared with other carbon-based materials, graphene shows high electrical properties. However, the restacking and aggregation, which is driven by the strong π-π interactions between the graphene sheets limits the electrochemical performance of graphene-based energy storage devices .Therefore, graphene and other forms of carbonaceous materials have been successfully incorporated into faradic materials to obtain hybrid composites with increasing conductivity as well as electrochemical properties [14,15].

20

Activated carbon (ACs) are mainly used as the electrode material in electrochemical capacitors because of their good electrochemical stability, better porous nature low cost of preparation, high surface area (> 2000 m^2 g^{-1}), nontoxicity, environmental friendliness and high cycling stability [16]. Generally, the specific capacitance resulted from the electric double layer formed at the interface between the electrolyte and the internal surface of pore structure determines the specific capacitance (SSA) of electrodes [17]. However, although the high SSA constitutes a large space for storing ions, the complex network of pore structure may make difficulties for ion storage and transport mechanism, and also might increase diffusion distance and high ion transport resistance during the charge/discharge process [18]. These issues can poorly affect the high power capability of the supercapacitor performance. The porosity of activated carbon can be tailored to the desired pore size distribution by changing the activation process parameters or the type of the synthesis precursor [19]. It has been established that the carbonization and activation of carbon precursor in the presence of graphene, can form composites with better pore structure.

Faradic materials such as metal oxides/hydroxides, transition metal chalcogenides and conducting polymer materials have proven to exhibit excellent specific capacitance as compared to the EDLCs carbon-based materials due to their fast, reversible electrosorption and redox processes taking place at or near the solid electrode surface.

Several pseudocapacitor and/or faradic-type materials like the transition metal oxides/ hydroxides (tMOs and tM-OH)) [20], layered double hydroxides (LDHs) [21] and metal chalcogenides [22] have been developed for energy storage applications due to their stable nanostructures, high theoretical capacity, low preparation cost, environmental friendly nature, ability to conduct charges in fast and reversible faradic reactions at the electrode/electrolyte interface [23]. The morphology of these materials alongside their redox ability makes them

21

suitable candidates for use in ECs. Unfortunately, they are plagued with relatively low mechanical, low conductivity and low cyclic stability.

Among transition metal oxides/hydroxides, cobalt oxide-based nanomaterials such as cobalt hydroxide carbonate and cobalt oxyhydroxide (CoOOH) have been widely adopted as the electrode material for supercapacitor due to their flexibility in tuning their structure and morphology to attain high specific capacitances [24,25]. Even so, cobalt oxyhydroxide (CoOOH) which is an active transition metal hydroxide material with a uniquely defined mesoporous nanosheet-like morphology and low conductivity, has been developed by researchers as a promising alternative electrode material for supercapacitor applications [26]. On the other hand, cobalt hydroxide carbonate has also been used as an electrode material for energy storage due to its controllable morphology done by adjusting the interaction properties between the positively charged layers and anions [27].

In addition, other transition metal hydroxides such as layered double hydroxides (LDHs) containing double metals in a unique pattern have been widely adopted as interesting and promising electrode materials for supercapacitor application [20]. Transitional metal chalcogenides materials have also been considered for electrochemical energy storage applications due to their diverse chemical and physical properties [22]. For example, two-dimensional (2D) layered transition-metal dichalcogenides (tMDs) have been extensively studied for applications in electrochemical supercapacitors due to their promising electrochemical performance, mechanical and thermal stability, cyclability and unique morphology [28]. Furthermore, layered transition-metal dichalcogenides (TMDs) nanostructures provide a much higher specific surface area as compared with bulk counterparts, which is advantageous for energy storage devices because of the possibility of improvement of the contact between the device and the interaction media [22]. Although (tMOs, tM-OH)) and (tMDs) exhibit higher specific capacitance and better cycling stability

22

as compared to the EDLC materials, their poor electrical conductivity and low accessible surface areas limit their use as supercapacitor electrodes.

EDLCs still show a lower specific capacitance as compared to faradic-type capacitors which have much higher specific capacitance values of over 10-100 times, although the electrochemical stability of EDLCs is still way higher than the latter. Therefore, the design and synthesis of electrode materials with improved electrochemical and physical properties are some of the proposed factors which could lead to achieving high energy density and power density for supercapacitors. The poor electrical conductivity of the faradic materials as a result of the structural degradation of the electrode material during redox process adds to the poor stability recorded in faradic-type capacitors and this presents a challenge for their application as the sole materials for supercapacitor electrodes.

It has been observed that modifying the faradic materials with more conductive and electrochemically stable carbon materials to form a composite material is one of the common and effective methods of increasing the conductivity of the combined electrode material as well as its electrochemical properties [29,30]. For example, the enhanced electron transport in graphene material is one of the reasons why most researchers adopt it as a material of choice in making composites with faradic materials applicable in charge storage devices.

Lately, a recent study on the fabrication of reduced graphene oxide-based composites by introducing layered double hydroxides nano-platelets into the interlayer of graphene oxide nanosheets has been reported [21]. An enhancement in the electrochemical performance of the CoAl-LDH/rGO composite probably arose from the addition of porous and conducting graphene to the CoAl-LDH matrix which provides an enhanced electron transfer rate and improved structural support for the growth of CoAl-LDH nanoplatelets on the graphene sheets [21].

Numerous methods have been extensively carried out to synthesize graphene such as substrate-free-gas phase synthesis [31], liquid-phase exfoliation [32], mechanical exfoliation of graphite using scotch tape [33], unzipping of carbon nanotubes [34] and chemical vapor deposition (CVD) [35]. Amongst these methods, graphene synthesized by CVD offers better properties, such as the large crystal domains, mono- to few-layer structure and less defect concentration in the graphene sheets, which are beneficial in increasing carrier mobility for energy storage applications [36].

Graphene foam (GF) nanostructure has been widely adopted in the synthesis of functional composite materials for energy storage [37]. CVD method is used to synthesize the 3D graphene foam nanostructures by using nickel foam (NF) as a growth template and catalyst. The as-obtained GF is characterized by a continuous conducting structure accompanied by a low density (~20 mg cm^{-3}) which makes graphene foam an ideal support matrix for the growth of metal nanostructures leading to high surface area and high conductivity of the composite materials [37]. High conductivity GF obtained from CVD technique facilitates the fast electron transport between the active materials and the current collector.

The combination of faradic materials with the graphene foam further improves the specific capacitance as the faradic materials work as the redox centers [38]. The improved supercapacitor performance of the composites is commonly attributed to the synergetic electrochemical performance effect of graphene and the other material components making up the composite. In another instance, certain faradic materials act as spacing agents to prevent re-stacking between the graphene sheets which on their own part offer an interconnected electrically conductive channel for fast charge transport and easy accessibility of electrolyte ions to the composite electrode. By doing so, it preserves the good performance of electrode even at a high charge-discharge current density [39].

24

There are two main routes adopted for activated carbon synthesis for its large amount production with the high specific surface area: The physical and chemical activation methods. The physical activation process involves the carbonization of carbon-containing raw material followed by the activation of the resulting product in the existence of activating agents such as CO_2 or steam.

Chemical activation involves the impregnation of the carbonaceous raw material with activating agents such as phosphoric acid (H_3PO_4), potassium hydroxide (KOH), potassium carbonate (K_2CO_3), or Zinc chloride ($ZnCl_2$). The impregnated materials are then heat-treated in an inert gas atmosphere at high temperatures to obtain the final AC products [40,41]. Activated carbons prepared by physical or chemical activation have wide pore size distribution from ultra micropores (< 0.7 nm), micropores (< 2 nm), mesopores (~ 2 - 50 nm) and macropores (> 50 nm). In general, chemical activation is usually preferred to physical activation due to the ability to actively control the material properties towards obtaining the desired product for a specific application [7].

Based on a different design pattern, carbon-based nanomaterials can also be combined with faradic-type (or pseudocapacitive) materials in a dissimilar electrode configuration to obtain asymmetric supercapacitors. The advantage of this design lies in combining the electrode material properties without altering the individual material electrochemical performance. Albeit, the previous technique of actively mixing materials with different charge storage mechanisms to produce a composite, also provides an avenue for harvesting other material properties in addition to those attributed to charge storage.

The importance of fabricating an asymmetric cell is to use electrode materials which are stable in different operating potential range in the same electrolyte in order to increase the full cell voltage. The asymmetric supercapacitor combines the properties of the faradic-type material (as the positive electrode) with that of the electric double layer (as the negative

electrode) to increase the full cell voltage. Thus, this improves the energy density more effectively by providing a wider operating voltage window of the full SC device [42].

In this work, a facile CVD method was used to synthesize 3D graphene foam nanostructures by using nickel foam (NF) as a substrate with subsequent acid etching. The GF product was then actively mixed in different mass proportions with faradic-type materials to obtain a graphene-based composite material.

The activated carbon (AC) was also prepared by initial carbonization of the precursor materials with further chemical activation using KOH pellets before being used as a constituent in a composite material as well as the negative electrode for hybrid asymmetric supercapacitors due to the several advantages listed.

1.2 Aims and Objectives

The aim and objectives of this research study are as follows:

- ·Preparation of 3D graphene foam from chemical vapor deposition (CVD) using the nickel foam (NF) template

- Synthesis and characterization of activated carbon (AC) based on graphene foam and from expanded graphite

- Study effect of growth time of hydrothermally grown cobalt hydroxide carbonates on its supercapacitor performance

- Preparation and electrochemical investigation of the cobalt hydroxide carbonate/activated carbon nanocomposites for supercapacitor performance

- Preparation of cobalt oxyhydroxide from CoAl LDH on Ni-GF template and its supercapacitor performance

- Fabrication MoS_2 and VS_2 metal disulphide-graphene composites using hydrothermal technique with graphene in the different configurations such as nanostructured

26

graphene foam and nickel foam – graphene (NF-G) templates as current collectors for high-performance supercapacitor applications

1.3 Thesis Structure

The structure of this thesis can be summarized as follows

- Chapter 1 presents an introduction to the electrochemical supercapacitor device concept and the techniques to improve the device performance. The aim and objectives of this research followed by the organization of the thesis are also included.

- Chapter 2 presents the literature review on the working principles and electrode materials for electrochemical supercapacitor

- Chapter 3 presents the synthesis and characterization techniques employed in this study

- Chapter 4 presents the research results obtained and discussion of the results. A summary of the conclusions from each experimental result will be presented in different sections of chapter 4

- Chapter 5 contains general conclusions from the entire thesis and details of the future work to be performed based on this research study

Bibliography

[1]   A. González, E. Goikolea, J. Andoni, R. Mysyk, Review on supercapacitors : Technologies and materials, 58 (2016) 1189–1206.

[2]   D. Guo, L. Lai, A. Cao, H. Liu, S. Dou, J. Ma, Nanoarrays: design, preparation and supercapacitor applications, RSC Adv. 5 (2015) 55856–55869.

[3]   V.V.N. Obreja, On the performance of supercapacitors with electrodes based on carbon nanotubes and carbon activated material-A review, Phys. E Low-Dimensional Syst. Nanostructures. 40 (2008) 2596–2605.

[4]   J.W. Long, B. Dunn, D.R. Rolison, H.S. White, Three-dimensional battery architectures, Chem. Rev. 104 (2004) 4463–4492.

[5]   Y.-G. Wang, L. Cheng, Y.-Y. Xia, Electrochemical profile of nano-particle CoAl double hydroxide/active carbon supercapacitor using KOH electrolyte solution, J. Power Sources. 153 (2006) 191–196.

[6]   L.L. Zhang, R. Zhou, X.S. Zhao, Graphene-based materials as supercapacitor electrodes, J. Mater. Chem. 20 (2010) 5983–5992.

[7]   M. Sevilla, R. Mokaya, Energy storage applications of activated carbons: supercapacitors and hydrogen storage, Energy Environ. Sci. 7 (2014) 1250–1280.

[8]   E. Frackowiak, V. Khomenko, K. Jurewicz, K. Lota, F. Béguin, Supercapacitors based on conducting polymers/nanotubes composites, J. Power Sources. 153 (2006) 413–418.

[9]   W. Liu, X. Li, M. Zhu, X. He, High-performance all-solid state asymmetric supercapacitor based on Co_3O_4 nanowires and carbon aerogel, J. Power Sources. 282 (2015) 179–186.

[10]   V. Presser, M. Heon, Y. Gogotsi, Carbide-derived carbons - from porous networks to nanotubes and graphene, Adv. Funct. Mater. 21 (2011) 810–833.

[11] D. Pech, M. Brunet, H. Durou, P. Huang, V. Mochalin, Y. Gogotsi, et al., Ultrahigh-power micrometre-sized supercapacitors based on onion-like carbon, Nat. Nanotechnol. 5 (2010) 651–654.

[12] J. Yan, Z. Fan, W. Sun, G. Ning, T. Wei, Q. Zhang, et al., Advanced asymmetric supercapacitors based on $Ni(OH)_2$/graphene and porous graphene electrodes with high energy density, Adv. Funct. Mater. 22 (2012) 2632–2641.

[13] Y. Bin Tan, J.-M. Lee, Graphene for supercapacitor applications, J. Mater. Chem. A. 1 (2013) 14814.

[14] C. Liu, Z. Yu, D. Neff, A. Zhamu, B.Z. Jang, Graphene-based supercapacitor with an ultrahigh energy density, Nano Lett. 10 (2010) 4863–4868.

[15] J. Radich, P. McGinn, P. Kamat, Graphene-based Composites for Electrochemical Energy Storage, Electrochem. Soc. Interface. 20 (2011) 63–66.

[16] L.L. Zhang, Y. Gu, X.S. Zhao, Advanced porous carbon electrodes for electrochemical capacitors, J. Mater. Chem. A. 1 (2013) 9395–9408.

[17] F. Lufrano, P. Staiti, Mesoporous carbon materials as electrodes for electrochemical supercapacitors, Int. J. Electrochem. Sci. 5 (2010) 903–916.

[18] S. Bose, T. Kuila, A.K. Mishra, R. Rajasekar, N.H. Kim, J.H. Lee, Carbon-based nanostructured materials and their composites as supercapacitor electrodes, J. Mater. Chem. 22 (2012) 767.

[19] E. Frackowiak, Q. Abbas, F. Béguin, Carbon/carbon supercapacitors, J. Energy Chem. 22 (2013) 226–240.

[20] F. Shi, L. Li, X. Wang, C. Gu, J. Tu, Metal oxide/hydroxide-based materials for supercapacitors, RSC Adv. 4 (2014) 41910–41921.

[21] L. Zhang, K.N. Hui, K.S. Hui, H. Lee, Facile synthesis of porous CoAl-layered double hydroxide/graphene composite with enhanced capacitive performance for

supercapacitors, Electrochim. Acta. 186 (2015) 522–529.

[22] M.-R. Gao, Y.-F. Xu, J. Jiang, S.-H. Yu, Nanostructured metal chalcogenides: synthesis, modification, and applications in energy conversion and storage devices., Chem. Soc. Rev. 42 (2013) 2986–3017.

[23] G. Wang, L. Zhang, J. Zhang, A review of electrode materials for electrochemical supercapacitors, Chem. Soc. Rev. 41 (2012) 797.

[24] H. Wang, H.S. Casalongue, Y. Liang, H. Dai, $Ni(OH)_2$ nanoplates grown on graphene as advanced electrochemical pseudocapacitor materials, J. Am. Chem. Soc. 132 (2010) 7472–7477.

[25] J. Deng, L. Kang, G. Bai, Y. Li, P. Li, X. Liu, et al., Solution combustion synthesis of cobalt oxides (Co_3O_4 and Co_3O_4/CoO) nanoparticles as supercapacitor electrode materials, Electrochim. Acta. 132 (2014) 127–135.

[26] K.K. Lee, W.S. Chin, C.H. Sow, Cobalt-based compounds and composites as electrode materials for high-performance electrochemical capacitors, J. Mater. Chem. A. 2 (2014) 17212–17248.

[27] Z. Zhao, F. Geng, J. Bai, H.M. Cheng, Facile and controlled synthesis of 3D nanorods-based urchinlike and nanosheets-based flowerlike cobalt basic salt nanostructures, J. Phys. Chem. C. 111 (2007) 3848–3852.

[28] D. Merki, X. Hu, Recent developments of molybdenum and tungsten sulfides as hydrogen evolution catalysts, Energy Environ. Sci. 4 (2011) 3878–3888.

[29] M.A. Bissett, I.A. Kinloch, R.A.W. Dryfe, Characterization of MoS_2-Graphene Composites for High-Performance Coin Cell Supercapacitors, ACS Appl. Mater. Interfaces. 7 (2015) 17388–17398.

[30] K.-J. Huang, L. Wang, Y.-J. Liu, Y.-M. Liu, H.-B. Wang, T. Gan, et al., Layered MoS_2-graphene composites for supercapacitor applications with enhanced capacitive

performance, Int. J. Hydrogen Energy. 38 (2013) 14027–14034.

[31]   A. Dato, M. Frenklach, V. Radmilovic, L.E.E. Zonghoon, Substrate-free gas-phase synthesis of graphene sheets, (2010).

[32]   Y. Hernandez, V. Nicolosi, M. Lotya, F.M. Blighe, Z. Sun, S. De, et al., High-yield production of graphene by liquid-phase exfoliation of graphite, Nat. Nanotechnol. 3 (2008) 563–568.

[33]   G.S. Shmavonyan, G.G. Sevoyan, V.M. Aroutiounian, Enlarging the surface area of monolayer graphene synthesized by mechanical exfoliation, Armen. J. Phys. 6 (2013) 1–6.

[34]   D. V Kosynkin, A.L. Higginbotham, A. Sinitskii, J.R. Lomeda, A. Dimiev, B.K. Price, et al., Longitudinal unzipping of carbon nanotubes to form graphene nanoribbons, Nature. 458 (2009) 872–876.

[35]   A. Reina, X. Jia, J. Ho, D. Nezich, H. Son, V. Bulovic, et al., Large area, few-layer graphene films on arbitrary substrates by chemical vapor deposition, Nano Lett. 9 (2008) 30–35.

[36]   L.L. Zhang, R. Zhou, X.S. Zhao, Graphene-based materials as supercapacitor electrodes, J. Mater. Chem. 20 (2010) 5983.

[37]   X. Huang, X. Qi, F. Boey, H. Zhang, Graphene-based composites, Chem. Soc. Rev. 41 (2012) 666–686.

[38]   M. Zhi, C. Xiang, J. Li, M. Li, N. Wu, Nanostructured carbon--metal oxide composite electrodes for supercapacitors: a review, Nanoscale. 5 (2013) 72–88.

[39]   X. Cao, Z. Yin, H. Zhang, Three-dimensional graphene materials: preparation, structures and application in supercapacitors, Energy Environ. Sci. 7 (2014) 1850–1865.

[40]   J. Hayashi, T. Horikawa, I. Takeda, K. Muroyama, F.N. Ani, Preparing activated

carbon from various nutshells by chemical activation with K_2CO_3, Carbon N. Y. 40 (2002) 2381–2386.

[41] Y. Sudaryanto, S.B. Hartono, W. Irawaty, H. Hindarso, S. Ismadji, High surface area activated carbon prepared from cassava peel by chemical activation, Bioresour. Technol. 97 (2006) 734–739.

[42] J. Zhang, J. Jiang, H. Li, X.S. Zhao, A high-performance asymmetric supercapacitor fabricated with graphene-based electrodes, Energy Environ. Sci. 4 (2011) 4009.

CHAPTER 2

2.1 Literature Review

Supercapacitors are energy storage devices that make use of high surface area electrode materials and thin electrolytic dielectrics to attain capacitance values that are greater than those of the conventional capacitors [1,2]. Due to high surface area and thin electrolytic dielectrics, supercapacitors are capable of accomplishing high energy densities as compared to conventional capacitors while maintaining high power densities as compared to batteries. The performance of a supercapacitor device as compared to other energy storage devices is shown in Fig. 2.1; known as the "Ragone plot". This graph shows a clear comparison of the energy densities versus the power densities of these devices. From this graph, it can be seen that supercapacitor bridges the gap between conventional capacitors and batteries in terms of both power and energy densities. In other words, batteries are well known for their high energy densities but suffer from low power densities, whereas conventional capacitors display high power densities but suffer from low energy densities and supercapacitors have energy and power densities values comprised between those of these two devices as shown in Fig. 2.1.

33
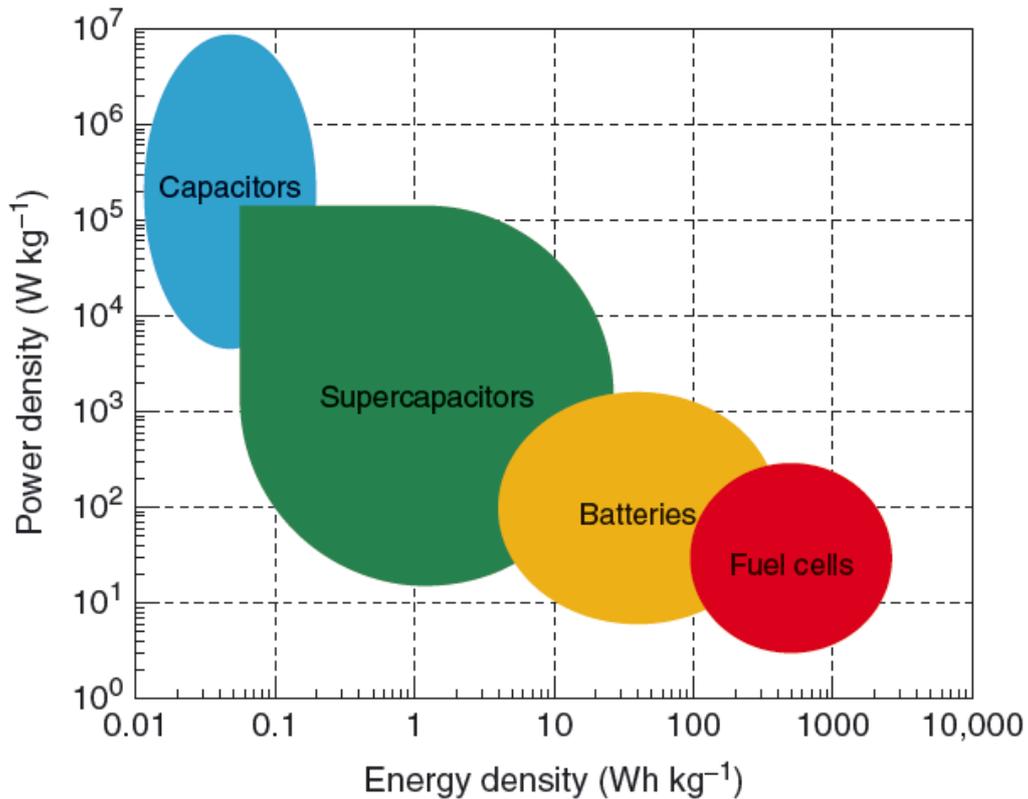
Figure 2.1: Ragoneplot showing the energy density against power density for various energy storage systems [3].

Table 2.1 put into perspective some parameters of supercapacitors, batteries and conventional capacitors. Although supercapacitors have greater specific capacitance than conventional capacitors, they are yet to match the energy densities of batteries and fuels cells. To that regard, most of the current research is focusing on the development of cost-effective suitable electrode materials with high specific capacitance and large working potential, which will improve the energy density of the corresponding supercapacitor.

34

Table 2.1: Comparison of capacitor, supercapacitor and battery characteristics [4].

Parameters	Capacitor	Supercapacitor	Battery
Charge time	10^{-5}-10^{-3} sec	1-30 sec	3-4 hrs
Discharge time	10^{-5}-10^{-3} sec	1-30 sec	1-5 hrs
Energy density(W.h/kg)	<0.1	1-10	20-100
Power density (W/Kg)	>10 000	1000-2000	50-200
Cycle life	>500 000	>100 000	500-2000
Charge/discharge efficiency	~ 1.0	0.90~0.95	0.7~0.85

Supercapacitors consist of two electrodes immersed in an electrolyte separated by a dielectric separator, as shown in Fig. 2.2. During charging, ions from the electrolyte move between the positive and negative electrodes. The positive electrode attracts negative ions, whereas the negative electrode attracts positive ions, thus, creating an electric field that permits the capacitor to store energy. The electrode/electrolyte interface can be regarded as conventional dielectric capacitor, with the capacitor C defined as the ratio of stored charge Q to the applied voltage V as defined in equation 2.1:

$$C = \frac{Q}{V}$$

2.1
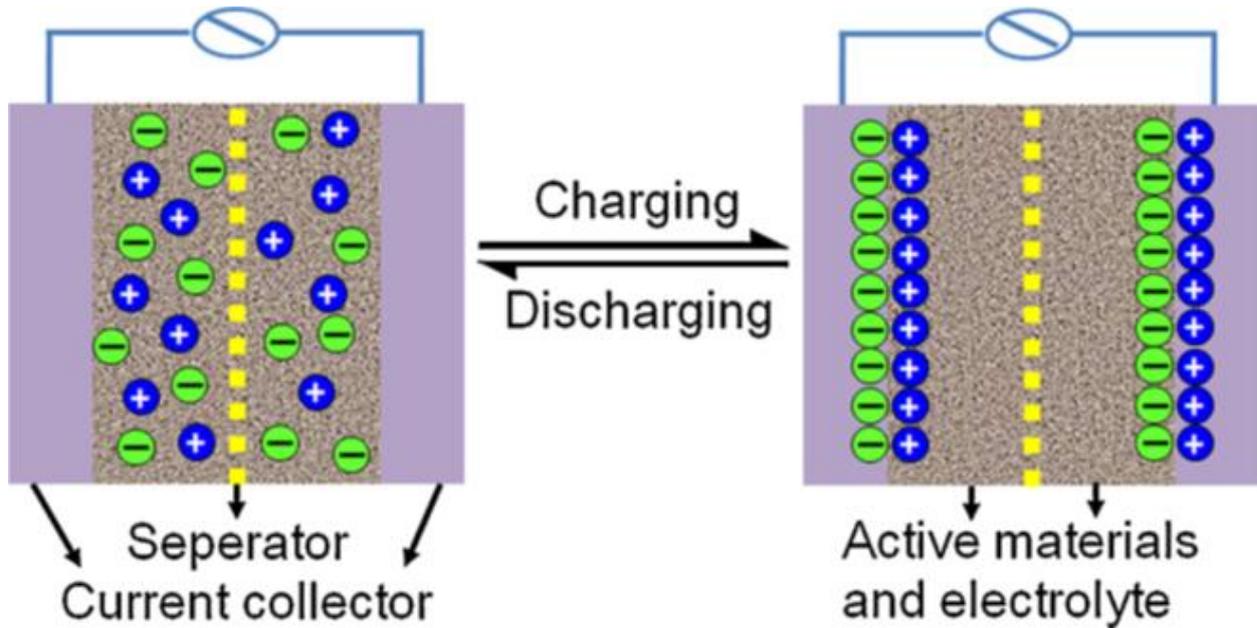
Figure 2.2: Schematic sketch of the charging-discharging process in the supercapacitor [5].

The two main characteristics of any energy storage devices are their energy and power densities. Energy density describes the amount of energy that can be stored while the power density describes how fast the energy stored is released. The maximum energy (E) stored and maximum power (P) for a capacitor are calculated using equation 2.2 and 2.3.

$$E = \frac{1}{2}C_{sp}V^2 \qquad\qquad 2.2$$

$$P = \frac{V^2}{4R_s M} \qquad\qquad 2.3$$

where V is cell voltage (in volts), C_{sp} is the total specific capacitance of the cell (F g^{-1}) and R$_s$ is the equivalent series resistance (ESR) which consists of the electrode resistance, electrolyte resistance and resistance due to the diffusion of ions in the electrode pores and M is the total mass of the two electrodes. To achieve a supercapacitor with high performance, the essential requirements are high operating cell voltage, the large specific capacitance associated to low ESR value. These parameters are intimately related to the specific surface area, the pore size distribution and the conductivity of the electrode material.

36

The selection of the electrode material and also the electrolyte solution is critical in improving the performance of the supercapacitor. For a given electrolyte, the performance of the cell depends on upon the electrochemical performance of the electrode themselves. As a result, it is important to design electrode materials with suitable microstructure and required chemo-physical properties that support the enhancement of specific surface area and porosity. In other words, the electrochemical performance of an EC mostly depends on upon the performance of the two electrodes in the given electrolyte. Therefore, electrode material selection is a very important aspect affecting the supercapacitor performance. As shown in Fig. 2.3, electroactive materials that are ideal for supercapacitor should have good electric conductivity which can be improved by decreasing the size of the electroactive material-, larger specific surface area -which can be developed by producing nano-sized particles with micro, and mesoporous structure that facilitate good ion transportation , and appropriate ion transportation, which can be accomplished by arranged meso and macro porous electroactive materials with systematic pores for fast ions transportation at high rates.
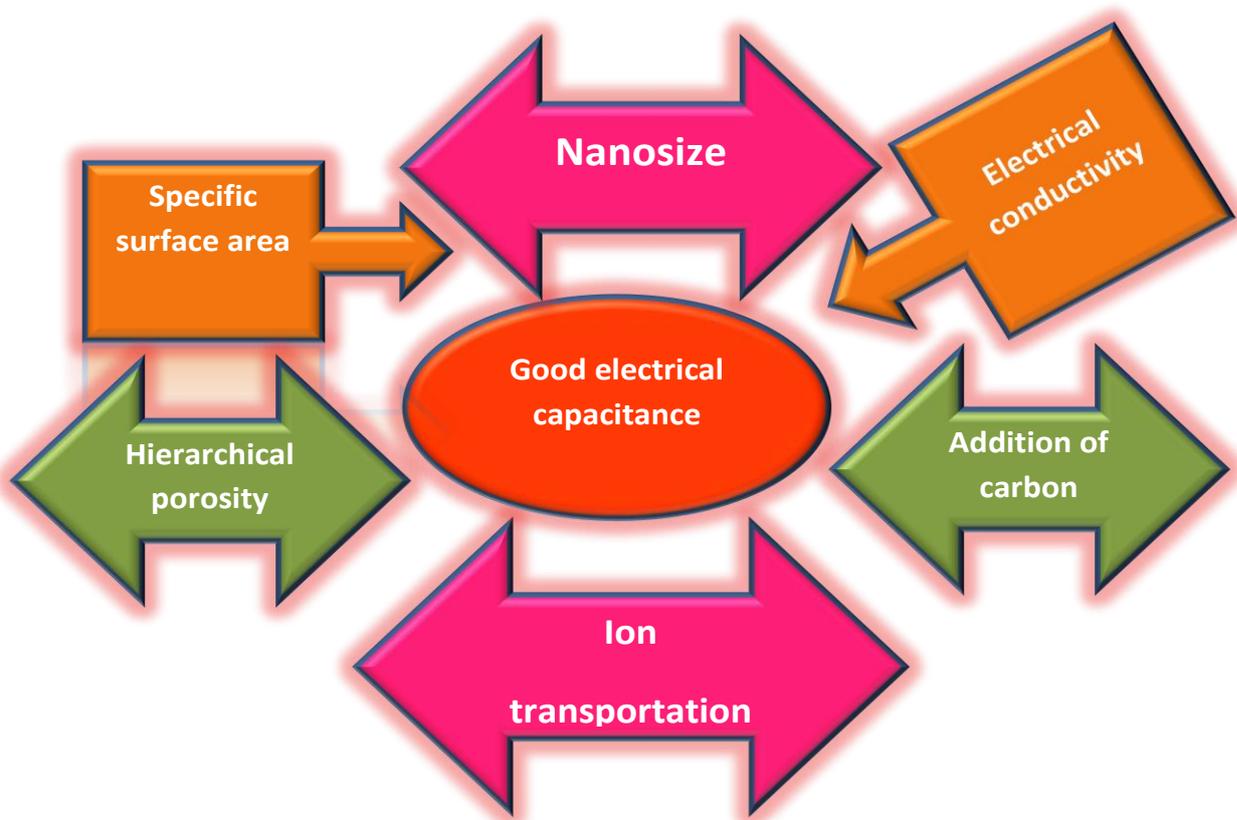
Figure 2.3: Diagram presenting factors contributing to the good electrochemical performance of ECs materials.

2.2 Storage Mechanism of Supercapacitor

Supercapacitors device can be divided into three types depending on the charge storage mechanism, namely: electrical double-layer capacitors (EDLCs), faradaic capacitors and hybrid systems as shown in Fig. 2.4. Each class is characterized by its distinctive mechanism for storing the charge as explained in the introduction of this work. This section will present an overview of each of these three classes of supercapacitors and their subclasses with distinguished electrode materials. Although the classification is based on the type of electrodes used, it also controls the way in which charges are generated and stored.

38
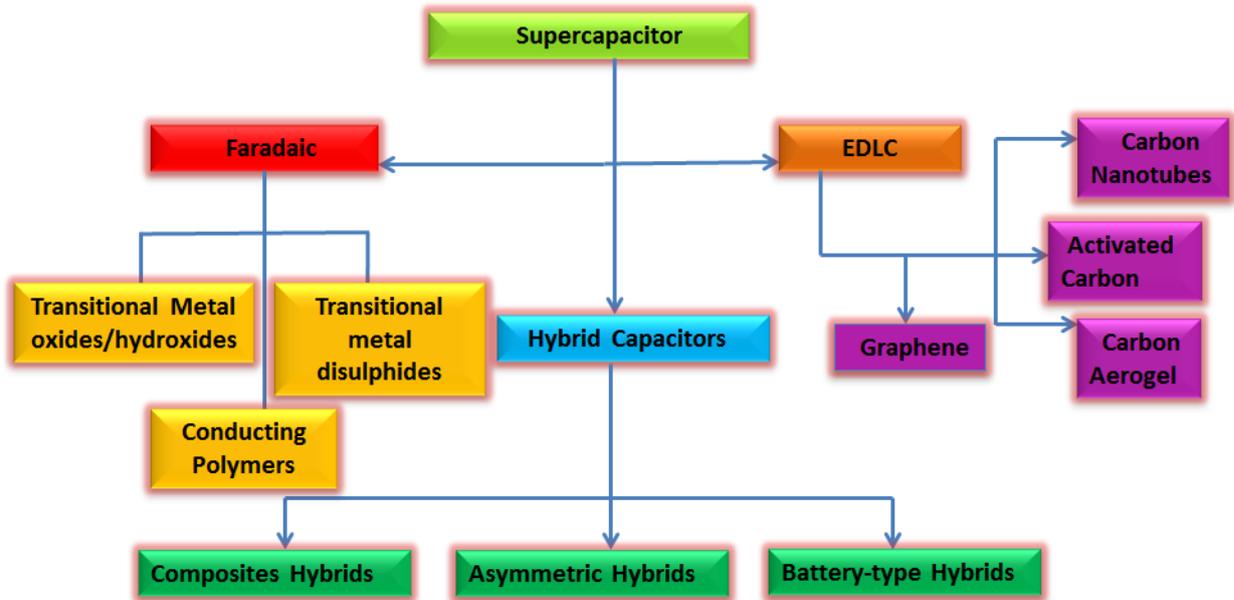
Figure 2.4: Chart showing the different types of supercapacitors.

2.2.1 Electrical Double-Layer Capacitors (EDLCs)

In EDLCs, the charge is stored electrostatically through the accumulation of the electrolyte ions onto the surface of the active materials and thus forming a double layer at the electrode/electrolyte interface as shown in Fig. 2.5. EDLCs electrodes are based on carbon materials. During the process of charging, cations travel towards the negative electrodes while anions accumulate near the positive electrode surface. For that reason, energy is stored in the electric double-layer interface [6]. When the charges are released, the reverse process takes place within the electrolyte. There is no transfer of charge between the electrolyte and electrode or no ion exchanges occur between the electrode and the electrolyte and the storage of electric charge and energy is mostly electrostatic in nature [7]. This indicates that the electrolyte concentration remains constant during the charging/discharging processes.

39
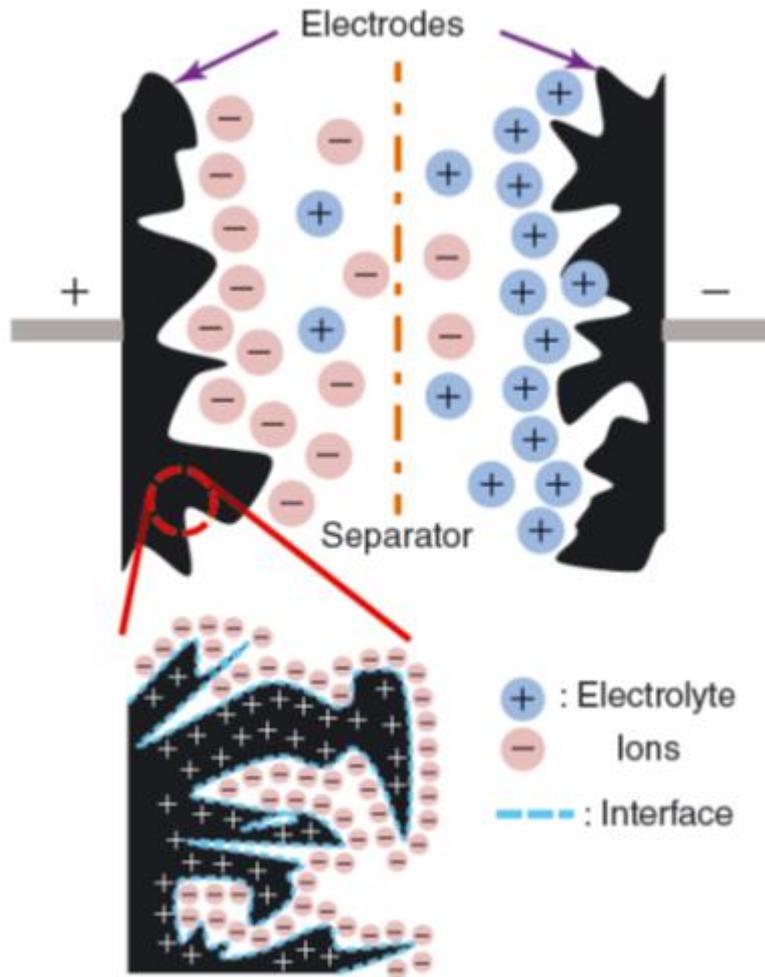
Figure 2.5: Schematic of EDLC based on porous carbon electrode material [3].

This double-layer capacitance was first proposed by von Helmholtz in the 19th century describing the distribution of opposite charges at the interface of colloidal particles [8]. The Helmholtz double layer model states that two adjacent layers of opposite charges are produced and focused at the electrode/electrolyte interface representing the conventional parallel plate capacitor. Ions of opposite sign diffuse through the electrolyte to form a condensed layer in a plane parallel to the electrode surface ensuring charge neutrality which is called electric double layer (EDL) as shown in Fig. 2.6 (a)
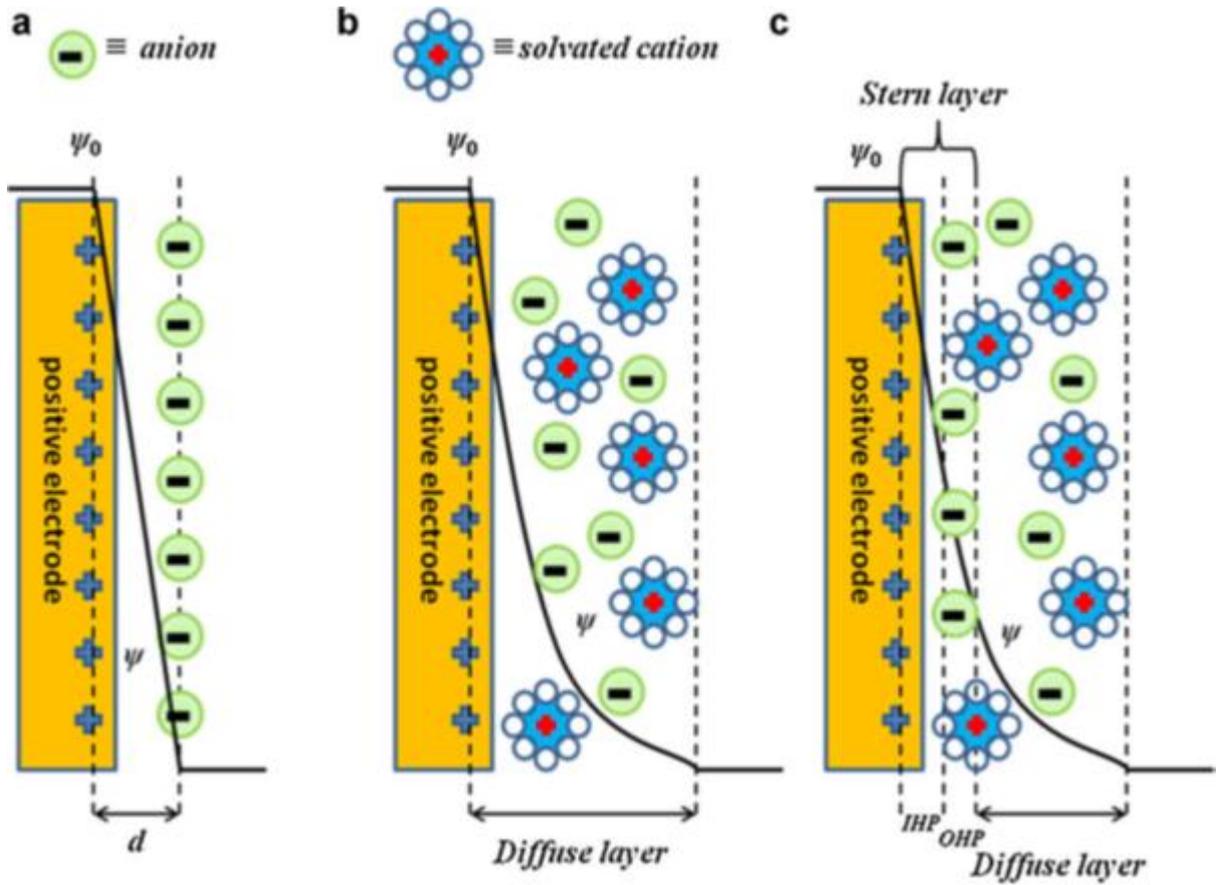
Figure 2.6: (a) Helmholtz, (b) Gouy-Chapman and (c) Stern-model of the electric double layer formed at a positively charged electrode in an aqueous electrolyte [9].

The capacitor can be described according to equation 2.4 below.

$$C = \frac{\varepsilon_0 \varepsilon_r A}{d}$$

2.4

where C is the EDL capacitance (F g^{-1}), ε_0 is the dielectric constant or permittivity of electrolyte (ε_0 =8.854 ×10^{-12} F m^{-1}), ε_r is the relative permittivity of the dielectric electrolyte, A is the specific surface area (cm^2 g^{-1}) and d is the distance between the centers of the ions and the porous electrode surface.

This capacitance model was later refined by Gouy and Chapman by suggesting a constant distribution of electrolyte ions (both cations and anions) in the electrolyte solution, determined by the thermal motion which is described as the diffuse layer, as shown in (Fig.

41

2.6 (b)) [10]. Nevertheless, the Gouy-Chapman model overestimated the EDL capacitance since capacitance of two separated arrays of charges increase inversely with their separation distance and a very large capacitance value would be obtained in the case of point charge ions close to the electrode surface [11]. Later, Sterns in 1924 proposed a model by combining the Helmholtz and Gouy-Chapman models by taking into account the accumulation of the ions close to the electrode surface and the hydrodynamic motion of the ionic species in the diffuse layer (Fig 2.6 (c)) [12]. These two layers are equivalent to two capacitors in series: C_H and C_D. The total capacitance of the electrode (C_{DL}) is given by the following equation:

$$\frac{1}{C_{dl}} = \frac{1}{C_H} + \frac{1}{C_D}$$

2.5

where C_{dl} is the capacitance in the EDL from two regions. C_H is the Helmholtz capacitance arising from the compact double layer and C_D is the diffusion capacitance arising from the diffusion region of the double layer capacitance. Different forms of carbon materials that can be used in EDLC electrodes are graphene, activated carbons, carbon nanotubes and carbon aerogels.

2.2.2   Faradaic Capacitors

In faradic capacitors, most of the charge is transferred at the surface or in the bulk near the surface of the solid electrode material. Therefore, the interaction between the solid material and the electrolyte consists of faradaic reactions, which can be designated as charge transfer reactions.

The charge in these reactions is voltage-dependent resulting in the faradaic capacitors. The electrochemical charge storage in faradaic capacitors occurs based on certain faradic mechanism such as electrosorption, reduction-oxidation reactions and intercalation as shown in Fig 2.7 [13]. Electrosorption underpontential deposition takes place when the electroactive

42

species from the electrolyte gets adsorbed on the surface of the electrode and undergoes redox reaction at particular potential. One example is the deposition of lead on the surface of a gold (Au) electrode [14]. The reduction-oxidation process occurs when ions are electrochemically adsorbed on the surface or near the surface of an electrode material with associated faradaic charge transfer. Intercalation process involves the insertion of ions into the tunnels or layer of redox active material accompanied by a faradaic charge transfer with no crystallographic phase change [15]. These processes may allow faradaic capacitors to achieve greater capacitance and energy density than EDLCs, since the electrochemical process occur both on the surface and in the bulk near the surface of the solid electrode. Reactions that results in faradaic charge transfer process are mainly of redox type similar to battery materials. The difference between materials suitable for faradaic and batteries remain in the surface reactions. Faradaic materials are based on kinetic behavior, while the battery materials utilize the bulk solid state to store energy. Furthermore, reactions that occur at the surface of the electrode are limited by the surface available and not by solid-state diffusion and then display high rate capability whereas battery materials are limited by the solid-state diffusion within the cathode and the anode inhibiting its power capability [15]. Faradaic charge storage can be intrinsic or extrinsic to the materials. Intrinsic faradaic materials are those which show redox capacity for a broad range of particle sizes and morphologies[16]. These are materials such as MnO_2 , $Nb_2 O_5$ and $RuO_2.nH_2O$ [17–19] . While the extrinsic materials during ion storage do not exhibit any faradaic in the bulk state due to phase transformations, these materials increase the surface area through nanostructure to enhance high-rate behavior due to a decrease in diffuse distances [16]. Example of widely used extrinsic faradaic material is $LiCoO_2$ [20].

a) Underpotential Deposition

$Au + xPb^{2+} + 2xe^- \rightarrow Au \cdot xPb_{ads}$

b) Redox Pseudocapacitance

$RuO_x(OH)_y + \delta H^+ + \delta e^- \leftrightarrow RuO_{x-\delta}(OH)_{y+\delta}$

c) Intercalation Pseudocapacitance

$Nb_2O_5 + xLi^+ + xe^- \leftrightarrow Li_xNb_2O_5$
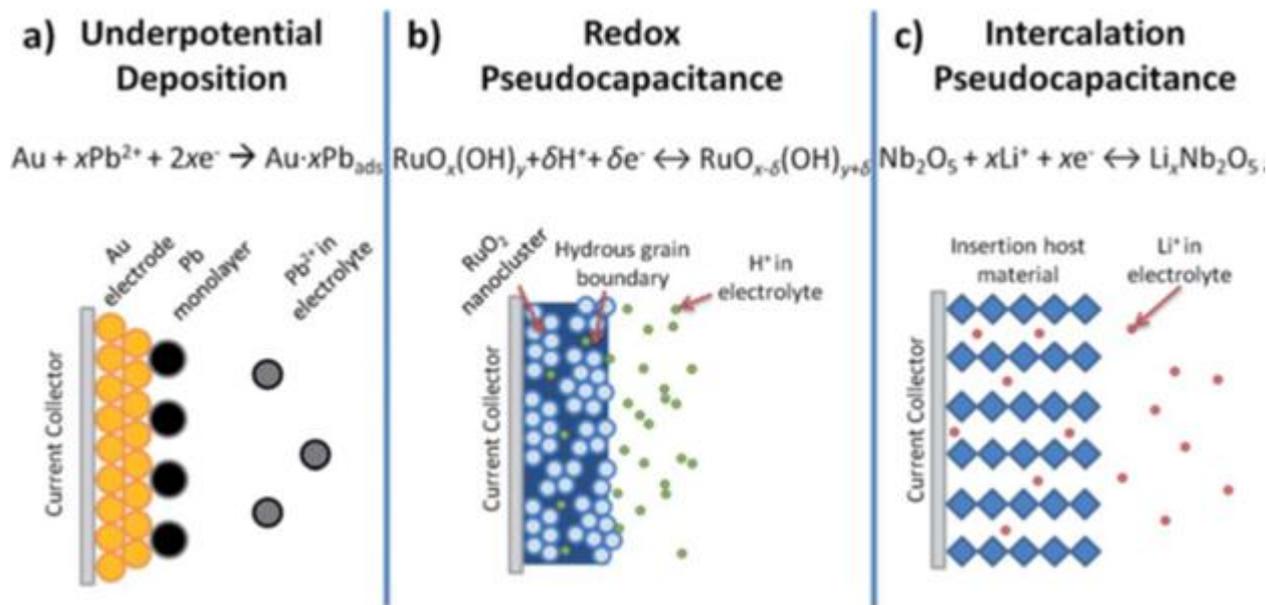
Figure 2.7: Different types of reversible redox mechanisms that give rise to faradaic (a) electrosorption underpotential deposition, (b) redox and (c) intercalation [15].

The faradaic electrode materials commonly used are transition metal oxides/hydroxides, conductive polymers and transition-metal dichalcogenides. Hydrous ruthenium dioxide (RuO_2) was the first faradaic electrode materials discovered in 1971 and has been extensively studied [21]. Ruthenium oxide (RuO_2) especially in its hydrated form ($RuO_2.xH_2O$) is considered to be the most advantageous electrode material due to its high theoretical specific capacitance (about 1000 F g^{-1}), good thermal stability, high rate capability, metallic-type conductivity, long cycle life, high reversible redox reactions and high proton conductivity [22]. The faradaic behavior of both amorphous and crystalline forms of ruthenium oxides have been widely studied in the different acidic electrolyte. It was revealed that amorphous hydrous ruthenium oxide $(RuO_2.xH_2O)$ displays a much higher specific capacitance of 720 Fg^{-1} than anhydrous ruthenium oxide [17]. This was attributed to the mixed proton-electron conductivity within $RuO_2.xH_2O$, as the superficial redox transitions of ruthenium oxide consist of proton and electron double injection/expulsion according to the following equation.

44

$$RuO_x(OH)_y + \delta H^+ + \delta e^- \Leftrightarrow RuO_{x-\delta}(OH)_{y+\delta} \qquad\qquad 2.6$$
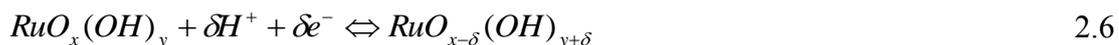
where $RuO_x(OH)_y$ and $RuO_{x-\delta}(OH)_{y+\delta}$ signifies the interfacial oxyruthenium species at higher and lower oxidation states. When Ruthenium oxide is used as an electrode material, a series of redox process occur, resulting in the variation of oxidation state among the Ru^{4+}, Ru^{3+}, and Ru^{2+}. The good conductivity, larger surface area and rapid proton transport all contribute to the rapid and reversible faradaic reactions with high capacitance. Hu *et al* reported specific capacitance of 1300 F g^{-1} for a pure bulk nanostructured $RuO_2.xH_2O$ electrode [23]. The higher electrochemical performance of $RuO_2.xH_2O$ is related to its tailored nanotubular arrayed porous architecture with metallic conductivity as well as hydrous nature. As shown in equation (2.7) the reversible redox reactions depend on both proton exchange and electron-hopping process. The tubular arrayed porous structure and metallic conductivity provided an operative pathway for electrolyte and electron transportation. Additionally, Long *et al* reported that hydrous nature of $RuO_2.xH_2O$ confirms a high rate of proton exchange because the surface of the hydrous oxide reflected to be a proton liquid [24]. Therefore, the considered nanostructure is a promising electrode for supercapacitor. However, commercial application of ruthenium oxide is obstructed due to its high cost, low porosity and toxic nature. Alternatively, other faradaic materials which are cost effective in production, have low toxicity and are environmental friendly have been considered for supercapacitor application. Other transition metal oxides, metal hydroxides, layered double hydroxides (LDHs) and metal chalcogenides have been explored and will be explained in coming sections. Although faradaic capacitors offer much higher energy density compared to a EDLCs, they usually suffer from relatively lower power density than EDLCs because the redox electrodes typically have poor electrical conductivity and faradaic processes are generally slower than non-faradaic processes. Additionally, they often sustain

45

poor stability during cycling owing to redox reactions. Therefore, it has been established that the composites of these metal hydroxides, layered double hydroxides and metal chalcogenides with carbon materials to form so-called hybrid materials enhance the charge transfer of the faradaic materials.

2.2.3 Hybrid Capacitors

Hybrid capacitors combine two electrodes with different charge storage behavior, one electrode being an EDLC (non-faradaic) and the other being faradaic material in order to attain better performance. Utilizing both faradaic and non-faradaic processes to store charge, hybrid capacitors have attained energy and power densities greater than EDLCs with higher cycling stability that has limited the success of faradic capacitors. Research has focused on three different types of hybrid capacitors, distinguished by their electrode structure, namely composites, asymmetrical, and battery-like hybrids respectively as shown in Fig. 2.4.

2.2.3.1 Composite Hybrid

Composites electrodes incorporate EDLCs (non-Faradaic) materials with faradaic materials and combine both chemical and physical charge storage together in a single electrode. Therefore fabrications of composites by using carbon as a support for faradic materials not only increase the effective utilization of the active materials, but also improve the electrical conductivity and mechanical strength of the composite materials. Carbon has been used with other faradaic materials in order to increase the contact between the faradaic material and the electrolyte, but also to increase the composite electrodes capacity through faradaic reaction. Carbon materials provide interconnecting mesostructured supports that can facilitate good nanoparticle dispersion and electron transport. Carbon materials such as graphene, activated carbon and carbon nanotubes are widely used for this purpose.

46

2.2.3.2 Asymmetric Hybrids

In an asymmetric supercapacitor, two different electrodes based on different charge storage mechanism are used. This configuration has increased attention because it has shown to reach higher energy density while maintaining high power density of the device [95]. This is achieved by using different types of materials as electrodes that work in different electrochemical potential window ranges within the same electrolyte. As a result, this will increase the device potential and subsequently its energy density [25]. Carbon-based materials such as activated carbon (AC), carbon nanotubes (CNTs), graphene [26,27] are frequently used as the negative electrodes of asymmetric supercapacitors due to their stability in the negative potential region, good electronic conductivity, large surface area and relatively low-cost [28]. Various transition metal oxides, transition-metal dichalcogenides and conductive polymers are mostly used as positive electrodes due to their fast and reversible electron exchange reactions at the electrode interface which contribute to the high power densities and high capacitance of asymmetric supercapacitors [29,30]. Activated carbon (AC) is the most suitable negative electrode material adopted for asymmetric capacitors due to the numerous merits listed above but also due to its facile preparation process [31,32].

2.2.3.3 Battery-type Hybrid

Comparable to asymmetric, battery-type combine two different electrodes. In other words, it is a combination of an EDLC and battery materials, for example, lead dioxide, LTO ($Li_4Ti_5O_{12}$) and activated carbon as the other [33,34]. This particular configuration reflects the demand for higher energy supercapacitors and higher power batteries, combining the energy characteristics of batteries with the power, cycle life, and recharging times of supercapacitors.

47

2.3 Electrodes Materials for Supercapacitor

The performance of supercapacitor is determined by the combination of the nature of the electrodes and electrolyte used. Supercapacitors are mostly classified through the electrodes used. In general, electrode materials including carbon materials, conducting polymers and transition metal oxides and their composites have been used for supercapacitor [11]. The electrode materials showing either EDLC or faradaic behaviour each have their particular advantages and disadvantages [35]. Some properties that are required by a material for EC application are listed as follows:

- Cycling capability ($>10^5$) and resulting high stable cycle life

- Lack of functional groups to undergo an irreversible redox process along the material surface

- High specific surface area to develop the electric double layer, in the range of (1000-2000 m^2g^{-1})

- Thermodynamic stability beyond the potential window of operation

- Controlled pore size distribution to develop high capacitance while minimizing internal resistance.

- Surface wettability of the electrolyte

- Mechanical reliability for its integration into a practical electrochemical capacitor (EC) cell

2.3.1 Electrode Material for EDLC Supercapacitors

2.3.1.1 Carbon-based materials

Different forms of carbon materials that can be used to store charge in EDLC electrodes such as carbon nanotubes, activated carbon, carbon nanofibers and graphene have been intensively studied in recent times due to their unique structural and morphological properties [35]. A

48

wide range of structures is attainable as a result of four crystalline allotropes of carbon, including diamond (sp^3 bonding), graphite (sp^2), fullerenes (distorted sp^2) and carbide (sp) [36]. The important factors influencing the electrochemical performance of carbon materials are the specific surface area, pore-size distribution, pore shape and structure, electrical conductivity, and surface functionality.

a) Graphene

Graphene is a promising candidate as electrode material for EDLC supercapacitor. Due to its unique hexagonal lattice structure (Fig 2.8), graphene exhibit appealing properties which were already discussed in chapter 1. Graphene layer can be considered as the basic building block for carbon materials of all allotropic dimensionalities such as 0D fullerene, 1D nanotubes and 3D graphite as shown in Fig 2.8. Experimental synthesis, firstly done by Geim and Novoselov *et al*. in 2004, has enticed wide interest because of its unique two dimension (2D) structure [37]. The electrical conductivity of graphene is high; it has excellent mechanical, chemical and electrical properties. However, graphene suffers from irreversible capacity loss due to the re-stacking of the graphene sheets because of their strong π-π bond interaction between the neighboring sheets, leading to inter-sheet resistance, decrease in the accessible of surface area for electrolyte ions, resulting to low specific capacitance for the pristine graphene electrode. Furthermore, 2D pristine graphene sheets also show several limitations for their direct applications, arising from zero band gaps, propensity of aggregation and poor diffusion in common solvents, which lessen the accessible surface areas, perimeter electron and ion transportation and thus modest improvement in the cell performance. Also disordered nanocomposite films containing aggregated graphene makes it difficult for ions to gain access to the electrode surface and therefore become a challenge [38].

49
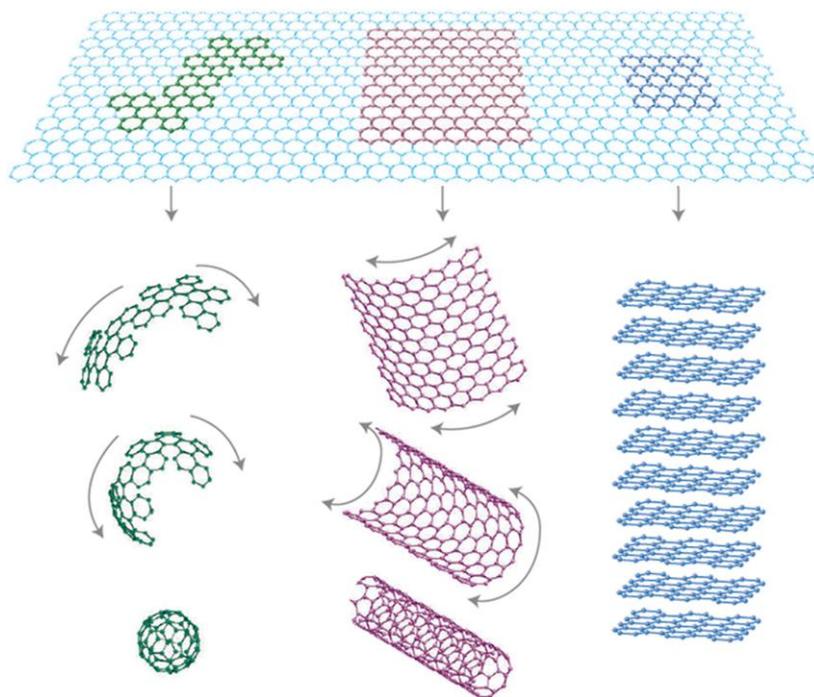
Figure 2.8: Graphene building block for carbon materials with different dimensionalities [39] .

To avoid the re-stacking of graphene sheets, composites made of graphene and faradaic materials seem to be a good solution. This is beneficial for both materials because of their synergistic effect. Faradaic materials prevent graphene from re-stacking, and hence increase the available surface area. Graphene helps the formation of nanostructured faradaic materials with uniformly dispersed and controlled morphologies, suppressing the volume change and agglomeration of faradaic materials. Most results on graphene-based nanocomposites have been achieved by incorporating various nanostructures. Here will give examples of such reports for Co based oxides/hydroxides and metal chalcogenides which are the materials of the interest in this study.

For example Zhang et *al*. reported a synthesized porous CoAl-layered double hydroxide/graphene composite by simple gas-liquid interfacial method .The composites provided the specific capacitance of 479.2 Fg^{-1} at current density of 1 Ag^{-1} with enhanced capacitive performance for supercapacitor. The improvement in the CoAl-layered double hydroxide/graphene was attributed to homogeneously attachment of CoAl-LDHs crystallites

50

to conductive graphene [40]. Huang *et al.* also synthesized CoAl-LDHs on graphene oxide nanosheets by hydrothermal method, explaining the growth mechanism and final application as electrodes for electrochemical capacitors. The formation of CoAl-LDHs platelets on graphene nanosheets prevent the restacking of the as-reduced graphene nanosheets which contribute to the improvement of specific capacitance of LDHs [41]. Wang *et al.* synthesized Co-Al LDH-NS/GO by mixing Co-Al LDH-NS dispersed in the formamide and GO dispersed in water as electrode materials for supercapacitor in which they showed an improved electrochemical performance as a result of the incorporation of graphene oxide nanosheets [42]. In another report, Fang *et al.* provided a complete study of microwave-assisted synthesis of CoAl-layered double hydroxide/graphene oxide composite The results exhibited a high specific capacitance of 772 Fg^{-1} at 1 Ag^{-1} which shows fabrication of graphene oxide and CoAl-LDH enhanced their contact area and electron transport between active materials and charge collector [43]. Ramachandran et *al.* have prepared Co_9S_8-graphene composites by a simple chemical route. In their work, they provided a maximum specific capacitance of 808 Fg^{-1} at scan rate of 5 mVs^{-1} with 9 wt% graphene loading .The composite electrode showed enhanced specific capacitance due to contribution of high electrical conductivity of graphene and Co_9S_8 [44]. da Silveira Firmiano *et al* also reported MoS_2 deposited by microwave heating on a reduced graphene oxide with different concentrations of MoS_2 loaded on graphene oxide. In their work, they produced a specific capacitance of 128, 265 and 148 Fg^{-1} with low, medium and high concentration of MoS_2 The good capacitive behavior was due to the combination of faradic and non-faradic process of active MoS_2 layers coupled with high conductive graphene sheets [45] . Recently Patil *et al* synthesized MoS_2/GO composites using facile electrophoretic deposition method. In their study, they provided a high specific capacitance of 613 Fg^{-1} with the energy density of 23 Wh kg^{-1} and power density of 17 $kWkg^{-1}$ at scan rate of at 25 mVs^{-1}. The improved

51

supercapacitive performance of MoS_2/GO composites arises from the synergistic support between graphene and MoS_2 nanosheets.

During the past years, numerous methods have been established to synthesize graphene such as substrate-free-gas phase synthesis [46], liquid-phase exfoliation [47], mechanical exfoliation of graphite using scotch tape [48], unzipping of carbon nanotubes [49] and chemical vapour deposition(CVD) [50], as shown in Fig 2.9. To further increase the performance of graphene as electrode in supercapacitor, three-dimensional (3D) structural design of graphene (e.g. foams, networks, gels), that could mitigate the poor ionic and electronic transport in the electrode materials, resulting in high performance devices have been recently established [51,52].
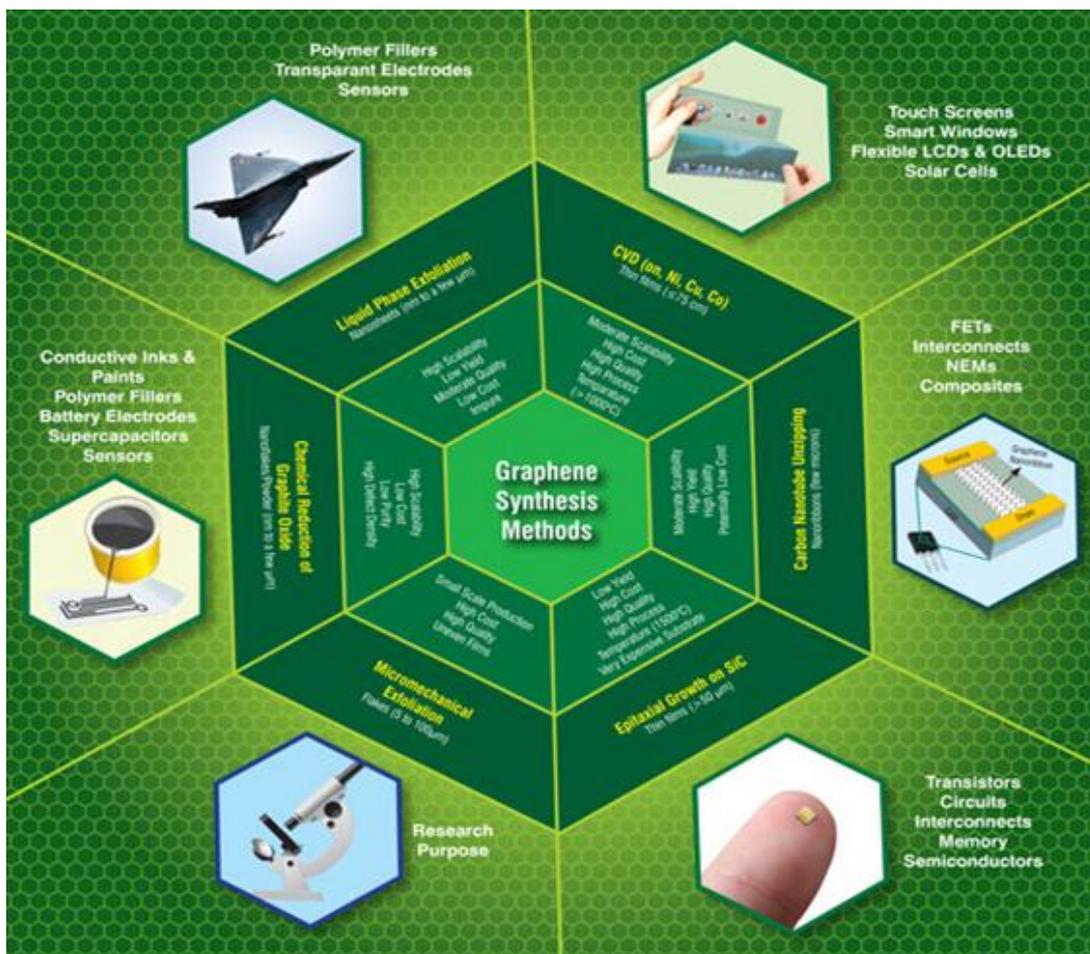
Figure 2.9: A schematic showing the conventional methods commonly used for the synthesis of graphene along with their key features, and the current and future applications [53].

52

So far various synthesis strategies for 3D graphene have been developed including hydrogels and aerogels [54,55], graphene sheets for 3D sponges [56] and foams [57] and the direct synthesis via chemical vapour deposition (CVD) for 3D graphene foams [58,59]. Among all the methods, the preparation of graphene by CVD method has drawn tremendous attention. Cheng *et al.* synthesized 3D graphene on nickel foam by CVD, which showed good mechanical and electrical properties [58]. The 3D graphene not only retained the intrinsic properties of graphene but also offer high specific surface area, good mechanical strength, and excellent electrical conductivity and also exhibits fast transfer of electrolytes ions. 3D Graphene-based materials have been widely investigated as a conducting template to support the redox reaction of transition metal oxides [60], metal hydroxides [61], layered double hydroxides (LDHs) [61], metal chalcogenides [29] and conducting polymers[62]. This process facilitates the diffusion of metal oxides/hydroxides and metal chalcogenides nanoparticles and the foam acts as a highly conductive matrix to enhance the cycling properties and rate performance. Graphene also has a chemical resistance appropriate for use as a substrate and can be employed to develop composites by incorporation of faradaic materials to further enhance the energy density. In this thesis, we will focus on CVD grown 3D graphene foam electrode.

b) Carbon nanotubes

Carbon nanotubes (CNTs) have attracted a great deal of attention in supercapacitor application due to superior electrical properties, unique pore structure and good thermal and mechanical stability [63–65]. These nanostructured materials which can be classified as single-walled carbon nanotubes (SWNTs) or multi-walled carbon nanotubes (MWNTs), keep a high electrical conductivity and great mechanical and thermal stability, which are advantageous properties for characteristically high power, exceptionally stable

53

electrochemical capacitors. Their use as a pure electrode materials can results in a specific capacitance that range between 15 and 200 F g^{-1}, which is mainly affected by their production procedure, that influences their morphology and purity [66]. The tube entanglements can result in an irregular pore distribution that both decrease the mobility and availability of ions through the material. This effect was reported by Futaba *et al.* using arranged carbon nanotubes with larger organic electrolyte ions to achieve high energy density of 35 Whkg^{-1} and a lower operation resistance compared with an entangled network [67]. The active surface area can be increased using chemical activation techniques, but this process can affect the electrical conductivity and the stability and hence there is a need for further optimization to make sure that an overall performance enhancement is achieved. CNT together with carbon aerogel have been used to develop a composite through the uniform distribution of the aerogel into the CNT matrix. This was accomplished without affecting the unique properties of the matrix to produce a composite with a high specific surface area of 1059 m^2 g^{-1} and large specific capacity of 524 Fg^{-1} [68]. However, the difficulty in preparing this material is an important drawback regarding commercial product [68]. The commercialization CNT based EDLCs faces the challenge of improving the restricted energy density of the material by means of a low-cost procedure of producing high quality mass production of CNTs.

c) Activated carbon

Amongst carbon-based materials, activated carbon (AC) is the mostly used electrode material in commercial supercapacitor due to the well-developed manufacturing technologies of its porous structure, high specific surface area, and easy production in large quantities at low cost, its electrochemical stability and its high electrical conductivity. Activated carbon consists of a variety of materials ranging from an amorphous carbon to ordered graphite. Activated carbon can be produced using either physical and chemical processes or a

54

combination of both with various carbonaceous precursors such as coconut shells [69], pine tree, rice husk [70], cigarette filter peat [71], coal, yeast cells [72], seaweeds [73], hemp basts [74] and wood sawdust [75].

The physical activation process consists of gasification of the carbon produced from carbonization at elevated temperature (up to $1200^{°}C$) with an oxidizing gas such as air, O_2, CO_2, argon, steam or their mixture to generate pores. Chemical activation process is usually carried out at relatively low temperatures (400 to 800 $^{°}C$) with an activation agent such as such HNO_3, KOH, H_3PO_4, NaOH and $ZnCl_2$. During the chemical activation process, carbonization and activation are done via thermal decomposition of the precursor soaked with a activating chemical. This increases the porosity and the specific capacitance of the material which removes disordered carbon from the structure in an oxidizing atmosphere, where large variety of carbonaceous can be converted into activated carbon. The properties of the activated carbon depend on the nature of the activating agent, the nature of the raw material used and the condition of the activation process. Activated carbon materials produced using the activation methods have different pore size distributions including micropores, (< 2 nm), mesopores (2- 50nm) and macropores (> 50 nm) to achieve high specific surface area as show in Fig. 2.10. With the use of aqueous and organic electrolytes, capacitance values ranging from 150 to 300 Fg^{-1} were obtained from using AC as electrode material [76]. The difference in capacitance observed through the use of distinct electrolytes is due to the relation between pore and ions size, where organic ions are larger than their aqueous counterparts and thus cannot penetrate the pore volume.
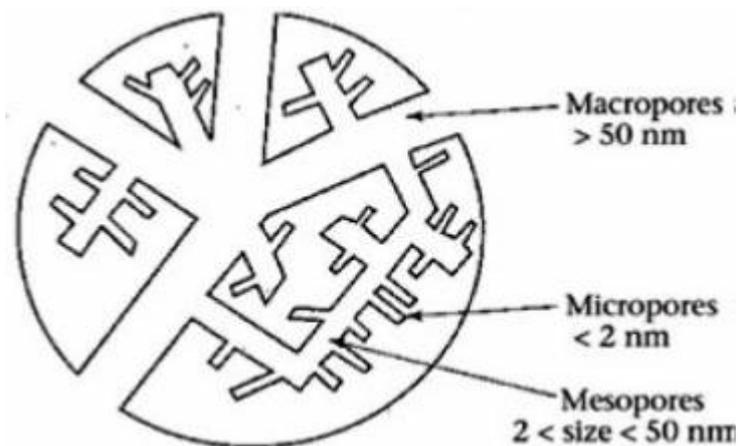
Figure 2.10: Schematic diagram of the pore size network of an activated carbon [77].

High capacitance of an AC derived from a highly functionalized pitch was achieved by Alonso *et al.* (400 Fg^{-1}), and this result was attributed to the high KOH/C ratio, furthering the degree of chemical activation to improve the surface area. Zhai *et al.* reported controlled adjustment to the microcrystallinity and subsequent pore size distribution through pre-carbonization treatments, including a reduction in pore size ranging from 1.5 to 2.4 nm. Morphological effects from pyrolysis and carbonization treatments and pre-carbonization to any subsequent faradaic contribution are both important factors that affect the resulting capacitive ability of the material. Wettability as an important factor to increase the accessible surface of ACs which be improved through surface fictionalization, enhancing the attraction between the electrolyte and carbon [78]. Despite a wide choice of precursors for the production of AC, the improvement in capacitance is based on the enhancement of the surface area, the porosity and the structure through activation techniques, as well as the optimization of functional groups so that conductivity and operational stability is not compromised.

56

2.4 Electrode Materials for Faradaic Supercapacitors

Faradaic electrodes materials offer high energy density than carbon materials, and better electrochemical stability than conducting polymer materials. Several faradaic materials like transition metal oxides [60], metal hydroxides [79], layered double hydroxides (LDHs) [61] and metal chalcogenides [29] have been developed for energy storage applications.

2.4.1 Transition metal oxide/hydroxide

Transition metal oxides or hydroxides are considered to be suitable candidate for electrochemical capacitor due to their high specific capacitance, great flexibility in structure and morphology, together with very low resistance resulting in high specific power, quick and reversible redox reactions involved in the charge storage/delivery process, making them very attractive for commercial applications. Among the transitional oxides, ruthenium oxides and manganese oxide are the most promising electrode materials which show pseudocapacitance behavior, due to its long life cycle, high conductivity, high specific capacitance, good electrochemical reversibility and high rate capability [80–82]. These materials have the electrochemical signature of capacitive electrode such as observed in EDLCs materials, that is displaying a linear dependence of the charge-discharge curves as function of time, however the charge storage originates from different reaction mechanisms from that EDLCs [83].The capacitance of ruthenium oxide is obtained through the insertion and de-insertion, or intercalation of proton into its amorphous structure.

Similarly, over the past few decades transitional metal hydroxide nanostructures with different morphologies ranging from nanowires to nanosheets have also been fabricated and tested for supercapacitor applications. These materials exhibit faradaic behaviour because of involving quick redox reactions for charge storage and are normally called battery like materials.

57

Among other transition metal oxides, cobalt –based hydroxides such as cobalt hydroxide [84] carbonate, cobalt hydroxide [85–87] and cobalt oxyhydroxides [88] have attracted major research interests as electrode material for energy storage in supercapacitor due to their low cost, environmental friendliness, high aerial capacitance (25 F cm^{-2}) based on high mass loading [89] and cycling stability up to 10 000 cycles [90]

The oxidation mechanism between different cobalt compounds is crucial, based on the synthesis methods which results into different phases such as cobalt hydroxide, cobalt hydroxide carbonates and cobalt oxyhydroxide [91]. The oxidation mechanism is relevant to the electrochemical cycling rate and stability as well as the thermal stability of the electrodes.

2.4.1.1 Cobalt based electrode materials

Cobalt hydroxide has arisen as a promising alternative faradic electrode material for supercapacitor application due to its low cost, good resistance to corrosion, layered structures with large interlayer spacing, environmental friendliness and well-defined redox activity and the possibility of enhanced performance through different preparation methods [92,93]. Cobalt hydroxide has a hexagonal-layered structure which can be divided into α and β-Co (OH) $_2$, where α- Co (OH) $_2$ has a better capacitive performance because of its larger interlayer spacing compared to β-Co (OH) $_2$. The possible reactions mechanism can be expressed by equation 2.7 and 2.8 below [94].

$$CoOOH + OH^- \leftrightarrow CoO_2 + H_2O + e^-$$ 2.7

$$Co(OH)_2 + OH^- \leftrightarrow CoOOH + H_2O + e^-$$ 2.8

The theoretical specific capacitance of $Co(OH)_2$ is about 3600 - 3700 F g^{-1} and practical specific capacitance can reach a high rate [95].The capacitive performance of the electrode materials strongly depends on the morphology, and as a result also on the specific surface

58

area. Therefore, hierarchical structures of $Co(OH)_2$ such as flowerlike shapes [96], nanocone arrays [97], mesoporous nanowires [98], nanoflake films [99], coral-like shapes [100] and hollow core-shell structures were fabricated and developed for electrochemical capacitor applications. Surfactant content, ion concentration, the reaction temperature and aging play significant role in the size and morphology of $Co(OH)_2$ nanocrystals. The surface of $Co(OH)_2$ structures displays randomly distributed, interconnecting configurations, resulting in a network-like structure with many cavities between the adjacent blocks. The high specific surface area and numerous pores in the $Co(OH)_2$ can facilitate the penetration of electrolytes, and thus contribute to the excellent capacitive properties. Chanchal *et al.* demonstrated the fabrication of porous 3D β-$Co(OH)_2$ nanoflower at room temperature. The 3D β-$Co(OH)_2$ nanoflower demonstrated an enhanced supercapacitor with a specific capacitance of 416 F g^{-1} at 1 A g^{-1} current density. The porous nanostructure with high surface area facilitates the contact and transport of electrolyte, providing longer electron pathways and therefore giving rise to highest capacitance in nanoflower morphology [101]. Cao *et al.* also prepared $Co(OH)_2$ nanocone arrays by facile hydrothermal method. The $Co(OH)_2$ nanocone arrays display a specific capacitance of 562 F g^{-1} at 2 A g^{-1} and good cycling stability. The improved electrochemical capacitive performance is due to the porosity and large surface area of the porous 1D array architecture [97]. Xue *et al.* investigated the influence of electrochemical parameters and heat treated temperature on mesoporous $Co(OH)_2$ nanowires structure and its electrochemical behavior. The $Co(OH)_2$ nanowires structure provided a specific capacitance of 993 Fg^{-1} at 1 Ag^{-1} current density [98].

Cobalt oxyhydroxide (CoOOH) is another faradaic material with controlled morphology in micrometer/nanometer scale [102,103]. Layered hydroxide cobalt acetate (LHCA) were first prepared by chemical bath deposition (CBD) method, the as-synthesized LHCA films were then transformed to CoOOH by alkaline treatment [102]. This CoOOH retains the specific

59

capacitance of 200 F g^{-1} at a scan rate at 10 mV s^{-1}, because of its relatively low conductivity [102]. To improve the ionic transport and electrical conductivity, composites of CoOOH and carbon materials were considered. Zheng *et al.* synthesized carbon nanotubes/cobalt oxyhydroxide nanoflake through electrodeposition method. The multi-walled carbon nanotubes provided a large surface area for the deposition of CoOOH layer that facilitated the transportation of the electrolyte ions, resulting in improved capacitance performance of CoOOH to 389 F g^{-1} [88]. Zhu *et al.* also synthesized composites of CoOOH nanoplates with conducting multi-walled carbon nanotubes by hydrothermal-oxidation two-step method. The pristine CoOOH electrode exhibits specific capacitance of 126 Fg^{-1} and 270 Fg^{-1} for composites at 1 Ag^{-1} current density. The good capacitive behavior is due to MWCNTs spread into the CoOOH nanoplates, creating an interconnected conductive network [104]. Zheng *et al.* also fabricated multilayered films of cobalt oxyhydroxide nanowires/manganese oxide nanosheets by potentiostatic deposition and electrostatic self-assembly on indium-tin oxide coated glass substrate. The multilayered film electrodes exhibit excellent specific capacitance of 507 Fg^{-1} and cycling stability with capacity loss of less than 2 % after 5000 charge-discharge cycles [105].

Cobalt hydroxide carbonates nanostructures with different morphologies intercalated with carbonate anions have been effectively produced using block copolymers or surfactants which resulted in different structures such as nanorods , sisal-like, dandelion-like ,nanowires , urchin-like , pinecone-like and flower-like [106–111]. For examples, Zhao *et al.* [112] produced 3D nanorods-based urchin-like and nanosheets-based flower-like cobalt basic salt nanostructures. Nevertheless, pure cobalt hydroxide carbonate show low specific capacitance compared with other TMOs, hence several methods have been developed to improve the capacitance [113–116]. Lu *et al.* reported cobalt carbonate hydroxide (MPCCH) nanosheets fabricated from Co-Al LDH nanosheets. The removal of the Al cations by alkali etching

60

thinned the nanosheets, generated pores and improved the surface area, which are important parameters for better penetration of electrolytes into the electrodes and shortening of the diffusion distance. The basic etched electrode shows enhanced specific capacitance of 1075 F g^{-1} at 5 mA cm^{-2}, much higher than that of Co-Al LDH nanosheets (~390 Fg^{-1}). Furthermore, the MPCCH retained 72.4 % of its highest capacitance, whereas the Co-Al LDH only retained 56.8 % of its highest capacitance after 2000 cycles [117]. Garakani *et al.* prepared cobalt carbonate/graphene aerogel composites through one-pot hydrothermal process [118]. The interface between the cobalt carbonate hydroxide and graphene aerogel were successfully improved capacitive performance, because large surface area of the graphene aerogel presented large reaction sites that were available to electrolyte ions, whereas its excellent electrical conductivity reduced the charge transfer resistance of electrons. Furthermore, by depositing highly capacitive nano-shape on conducting micro-substrate enhanced the performance of supercapacitor. Xie *et al* also prepared composite of cobalt carbonate hydroxide (CCH) nanowire on N-doped graphene (NG) nanosheets by one –step hydrothermal method. The composite exhibited a specific capacitance of 1358 Fg^{-1} at current density of 10 Ag^{-1} and cycling stability retaining 94.2 % after 10 000 cycles .The assembled asymmetric supercapacitor based on the optimal composite showed a high discharge areal capacitance of 153.5 mF cm^{-2} and high energy density of 0.77 Wh m^{-2} and power density of 25.3 Wm^{-2} [119].

2.4.1.2   Cobalt based Layered Double Hydroxides (Co Al-LDH)

Layered double hydroxides (LDHs) are class of two-dimensional anionic clays consisting of positively charged brucite-like host layers and exchangeable charge-balancing interlayer anions that can be represented by the general chemical formula $[M_{1-x}^{2+}M_x^{3+}(OH)_2][A^{n-}]_{x/n}.yH_2O$ [61]. A fraction of divalent metal ions such as Mg^{2+}, Zn^{2+}

61

,Ni^{2+} and Co^{2+} coordinated octahedrally by hydroxyl groups in the brucite-like layers are homogenously replaced by trivalent metals such as Al^{3+} ,Fe^{3+} ,Mn^{3+} ,Cr^{3+} or Fe^{3+} with the molar ratio of $M^{3+}/(M^{3+}+M^{2+})$ (the value of x) normally between 0.2 and 0.4 [120]. LDHs containing transition metals such as (Co-Al, Fe-Al and Ni-Al have been reported as excellent candidates for faradaic capacitors due to their high redox activity and effective utilization of metal atoms [121]. Su *et al.* reported CoAl-LDH nanoparticle material synthesized by the traditional co-precipitation method which only gave a limited specific capacitance of 145 F g^{-1} at 2 A g^{-1}. Wang *et al.* also showed the electrochemical properties of double oxides obtained from the annealing of CoAl LDH, which had a specific capacitance of 684 F g^{-1} at a current density of 60 mA g^{-1} [122]. However, the low electric conductivity of LDH limits electron transfer, resulting in poor charge and discharge capability that poorly affects the performance of electrode materials. To solve this problem, some efforts have been made to improve the performance of LDHs based supercapacitors by hybridizing with carbon materials. These composites exhibited improved electrochemical properties such as good rate capability, higher cycling stability and higher surface area. Zhang et *al.* prepared a facile synthesis of porous CoAl-layered double hydroxide/graphene composite by simple gas-liquid interfacial method. The results showed that this composite ,gave the specific capacitance of 479.2 Fg^{-1} at current density of 1 Ag^{-1} [123]. Shu *et al.* also reported the immobilization of Co-Al Layered double hydroxides on graphene oxide nanosheets by hydrothermal treatment, which showed improved capacitive performance. The specific capacitance of LDHs was enhanced by presence of GNS which prevented the restacking of the as reduced graphene nanosheets [41]. Johong *et al.* also provided synthesis of CoAl-layered double hydroxide/graphene oxide composite by a microwave-assisted reflux method and its application in a supercapacitor which showed that assembly of graphene oxide and CoAl-LDH improved their contact area and electron transport between active materials and current collector. The composites showed

the specific capacitance of 772 Fg^{-1} at 1 Ag^{-1} with cycling stability of 73 % at 6 Ag^{-1} after 10 000 cycles [43]. In another report Kim *et al.* synthesized GNS/CoAl-LDH through a layer-by-layer deposition process while varying the concentration of graphene. The as-prepared composites showed the specific capacitance 971 Fg^{-1} at a scan rate of 10 mVs^{-1} [124].

2.4.2 Transition Metal Dichalcogenides (TMDs)

Two-dimensional (2D) layered transition-metal dichalcogenides (TMDs) have attracted great attention due to the unique chemical, electronic, physical, mechanical, optical and magnetic properties [125] for supercapacitor. 2D layered transition-metal dichalcogenides (TMDs) such as MoS_2, CoS_2, VS_2 and NiS_2 have been extensively studied for applications in electrochemical supercapacitors because they are known to be electrochemically active with good electrochemical performance [126] and have analogous structure like graphene. Depending on the co-ordination and oxidation states of the metal atoms, TMDs can be metal, semi-metal or semiconductor. Originating from the cooperation between the cationic d-levels and anionic sp-levels, most transition metal atoms (M) will react with chalcogen atoms (X) to form a X-M-X configuration with stoichiometry MX_2 [127]. Although the bonding within the hexagonal M layer and two X layers is covalent, adjacent sheets stack via weak van der Waals interactions to form a 3D crystal. Among TMDs being considered for electrode materials, MoS_2 which has a graphene-like single layer structure has attracted great interest in phototransistors, catalysis, lithium ion batteries and supercapacitor due to its intrinsic fast ionic conductivity and higher theoretical capacity, electrical properties and unique morphology [128–130]. In order to increase the active surface area and the density of the edge sites of MoS_2, hydrothermal techniques have been implemented to produce different nanostructures of MoS_2 [131,132]. However poor crystallinity and aggregation of layers MoS_2 constrain its performance in supercapacitor application. In order to improve the

63

electrochemical performance of MoS_2, constructing composites or hybrids with carbon materials is one of the most effective ways of increasing the conductivity as well as its electrochemical performance. Hun *et al.* reported porous tubular C/MoS_2 nanocomposites and bulk MoS_2 using porous anodic aluminium oxide as a template. The C/MoS_2 nanocomposites exhibit the specific capacitance of 210 Fg^{-1} at 1 Ag^{-1} with excellent stability of 94.1 % after 1000 cycles [133]. Fan *et al.* also synthesized flower-like MoS_2/C composite by hydrothermal method. The results showed specific capacitance of 201 Fg^{-1} at current density of 2.7 Ag^{-1} [134].

Among other TMDs with intrinsically high conductivity, VS_2 could be an alternative to graphene. VS_2 is a hexagonal crystal with layered, graphite-like structure, with a S-V-S stacking layers and the layers are connected via interlamination Van der Waals forces [135]. Few researchers have demonstrated that various stoichiometrically different forms of VS_2 can be synthesized through facile hydrothermal techniques for various applications [136–140]. Feng *et al.* has demonstrated that VS_2 shows exceptional in-plane supercapacitor properties due to the correlation between electrons of vanadium atoms [141].The fabricated in plane device displayed a specific capacitance of 317 F cm^{-3}, similar to graphene-based electrode, with a good stability of 90% after 1000 cycles. These results showed that VS_2 has the required physical and electrochemical properties to be used extensively in energy storage application.

2.5 Electrolytes

Electrolyte plays the important role in electrochemical supercapacitor performance, providing ionic conductivity and thus facilitating charge compensation on each electrode in the cell. The electrolyte contains dissolved and solvated ions that migrate to and from the electrodes

64

during charge and discharge .The physical and chemical properties of the electrolyte are the temperature coefficient and conductivity which are the important factor, and mainly determine the internal resistant and the operating voltage of the cell of the electrochemical supercapacitor. Other requirements of the electrolytes in electrochemical supercapacitor include high chemical and electrochemical stability, low solvated ionic radius, low viscosity, low toxicity, low cost ,wide voltage window and availability at high purity [142]. Both two key parameters, namely energy and power densities of electrochemical capacitors are affected by the types of the electrolytes used. The energy density is affected by voltage window and ion concentration of the electrolyte while the power density is impacted by the resistance of the electrolyte. The types of electrolytes used in the supercapacitor research can be classified into three groups (i) aqueous, (ii) organic and (iii) ionic liquids electrolytes. The choice of the electrolytes depends on the three parameters, namely the resistance, ease of production and potential window in which the electrolyte will remain stable.

2.5.1   Aqueous Electrolytes

Aqueous electrolytes such as basic solution (KOH), neutral (Na_2SO_4) and acidic (H_2SO_4) are the most commonly used electrolytes because of high ionic conductivity, low cost, non-flammability , safety , non-corrosive and convenient assembly in air compared to organic electrolytes which are believed to be less conductive, expensive usually flammable and higher toxic. Aqueous electrolytes composed of strong acids, bases or strong acids dissolved in water and high conductivity. However, aqueous electrolytes preserve both high conductivity resulting in high power density and high capacitance but working voltage have the thermodynamic limit of (~ 1.23 V) restricted by the decomposition of water and this limits the amount of energy that can be stored. The introduction of redox active material in

65

aqueous electrolytes can successfully enhance the capacitance through extra redox reaction between the electrode and electrolyte due to the ionic concentration and smaller ionic radius.

2.5.2 Organic Electrolytes

Organic electrolytes are the most often used electrolytes in commercial supercapacitors due to their high operation potential window of almost 3.5 V compared to aqueous electrolytes. The increased operation cell voltage can offer a significant improvement in both the energy and power densities. However, organic electrolytes consist of difficult purification and assembling processes in a strictly controlled environment to remove any residual impurities that can lead to large performance degrading and serious self-discharge and hence these make them be non-cost effective for industrial use [13]. The most widely used organic electrolytes for the commercial EDLCs comprises of a quaternary ammonium salts such as tetraethylammonium tetrafluoroborate (TEABF$_4$), tetraphosphonium, tetrafluoroborate and triethylmethylammonium that dissolve in the acetonitrile (ACN) and propylene carbonate (PC). ACN is capable of dissolving larger amounts of salts, but is toxic, whereas PC-based electrolytes are more environmentally friendly, presenting a wide working temperature, wide working voltage and lower but relatively good conductivity [143]. Although higher operating voltage of the cell gives the reasonable advantage of organic electrolytes over aqueous electrolytes, they still have disadvantages like relatively high equivalent series resistance (ESR), lower conductivity (20 mS/cm), high cost, toxicity and vulnerable to moisture [144].

2.5.3 Ionic Liquids Electrolytes

Ionic liquids (ILs) electrolytes are room temperature molten salts and are totally composed of cation and anions, which affect the physical and chemical or electrochemical properties. Mostly, the cation confines the negative potential window while the anion affects the positive potential window as well as the melting point, which affects the working temperature range.

66

Ionic liquids electrolyte exhibit negligible vapor pressure, wide electrochemical windows, good conductivity at temperatures ($\geq$ 60°C), non-volatility and non-flammability and excellent electrochemical and thermal stabilities [145]. They have been studied and employed in various applications such as catalysis [146], fuel cells [147], pharmaceutical [148] and electrochemical synthesis [149]. As electrolytes in supercapacitor they have been used for providing a large stability potential window when used with a non-porous electrodes [150]. Various studies has shown that ionic liquids can enable operative voltages up to 4.5 V while displaying higher viscosities and thus lower conductivities compared to aqueous and organic electrolytes leading to higher internal resistance and reduced power capabilities [151]. The increase in operative voltage in combination with a comparable viscosity and conductivity significantly influences the energy and power storage capabilities of the devices. Using ionic liquids can also reduce the safety and environmental concern since ionic liquids electrolytes have excellent thermal stability, non-volatility and non-flammability [152]. Regardless of several advantages of ionic liquids their application in electrochemical supercapacitor is affected by low conductivity which intensifies the power response.

The ILs electrolytes mainly studied for supercapacitors application are commonly created on imidazolium, pyrrolidinium, ammonium, sulfonium, phosphonium cations and salts of anions like tetrafluoroborate, trifluoromethanesulfonate, bis(trifluoromethanesulfonyl)imide, bis (fluoromethanesulfonyl) imide, bis(fluorosulfonyl)imide and dicyanamide [153].

2.6 Electrode Preparation and Electrochemical Characterization

The test-cell configuration for the electrode materials performance typically consists of the two (2), three (3) or/and four (4) electrodes. Electrodes cell consist of a reference electrode (RE), a working electrode (WE) and counter electrode (CE). The working electrode contains the active material that is being tested for its electrochemical properties .The working

electrode is generally coated on the current collector by active electrode materials being tested .Typically, the binder such as polytetrafluoroethylene (PTF) or polyvinylidene (PVDF) and conducting agents such as acetylene black and carbon black are part of active electrode materials to make sure that the material is bound properly together and provide good electrical conductivity and make sure enough interaction and mechanical permanence are reached upon electrochemical cycling.

Reference electrodes such as saturated calomel electrode and silver/silver chloride electrode (Ag/AgCl) are electrodes which have stable and well –known electrode potential and they are often used as a point of reference in the electrochemical cell for the potential control and measurements. The counter electrode (CE) is an electrode which is used to close the current circuit in the electrochemical cell. It is usually made of the inert materials such as Pt, Au, graphite and glassy carbon. The suitable materials for CE are conductive materials which do not react with electrolytes in which they are exposed to. Therefore, the choice of electrolytes is highly associated with the counter and reference electrodes. For example, in alkaline aqueous solutions a mercury/mercury oxide electrode (Hg/HgO) is used as the reference electrode. In acidic aqueous solutions, a current collector of working electrode should be titanium, the counter electrode is platinum or carbon and the reference electrode is saturated calomel electrode (SCE) or silver/silver chloride electrode (AG/AgCl). In neutral aqueous solutions, basically the same configuration is used but nickel foam and carbon paper can be used for a current collector and the counter electrode. For non-aqueous electrolyte solutions case by case approach is required depending on the composition of electrolyte [153].

2.6.1 Two Electrodes Setup
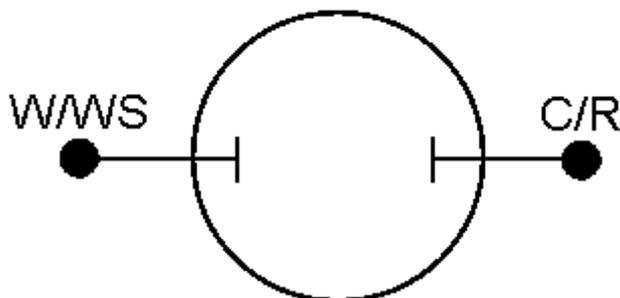
Figure 2.11: Schematic view of two electrode setup [154].

Unlike three electrode configuration, the "full cell" 2-electrode configuration usually takes place in a two electrode system, and shows the more practical performance of active materials than the half-cell, because full cell test works similar to a practical supercapacitor which has a positive electrode and negative electrode. In a full cell both electrodes are assembled with active materials soaked and separated by a separator.

Figure 2.11 below shows such setup. The setup of two electrode experiments has the current and sense leads connected together. Working sense measures or controls the voltage between itself and the sense electrode. Working and working sense are connected together as the positive (working) electrode and reference and counted are connected together as the negative (second) electrode.

2.6.2 Three Electrodes Setup

In order to characterize the electrode materials, an active material can be tested in a three electrode. To record the potential of the working electrode, a reference electrode whose potential is almost a constant in a narrow potential range is used.

69
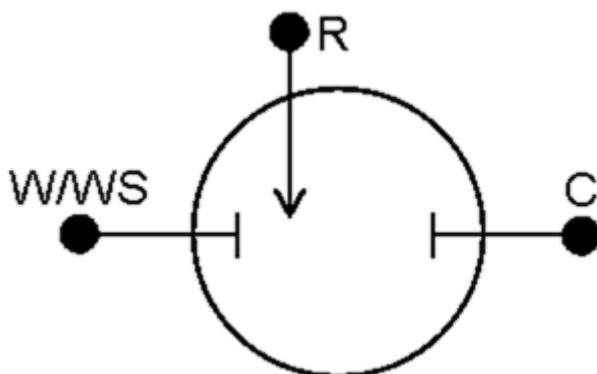
Figure 2.12: Schematic view of three electrode setup [154].

In addition, a counter electrode is also essential to transmit the current coming across from the working electrode, which can inhibit the reference electrode from carrying current leading to the potential change of the reference electrode (see schematic diagram in figure 2.12). In the three-electrode experiment the reference is separated from the counter .The reference electrode is most frequently situated so that it is evaluating point very close to the working electrode (which has both working and working sense leads attached).

2.6.3 Four Electrode Setup

Four electrode cell is used to investigate process taking place within the electrolyte, between two measuring electrodes separated by a membrane. In this configuration, the working and the counter electrodes allow current to flow and used to achieve electronic or ionic conductivity measurements. The setup in the four-electrode setup is comparatively uncommon in electrochemistry. The four-electrode experiment measures the effect of an applied current on the solution itself or some barrier in the solution (see schematic diagram in figure 2.13).

70
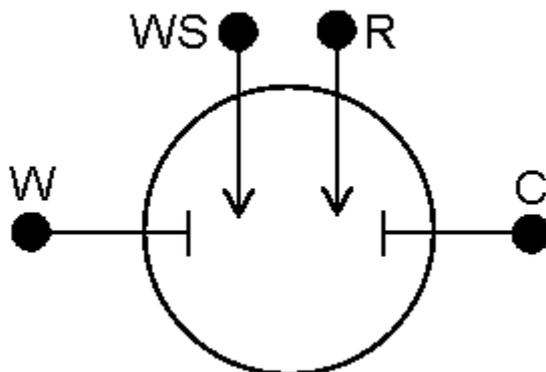
Figure 2.13: Schematic view of four electrode setup [154].

2.7 Electrode fabrication for electrochemical capacitors

The electrode material forms the main component of the cell, and controls the electrochemical supercapacitor performance in terms of life expectation, capacity, self-discharge, and resistance. However, the electrolyte, the current collector and the separator are important parameters to consider for fabrication of a supercapacitor. Electrodes must have good electronic conductivity, high temperature stability, high corrosion resistance, long-term chemical stability, and high surface area per unit volume and mass. Therefore, the electrode fabrication as well as an active material covering process is the most significant step to attain both high performance and durability. Generally, nickel foam because of its chemical stability, high current-carrying, commercial availability, high processability and low price is mostly used as a current collector. In the method of coating electrodes on the current collector, initially active materials, binder e.g. polyvinylidene fluoride (PVDF) or poly (tetrafluoroethylene) (PTFE) and conductive additives e.g. acetylene black and carbon black are mixed to obtained a homogeneous slurry with the wanted density, and the slurry is uniformly pasted on a nickel foam current collector or roll-pressing to attain a uniform electrode coating layer. The mass of the electrode materials must be known and if possible the electrode volume or area should be measured.

71
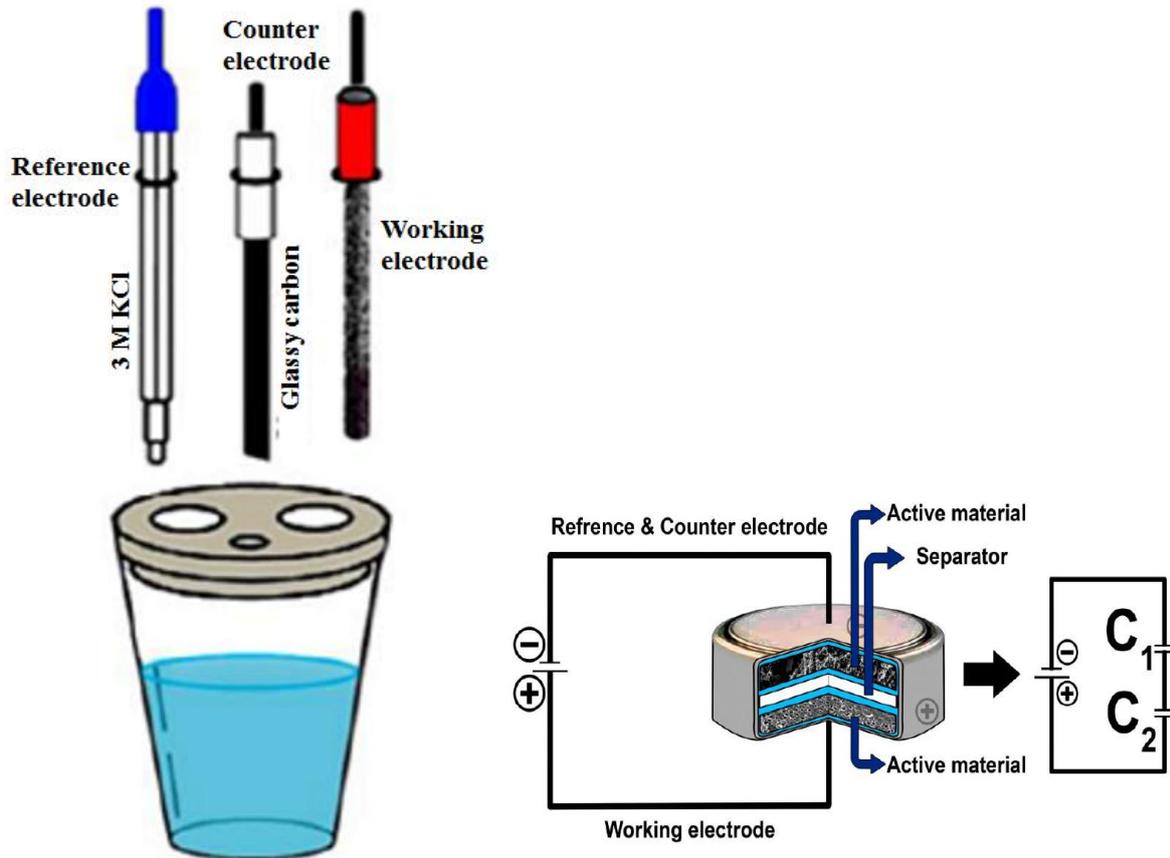
Figure 2.14: Schematic view of (a) three and (b) two electrode setup for testing in electrode material [155].

Depending on the active material used and the suggested application the electrode thickness is usually a few micrometers to sub-millimeter. The acquired active material served as working electrode. Electrochemical test cells ,whether for EDLC or faradaic evaluation can be fabricated using a three -electrode or two-electrode cell configuration which is used in supercapacitor application as shown in Fig 2.14 [156].

The three-electrode system is normally used for examining the fundamental electrochemical properties of the electrode material like electrolyte potential window stability and whether the electrode material works better in the negative or positive potential widow and the two electrode used to characterized fully fabricated device. If the active materials in the two electrodes are the same and are not the same, the supercapacitor is referred to as symmetric and asymmetric respectively.

72

A two-electrode supercapacitor cell can be considered as two capacitors in series, and the total capacitance (C_T) of the cell can be calculated as follows:

$$\frac{1}{C_{cell}} = \frac{1}{C_p} + \frac{1}{C_n}$$

2.9

In which C_{cell} is the capacitance in (F g^{-1}), C_p and C_n are the capacitance of the positive (anode) and negative (cathode) electrodes based on the two-electrode setup, respectively. If ($C_p = C_n$) the corresponding supercapacitor is called a symmetric supercapacitor. For symmetric supercapacitor the total capacitance value equals half the value of single electrode. The symmetric supercapacitor can be expressed in terms of the specific capacitance (Fg^{-1}) of a single electrode (C_{sp}) which is related to the specific capacitance of the cell. With the galvanostatic charge-discharge plots based on the two-electrode cell, the specific capacitance of single electrode, the maximum energy density(E_m) (Wh kg^{-1}) and the power density (P_m) (kW kg^{-1}) of the supercapacitor are calculated using the following equations below [157]

$$C_{sp} = 4C_T = \frac{4I\Delta t}{m\Delta v}$$

2.10

$$E_M = \frac{1}{2}C(\Delta V)^2 = \frac{1000 \times C_S \times \Delta V^2}{2 \times 4 \times 3600} = \frac{C_S \times \Delta V^2}{28.8}$$

2.11

and

$$P_M = \frac{3600 \times E_M}{1000 \times \Delta t} = \frac{3.6 \times E_M}{\Delta t}$$

2.12

where C_{sp} is the specific capacitance of single electrode of the cell, I is the constant discharge current (A), Δt is the discharge time(s), ΔV is the voltage window (V), and m is the total mass (g) of the active material in both electrode, respectively. The maximum power density

(P_m) (kW kg^{-1}) can also be calculated by using equivalent series resistance (ESR) with the following equation [158]

$$P = \frac{V^2}{4 \times (ESR)m}$$ 2.13

where, m is the total mass of active material and V is the voltage window (V).

In the case ($C_p \neq C_n$) (the anode and the cathode have two different electrode materials, the corresponding electrochemical supercapacitor is called an asymmetric. In order to obtain the optimal performance of the asymmetric full cell supercapacitors, a charge balance $Q_+ = Q_-$ between the two electrodes should be done; where Q_+ and Q_- are the charges stored in the positive and negative electrodes, respectively. The charge can be expressed by [159]:

$$Q = C_s \times m\Delta U$$ 2.14

where C_s is the specific capacitance of the active material, m is the mass of each active material and ΔU is the potential range during the charge–discharge process. In order to get $Q_+ = Q_-$, the mass balancing follows the equation

$$\frac{m_+}{m_-} = \frac{C_{S-}\Delta U_-}{C_{S+}\Delta U_+}$$ 2.15

The energy density (E, in Wh kg^{-1}) of supercapacitor can be calculated from specific capacitance, C_s according to the following equations:

$$E_d = \frac{1}{2}C_S\Delta U^2 = \frac{1000 \times C_S \times \Delta U^2}{2 \times 3600} = \frac{C_S \times \Delta U^2}{7.2}$$ 2.16

The power density (P, in W kg^{-1}) of a supercapacitor can be determined by

$$P_d = \frac{E_d}{t} = \frac{3600 \times E_d}{1000 \times \Delta t} = \frac{3.6 \times E_d}{\Delta t}$$ 2.17

74

where E_d is the average energy density (W h kg^{-1}), C_s is the specific capacitance based on the electro-active material (Fg^{-1}), ΔU is the potential window, P_d is the average power density (W kg^{-1}) and t is the discharge time (seconds).

The above equations normally work well for EDLCs especially eqn 2.10 where charge-discharge (CD) curves show the linear dependence of voltage vs CD time. But for faradic materials one normally talks of specific capacity which can indeed be converted into specific capacitance. The specific capacity for non-EDLC material can be calculated using the following expression

$$Q_D = \frac{I \times t_D}{m \times 3.6} \qquad\qquad 2.18$$

where I is the discharge current (A), t is the discharge time (s), m is the mass of the active material (g), and Q_D is the specific discharge capacity (mAh g^{-1}).

2.8 Measurements Techniques for Evaluating the Performance of a Supercapacitor

To evaluate supercapacitor performance parameters such as cell (total) capacitance, C_T, operating voltage V_0 and equivalent series resistance(R_S) are often used to determine energy and power performance. In order to calculate the above-mentioned parameters various test modes have been developed and applied to characterize the electrochemical performance of supercapacitors. Cycling voltammetry (CV), Galvanostic charge-discharge (GCD) and electrochemical impedance spectroscopy (EIS) are employed as electrochemical measurements techniques in analyzing the performance of supercapacitor. All such methods can be used to measure the three fundamental parameters such as voltage, current and time and other metrics including the capacitance, equivalent series resistance, operating voltage

75

and successively the time constant, energy and power performance of supercapacitors can be derived from them.

2.8.1 Cycling Voltammetry (CV)

Cycling voltammetry is a common electrochemical characterization technique used to study the electrochemical property of a material. CV testing applies a linear change in electric potential between positive and negative electrodes for two electrodes, or between the reference and working electrodes for three electrodes. The characteristics of the CV is determined by number of factors

- The voltage scans rate

- The rate of the electron transfers reactions

- The chemical reactivity of the electroactive types.

The speed of the potential change in mVs^{-1} is designated as the sweep rate or scan rate v and the range of potential change are called the potential window or operating potential. To study the charge storage mechanisms of supercapacitors materials where EDLCs and faradaic types are separated, CV testing with the three electrode setup is considered as the most suitable approach. The experimental results can first be examined by investigating the shape of the CV curves for both EDLC and faradaic materials. The shape of the EDLC curves is relatively rectangular suggesting a pure capacitive behaviour of an ideal double layer capacitor without any chemical reaction whereas faradaic can be marked by redox peaks occurring in a highly reversible method as shown in Fig 2.15. CV test are also suitable to determine the operating voltage or potential window for supercapacitor materials through reversal of potential in a three electrode system and the reversibility of the charge and discharge process can be studied simultaneously. Further the specific capacitance of the supercapacitor materials can be obtained via the integration of the CV curves.

76
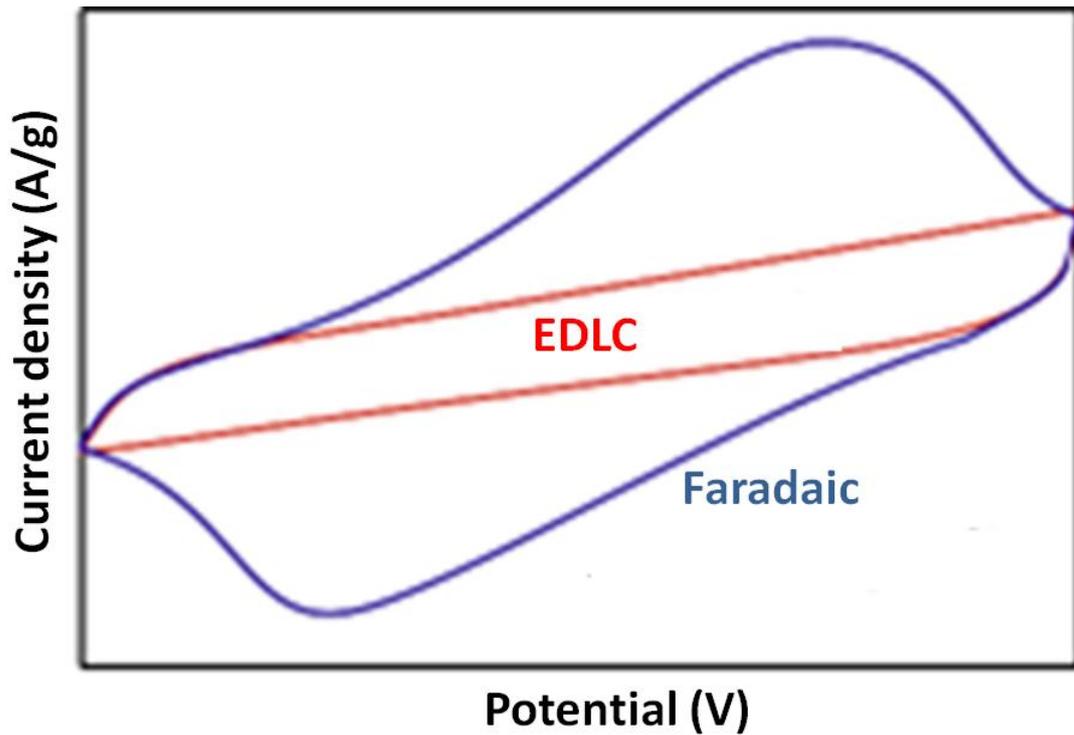
Figure 2.15: Cyclic voltammograms showing rectangular features for an EDLC system and superimposed reduction and oxidation peaks for redox active faradaic [157].

From the area of the CV curve, the specific capacitance for both electrode that is exhibiting EDLCs and battery-like (faradaic) materials calculated with the following equation [160]:

$$C = \frac{1}{mv(V_a - V_c)} \int_{V_a}^{V_c} I(V)dv \qquad\qquad 2.19$$

where I is the average current (A) ,V is the voltage difference (V), v is the potential sweep rate (mVs^{-1}) ,m is the mass of the active material (g) and $(V_a - V_c)$ represents the potential window.

2.8.2 Galvanostatic Charge-Discharge (GCD)

Galvanostatic charge-discharge (GCD) testing is most commonly used method for characterization of supercapacitor under direct current. Constant current charge -discharge is a more accurate technique to calculate the specific capacitance of active materials of supercapacitor under direct current. It is conducted by monotonous charging and discharging of the supercapacitor device or the working electrode at a constant current level with or without a dwelling period and normally a plot of the potential *(E)* vs. time(*s*) is the output. All the parameters of supercapacitor devices such as C_T , R_{ES} ,V_o can be tested through GCD and successively used to derive most of the other properties such as the time constant, leakage and peak currents, power and energy densities. Additionally, it is suitably used to study the cycling stability of supercapacitor devices. Furthermore, by using a three electrode setup the specific capacitance, reversibility and potential window for supercapacitor materials can also be attained through GCD test. A typical GCD curve is shown in Fig. 2.16, in which the voltage is drawn as a function of the time. Meanwhile EDLCs display linear charge/discharge behavior with a constant slope and the specific capacitance is basically unchanged over the full potential range. For faradaic materials, the discharge curve can be definitely non-linear due to redox reaction taking place during discharge process. The specific capacitance of EDLCs electrode materials is best determined from the GCD by the potential window, current density and discharge time with the following equation which is similar to 2.12

$$C_m = \frac{I \times t}{m \times \Delta V} \qquad\qquad 2.20$$

where I is the discharge current (A), t is the discharge time (s), m is the mass of active material (g), ΔV is the potential range of discharge (V), and C_m is the specific capacitance (F/g).

78
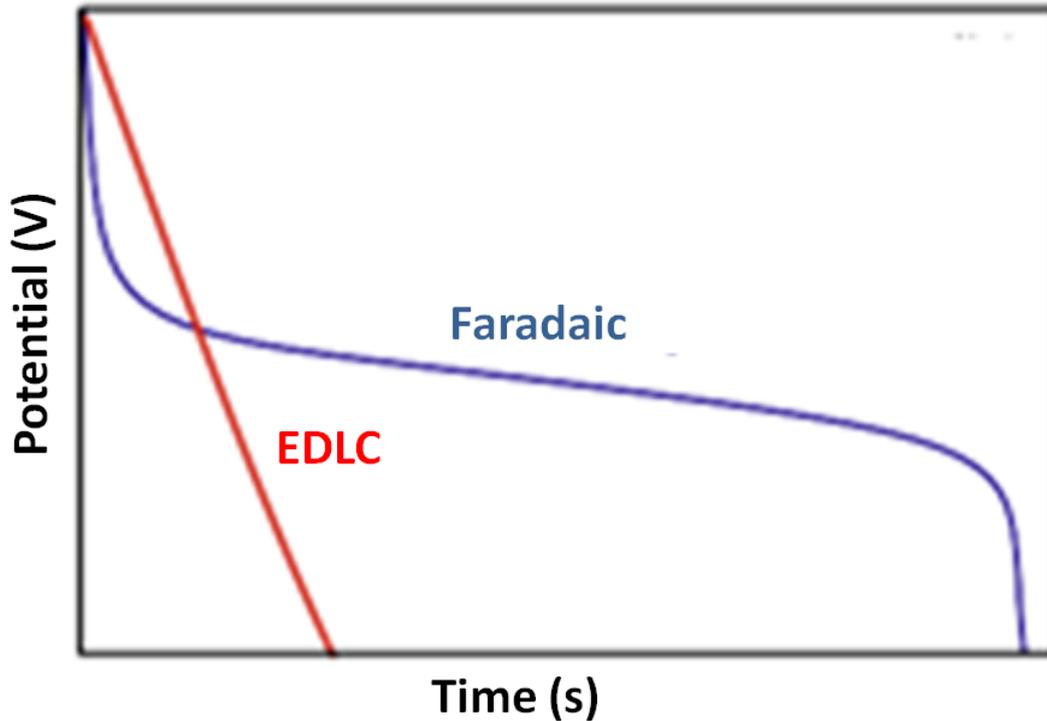
Figure 2.16: Discharge curves for an EDLC and faradaic [157].

2.8.3 Electrochemical impedance spectroscopy (EIS)

EIS testing is known as the dielectric spectroscopy testing, analyses the impedance of a power cell as a function of frequency by applying a low amplitude alternative voltage (normally 5 mV) superimposed on a steady-state potential. The resulting data are generally articulated graphically in a Bode plot to determine the cell response between the phase angle and frequency, and in a Nyquist plot to demonstrate the imaginary and real parts of the cell impedances on a complex plane [62, 63]. Furthermore, for supercapacitor materials EIS has also been used to describe the charge transfer, mass transport and charge storage mechanisms as well as to evaluate the capacitance, energy and power properties [64, 65]. The Nyquist plot is characterized by two distinct parts, a semi-circle loop at high frequency and the linear line at low-frequency regions, signifying different electrochemical phenomena during the electrochemical process on the electrode surface as shown in Fig 2.18.

79
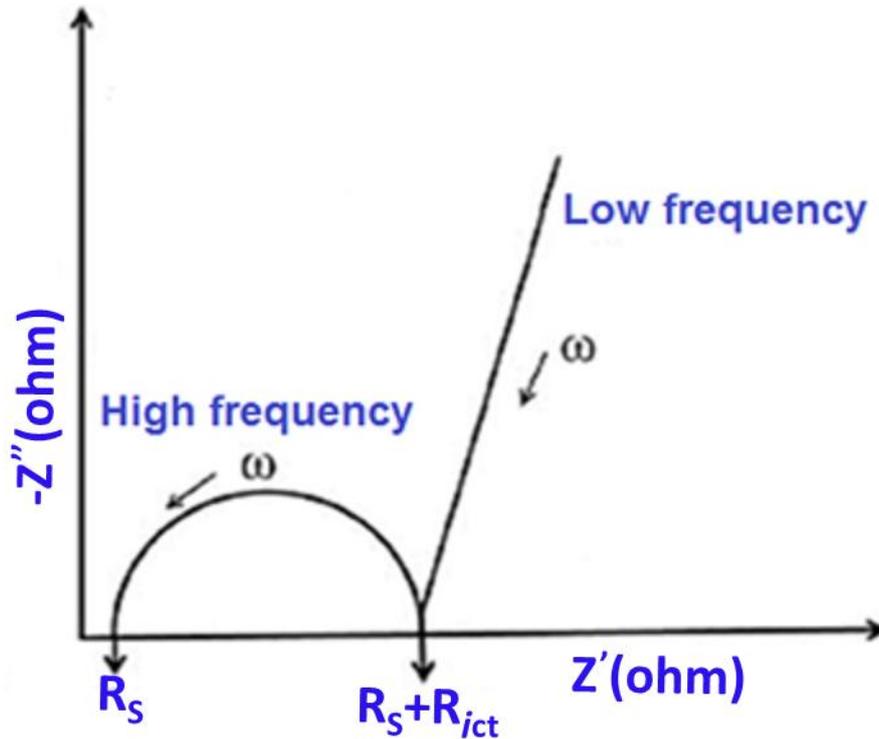
Figure 2.17: Scheme of the impedance plane (Nyquist plot).

The semicircle at high frequency represents (larger than 10^4 HZ) the charge transfer resistance (R_{CT}) in the equivalent circuit ,which depends on the conductivity at the interface between the active material and the electrolyte, the porous morphology of the electrode material and the thickness of the active material [161], while at medium frequency region (10 to 1 Hz) it displays a faradaic charge transfer résistance, which is recognized to the porous electrode used. R_s corresponds to the solution (electrolyte) resistance and is the same as ESR. The Bode phase angle is another representative of EIS, which represents the plot of phase angle against the applied frequency. For an ideal capacitive material, the phase angle is closer to 90° and for faradaic material, the phase angle is closer to 45° [165,166]. Based on this model, the real and imaginary part of the capacitance as a function of the frequency can be calculated using equations below;

80

$$C = \frac{-1}{(\omega Z'')} \qquad\qquad 2.21$$

$$C(\omega) = C'(\omega) - jC''(\omega) \qquad\qquad 2.22$$

$$C' = \frac{z''(\omega)}{\omega |z(\omega)|^2} \qquad\qquad 2.23$$

$$C'' = \frac{z'(\omega)}{\omega |z(\omega)|^2} \qquad\qquad 2.24$$

where Z is the complex impedance written as $Z(\omega) = Z'(\omega) + Z''(\omega)$, $\omega = 2\pi f$, $C'(\omega)$ represents the real accessible capacitance of the cell at the corresponding frequency which signifies the deliverable capacitance, while $C''(\omega)$ represents the energy loss due to the irreversible process of the electrodes. Z' and Z'' represent the real and imaginary parts of the Nyquist plot respectively [167]. The specific capacitance can be calculated from the Bode plot as shown in the following equation

$$C = \frac{1}{2\Pi f m(Z)} \qquad\qquad 2.25$$

where C is the specific capacitance, f is the frequency and Z'' is the imaginary component. Another method introduced by Simon $et\ al$ is [167] use the equations below for calculation of real and imaginary capacitances

$$Re(C) = \frac{-Im(Z)}{\omega |z|^2} \qquad\qquad 2.26$$

$$Im(C) = \frac{Re(Z)}{\omega |z|^2} \qquad\qquad 2.27$$

Where $Z = \sqrt{Re(Z)^2 + Im(Z)^2}$ is the overall complex impedance, $\omega = 2\pi f$ is angular velocity, $Re(Z)$ is the real part of the complex impedance, $Re(C)$ and $Im(C)$ are the real and

81

imaginary capacitances, respectively. $\text{Im}(C)$ is the term related to the energy dissipation of the cell and $\text{Re}(C)$ calculated at the lowest-frequency applied, indicates the energy stored. The maximum in capacitance $C''(\omega)$ versus frequency curve is associated with frequency f_0 which can be used to calculate the relaxation time $\tau = \dfrac{1}{2\pi f_0}$ [78,168]. The relaxation time constant is a measure of how fast the device can be charged and discharge reversibly.

2.8.4 Cycle Stability

Cycle performance of the electrode is very important for practical application in the supercapacitor. Cycle life is also determined by using both charge-discharge and CV cycles. The coulombic efficiency can be calculated by the following equation:

$$\eta = \frac{t_D}{t_C} \times 100\% \qquad\qquad 2.28$$

where η is the coulombic efficiency, t_D is the discharging time(s), t_C is the charging time (s). The coulombic efficiency can also be calculated from CV by comparing the first and the end cycle [169].

82

Bibliography

[1]   B.E. Conway, Electrochemical Supercapacitors Scientific Fundamentals and Technological Applications, (1999) 736.

[2]   R. Kötz, R. Kötz, M. Carlen, M. Carlen, Principles and applications of electrochemical capacitors, Electrochim. Acta. 45 (2000) 2483–2498.

[3]   B.K. Kim, S. Sy, A. Yu, J. Zhang, Electrochemical supercapacitors for energy storage and conversion, Handb. Clean Energy Syst. (2015).

[4]   P. Jampani, A. Manivannan, P.N. Kumta, Advancing the supercapacitor materials and technology frontier for improving power quality, Electrochem. Soc. Interface. 19 (2010) 57–62.

[5]   X. Zhang, H. Zhang, C. Li, K. Wang, X. Sun, Y. Ma, Recent advances in porous graphene materials for supercapacitor applications, RSC Adv. 4 (2014) 45862–45884.

[6]   H. Ji, X. Zhao, Z. Qiao, J. Jung, Y. Zhu, Y. Lu, et al., Capacitance of carbon-based electrical double-layer capacitors, Nat. Commun. 5 (2014).

[7]   C.Z. Yuan, B. Gao, L.F. Shen, S.D. Yang, L. Hao, X.J. Lu, et al., Hierarchically structured carbon-based composites: design, synthesis and their application in electrochemical capacitors, Nanoscale. 3 (2011) 529–545.

[8]   H. v Helmholtz, Ueber einige Gesetze der Vetheilung elektrischer Stroeme im koerpeflichen Leitern, Mit Anwendung Auf Die Theirischelektrischen Versuche. Ann. Phys. Chem. 89 (1853) 21.

[9]   L.L. Zhang, X.S. Zhao, Carbon-based materials as supercapacitor electrodes., Chem. Soc. Rev. 38 (2009) 2520–2531.

[10]   D.L. Chapman, LI. A contribution to the theory of electrocapillarity, London, Edinburgh, Dublin Philos. Mag. J. Sci. 25 (1913) 475–481.

[11]   L.L. Zhang, X.S. Zhao, Carbon-based materials as supercapacitor electrodes, Chem.

83

Soc. Rev. 38 (2009) 2520–2531.

[12] O. Stern, The theory of the electrolytic double-layer, Z. Elektrochem. 30 (1924) 1014–1020.

[13] B.E. Conway, Conway, B. E. Electrochemical Supercapacitors: Scientific Fundamentals and Technological Applications;, Kluwer Academic/ Plenum, New York, 1999.

[14] E. Herrero, L.J. Buller, H.D. Abruña, Underpotential deposition at single crystal surfaces of Au, Pt, Ag and other materials, Chem. Rev. 101 (2001) 1897–1930.

[15] V. Augustyn, P. Simon, B. Dunn, Pseudocapacitive oxide materials for high-rate electrochemical energy storage, Energy Environ. Sci. 7 (2014) 1597–1614.

[16] V. Augustyn, P. Simon, B. Dunn, Pseudocapacitive oxide materials for high-rate electrochemical energy storage, Energy Environ. Sci. 7 (2014) 1597.

[17] J.P. Zheng, P.J. Cygan, T.R. Jow, Hydrous ruthenium oxide as an electrode material for electrochemical capacitors, J. Electrochem. Soc. 142 (1995) 2699–2703.

[18] V. Augustyn, J. Come, M.A. Lowe, J.W. Kim, P.-L. Taberna, S.H. Tolbert, et al., High-rate electrochemical energy storage through Li+ intercalation pseudocapacitance, Nat. Mater. 12 (2013) 518–522.

[19] T. Brousse, M. Toupin, R. Dugas, L. Athouël, O. Crosnier, D. Bélanger, Crystalline MnO_2 as possible alternatives to amorphous compounds in electrochemical supercapacitors, J. Electrochem. Soc. 153 (2006) A2171–A2180.

[20] M. Okubo, E. Hosono, J. Kim, M. Enomoto, N. Kojima, T. Kudo, et al., Nanosize effect on high-rate Li-ion intercalation in $LiCoO_2$ electrode, J. Am. Chem. Soc. 129 (2007) 7444–7452.

[21] T.-F. Hsieh, C.-C. Chuang, W.-J. Chen, J.-H. Huang, W.-T. Chen, C.-M. Shu, Hydrous ruthenium dioxide/multi-walled carbon-nanotube/titanium electrodes for

supercapacitors, Carbon N. Y. 50 (2012) 1740–1747.

[22] P.J. Hall, M. Mirzaeian, S.I. Fletcher, F.B. Sillars, A.J.R. Rennie, G.O. Shitta-Bey, et al., Energy storage in electrochemical capacitors: designing functional materials to improve performance, Energy Environ. Sci. 3 (2010) 1238.

[23] C.-C. Hu, K.-H. Chang, M.-C. Lin, Y.-T. Wu, Design and tailoring of the nanotubular arrayed architecture of hydrous RuO_2 for next generation supercapacitors, Nano Lett. 6 (2006) 2690–2695.

[24] J.W. Long, K.E. Swider, C.I. Merzbacher, D.R. Rolison, Voltammetric characterization of ruthenium oxide-based aerogels and other RuO_2 solids: the nature of capacitance in nanostructured materials, Langmuir. 15 (1999) 780–785.

[25] J. Zhang, J. Jiang, H. Li, X.S. Zhao, A high-performance asymmetric supercapacitor fabricated with graphene-based electrodes, Energy Environ. Sci. 4 (2011) 4009–4015.

[26] T.-W. Lin, C.-S. Dai, T.-T. Tasi, S.-W. Chou, J.-Y. Lin, H.-H. Shen, High-performance asymmetric supercapacitor based on Co_9S_8/3D graphene composite and graphene hydrogel, Chem. Eng. J. 279 (2015) 241–249.

[27] T. Peng, H. Wang, H. Yi, Y. Jing, P. Sun, X. Wang, Co $(OH)_2$ Nanosheets Coupled With CNT Arrays Grown on Ni Mesh for High-Rate Asymmetric Supercapacitors with Excellent Capacitive Behavior, Electrochim. Acta. 176 (2015) 77–85.

[28] L.L. Zhang, R. Zhou, X.S. Zhao, Carbon-based materials as supercapacitor electrodes, J. Mater. Chem. 38 (2009) 2520–2531.

[29] M.-R. Gao, Y.-F. Xu, J. Jiang, S.-H. Yu, Nanostructured metal chalcogenides: synthesis, modification, and applications in energy conversion and storage devices., Chem. Soc. Rev. 42 (2013) 2986–3017.

[30] G. Wang, L. Zhang, J. Zhang, A review of electrode materials for electrochemical supercapacitors, Chem. Soc. Rev. 41 (2012) 797.

85

[31] P. Simon, Y. Gogotsi, Capacitive energy storage in nanostructured carbon--electrolyte systems, Acc. Chem. Res. 46 (2012) 1094–1103.

[32] Y.-G. Wang, Z.-D. Wang, Y.-Y. Xia, An asymmetric supercapacitor using RuO_2/TiO_2 nanotube composite and activated carbon electrodes, Electrochim. Acta. 50 (2005) 5641–5646.

[33] H. Li, L. Cheng, Y. Xia, A hybrid electrochemical supercapacitor based on a 5 V Li-ion battery cathode and active carbon, Electrochem. Solid-State Lett. 8 (2005) A433–A436.

[34] X. Wang, J.P. Zheng, The optimal energy density of electrochemical capacitors using two different electrodes, J. Electrochem. Soc. 151 (2004) A1683–A1689.

[35] S. Bose, T. Kuila, A.K. Mishra, R. Rajasekar, N.H. Kim, J.H. Lee, Carbon-based nanostructured materials and their composites as supercapacitor electrodes, J. Mater. Chem. 22 (2012) 767.

[36] B. McEnaney, Structure and bonding in carbon materials, Carbon Mater. Adv. Technol. (1999) 1–33.

[37] K.S. Novoselov, A.K. Geim, S. V Morozov, D. Jiang, Y. Zhang, S. V Dubonos, et al., Electric field effect in atomically thin carbon films, Science (80-)306 (2004) 666–669.

[38] D. Guo, L. Lai, A. Cao, H. Liu, S. Dou, J. Ma, Nanoarrays: design, preparation and supercapacitor applications, RSC Adv. 5 (2015) 55856–55869.

[39] A.K. Geim, K.S. Novoselov, The rise of graphene., Nat. Mater. 6 (2007) 183–191.

[40] L. Zhang, K.N. Hui, K.S. Hui, H. Lee, Facile synthesis of porous CoAl-layered double hydroxide/graphene composite with enhanced capacitive performance for supercapacitors, Electrochim. Acta. 186 (2015) 522–529.

[41] S. Huang, G.-N. Zhu, C. Zhang, W.W. Tjiu, Y.-Y. Xia, T. Liu, Immobilization of Co--Al layered double hydroxides on graphene oxide nanosheets: growth mechanism and

supercapacitor studies, ACS Appl. Mater. Interfaces. 4 (2012) 2242–2249.

[42]   L. Wang, D. Wang, X.Y. Dong, Z.J. Zhang, X.F. Pei, X.J. Chen, et al., Layered assembly of graphene oxide and Co--Al layered double hydroxide nanosheets as electrode materials for supercapacitors, Chem. Commun. 47 (2011) 3556–3558.

[43]   J. Fang, M. Li, Q. Li, W. Zhang, Q. Shou, F. Liu, et al., Microwave-assisted synthesis of CoAl-layered double hydroxide/graphene oxide composite and its application in supercapacitors, Electrochim. Acta. 85 (2012) 248–255.

[44]   R. Ramachandran, M. Saranya, C. Santhosh, V. Velmurugan, B.P.C. Raghupathy, S.K. Jeong, et al., Co_9S_8 nanoflakes on graphene (Co_9S_8/G) nanocomposites for high performance supercapacitors, RSC Adv. 4 (2014) 21151.

[45]   E.G. da Silveira Firmiano, A.C. Rabelo, C.J. Dalmaschio, A.N. Pinheiro, E.C. Pereira, W.H. Schreiner, et al., Supercapacitor electrodes obtained by directly bonding 2D MoS_2 on reduced graphene oxide, Adv. Energy Mater. 4 (2014).

[46]   A. Dato, M. Frenklach, V. Radmilovic, L.E.E. Zonghoon, Substrate-free gas-phase synthesis of graphene sheets, (2010).

[47]   Y. Hernandez, V. Nicolosi, M. Lotya, F.M. Blighe, Z. Sun, S. De, et al., High-yield production of graphene by liquid-phase exfoliation of graphite, Nat. Nanotechnol. 3 (2008) 563–568.

[48]   G.S. Shmavonyan, G.G. Sevoyan, V.M. Aroutiounian, Enlarging the surface area of monolayer graphene synthesized by mechanical exfoliation, Armen. J. Phys. 6 (2013) 1–6.

[49]   D. V Kosynkin, A.L. Higginbotham, A. Sinitskii, J.R. Lomeda, A. Dimiev, B.K. Price, et al., Longitudinal unzipping of carbon nanotubes to form graphene nanoribbons, Nature. 458 (2009) 872–876.

[50]   A. Reina, X. Jia, J. Ho, D. Nezich, H. Son, V. Bulovic, et al., Large area, few-layer

graphene films on arbitrary substrates by chemical vapor deposition, Nano Lett. 9 (2008) 30–35.

[51]   D.R. Rolison, J.W. Long, J.C. Lytle, A.E. Fischer, C.P. Rhodes, T.M. McEvoy, et al., Multifunctional 3D nanoarchitectures for energy storage and conversion, Chem. Soc. Rev. 38 (2009) 226–252.

[52]   X.-C. Dong, H. Xu, X.-W. Wang, Y.-X. Huang, M.B. Chan-Park, H. Zhang, et al., 3D graphene--cobalt oxide electrode for high-performance supercapacitor and enzymeless glucose detection, ACS Nano. 6 (2012) 3206–3213.

[53]   A. Jain, S. Jaiswal, A. Vikey, B. Bagulkar, A. Bhat, Graphene-An emerging star in the field of nanotechnology, (n.d.).

[54]   Y. Xu, K. Sheng, C. Li, G. Shi, Self-assembled graphene hydrogel via a one-step hydrothermal process, ACS Nano. 4 (2010) 4324–4330.

[55]   H.-P. Cong, X.-C. Ren, P. Wang, S.-H. Yu, Macroscopic multifunctional graphene-based hydrogels and aerogels by a metal ion induced self-assembly process, ACS Nano. 6 (2012) 2693–2703.

[56]   F. Liu, T.S. Seo, A Controllable Self-Assembly Method for Large-Scale Synthesis of Graphene Sponges and Free-Standing Graphene Films, Adv. Funct. Mater. 20 (2010) 1930–1936.

[57]   X. Huang, K. Qian, J. Yang, J. Zhang, L. Li, C. Yu, et al., Functional nanoporous graphene foams with controlled pore sizes, Adv. Mater. 24 (2012) 4419–4423.

[58]   Z. Chen, W. Ren, L. Gao, B. Liu, S. Pei, H.-M. Cheng, Three-dimensional flexible and conductive interconnected graphene networks grown by chemical vapour deposition, Nat. Mater. 10 (2011) 424–428.

[59]   X. Cao, Y. Shi, W. Shi, G. Lu, X. Huang, Q. Yan, et al., Preparation of novel 3D graphene networks for supercapacitor applications, Small. 7 (2011) 3163–3168.

[60] C. Yuan, H. Bin Wu, Y. Xie, X.W. Lou, Mixed transition-metal oxides: Design, synthesis, and energy-related applications, Angew. Chemie - Int. Ed. 53 (2014) 1488–1504.

[61] F. Shi, L. Li, X. Wang, C. Gu, J. Tu, Metal oxide/hydroxide-based materials for supercapacitors, RSC Adv. 4 (2014) 41910–41921.

[62] J. Zhang, X.S. Zhao, Conducting polymers directly coated on reduced graphene oxide sheets as high-performance supercapacitor electrodes, J. Phys. Chem. C. 116 (2012) 5420–5426.

[63] H. Zhang, G. Cao, Z. Wang, Y. Yang, Z. Shi, Z. Gu, Growth of manganese oxide nanoflowers on vertically-aligned carbon nanotube arrays for high-rate electrochemical capacitive energy storage, Nano Lett. 8 (2008) 2664–2668.

[64] C. Niu, E.K. Sichel, R. Hoch, D. Moy, H. Tennent, High power electrochemical capacitors based on carbon nanotube electrodes, Appl. Phys. Lett. 70 (1997) 1480–1482.

[65] E. Frackowiak, K. Jurewicz, S. Delpeux, F. Beguin, Nanotubular materials for supercapacitors, J. Power Sources. 97 (2001) 822–825.

[66] C. Liu, F. Li, L.-P. Ma, H.-M. Cheng, Advanced materials for energy storage, Adv. Mater. 22 (2010) E28–E62.

[67] D.N. Futaba, K. Hata, T. Yamada, T. Hiraoka, Y. Hayamizu, Y. Kakudate, et al., Shape-engineerable and highly densely packed single-walled carbon nanotubes and their application as super-capacitor electrodes, Nat. Mater. 5 (2006) 987–994.

[68] T. Bordjiba, M. Mohamedi, L.H. Dao, New Class of Carbon-Nanotube Aerogel Electrodes for Electrochemical Power Sources, Adv. Mater. 20 (2008) 815–819.

[69] K. Yang, J. Peng, C. Srinivasakannan, L. Zhang, H. Xia, X. Duan, Preparation of high surface area activated carbon from coconut shells using microwave heating, Bioresour.

Technol. 101 (2010) 6163–6169.

[70] S. Kumagai, M. Sato, D. Tashima, Electrical double-layer capacitance of micro-and mesoporous activated carbon prepared from rice husk and beet sugar, Electrochim. Acta. 114 (2013) 617–626.

[71] M. Lee, G.-P. Kim, H.D. Song, S. Park, J. Yi, Preparation of energy storage material derived from a used cigarette filter for a supercapacitor electrode, Nanotechnology. 25 (2014) 345601.

[72] H. Sun, W. He, C. Zong, L. Lu, Template-free synthesis of renewable macroporous carbon via yeast cells for high-performance supercapacitor electrode materials, ACS Appl. Mater. Interfaces. 5 (2013) 2261–2268.

[73] E. Raymundo-Piñero, M. Cadek, F. Béguin, Tuning carbon materials for supercapacitors by direct pyrolysis of seaweeds, Adv. Funct. Mater. 19 (2009) 1032–1039.

[74] H. Wang, Z. Xu, A. Kohandehghan, Z. Li, K. Cui, X. Tan, et al., Interconnected carbon nanosheets derived from hemp for ultrafast supercapacitors with high energy, ACS Nano. 7 (2013) 5131–5141.

[75] L. Wei, M. Sevilla, A.B. Fuertes, R. Mokaya, G. Yushin, Hydrothermal Carbonization of Abundant Renewable Natural Organic Chemicals for High-Performance Supercapacitor Electrodes, Adv. Energy Mater. 1 (2011) 356–361.

[76] A. Davies, A. Yu, Material advancements in supercapacitors: From activated carbon to carbon nanotube and graphene, Can. J. Chem. Eng. 89 (2011) 1342–1357.

[77] P. Simon, Y. Gogotsi, Charge storage mechanism in nanoporous carbons and its consequence for electrical double layer capacitors, Philos. Trans. R. Soc. London A Math. Phys. Eng. Sci. 368 (2010) 3457–3467.

[78] B. Fang, L. Binder, A novel carbon electrode material for highly improved EDLC

performance, J. Phys. Chem. B. 110 (2006) 7877–7882.

[79] J.P. Cheng, J. Zhang, F. Liu, Recent development of metal hydroxides as electrode material of electrochemical capacitors, RSC Adv. 4 (2014) 38893.

[80] H. Lee, M.S. Cho, I.H. Kim, J. Do Nam, Y. Lee, RuO$_x$/polypyrrole nanocomposite electrode for electrochemical capacitors, Synth. Met. 160 (2010) 1055–1059.

[81] I.-H. Kim, K.-B. Kim, Electrochemical characterization of hydrous ruthenium oxide thin-film electrodes for electrochemical capacitor applications, J. Electrochem. Soc. 153 (2006) A383–A389.

[82] K. Sakiyama, S. Onishi, K. Ishihara, K. Orita, T. Kajiyama, N. Hosoda, et al., Deposition and properties of reactively sputtered ruthenium dioxide films, J. Electrochem. Soc. 140 (1993) 834–839.

[83] T. Brousse, D. Bélanger, J.W. Long, To be or not to be pseudocapacitive?, J. Electrochem. Soc. 162 (2015) A5185–A5189.

[84] L. Hu, Q. Peng, Y. Li, Selective synthesis of Co$_3$O$_4$ nanocrystal with different shape and crystal plane effect on catalytic property for methane combustion, J. Am. Chem. Soc. 130 (2008) 16136–16137.

[85] E. Hosono, S. Fujihara, I. Honma, H. Zhou, Fabrication of morphology and crystal structure controlled nanorod and nanosheet cobalt hydroxide based on the difference of oxygen-solubility between water and methanol, and conversion into Co$_3$O$_4$, J. Mater. Chem. 15 (2005) 1938–1945.

[86] L.-X. Yang, Y.-J. Zhu, L. Li, L. Zhang, H. Tong, W.-W. Wang, et al., A Facile Hydrothermal Route to Flower-Like Cobalt Hydroxide and Oxide, Eur. J. Inorg. Chem. 2006 (2006) 4787–4792.

[87] Y. Ding, L. Xu, C. Chen, X. Shen, S.L. Suib, Syntheses of nanostructures of cobalt hydrotalcite like compounds and Co$_3$O$_4$ via a microwave-assisted reflux method, J.

Phys. Chem. C. 112 (2008) 8177–8183.

[88]   M. Wang, W. Ren, Y. Zhao, H. Cui, Synthesis of nanostructured CoOOH film with high electrochemical performance for application in supercapacitor, J. Nanoparticle Res. 16 (2014) 1–7.

[89]   Z. Lu, Q. Yang, W. Zhu, Z. Chang, J. Liu, X. Sun, et al., Hierarchical Co_3O_4@ Ni-Co-O supercapacitor electrodes with ultrahigh specific capacitance per area, Nano Res. 5 (2012) 369–378.

[90]   S.H. Kim, Y. Il Kim, J.H. Park, J.M. Ko, Cobalt-manganese oxide/carbon-nanofiber composite electrodes for supercapacitors, Int. J. Electrochem. Sci. 4 (2009) 1489–1496.

[91]   K.K. Lee, W.S. Chin, C.H. Sow, Cobalt-based compounds and composites as electrode materials for high-performance electrochemical capacitors, J. Mater. Chem. A. 2 (2014) 17212–17248.

[92]   R.S. Jayashree, P.V. Kamath, Electrochemical synthesis of α-cobalt hydroxide, J. Mater. Chem. 9 (1999) 961–963.

[93]   T. Zhao, H. Jiang, J. Ma, Surfactant-assisted electrochemical deposition of α-cobalt hydroxide for supercapacitors, J. Power Sources. 196 (2011) 860–864.

[94]   Y. Liang, M.G. Schwab, L. Zhi, E. Mugnaioli, U. Kolb, X. Feng, et al., Direct access to metal or metal oxide nanocrystals integrated with one-dimensional nanoporous carbons for electrochemical energy storage, J. Am. Chem. Soc. 132 (2010) 15030–15037.

[95]   J. Jiang, J. Liu, R. Ding, J. Zhu, Y. Li, A. Hu, et al., Large-scale uniform α-Co $(OH)_2$ long nanowire arrays grown on graphite as pseudocapacitor electrodes, ACS Appl. Mater. Interfaces. 3 (2010) 99–103.

[96]   X. Ji, P.M. Hallam, S.M. Houssein, R. Kadara, L. Lang, C.E. Banks, Printable thin

film supercapacitors utilizing single crystal cobalt hydroxide nanosheets, RSC Adv. 2 (2012) 1508–1515.

[97] F. Cao, G.X. Pan, P.S. Tang, H.F. Chen, Hydrothermal-synthesized $Co(OH)_2$ nanocone arrays for supercapacitor application, J. Power Sources.216 (2012)395–399.

[98] T. Xue, J.-M. Lee, Capacitive behavior of mesoporous Co $(OH)_2$ nanowires, J. Power Sources. 245 (2014) 194–202.

[99] W.-J. Zhou, D.-D. Zhao, M.-W. Xu, C.-L. Xu, H.-L. Li, Effects of the electrodeposition potential and temperature on the electrochemical capacitance behavior of ordered mesoporous cobalt hydroxide films, Electrochim. Acta. 53 (2008) 7210–7219.

[100] J.P. Cheng, X. Chen, J.-S. Wu, F. Liu, X.B. Zhang, V.P. Dravid, Porous cobalt oxides with tunable hierarchical morphologies for supercapacitor electrodes, CrystEngComm. 14 (2012) 6702–6709.

[101] C. Mondal, M. Ganguly, P.K. Manna, S.M. Yusuf, T. Pal, Fabrication of porous β-Co $(OH)_2$ architecture at room temperature: A high performance supercapacitor, Langmuir. 29 (2013) 9179–9187.

[102] E. Hosono, S. Fujihara, I. Honma, M. Ichihara, H. Zhou, Synthesis of the CoOOH fine nanoflake film with the high rate capacitance property, J. Power Sources. 158 (2006) 779–783.

[103] K.K. Lee, P.Y. Loh, C.H. Sow, W.S. Chin, CoOOH nanosheets on cobalt substrate as a non-enzymatic glucose sensor, Electrochem. Commun. 20 (2012) 128–132.

[104] L. Zhu, W. Wu, Y. Zhu, W. Tang, Y. Wu, Composite of CoOOH nanoplates with multiwalled carbon nanotubes as superior cathode material for supercapacitors, J. Phys. Chem. C. 119 (2015) 7069–7075.

[105] H. Zheng, F. Tang, M. Lim, A. Mukherji, X. Yan, L. Wang, et al., Multilayered films

of cobalt oxyhydroxide nanowires/manganese oxide nanosheets for electrochemical capacitor, J. Power Sources. 195 (2010) 680–683.

[106] R. Xu, H.C. Zeng, Dimensional control of cobalt-hydroxide-carbonate nanorods and their thermal conversion to one-dimensional arrays of Co_3O_4 nanoparticles, J. Phys. Chem. B. 107 (2003) 12643–12649.

[107] H. Zhang, J. Wu, C. Zhai, X. Ma, N. Du, J. Tu, et al., From cobalt nitrate carbonate hydroxide hydrate nanowires to porous Co_3O_4 nanorods for high performance lithium-ion battery electrodes., Nanotechnology. 19 (2008) 035711.

[108] Z. Zhao, F. Geng, J. Bai, H.-M. Cheng, Facile and controlled synthesis of 3D nanorods-based urchinlike and nanosheets-based flowerlike cobalt basic salt nanostructures, J. Phys. Chem. C. 111 (2007) 3848–3852.

[109] R. Xu, H.C. Zeng, Mechanistic investigation on self-redox decompositions of cobalt-hydroxide-nitrate compounds with different nitrate anion configurations in interlayer space, Chem. Mater. 15 (2003) 2040–2048.

[110] B. Li, Y. Xie, C. Wu, Z. Li, J. Zhang, Selective synthesis of cobalt hydroxide carbonate 3D architectures and their thermal conversion to cobalt spinel 3D superstructures, Mater. Chem. Phys. 99 (2006) 479–486.

[111] S.L. Wang, L.Q. Qian, H. Xu, G.L. Lü, W.J. Dong, W.H. Tang, Synthesis and structural characterization of cobalt hydroxide carbonate nanorods and nanosheets, J. Alloys Compd. 476 (2009) 739–743.

[112] Z. Zhao, F. Geng, J. Bai, H.M. Cheng, Facile and controlled synthesis of 3D nanorods-based urchinlike and nanosheets-based flowerlike cobalt basic salt nanostructures, J. Phys. Chem. C. 111 (2007) 3848–3852.

[113] A. Yuan, Q. Zhang, A novel hybrid manganese dioxide/activated carbon supercapacitor using lithium hydroxide electrolyte, Electrochem. Commun. 8 (2006)

1173–1178.

[114] S.X. Deng, D. Sun, C.H. Wu, H. Wang, J.B. Liu, Y.X. Sun, et al., Synthesis and electrochemical properties of MnO_2 nanorods/graphene composites for supercapacitor applications, Electrochim. Acta. 111 (2013) 707–712.

[115] O. Ghodbane, J.L. Pascal, F. Favier, Microstructural effects on charge-storage properties in MnO_2-based electrochemical supercapacitors, ACS Appl. Mater. Interfaces. 1 (2009) 1130–1139.

[116] J. Li, E. Liu, W. Li, X. Meng, S. Tan, Nickel/carbon nanofibers composite electrodes as supercapacitors prepared by electrospinning, J. Alloys Compd. 478 (2009) 371–374.

[117] Z. Lu, W. Zhu, X. Lei, G.R. Williams, D. O'Hare, Z. Chang, et al., High pseudocapacitive cobalt carbonate hydroxide films derived from CoAl layered double hydroxides, Nanoscale. 4 (2012) 3640–3643.

[118] M.A. Garakani, S. Abouali, B. Zhang, Z.-L. Xu, J. Huang, J.-Q. Huang, et al., Controlled synthesis of cobalt carbonate/graphene composites with excellent supercapacitive performance and pseudocapacitive characteristics, J. Mater. Chem. A. 3 (2015) 17827–17836.

[119] H. Xie, S. Tang, J. Zhu, S. Vongehr, X. Meng, A high energy density asymmetric all-solid-state supercapacitor based on cobalt carbonate hydroxide nanowire covered N-doped graphene and porous graphene electrodes, J. Mater. Chem. A. 3 (2015) 18505–18513.

[120] Q. Wang, D. O'Hare, Recent advances in the synthesis and application of layered double hydroxide (LDH) nanosheets, Chem. Rev. 112 (2012) 4124–4155.

[121] Z. Gao, J. Wang, Z. Li, W. Yang, B. Wang, M. Hou, et al., Graphene nanosheet/Ni^{2+}/Al^{3+} layered double-hydroxide composite as a novel electrode for a supercapacitor, Chem. Mater. 23 (2011) 3509–3516.

[122] Y. Wang, W. Yang, S. Zhang, D.G. Evans, X. Duan, Synthesis and electrochemical characterization of Co--Al layered double hydroxides, J. Electrochem. Soc. 152 (2005) A2130–A2137.

[123] L. Zhang, K.N. Hui, K. San Hui, H. Lee, Facile synthesis of porous CoAl-layered double hydroxide/graphene composite with enhanced capacitive performance for supercapacitors, Electrochim. Acta. 186 (2015) 522–529.

[124] Y. Kim, S. Kim, Electrochimica Acta Direct growth of cobalt aluminum double hydroxides on graphene nanosheets and the capacitive properties of the resulting composites, Electrochim. Acta. 163 (2015) 252–259.

[125] C. Tan, H. Zhang, Two-dimensional transition metal dichalcogenide nanosheet-based composites., Chem. Soc. Rev. 44 (2015) 2713–2731.

[126] H. Wang, H. Feng, J. Li, Graphene and Graphene-like Layered Transition Metal Dichalcogenides in Energy Conversion and Storage, Small. 10 (2014) 2165–2181.

[127] M. Bouroushian, Electrochemistry of metal chalcogenides, Springer Science & Business Media, 2010.

[128] D. Merki, X. Hu, Recent developments of molybdenum and tungsten sulfides as hydrogen evolution catalysts, Energy Environ. Sci. 4 (2011) 3878–3888.

[129] K. Chang, W. Chen, In situ synthesis of MoS_2/graphene nanosheet composites with extraordinarily high electrochemical performance for lithium ion batteries, Chem. Commun. 47 (2011) 4252–4254.

[130] Y. Li, H. Wang, L. Xie, Y. Liang, G. Hong, H. Dai, MoS_2 nanoparticles grown on graphene: an advanced catalyst for the hydrogen evolution reaction, J. Am. Chem. Soc. 133 (2011) 7296–7299.

[131] L. Cao, S. Yang, W. Gao, Z. Liu, Y. Gong, L. Ma, et al., Direct laser-patterned micro-supercapacitors from paintable MoS_2 films, Small. 9 (2013) 2905–2910.

96

[132] M. Acerce, D. Voiry, M. Chhowalla, Metallic 1T phase MoS2 nanosheets as supercapacitor electrode materials, Nat. Nanotechnol. 10 (2015) 1–15.

[133] B. Hu, X. Qin, A.M. Asiri, K.A. Alamry, A.O. Al-Youbi, X. Sun, Synthesis of porous tubular C/MoS_2 nanocomposites and their application as a novel electrode material for supercapacitors with excellent cycling stability, Electrochim. Acta. 100 (2013) 24–28.

[134] L.-Q. Fan, G.-J. Liu, C.-Y. Zhang, J.-H. Wu, Y.-L. Wei, Facile one-step hydrothermal preparation of molybdenum disulfide/carbon composite for use in supercapacitor, Int. J. Hydrogen Energy. 40 (2015) 10150–10157.

[135] M. Zhong, Y. Li, Q. Xia, X. Meng, F. Wu, J. Li, Ferromagnetism in VS_2 nanostructures: Nanoflowers versus ultrathin nanosheets, Mater. Lett. 124 (2014) 282–285.

[136] S. Ratha, S.R. Marri, N.A. Lanzillo, S. Moshkalev, S.K. Nayak, J.N. Behera, et al., Supercapacitors based on patronite--reduced graphene oxide hybrids: experimental and theoretical insights, J. Mater. Chem. A. 3 (2015) 18874–18881.

[137] L. Li, S. Kim, W. Wang, M. Vijayakumar, Z. Nie, B. Chen, et al., A Stable Vanadium Redox-Flow Battery with High Energy Density for Large-Scale Energy Storage, Adv. Energy Mater. 1 (2011) 394–400.

[138] H.A. Therese, F. Rocker, A. Reiber, J. Li, M. Stepputat, G. Glasser, et al.,VS_2 Nanotubes Containing Organic-Amine Templates from the $NT-VO_x$ Precursors and Reversible Copper Intercalation in $NT-VS_2$, Angew.Chemie Int. Ed. 44 (2005) 262–265.

[139] J. Feng, L. Peng, C. Wu, X. Sun, S. Hu, C. Lin, et al., Giant moisture responsiveness of VS_2 ultrathin nanosheets for novel touchless positioning interface, Adv. Mater. 24 (2012) 1969–1974.

[140] J. Feng, X. Sun, C. Wu, L. Peng, C. Lin, S. Hu, et al., Metallic few-layered VS_2

ultrathin nanosheets: high two-dimensional conductivity for in-plane supercapacitors, J. Am. Chem. Soc. 133 (2011) 17832–17838.

[141] J. Feng, X. Sun, C. Wu, L. Peng, C. Lin, S. Hu, et al., Metallic few-layered VS_2 ultrathin nanosheets: High two-dimensional conductivity for in-plane supercapacitors, J. Am. Chem. Soc. 133 (2011) 17832–17838.

[142] Y. Zhang, H. Feng, X. Wu, L. Wang, A. Zhang, T. Xia, et al., Progress of electrochemical capacitor electrode materials: A review, Int. J. Hydrogen Energy. 34 (2009) 4889–4899.

[143] G. Wang, L. Zhang, J. Zhang, A review of electrode materials for electrochemical supercapacitors, Chem. Soc. Rev. 41 (2012) 797.

[144] E. Frackowiak, Q. Abbas, F. Béguin, Carbon/carbon supercapacitors, J. Energy Chem. 22 (2013) 226–240.

[145] F. Béguin, V. Presser, A. Balducci, E. Frackowiak, Carbons and electrolytes for advanced supercapacitors, Adv. Mater. 26 (2014) 2219–2251.

[146] C.P. Mehnert, R.A. Cook, N.C. Dispenziere, M. Afeworki, Supported ionic liquid catalysis-a new concept for homogeneous hydroformylation catalysis, J. Am. Chem. Soc. 124 (2002) 12932–12933.

[147] R.F. De Souza, J.C. Padilha, R.S. Gonçalves, J. Dupont, Room temperature dialkylimidazolium ionic liquid-based fuel cells, Electrochem. Commun. 5 (2003) 728–731.

[148] J. Stoimenovski, D.R. MacFarlane, K. Bica, R.D. Rogers, Crystalline vs. ionic liquid salt forms of active pharmaceutical ingredients: a position paper, Pharm. Res. 27 (2010) 521–526.

[149] W. Lu, A.G. Fadeev, B. Qi, E. Smela, B.R. Mattes, J. Ding, et al., Use of ionic liquids for π-conjugated polymer electrochemical devices, Science (80-.). 297 (2002) 983–

987.

[150] A. Lewandowski, A. Olejniczak, M. Galinski, I. Stepniak, Performance of carbon-- carbon supercapacitors based on organic, aqueous and ionic liquid electrolytes, J. Power Sources. 195 (2010) 5814–5819.

[151] S. Pohlmann, T. Olyschläger, P. Goodrich, J.A. Vicente, J. Jacquemin, A. Balducci, Mixtures of Azepanium Based Ionic Liquids and Propylene Carbonate as High Voltage Electrolytes for Supercapacitors, Electrochim. Acta. 153 (2015) 426–432.

[152] M. Armand, F. Endres, D.R. MacFarlane, H. Ohno, B. Scrosati, Ionic-liquid materials for the electrochemical challenges of the future, Nat. Mater. 8 (2009) 621–629.

[153] C. Zhong, Y. Deng, W. Hu, J. Qiao, L. Zhang, J. Zhang, A review of electrolyte materials and compositions for electrochemical supercapacitors., Chem. Soc. Rev. 44 (2015) 7484–7539.

[154] Electrode Experiments: Gamry Potentiostat 4-Probe Instrument, (n.d.). http://www.gamry.com/application-notes/electrodes-cells/two-three-and-four-electrode-experiments/ (accessed August 2, 2016).

[155] F. Barzegar, Synthesis and characterization of activated carbon materials for supercapacitor applications, University of Pretoria, 2016.

[156] M.D. Stoller, R.S. Ruoff, Best practice methods for determining an electrode material's performance for ultracapacitors, Energy Environ. Sci. 3 (2010) 1294–1301.

[157] D.S. Achilleos, T.A. Hatton, Surface design and engineering of hierarchical hybrid nanostructures for asymmetric supercapacitors with improved electrochemical performance, J. Colloid Interface Sci. 447 (2015) 282–301.

[158] R. Vellacheri, A. Al-Haddad, H. Zhao, W. Wang, C. Wang, Y. Lei, High performance supercapacitor for efficient energy storage under extreme environmental temperatures, Nano Energy. 8 (2014) 231–237.

[159] A. Bello, F. Barzegar, D. Momodu, J. Dangbegnon, F. Taghizadeh, M. Fabiane, et al., Asymmetric supercapacitor based on nanostructured graphene foam/polyvinyl alcohol/formaldehyde and activated carbon electrodes, J. Power Sources. 273 (2015) 305–311.

[160] V. Srinivasan, J.W. Weidner, Capacitance studies of cobalt oxide films formed via electrochemical precipitation, J. Power Sources. 108 (2002) 15–20.

[161] C. Lei, F. Markoulidis, Z. Ashitaka, C. Lekakou, Reduction of porous carbon/Al contact resistance for an electric double-layer capacitor (EDLC), Electrochim. Acta. 92 (2013) 183–187.

[162] Y. Wang, Z. Shi, Y. Huang, Y. Ma, C. Wang, M. Chen, et al., Supercapacitor devices based on graphene materials, J. Phys. Chem. C. 113 (2009) 13103–13107.

[163] D. Qu, Studies of the activated carbons used in double-layer supercapacitors, J. Power Sources. 109 (2002) 403–411.

[164] E. Umeshbabu, G. Rajeshkhanna, P. Justin, G.R. Rao, Synthesis of mesoporous $NiCo_2O_4$-rGO by a solvothermal method for charge storage applications, RSC Adv. 5 (2015) 66657–66666.

[165] K. Krishnamoorthy, G.K. Veerasubramani, S. Radhakrishnan, S.J. Kim, One pot hydrothermal growth of hierarchical nanostructured Ni_3S_2 on Ni foam for supercapacitor application, Chem. Eng. J. 251 (2014) 116–122.

[166] J.L. Qi, X. Wang, J.H. Lin, F. Zhang, J.C. Feng, W.-D. Fei, Vertically oriented few-layer graphene-nanocup hybrid structured electrodes for high-performance supercapacitors, J. Mater. Chem. A. 3 (2015) 12396–12403.

[167] P.L. Taberna, P. Simon, J.-F. Fauvarque, Electrochemical characteristics and impedance spectroscopy studies of carbon-carbon supercapacitors, J. Electrochem. Soc. 150 (2003) A292–A300.

[168] P. Syedvali, G. Rajeshkhanna, E. Umeshbabu, G.U. Kiran, G.R. Rao, P. Justin, In situ fabrication of graphene decorated microstructured globe artichokes of partial molar nickel cobaltite anchored on a Ni foam as a high-performance supercapacitor electrode, RSC Adv. 5 (2015) 38407–38416.

[169] G. Wang, M. Qu, Z. Yu, R. Yuan, LiNi$_{0.8}$Co$_{0.2}$O$_2$/MWCNT composite electrodes for supercapacitors, Mater. Chem. Phys. 105 (2007) 169–174.

CHAPTER 3

3.1 Experimental Procedure and Characterization Techniques

To achieve the research task, all the experiments were done in the laboratory, followed by the characterizations of the obtained materials and evaluation of their electrochemical performance. This chapter describes the experimental procedures used and typical materials synthesis methods. This includes a description of the equipment used for materials characterization.

3.1.1 Atmospheric Pressure Chemical Vapour Deposition (AP-CVD)

The atmospheric pressure chemical vapour deposition (AP-CVD) has been considered as the most promising, inexpensive, high efficiency and feasible method for the preparation and production of large-area graphene with optical and excellent properties appropriate for device electrode applications [1]. Transitional metal substrates such as nickel (Ni) and copper (Cu) and the mixture of gases of high purity (i.e. argon (Ar), grade 5-99.999%), hydrogen (H_2), grade 5-99.999% and methane (CH_4), grade 4-99.999%) are commonly used as catalysts in CVD for production of large-area graphene. Ni and Cu have received the most consideration as substrates in CVD because of their low-cost and high etchability [1,2].

Fig 3.1(a) represents the CVD system used in this work. This study focuses on the graphene foam growth using polycrystalline Ni foam (Ni-F) (3D scaffold template with a macroporous structure with an areal density of 420 g m^{-2} and 1.6 mm in thickness, as shown in Fig 3.1(b). Nickel foam is used due to large and uniform macropores, large supporting area and high electrical conductivity which plays the vital role in the electrochemical applications. For graphene foam growth, the Ni-F substrate was treated with dilute hydrochloric acid, ethanol and distilled water to clean the surface of the foam. A cleaned Ni-F was put at the centre of the AP-CVD quartz tube for graphene growth and annealed at 1000 °C under a flow of Ar

102

(300 sccm) and H_2 (200 sccm) gases for 60 min to remove any surface contamination that might have originated from the manufacturing or packaging processes. The growth of graphene was performed at 1000 °C under the flow mixture of the Ar: H_2: CH_4 (300: 200: 10 sccm) gases for 10 min as shown in Fig 3.1. Immediately, after the growth, the CH_4 flow was stopped and samples were cooled down to room temperature under Ar (300 sccm) and H_2 (200 sccm) gases by pushing the quartz tube to the cooler region of the furnace. After growth; a micrograph of graphene on Ni foam shows wrinkles and ripples of graphene sheets. In CVD, the CH_4 act as the carbon source and during graphene growth, the amount of carbon precipitating on the nickel surface is strongly determined by the cooling rates (quenching) as shown in Fig 3.2.

Figure 3.1:(a) The CVD system used in this work (b) A schematic view of AP-CVD setup showing a quartz tube with gas inlet and outlet. Ni foam was placed at a centre of a quartz tube for graphene growth from a mixture of Ar: H_2: CH_4 gases at a temperature of 1000 °C for 10 min.

103

An extremely fast and slow rate usually gives patches of graphene deposition on the Ni substrate. Then, a medium cooling rate gives an appropriate amount of carbon in the nickel substrate surface which produces few layer graphene.

Furthermore, in order to get the free-standing graphene foam; the graphene on Ni foam samples were further soaked in 3.0 M HCl and placed on a hot plate at 60 °C to ensure complete etching of the Ni supporting structure. After complete etching of the Ni, the remaining graphene foam was washed several times with deionized water and dried in an oven to obtain the final GF product. The synthesized Ni foam graphene (Ni-FG) substrate and graphene foam samples were used in this study for electrochemical applications. Graphene foam was mixed with other materials as will be discussed below to form composites using hydrothermal methods technique.

Figure 3.2: Illustration of different cooling rates during graphene growth [3].

3.1.2 Hydrothermal Method

The hydrothermal synthesis is an inexpensive, simple, effective and convenient process to prepare highly ordered nanostructures on substrate, converting metal oxide/hydroxide and transitional metal disulphide into desired nanostructured materials and composites materials of different nanostructures materials like nanorods, nanoflowers, nanowires, nanoribbons, nanoparticles, nanotubes and nanosheets with their corresponding chemical and physical properties suitable for supercapacitor application [5–9]. The hydrothermal process uses water as the reaction medium in sealed stainless-steel autoclave system, which is adapted for ensuring the high temperature and pressure build-up. The temperature used is often higher than 100 °C so that the autogenous pressure will be established in a closed system. Figure 3.3 below shows the complete hydrothermal system that was used in this work which shows in (a) the stainless steel autoclave system with 120 mL Teflon lining and (b) showing the electric oven often used.

(a)   **(b)**

Figure 3.3: Complete system for the hydrothermal growth, (a) shows the stainless steel autoclave system with the Teflon lining (b) shows the electric oven used for heating.

The pressure produced within the reactor is not strongly determined by the reaction temperature only, but also depends on the experimental factors such as the amount of liquid added and any dissolved salts.

The characteristics of hydrothermal method are that when the starting materials are exposed to special conditions, some relative reaction takes place, followed by the formation of morphologies. Furthermore, the morphologies can be controlled by changing the parameters in the reaction system such as choice of solvent, capping reagent/surfactant, control of temperature/time, changing of PH value [4].Typical reactions include an initial nucleation and growth of crystallites followed by the final assembly to form the final product. The hydrothermal process also prepares highly ordered nanostructures on numerous substrates which allow the in-situ fabrication of radical micro, meso and macro-particulate hybrid structures [5].

Solvothermal chemical growth used is similar to hydrothermal process**.** The solution used in solvothermal can be the aqueous and non-aqueous solution at the temperature higher than that of the boiling point of such solvent. At relatively high temperatures and pressures, solvothermal methods can significantly increase the solubility and reactivity of reactant.

In this study, hydrothermal growth was used to prepare cobalt hydroxide carbonate, CoAl-LDH, cobalt oxyhydroxide and MoS_2.

3.1.3   Synthesis of Activated Carbon (AC)

In this study two types of activated carbon (from Polyvinyl alcohol PVA and graphene foam denoted as AGF and from expanded graphite denoted as AEG) was produced using the hydrothermal technique, and they are discussed briefly below.

d) Synthesis of Activated Carbon from PVA and graphene foam

Activated carbon used for the production of the composite materials and asymmetric device was from the procedure reported by Fashard *et al* and Bello *et al* [6,7]: Briefly, a graphene foam (GF) and polyvinyl alcohol (PVA) were used as starting material for the production of hydrogel, which was then used to produce porous carbon materials after the activation process. Graphene foam (GF) was prepared by CVD as described above under CVD section. The three-dimensional hydrogel was synthesized via the hydrothermal process. The preparation was carried as follows; 100 mg of the GF was dispersed in 10 ml of polyvinyl alcohol (PVA) in a vessel glass by ultrasonication followed by addition of 1.5 ml of hydrochloric acid (HCl) as the cross-linker. The resultant mixture was transferred into a 150 ml Teflon-lined autoclave vessel and kept at 190 °C for 12 h [8]. After cooling to room temperature the hydrogel was washed with deionized water for several times and dried for 6 h. The as-prepared hydrogel was then soaked in aqueous KOH solution with a KOH/hydrogel mass ratio of 7 for 24 h. The composite mixture was then placed in a horizontal tube furnace ramped from room temperature to 800 °C at 10 °C/min under argon gas flow for 1 h of activation. This procedure transformed the composite hydrogel into carbon materials consisting of a continuous porous network material. The activated material denoted as AGF was neutralized with 0.1 ml HCl, washed with deionised water and dried at 120 °C for 12 h after which samples were characterized. This activated carbon was used to make the composite with other materials because it showed the existence of some functional groups which will make it easier to react with other materials.

107

e) Synthesis of Activated Carbon from Expanded Graphite (AEG)

Activated carbon from expanded graphite designated as AEG used for the making asymmetric devices was from the procedure reported by Fashard *et al* [12]. In a typical procedure, 1g of expanded graphite was dispersed in 100 ml of 10 wt % polyvinylpyrrolidone (PVP) solution to produce concentrated dispersions, and the mixture was transferred to a vessel glass and sonicated for 12 h. 5 g of KOH was then added to the solution ,which was stirred for 2 h at 60°C. After 2h of stirring, the EG formed a solid precipitate at the surface of the solution. The solid precipitate obtained was collected and dried at 70 °C for 12 h. The dried solid precipitate was then placed in a horizontal tube furnace ramped from room temperature to 800 °C at 5 °C/min under argon and hydrogen gas flow for 2 h of activation. The activated material was neutralized with 1 M HCl, washed with deionized water and dried at 60 °C for 12 h. This material was used as the negative electrode for the asymmetric devices that were studied in this work because it showed good stability and high specific capacitance when tested in the negative potential as compared to other activated carbon produced from PVA and graphene foam.

3.1.4 Hydrothermal Growth of Cobalt-Based and Composites Materials

The hydrothermal growth method is a bottom-up method used in this study to synthesize cobalt-based hydroxide and composites.

a) Synthesis of Cobalt Hydroxide Carbonate/Activated Carbon Composites

The cobalt hydroxide carbonate nanorods were first synthesized using the hydrothermal technique by varying the growth time. In a typical procedure: $CoCl_2 \cdot 6H_2O$ (1 mmol) and urea (1.0 mmol) were added to 20 mL of water and stirred for 10 minutes. The mixture was then transferred to a 120 mL Teflon-lined stainless steel autoclave and kept at $120^{\circ}C$ for 3, 6,

9 and 12 h growth times, respectively. After cooling to room temperature the light-pink product was washed with deionized water and dried at 60°C for further characterization and analysis.

In order to improve the electrochemical performance of the pure cobalt hydroxide carbonate, AGF was incorporated into cobalt hydroxide carbonate to produce cobalt hydroxide carbonate/AC composite.

This was prepared by the usual process of dissolving the precursor materials which included $CoCl_2.6H_2O$ (1 mmol) and urea (1.0 mmol) in 20 mL of deionized water containing 15 mg of activated carbon which had been earlier subjected to ultrasonication for 12 h for uniform dispersion at room temperature. The obtained solution was then transferred to a 120 mL Teflon-lined stainless steel autoclave and kept at 120 $^{\circ}$C for 6 h. After naturally cooling to room temperature the product cobalt hydroxide carbonate/activated carbon was washed with deionized water and dried at 60 °C for 6 h for further characterization and analysis.

b) Synthesis of Cobalt Aluminium – Layered Double Hydroxide (LDH)/Graphene Foam Composite and Cobalt Oxyhydroxide Derived From CoAl - LDH

Firstly, 1.09 g of $CoCl_2.6H_2O$, 1.2 g of $AlCl_3.6H_2O$ and1.2 g of Urea were added to 40 mL of water and stirred for 10 minutes for the synthesis of pure CoAl-LDH. The mixture was then carefully transferred into a sealed 120 mL Teflon-lined stainless-steel autoclave and kept at a temperature of 120 $^{\circ}$C for 18 h. After cooling to room temperature, the pinkish product was repeatedly washed with deionized water and ethanol several times to remove any unreacted precursor and residual. Following procedures to obtain the final product was in the same method as described for the cobalt hydroxide carbonate materials.

Figure 3.4: Preparation of CoAl-LDH/GF.

To improve the electrochemical performance of the pristine CoAl-LDH material, graphene foam material was added to produce CoAl-LDH/graphene composite through the same bottom-up approach described above. In the case of LDH/GF composite, the addition of porous and conducting graphene foam to the CoAl-LDH matrix provided an improved electron transfer rate and better structural support for the growth of CoAl-LDH flakes on the graphene sheets.

Fig 3.4 represents schematic diagram for the preparation of CoAl-LDH/GF composite. Typically, 25 mg of the as-synthesized GF was dispersed in 40 mL of water by ultrasonication for 12 h at room temperature. Then, 1.09 g of $CoCl_2.6H_2O$, 1.2 g of $AlCl_3.6H_2O$ and 1.2 g of urea were added to the pre-sonicated GF solution and the entire mixture was stirred for 10 min. The resulting mixture was then transferred to a 120 mL Teflon-lined stainless steel autoclave and kept at 120 °C for 18h. After naturally cooling to room temperature the product CoAl-LDH/GF composite was washed with deionized water and ethanol, and dried at 60 °C for 6 h.

The mesoporous nanosheets of cobalt oxyhydroxide (CoOOH) were also derived on Ni-FG by alkaline etching of the Al cations in CoAl-LDH using a NaOH solution.

In a typical procedure, a nickel foam graphene substrate was synthesized by growing graphene sheets on the polycrystalline Ni foam (3D scaffold template with a macroporous structure) using atmospheric pressure chemical vapour deposition (AP-CVD) as discussed

110

above. CoOOH nanosheets supported on nickel foam graphene were deduced from en-sute hydrothermally prepared CoAl-LDH on Ni-FG substrate by alkaline etching in concentrated NaOH solution as reported in ref [9]. A solution (pink in colour) for the hydrothermal reaction was prepared by adding Co $(NO)_3 \cdot 6H_2O$ (2 mmol), Al $(NO_3)_3 \cdot 6H_2O$ (2 mmol), NH_4F (8 mmol) and CO $(NH_2)_2$ (10 mmol) in 36 mL of deionized water and stirred for 10 min, as demonstrated in Fig 3.5. Ni-FG substrate was immersed into the above solution and then carefully transferred into a 120 mL sealed Teflon-lined stainless-steel autoclave and kept at a temperature of 100°C for 24 h. After 24 h and cooling of an autoclave to room temperature, the obtained CoAl-LDH coated on Ni-FG was cleaned with deionized water. Then, the CoAl-LDH coated Ni-FG was immersed in 5 mol L^{-1} NaOH for 48 h and subsequently rinsed with deionized water, followed by ethanol for 5 min using ultrasonic bath and dried at 60 °C for 6 h to obtain the final product CoOOH nanosheets (shown by micrograph image) on Ni-FG substrate, as demonstrated in Fig 3.5. The weight of the Co CoOOH film on Ni-FG substrate was measured by weighing the Ni-FG substrate before and after the hydrothermal process and a mass loading of ~5 mg cm^{-2} was obtained.

Figure 3.5: A schematic view of the hydrothermal growth of CoAL−LDH on graphene synthesized on Ni foam and alkaline etching in concentrated NaOH solution which produces a mesoporous structure of CoOOH on Ni foam graphene.

3.1.5   Synthesis of Transition Metal Dichalcogenides

c)   Synthesis of VS$_2$

The solvothermal process was used in this study to synthesize VS$_2$ nanosheets. Fig 3.6 presents the preparation process of VS$_2$ nanosheets. In a typical procedure, ammonium metavanadate (NH$_4$VO$_3$) (2 mmol) was added to an 18 ml mixture of 15 ml deionized water and 3 ml ammonia, accompanied by vigorous stirring to completely dissolve the ammonium vanadate. Subsequently, thioacetamide (CH$_3$CSNH$_2$) (10 mmol) was added to the above solution under vigorous stirring. The final homogeneous solution was transferred into a sealed Teflon-lined stainless-steel autoclave and kept at a temperature of 180° C for 20 h. After cooling to room temperature, the black powder was washed with deionized water and dried at 60 $^{\circ}$C.

112

Figure 3.6: Preparation procedure of VS_2 nanosheets.

d) Synthesis of MoS₂/Graphene Composites

Firstly, 1 mmol of ammonium molybdate was dissolved in 30 ml of deionized water under vigorous stirring for 20 min, 5 mmol of thiourea (CH_4N_2S) was then added to this solution and stirring of the mixture was further continued for 30 min. The mixture was then carefully transferred into a sealed 120 mL Teflon-lined stainless-steel autoclave and kept at a temperature of $150^°$ C for 20 h. After cooling to room temperature, the black powder samples were repeatedly washed with deionized water and ethanol several times and finally dried at $60^°$ C for 6 h.

To improve systematically the physical and electrochemical properties of MoS_2 material, different graphene foam mass loading from 50 mg to 200 mg were added to produce MoS_2/GF composite. Fig 3.7 presents the preparation of MoS_2/GF composite by the hydrothermal system in order to obtain the MoS_2/graphene foam (MoS_2/GF) composite. Typically, 50,100, 150 and 200 mg of laboratory synthesized GF samples were dispersed in 30 mL of water by ultrasonication for 12 h at room temperature. Then 1 mmol of ammonium molybdate and 5 mmol thiourea were added to the different GF solutions and the mixtures were all stirred for 10 min.

113

Figure 3.7: Preparation of MoS_2/GF

The obtained solutions were then transferred to 120 mL Teflon-lined stainless steel autoclave systems and kept at 150 $^{\circ}$C for 20h. After naturally cooling to room temperature, the final MoS_2/GF product containing different amounts of GF was washed with deionized water and dried at 60 °C for 6 h.

3.2 Material characterization

3.2.1 Structural and Qualitative Phase studies

e) X-Ray Powder Diffraction (XRD)

X-ray diffraction technique is the non-destruction technique which provides information about the crystallographic structure, lattice parameter, crystal orientation and particle sizes of materials and thin films. This technique is built on detecting the scattered intensity of an X-ray beam hitting a sample as a function of incident and scattered angles. The X-ray beam is scattered on the crystalline material and the intensity of the diffracted beam due to the periodic preparation of atoms in the sample is measured as the function of the diffraction angle 2θ as shown in Fig 3.8.

114

Figure 3.8: Schematic diagram of XRD.

The diffraction from crystals is defined by the well-known Bragg's equation:

$$2d \sin \theta = n\lambda \qquad\qquad 3.1$$

where d is the spacing between diffraction planes, θ is the incident angle, n is an integer value (1, 2, 3…), λ is the wavelength of the beam.

The number of peaks or lines, intensities of peaks or lines and the angular positions of peaks in terms of 2θ are used to identify the crystal structure of the material.X-ray diffraction (XRD) patterns of all prepared samples in this study were collected using an XPERT-PRO diffractometer (PANalytical BV, Netherlands) with theta/2theta geometry. Co $K1\alpha$ radiation with a wavelength of 1.7890 Å was used as the X-ray source and a tube was operated at 50 kV and 30 mA.

f) Raman Analysis

Raman spectroscopy is used to study low-frequency, vibrational and rotational modes of atomic and molecular system of a sample. In Raman spectroscopy, the sample is irradiated with a monochromatic laser beam which interacts with the molecules of the sample and emits

a scattered light. To construct a Raman spectrum, the scattered light having a frequency different from that of incident light (inelastic scattering) is used. A scattered radiation with a frequency equal to the frequency of incident radiation is known as Rayleigh scattering, but that with only a small fraction of scattered radiation being different from the frequency of incident radiation is known as Raman scattering. However, if the frequency of incident radiation is higher than frequency of scattered radiation, the Raman scattering is known as Stokes lines, [10]while in the case of the frequency of incident radiation being lower than the frequency of scattered radiation, then anti-Stokes lines are being observed [10].

Raman spectroscopy is usually used to analyze carbonaceous materials such as (graphene, activated carbon and carbon nanotubes) which are composed of first order and second order regions. In the first order region, the graphite bands (D and G bands) occur between 1100 - 1800 cm^{-1}. The spectra in this order is characterized by two main bands, the graphitic (G) band, which occur at ~ 1600 cm^{-1}, and the disorder (D) band, which occurs at ~1350 cm^{-1} (see Fig 3.9). The G-band represents in-plane vibrations of aromatic carbons in the graphitic structure. The G-band occur at about 1580 cm^{-1} and involves the in-plane bond stretching motion of pairs of carbon sp^2 atoms .

Figure 3.9 : Raman spectra of carbon showing the disordered (D), graphitic (G) and 2D bands.

116

All of the sp^2 carbon materials exhibit a strong peak in the range of 2700-2800 cm^{-1} in the Raman spectra called 2D (see Fig 3.9). The 2D band (double-phonon process) has a strong frequency which depends on the excitation laser because of the double resonance process which occurs between two K-points in the electronic band structure of graphene, for example [11].

In this study, Raman spectroscopy measurements were carried out using a Jobin Yvon Horiba TX 6400 micro-Raman spectrometer equipped with a triple monochromator system to eliminate contributions from Rayleigh lines and using LabSpec (Ver. 5.78.24) analytical software. The samples were analyzed with a 514 nm argon excitation laser and 1.5 mW laser power.

g) Fourier Transform Infra-red Resonance (FTIR) Spectroscopy

Fourier transformation infrared spectroscopy is used for identification the presence of certain functional groups in a molecule. In FTIR, absorption of IR radiation takes place when the photon is transferred to a molecule and excites it to higher energy states [12] . A transmission emission and absorption infrared spectrum are acquired over wide spectra range articulated as wavelength. FTIR measurements were done to determine the different vibration modes arising from the IR-excitation of the samples. Fourier transform infrared (FTIR) spectra of the samples were recorded using a Bruker Vertex 77 v FTIR spectrometer.

h) X-ray Photoelectron Spectroscopy (XPS)

X-ray photoelectron spectroscopy is a quantitative spectroscopic surface chemical analysis technique used to estimate the elemental composition, chemical and electronic state of the elements on the surface of a material. XPS works on irradiating the sample surface with monochromatic X-ray and the emitted photoelectrons are detected. The detected electron originates from only the top few atomic layers of the sample because the mean-free paths of

117

the emitted photoelectrons are very small. The kinetic energy of the photoelectrons depends on the energy of the photon

$$KE = hv - E_B \qquad\qquad 3.2$$

where E_B the binding energy of the particular electron in the atom, hv is the energy of the X-ray source and KE is the kinetic energy of the emitted electron that is measured. Electron spectrometer identifies the electrons emitted from the sample according to their kinetic energy. The binding energy is considered as ionization energy of the atom for the particular shell involved. Since there are different electrons and binding energies in an atom, there is the resultant variation of kinetic energies of the emitted electrons. Furthermore, there is the different possibility for each process. The energy intensity and position distribution of the photoelectrons lines are used as a fingerprint to identify the elements present and together with measured peak areas of well-defined cross sections.

In this study, X-ray photoelectron spectroscopy (XPS, K-alpha, and Thermo Fisher) with monochromatic Al Kα radiation as the X-ray source was used.

i) The Brunauer Emmet and Teller Techniques (BET)

The Brunauer-Emmett-Teller (BET) method is mostly used for determining the surface area, average pore volume, porosity, and the general pore size distribution of powders and porous materials. In this study, the surface area was calculated by the Brunauer–Emmett–Teller (BET) method from the adsorption branch in the relative pressure range (P/P$_0$) of 0.01–1.The pore size distribution of the synthesized materials was studied using Barrett-Joyner-Halenda (BJH) method from the desorption branch of the isotherm nitrogen at the temperature of 77K. Adsorption–desorption isotherms were measured at -196°C using a Micrometrics ASAP 2020. All the samples were degassed at 180° C for more than 12 h under vacuum conditions. The degassed sample was then transferred to the main chamber for the complete analysis

118

using N_2 gas at 77K. Firstly, the sample is dosed with a specific amount of gas which is then evacuated to get the quantity of gas absorbed by the sample in excess of a relative pressure range, P/P_0 (i.e.$0.01 < P/P_0 < 0.2$). The nature of the isotherm produced also gives an indication of types of pores and their sizes in the sample.

The first classification of physical adsorption isotherms was first presented by Brunauer in 1940 [13]. He suggested five isotherm types established on the known experiment. In 1985, the IUPAC Commission on Colloid and Surface Chemistry proposed the classification of pore sizes and gas sorption isotherms that reflect the relationship between porosity and sorption [14,15]. Depending on the pore structure of different materials, IUPAC classification of adsorption/desorption isotherm can be classified in various types as illustrated in Fig 3.11 (a). The six types of isotherms are characteristics of adsorbents that are microspores (type I), nonporous or macroporous (type II,III,VI), or mesoporous (type (IV and V) [14]. The adsorption hysteresis (IV and V) are classified and generally show that there is the association between the shape of the hysteresis loop and texture (e.g., pore geometry, pore size distribution and connectivity) of the mesoporous material. Such hysteresis loops show a wide variety of shapes as shown in Fig 3.11 (b). The type H1 is often associated with the porous material consisting of well-defined cylindrical-like pore channels or agglomerates of approximately uniform spheres. Type H2 attributes materials that are often disorder where the distribution of pore size and shapes are not well-defined. The H3 isotherms do not exhibit any limiting adsorption at $\dfrac{p}{p^o}$, with aggregates of plate-like particles giving rise to slit-shaped pores. H4 is associated with narrow slit-like pores [16].

Figure 3.10: (a) The IUPAC classification of adsorption isotherms showing both the adsorption and desorption pathways and (b) the relationship between the pore shape and the adsorption-desorption isotherm [17].

3.2.2 Morphological Studies

j) Scanning Electron Microscopy (SEM)

The scanning electron microscopy is used to give the microstructural morphology and elemental composition of the sample by using focused beam energy dispersive x-ray spectrometer (EDS) with the scanning electron microscopy. It uses focused electron beams which are made with a Schottky field emission source that utilizes a high applied field in an ultra-high vacuum to generate a variety of signals at the surface of solid specimens . Fig 3.12 shows the typical layout of SEM, which encompasses the electron gun which produces an electron beam (electron source and acceleration anode), electromagnetic lenses to focus the electrons, a vacuum chamber housing the specimen stage and a selection of detectors to collect the signals emitted from specimen. The electrons interact with specimen surfaces producing various signals that contain information about the composition and sample surface

120

topography recorded as signals by suitable detectors. The types of signals produced by SEM include secondary electrons(SE), reflected or back-scattered electrons(BSE), characteristics X-rays, bremsstrahlung X-rays, absorbed current (specimen current) transmitted electrons (thin samples) and cathodoluminescence .

Secondary electrons are used for imaging to obtain information about the morphology at the sample surface. High-resolution images of the order of 1 nm are visible with SEMs having secondary electron detectors for secondary electron imaging. X-ray emission consists of electron rearranging inside the energy levels of the electronic structure and as such the characteristics x-rays are used to identify composition and measure elemental quantity in the sample. The BSE is associated with the atomic number of the signatory element at the sample surface. As such, the BSE are frequently used to analytical SEM in conjunction with the x-ray to provide information about the elemental distribution of the sample. EDS characterization is usual integrated into SEM instrument and comprises a sensitive X-ray detector, a liquid nitrogen Dewar for cooling and software to collect and analyze energy spectra. EDS detector is used to separate the characteristic X-rays of different elements into an energy spectrum and EDS software is used to analyze the energy spectrum in order to determine the specific elements present in the sample [18]. EDS can also be sued to find the chemical composition of materials down to a spot size of a few microns, and to create an elemental composition. The morphology of all samples in this study was studied using the high-resolution Zeiss Ultra plus 55 fields emission scanning electron microscope (FE-SEM) operated at 2.0 kV. Energy dispersive x-ray (EDX) patterns were taken with a JEOL 5800LV microscope equipped with an energy-dispersive X-ray spectrometer operated at 20 kV and was used to estimate the elemental composition of the produced materials.

Figure 3.11: Schematic diagram of SEM [19].

k) Transmission Electron Microscopy (TEM)

Transmission electron microscopy (TEM) provides information from micro down to atomic scale. The TEM uses a high electron beam transmitted through a very thin sample (<50 nm) to image and analyzed the structure of materials. An (HRTEM) (Joel JEM-2100F Field Emission Electron Microscope, with a maximum analytical resolution of 200 KV and a probe size of 0.5 nm), with selected area electron diffraction (SAED) observations were used in this work to analyzed the morphology and structure of the samples. The samples were prepared by dissolving the active material in powder form in ethanol and ultrasonic to uniformly dissolve it. The ethanol solution containing the sample for the study was dropped on a lacey carbon-coated copper grid and left for particular minutes to dry before being loaded into the chamber for analysis.

122

3.2.3   Electrode Preparation and Electrochemical Characterization

The electrochemical measurements of all samples coated on nickel foam (NF) and nickel foam graphene (NF-G) as current collectors were carried out in both three and two electrodes configurations using a Biologic VMP-300 potentiostat (Knoxville TN 37,930, USA) controlled by the EC-Lab® V10.37 software. The PGSTAT workstation is an electronic instrument designed to control the potential difference applied to the working electrode (WE) with a current flow (in the form of either a half cell or a full cell) and the reference electrode (RE) with no current. The PGSTAT generates characteristics cycling voltammetry curves which give information about the possible electrochemical reactions in the system. For all electrochemical measurements performed in a three-electrode configuration, the as prepared electrodes served as the working electrodes, Ag/AgCl (3 M KCl) served as the reference electrode and glassy carbon plate as the counter electrode as shown in Fig 3.13 (a). In the two-electrode configuration, with coin-type cells using a glass micro fiber filter paper as the separator as shown in Fig 3.13(b). The electrodes for supercapacitor were prepared as follows: The synthesized material and polyvinylidene fluoride (PVDF) binder and carbon black (CB) to improve the conductivity (if the material conductivity is not good) were mixed in a weight ratio of 8:1:1 which was homogenized and dispersed in N-methylpyrrolidone (NMP) solution to obtain the slurry. The slurry was then uniformly coated on a nickel foam current collector and dried at 60° C in an oven for 8 h to ensure complete evaporation of the NMP. A 6 M KOH aqueous electrolyte which provides ionic conductivity and facilitates charge compensation on each electrode in the cell was used. Cycling voltammetry (CV), Galvanostatic charge-discharge (GCD) and electrochemical impedance spectroscopy (EIS) and cycling life were carried out for all the samples.

123

Figure 3.12: Schematic view of (a) three [20] and (b) two electrode setup for testing in the electrode material [21].

Bibliography

[1]   C. Miao, C. Zheng, O. Liang, Y. Xie, Chemical Vapor Deposition of Graphene, Phys. Appl. Graphene - Exp. (2011) 37–54.

[2]   A. Mohsin, Graphene synthesis and characterization on copper, (2012). http://ir.uiowa.edu/etd/3354/.

[3]   D. Shin, S. Bae, C. Yan, B.H. Hong, J. Ryu, J.-H. Ahn, et al., Synthesis and applications of graphene electrodes, Carbon Lett. 13 (2012) 1–16.

[4]   M.-R. Gao, Y.-F. Xu, J. Jiang, S.-H. Yu, Nanostructured metal chalcogenides: synthesis, modification, and applications in energy conversion and storage devices., Chem. Soc. Rev. 42 (2013) 2986–3017.

[5]   Q. Zhang, C. Xu, B. Lu, Super-Long Life Supercapacitors Based on the Construction of Ni Foam/Graphene/Co_3S_4 Composite Film Hybrid Electrodes, Electrochim. Acta. 132 (2014) 180–185.

[6]   F. Barzegar, a. Bello, D.Y. Momodu, J.K. Dangbegnon, F. Taghizadeh, M.J. Madito, et al., Asymmetric supercapacitor based on an α-MoO_3 cathode and porous activated carbon anode materials, RSC Adv. 5 (2015) 37462–37468.

[7]   A. Bello, F. Barzegar, D. Momodu, J. Dangbegnon, F. Taghizadeh, N. Manyala, Symmetric supercapacitors based on porous 3D interconnected carbon framework, Electrochim. Acta. 151 (2015) 386–392.

[8]   L. Zhang, F. Zhang, X. Yang, G. Long, Y. Wu, T. Zhang, et al., Porous 3D graphene-based bulk materials with exceptional high surface area and excellent conductivity for supercapacitors, Sci. Rep. 3 (2013).

[9]   Z. Lu, W. Zhu, X. Lei, G.R. Williams, D. O'Hare, Z. Chang, et al., High pseudocapacitive cobalt carbonate hydroxide films derived from CoAl layered double hydroxides, Nanoscale. 4 (2012) 3640.

125

[10] L.M. Malard, M.A. Pimenta, G. Dresselhaus, M.S. Dresselhaus, Raman spectroscopy in graphene, Phys. Rep. 473 (2009) 51–87.

[11] A.C. Ferrari, Raman spectroscopy of graphene and graphite: disorder, electron--phonon coupling, doping and nonadiabatic effects, Solid State Commun. 143 (2007) 47–57.

[12] S.J. Parikh, J. Chorover, FTIR spectroscopic study of biogenic Mn-oxide formation by Pseudomonas putida GB-1, Geomicrobiol. J. 22 (2005) 207–218.

[13] S. Brunauer, L.S. Deming, W.E. Deming, E. Teller, On a theory of the van der Waals adsorption of gases, J. Am. Chem. Soc. 62 (1940) 1723–1732.

[14] K.S.W. Sing, Reporting physisorption data for gas/solid systems with special reference to the determination of surface area and porosity (Recommendations 1984), Pure Appl. Chem. 57 (1985) 603–619.

[15] J.C.P. Broekhoff, Mesopore determination from nitrogen sorption isotherms: Fundamentals, scope, limitations, Stud. Surf. Sci. Catal. 3 (1979) 663–684.

[16] N. Rahmat, A.Z. Abdullah, A.R. Mohamed, A review: mesoporous Santa Barbara amorphous-15, types, synthesis and its applications towards biorefinery production, Am. J. Appl. Sci. 7 (2010) 1579.

[17] P. Kumar, K.-H. Kim, E.E. Kwon, J.E. Szulejko, Metal--organic frameworks for the control and management of air quality: advances and future direction, J. Mater. Chem. A. 4 (2016) 345–361.

[18] J. Goldstein, D.E. Newbury, P. Echlin, D.C. Joy, A.D. Romig Jr, C.E. Lyman, et al., Scanning electron microscopy and X-ray microanalysis: a text for biologists, materials scientists, and geologists, Springer Science & Business Media, 2012.

[19] Purdue University - Scanning Electron Microscope, (n.d.). https://www.purdue.edu/ehps/rem/rs/sem.htm (accessed August 2, 2016).

[20]   S. Gouws, Voltammetric Characterization Methods for the PEM Evaluation of Catalysts, INTECH Open Access Publisher, 2012.

[21]   F. Barzegar, Synthesis and characterization of activated carbon materials for supercapacitor applications, University of Pretoria, 2016.

CHAPTER 4

In this chapter, the results obtained from all experimental procedures outlined in the previous chapter are fully described. The resulting publications from each research topics are also presented afterwards.

4.1 Effect of Growth Time of Hydrothermally Grown Cobalt Hydroxide Carbonate on its Supercapacitive Performance

4.1.1 Introduction

Transitional metal oxides/hydroxides have attracted major research interests as electrode material for energy storage for supercapacitors because of their favourable capacitive characteristics and environmental friendliness.Specifically, cobalt-based hydroxides have been studied by researchers as faradic materials for supercapacitor due to good cycling stability layered structure with large interlayer spacing and the fact that their morphology may be successfully controlled by transforming the interface between the positively charged layers and anions [1].

Various morphology of cobalt hydroxide carbonates ($Co_2 (OH)_2 CO_3$) such as nanorods, nanowires, sisal-like, dandelion-like, pinecone-like, urchin-like and flower-like-structures have been successfully synthesized by different methods. As reported in previous studies the reaction temperature, surfactant content, ion concentration and aging time play important role in the morphology and size of cobalt hydroxide carbonate ($Co_2(OH)_2CO_3$) nanostructures [1–3]. Sun *et al* investigated the structural transformation and electrochemical characterization of cobalt hydroxide carbonates from non-crystal nanosheets to single –crystal nanorods and nanosheets using amino acid (glycine) as the direct reagent. In their work, they showed that glycine molecules play a crucial role in the transformation of phases and morphologies.

128

In this section, cobalt hydroxide carbonate nanorods were successfully synthesized using a hydrothermal method at a temperature of 120 °C with different synthesis times of 3, 6, 9 and 12 h, respectively. It was noticed that increasing growth time plays a crucial role in the transformation of phases and morphologies. The systematic study was made of the effect of growth time, the morphology and SSA of cobalt hydroxide carbonate nanorods. The electrochemical characterization of cobalt hydroxide carbonate nanorods was investigated using three-electrode configurations. After characterizing all the samples produced, it was realized that the sample grown for the longest time of 12 h had shown the well-defined compact nanorods, the highest specific surface area and the best electrochemical performance. It was also established that the increase in growth time beyond 12 h resulted in producing cobalt oxide with different electrochemical properties from the cobalt hydroxide carbonates.

4.1.2   Results and Discussions

A detailed summary of the results of the analysis of hydrothermal synthesized cobalt hydroxide carbonate nanorods and the effect of growth times on the electrochemical performance is presented in the paper below.

129

Effect of growth time of hydrothermally grown cobalt hydroxide carbonate on its supercapacitive performance

CrossMark

Tshifhiwa M. Masikhwa, Julien K. Dangbegnon, Abdulhakeem Bello, Moshawe J. Madito, Damilola Momodu, Farshad Barzegar, Ncholu Manyala *

Department of Physics, Institute of Applied Materials, SARCHI Chair in Carbon Technology and Materials, University of Pretoria, Pretoria 0028, South Africa

ABSTRACT

We present the time-dependent synthesis of cobalt hydroxide carbonate nanorods by hydrothermal method with a systematic increase of different parameters such as specific surface area and specific capacitance as a function of different synthesis time. Morphological characterization of the cobalt hydroxide carbonate nanorods were carried out by scanning electron microscopy (SEM) and transmission electron microscopy (TEM). The results show that variation of the time of reaction plays a crucial role in the transformation of samples' morphology. Cobalt hydroxide carbonate nanorods synthesized with 12 h reaction time, which is the reaction just before the materials transforms into cobalt oxide under the same synthesis conditions exhibited the highest specific capacitance of 466 F g^{-1} at a current density of 1 A g^{-1} in 6 M KOH electrolyte and also showed excellent stability with ~99% capacitance retention after 2000 cycles at a current density of 10 A g^{-1}. Based on the above results, the cobalt hydroxide carbonate nanorods show a considerable potential as electrodes materials for supercapacitor applications.

Crown Copyright © 2016 Published by Elsevier Ltd. All rights reserved.

1. Introduction

The development of alternative energy storage and conversion devices with high power and energy densities, long lifetime as well as large cycle number for solving critical energy and environmental issues has motivated intensive research by the global scientific community to address the failing environmental issues and the reduction of fossil fuels [1]. Supercapacitors (SCs) also known as electrochemical capacitors or ultracapacitors have been extensively researched in the field of energy storage due to their higher power density than batteries and higher energy density compared to conventional capacitors [2,3]. Beside these exceptional properties, supercapacitors also show excellent properties such as long cycle life, rapid energy delivery and long stability as compared to rechargeable batteries. SCs are currently being applied for use in electric vehicles, portable electronics, medical devices, industrial lasers, military systems and wireless communication systems for uninterrupted service [4].

The storage capability and performance of supercapacitors to a great extent depends on the nature of the electrode material [5]. They can be distinguished into three types according to their charge storage mechanism. These include; (i) the electric double

layer capacitors (EDLCs) which are characterized with non-faradaic process and are mainly composed of carbon material electrodes and their derivative as materials of choice, (ii) pseudocapacitors (or faradaic capacitors) which store charge due to faradaic-type reactions and (iii) the hybrid capacitors which combine the properties of electrodes with different charge storage behavior i.e. an EDLC and faradaic type material. The resulting hybrid device has properties of both a supercapacitor and a battery [6].

Some of the carbon materials reported in the literature include activated carbon (AC), carbon nanotubes (CNTs), graphene [7] and carbon nano onions (CNOs) [8]. Pseudocapacitive materials such as transition metal oxides (i.e., RuO_2, MnO_2, Co_3O_4 NiO,) [9–12], conducting polymers like polypyrrole (PPY), polyaniline (PANI) [13] have proven to exhibit excellent specific capacitance as compared to the EDLCs carbon-based materials. Among the transition metal oxides, hydrous ruthenium dioxide (RuO_2) has been considered to be the most promising electrode material due to its multiple redox states and good electrical conductivity [14,15]. Unfortunately, the high cost and toxic nature of this noble metal is a big hurdle for practical applications [16]. Therefore, much effort has been devoted to alternative cheap and environmentally friendly electrode materials. Other nanoscale materials, such as nanotubes, nanorods, and nanosheets have attracted a great deal due to their unique physical properties and potential applications as important components for devices such as supercapacitors at the nanoscale.

Among transition metal oxides, cobalt oxide-based nano materials such as cobalt hydroxide carbonate have attracted major research interests as electrode material for energy storage in electrochemical capacitors due to the fact that its morphology may be effectively controlled by adjusting the interaction between the positively charged layers and anions [17]. The cobalt hydroxide carbonates ($Co_2(OH)_2CO_3$) have been successfully synthesized by different methods. Zhao et al. [17] obtained 3D nanorods-based urchin-like and nanosheets-based flower-like cobalt basic salt nanostructures.Different morphologies of cobalt hydroxide nanostructures intercalated with carbonate anions such as nanorods and nanowires, and sisal-like, dandelion-like, pinecone-like, urchin-like and flower-like-structures [17–22] have been synthesized using block copolymers or surfactants. However, these hydroxides carbonates materials have not been tested as electrode materials for supercapacitor application. Only recently, Lu et al. synthesized cobalt hydroxide carbonate derived from CoAl layered double hydroxides. The electrochemical testing of this material as supercapacitor revealed a high specific capacitance value owing to the mesoporous nature of nanosheet structure [23].

In our previous work we looked into the influence of the activated carbon on electrochemical properties of cobalt hydroxide carbonate [24]. In this study cobalt hydroxide carbonate nanorods were successfully synthesized using a hydrothermal method at a temperature of 120 °C with different synthesis times of 3, 6, 9 and 12 h respectively. It is found that the cobalt hydroxide carbonates with the morphology of nanorods exhibited the crystal structure consisting of the mixture of both monoclinic and orthorhombic phases. The results show that the variation of growth time plays a crucial role in the transformation of phases and morphologies and also a systematic increase of specific capacitance occurs with increasing growth time. It is worth noting that further increase in growth time changes the phase to cobalt oxide and the variation of specific capacitance for electrodes based on cobalt oxide is totally different and is not in the scope of this study.

2. Experimental section

2.1. Materials

Cobalt chloride hexahydrate ($CoCl_2 \cdot 6H_2O$, purity $> 99.99\%$) was purchased from Sigma-Aldrich. Nickel Foam was purchased from (Alantum, Munich, Germany). Potassium hydroxide (KOH, min 85%) and urea (purity $\geq 98\%$) were purchased from Merck (South Africa).

2.2. Synthesis technique

The growth procedure for the cobalt hydroxide carbonate was similar to that reported in our previous work [24] which is modified from that of reference [25]. Briefly, $CoCl_2.6H_2O$ (1.0 mmol) and urea (1.0 mmol) were added to 20 mL of water and stirred for 10 min. The mixture was then transferred to a Teflon-lined stainless steel autoclave and kept at 120 °C for 3, 6, 9 and 12 h growth times, respectively. After cooling to room temperature, the light-pink product was washed several times with deionized water and dried overnight in normal air at a temperature of 60 °C. The formation of cobalt hydroxide carbonate involved a hydrolysis-precipitation process in which urea slowly provides both carbonate and hydroxyl anions to form cobalt hydroxide carbonate [22]. The main reactions in the system can be expressed as follows

$$H_2NCONH_2 + H_2O \rightarrow 2\,NH_3 + CO_2 \tag{1}$$

$$CO_2 + H_2O \rightarrow CO_3^{2-} + 2\,H^+ \tag{2}$$

$$NH_3 + H_2O \rightarrow NH_4^+ + OH^- \tag{3}$$

The formation of monoclinic cobalt hydroxide carbonate can be formulated as:

$$2\,Co^{2+} + 2\,OH^- + CO_3^{2-} \leftrightarrow Co_2(OH)_2CO_3 \tag{4}$$

The formation of orthorhombic cobalt hydroxide carbonate can be formulated as:

$$Co^{2+} + 0.35\,CO_3^{2-} + 1.1\,OH^- + 0.2\,Cl^- + 1.74\,H_2O$$
$$\rightarrow Co\,(CO_3)_{0.35}Cl_{0.2}\,(OH)_{1.1} \cdot 1.74\,H_2O \tag{5}$$

2.3. Characterization techniques

The morphology of the prepared cobalt hydroxide carbonate was investigated using the high-resolution Zeiss Ultra plus 55 field emission scanning electron microscope (FESEM) operated at 2.0 kV and transmission electron microscopy (TEM) carried out with a JEOL JEM-2100F microscope operated at 200 kV (Akishima-shi, Japan). X-ray diffraction (XRD) patterns of the samples were collected using an XPERT-PRO diffractometer (PANalytical BV, Netherlands) with theta/theta geometry, operating with a cobalt tube at 35 kV and 50 mA. The surface area of the synthesized materials was studied using the Barrett-Joyner-Halenda (BJH) method from the desorption branch of the isotherm. Fourier transform infrared (FT-IR) spectra of the cobalt hydroxide carbonate were recorded using a Bruker Vertex 77 v FT-IR spectrometer.

2.4. Electrode preparation and electrochemical characterization

The electrochemical properties were investigated using a Bio-Logic SP300 potentiostat (Knoxville TN 37,930, USA) in a three-electrode configuration controlled by the EC-Lab® V10.37 software. The cobalt hydroxide carbonate material served as the working electrode in a 6 M potassium hydroxide (KOH) electrolyte; glassy carbon plate was used as the counter electrode and Ag/AgCl (3 M KCl) served as the reference electrode. The cobalt hydroxide carbonate electrode was prepared according to the following steps: 85 wt% of cobalt hydroxide carbonate was mixed with 10 wt.% carbon black and 5 wt.% polyvinylidene difluoride (PVdF) binder in an agate mortar. The mixture was then dissolved with 1-methyl-2-pyrrolidinone (NMP) to form a paste. The homogenous paste was coated onto a Ni foam current collector and dried at 60 °C in an electrical oven for 8 h to ensure complete evaporation of the NMP. The cyclic voltammetry tests were carried out in the potential range of 0 to 0.45 V (vs. Ag/AgCl) at different scan rates ranging from 5 to 100 mV s^{-1}. The galvanostatic charge–discharge measurements were also carried out at different current densities from 1.0 to 15 A g^{-1} and the electrochemical impedance spectroscopy (EIS) measurements were done in the frequency range of 100 kHz–10 mHz in open circuit voltage.

3. Results and discussion

XRD was used to analyse the crystal structure and phase composition of the products obtained. Fig. 1(a) shows the XRD patterns of the samples grown at 120 °C with growth time of 3, 6, 9 and 12 h, respectively. Typical diffraction peaks observed are indexed to cobalt hydroxide carbonate phase using JCPDS card number 29-1416 (Sys.: Monoclinic, S.G.: P2$_1$/a, a: 9.368, b: 12.070 and c: 3.389) and JCPDS card number 48-0083, (Sys.: Orthorhombic, S.G.: not available, a: 8.792, b: 10.150 and c: 4.433) which

131

Fig. 1. (a) XRD patterns of samples grown for 3, 6, 9 and 12 h with the bottom panel showing standards for monoclinic and orthorhombic structures of cobalt hydroxide carbonate, (b) XRD pattern of the cobalt oxide for sample obtained at 16 h reaction time with standard show at the bottom of data and (c) FTIR spectra of the samples obtained after 3, 6, 9 and 12 h synthesis time for cobalt hydroxide carbonate.

are plotted at the bottom of the data, respectively. The XRD data suggest that cobalt hydroxide carbonate preferentially grows in the (110) and (001) low-index crystallographic direction hence would lead to nanorods formation. The data further suggest that the synthesized hydroxide carbonate nanorods are highly crystalline and have both monoclinic and orthorhombic crystal structure. The diffraction peaks are sharp, confirming that the sample is well crystallized. Fig. 1(b) shows the XRD pattern of the cobalt oxide phase as the growth time is increased to 16 h. All the diffraction peaks observed are indexed to Co_3O_4 using JCPDS card number 42-1567 which is plotted at the bottom of the data.

FTIR spectra (Fig. 1(c)) of as synthesized cobalt hydroxides carbonate samples were also recorded to ensure the chemical composition of the sample. The peaks at 3793, 3744 and 3513 cm^{-1} are due to the stretching vibrations of the O–H group of molecular water and hydrogen-bond O–H groups which indicates

the presence of hydroxyl ions due to the metal-OH layer and/or water in the crystal [20]. A shoulder at around 2367 cm^{-1} is from hydrogen bonding in the interlayer indicating the presence of interlayer water molecules in cobalt hydroxide carbonate [17]. The peak at 1620 cm^{-1} is due to the bending mode of water molecules [17]. The peak at 1527 and 1503 cm^{-1} are attributed to CO_3^{2-} ions, while the peak at 543 and 692 cm^{-1} corresponds to the Co-O vibrational modes, respectively [12,19,21].

The Morphology of the material significantly influences the suitability of the material for supercapacitor application. Fig. 2 shows the FESEM microstructures of the as-prepared samples. The morphology of the cobalt hydroxide carbonate obtained for 3 and 6 h (Fig. 2(a) and (b)) indicates that the product is mainly composed of nanorods. However, these nanorods are loosely arranged. This primary morphology evolves to chrysanthemum-like structure (see Fig. 2(c) and (d)) with increase in growth time. This new

132

Fig. 2. Low and high magnification SEM images of the cobalt hydroxide carbonate nanorods obtained at 120 °C with different synthesis times: of (a) 3 h, (b), 6 h, (c) 9 h and (d) 12 h respectively.

structure is compacted in a flower-like structure with low density of loose nanorods compared to sample grown for shorter time. This compact structure could improve the overall conductivity of the material and positively impacts on its electrochemical performance.

The morphology of the obtained cobalt hydroxide carbonates nanorods obtained at 120 °C for 3, 6, 9 and 12 h was also examined by TEM, as shown in Fig. 3. The images obtained confirmed the interpretation of the SEM results. In other words, the synthesized cobalt hydroxide carbonate shows nanorods-like structures that are well defined when the growth time is increased.

The Brunauer-Emmett-Teller (BET) method was used to determine the surface area of the samples and its pore size distribution. Fig. 4(a) and (b) show the N_2 gas isotherms and Pore size distribution obtained using Barrett-Joyner-Halenda (BJH) method respectively for the samples with synthesis time indicated in the figures. The nitrogen adsorption-desorption isotherm of the cobalt

hydroxide carbonate show a type III adsorption–desorption with H3 hysteresis isotherm behavior (Fig. 4(a)), indicating a weak interaction between the N_2 adsorbent and the material. The specific surface area (SSA) calculated is in the following order: 16.13, 16.87, 22.95 and 32.69 $m^2 g^{-1}$ for samples grown for 3, 6, 9 and 12 h, respectively. BET results show systematic increase of SSA with increase in the synthesis time with the sample grown for 12 h possessing largest SSA which may favor a higher electrochemical performance. Fig. 4(b) shows a concentration of pore volume around 4 nm (see inset to Fig. 4(b)), suggesting that pores present in this material are predominantly mesopores. The specific surface area is more dependent on the pore structure which is related to the morphology of prepared cobalt hydroxide carbonate. As explained above in the forming mechanism of cobalt hydroxide carbonate, the material obtained after 3 h and 6 h is composed of nanorods, whereas increasing growth time to 9 h and 12 h the structure evolves to chrysanthemum-like structure leading to

Fig. 3. TEM images of the cobalt hydroxide carbonate nanorods obtained at 120 °C with different synthesis times of (a) 3 h, (b) 6 h, (c), 9 h and (d) 12 h respectively.

Fig. 4. (a) N_2 absorption/desorption isotherms; and (b) pore size distribution of cobalt hydroxide carbonate obtained at 120 °C with different synthesis times indicated in the figures (insets show pore size distribution).

higher specific surface area. The high BET specific surface area and porous structure of chrysanthemum-like structure cobalt hydroxide carbonate provide the possibility of efficient transport of electrons and ions, which may result in high electrochemical capacity of these materials.

The sample grown for 12 h also exhibits the highest pore volume as depicted in Fig. 4b. To explore the potential application of the material for energy storage, we fabricated and characterized the electrodes made of the samples grown for different times, by cyclic voltammograms (CVs). Fig. 5(a) illustrates the overlaid cyclic voltammograms (CV) obtained in a three-electrode cell comparing the cobalt hydroxide carbonate nanorods at various growth times at scan rate of 50 mV s^{-1} in a potential window range of 0.0 to 0.45 V. All the electrode materials displayed redox peaks which are derived from the oxidation of Co^{2+} to Co^{3+} and its reverse mechanism, indicating their faradic capacitance contribution. The peaks at 0.33 V and 0.12 V are related to the anodic and cathodic peaks of the cobalt hydroxide carbonate nanorods material at a scan rate of 50 mV s^{-1}. It can also be clearly seen that the integral area of the cyclic voltammogram of the sample for 12 h growth time is the largest implying the highest specific capacitance. Fig. 5

(b) illustrates the overlaid galvanostatic charge discharge (GCD) curves comparing the samples at different synthesis times of 3, 6, 9 and 12 h respectively at current density of 1 A g^{-1}. From these results, the sample grown for 12 h still maintains longer discharge time; suggesting better specific capacitance as compared to the other electrode materials and this is in agreement with the results from the CV. In fact, the specific capacitance of the electrode materials was evaluated from the galvanostatic charge discharge (GCD) curves using Eq. (6):

$$C_{sp} = \frac{I \times t}{m \times \Delta v} \qquad (6)$$

where I is the discharge current (A), t is the discharge time (s), m is the mass of active material (g), ΔV is the potential range of discharge (V), and C_{sp} is the specific capacitance (F g^{-1}).

As shown in Fig. 5(c) the specific capacitances of cobalt hydroxide carbonate nanorods for 3, 6, 9 and 12 h growth times were found to be 208.0, 222.3, 456.0 and 466.0 F g^{-1} respectively, at current density of 1 A g^{-1}. This figure also shows systematic increase of specific capacitance values with increase of the SSA as the growth time is increased before the material is transformed

134

Fig. 5. (a) Cyclic voltammetry (b) galvanostatic charge–discharge and (c) specific capacitance and specific surface are comparison of cobalt hydroxide carbonate obtained for different synthesis times indicated, (d) CV and (e) galvanostatic charge–discharge of cobalt hydroxide carbonate obtained after 12 h synthesis time at different scan rates and current densities, respectively.

into cobalt oxides at higher growth time of 16 h as shown in Fig. 1 (b). However, the highest specific capacitance reported here for 12 h sample is still lower than the value reported for mesoporous cobalt hydroxide carbonate nanosheets that was derived from CoAl layered double hydroxide [23]. As stated 'earlier, there is a strong relation between the morphology and the specific surface area. Hence, the nanosheets structure reported in reference 23 could expose higher surface area than nanorod structure reported here.This also confirms the highest SSA cobalt hydroxide carbonate grown for 12 h as the sample with the highest specific capacitance in agreement with the observed electro analytic results from CV. Because of the superior properties of the sample

synthesized at 12 h the detailed CV and charge-discharge curves of this sample at a scan rates ranging from 5 to 100 mV s^{-1} and current densities ranging from 1 to 15 A g^{-1} was carried out and the results are shown in Fig. 5(d) and (e) respectively. The shapes of the CV curves shown in Fig. 5(d) demonstrate the faradic characteristics. Globally, two pairs of broad and poorly defined redox peaks are observed in the CV plots, which originate from the faradaic redox reactions. The current is enhanced with the increasing scan rate, while the shape of the CV curves remains mainly unchanged, except for the small shift of the peak position, thus revealing the prominent electrochemical reversibility and relative high-rate performance. Fig. 5(e) shows the rate capability

135

Fig. 6. (a) EIS overlays, and (b) specific capacitance vs. current density overlays of cobalt hydroxide carbonate nanorods obtained at 120 °C with different synthesis times indicated in the figures respectively. The inset to (a) is the magnified plot showing the R_s values for different electrodes.

Fig. 7. (a) Capacitance retention as a function of cycle number at a current density of 10 A g^{-1}. (b) Nyquist plot before and after cycling of cobalt hydroxide carbonates nanorods obtained at 120 °C for with 12 h synthesis time.

studies at current densities ranging from 1 to 15 A g^{-1}. Each discharge curve includes two clear voltage steps: a fast potential drop from 0.45 V to 0.25 V and a voltage plateau from 0.25 V to 0.16 V. The voltage plateau at around 0.2 V suggests the typical faradic characteristic which is in good agreement with the CV curves in Fig. 5(d)

To further evaluate the electrochemical behavior of the cobalt hydroxide carbonate nanorods electrochemical impedance spectroscopy (EIS) measurement was carried out at the potential of 0 V and the frequency between 10 mHz and 100 kHz as shown in Fig. 6 (a). From these data, several observations can be inferred from the high to the low frequency regions which correspond to different resistance phenomena during the electrochemical process. The cobalt hydroxide carbonate grown for 12 h displayed a small solution resistance R_s value (intercept to x-axis) of 0.69 Ω (see inset to the figure) as compared to the other samples. This small

Table 1
The SSA, C_{SP} and R_s of cobalt hydroxide carbonate obtained at 120 °C with (3, 6, 9 and 12 h) growth time.

Growth time	SSA (m^2 g^{-1})	C_{SP} (F g^{-1}) at 1 A g^{-1}	R_s (Ω)
3 h	16.13	208	0.76
6 h	16.87	222	0.72
9 h	22.95	456	0.71
12 h	32.69	466	0.69

resistance value combined with the short diffusion length displayed by this electrode material indicates the easiness of the movement of ions and the charge transfer towards the electrode/electrolyte interface. At the low frequency region, it is also observed that the vertical line is inclined to the real axis suggesting a deviation from the ideal [27] The R_s values extracted for the different electrodes clearly indicated by the inset to Fig. 6(a) are tabulated in Table 1 together with other parameters with show systematic behavior with the growth time. The pattern shown in the table is that the 12 h sample shows smallest solution resistance R_s which is the indication of good conductivity of this sample as compared to others. C_{sp} vs. the current density graph displaying the performance of all the prepared electrode materials is shown in Fig. 6(b). The 12 h sample still shows superior performance in all current densities with 52% of capacitance retention compared to only 44% for 9 h sample for instance.The sustainability of the electrochemical performance of the cobalt hydroxide carbonate electrodes at a high current density places these materials as good candidates for high power energy devices.

The stability of the electrode material is also a very important characteristic for their application as energy storage devices. In order to understand the stability of cobalt hydroxide carbonate electrodes, the samples were subjected to 2000 cycles at the high current density of 10 A g^{-1} and the result of the sample grown at 12 h is shown in Fig. 7(a) as an example. No capacitance loss was observed after 2000 cycles for the electrode, suggesting excellent

136

stability for this material as faradaic material for energy storage. The EIS measurements before and after cycling were compared in Fig. 7(b) for sample grown at 12 h. From this intercept an R_s value of 0.74 Ω after cycling was obtained, representing barely 7% increase from the initial R_s value before cycling. This shows that the material did not deteriorate significantly during cycling. Furthermore, no significant increase in the diffusion length after 2000 cycles was observed.

4. Conclusion

In summary, the cobalt hydroxide nanorods have been synthesized for different times; from 3 to 12 h. Different measurements that have been done on these samples show systematic improvements of the results as function of increasing reaction time. These range from surface morphology features to electrochemical properties where the sample grown for the longest time of 12 h had shown the well-defined compact nanorods, the highest specific surface area and the best electrochemical performance. Some of these parameters that clearly show superiority of 12 h sample over other samples, which represent the highest growth time to preserve cobalt hydroxide carbonate phase before the sample transforms to cobalt oxide, are summarized in Table 1 It is clear that 12 h growth time mark the best synthesis time for the cobalt hydroxide carbonate materials for their applications in energy storage with superior specific capacitance of 466 F g^{-1} at current density of 1 A g^{-1} and a capacity retention of 99% after 2000 cycles at a current density of 10 A g^{-1} before it transforms into cobalt oxide at higher synthesis time The excellent electrochemical performance coupled with the low cost and simple preparation process renders this material very promising for practical application as supercapacitor device.

Acknowledgments

References

[1] J. Yang, T. Lan, J. Liu, Y. Song, M. Wei, Supercapacitor electrode of hollow spherical V$_2$O$_5$ with a high pseudocapacitance in aqueous solution, Electrochim. Acta 105 (2013) 489–495.
[2] A. Yu, V. Chabot, J. Zhang, Electrochemical Supercapacitors for Energy Storage and Delivery: Fundamentals and Applications, CRC Press, New York, 2013.
[3] G. Yu, X. Xie, L. Pan, Z. Bao, Y. Cui, Hybrid nanostructured materials for high-performance electrochemical capacitors, Nano Energy 2 (2013) 213–234.
[4] C.-H. Lai, C.-K. Lin, S.-W. Lee, H.-Y. Li, J.-K. Chang, M.-J. Deng, Nanostructured Na-doped vanadium oxide synthesized using an anodic deposition technique for supercapacitor applications, J. Alloy. Compd. 536 (2012) S428–S431.
[5] L.L. Zhang, X.S. Zhao, Carbon-based materials as supercapacitor electrodes, Chem. Soc. Rev. 38 (2009) 2520–2531, http://dx.doi.org/10.1039/b813846j.
[6] T. Brousse, D. Belanger, J.W. Long, To be or not to be pseudocapacitive? J. Electrochem. Soc. 162 (2015) A5185–A5189, http://dx.doi.org/10.1149/2.0201505jes.
[7] L.L. Zhang, R Zhou, X.S. Zhao, Graphene-based materials as supercapacitor electrodes, J. Mater. Chem. 20 (2010) 5983–5992.
[8] M.E. Plonska-Brzezinska, L Echegoyen, Carbon nano-onions for supercapacitor electrodes: recent developments and applications, J. Mater. Chem. A 1 (2013) 13703–13714.
[9] H. Wang, H.S. Casalongue, Y. Liang, H. Dai, Ni (OH)$_2$ nanoplates grown on graphene as advanced electrochemical pseudocapacitor materials, J. Am. Chem. Soc. 132 (2010) 7472–7477.
[10] I.-H. Kim, J.-H. Kim, K.-B. Kim, Electrochemical characterization of electrochemically prepared ruthenium oxide/carbon nanotube electrode for supercapacitor application, Electrochem. Solid-State Lett. 8 (2005) A369–A372.
[11] Y. Shan, L. Gao, Formation and characterization of multi-walled carbon nanotubes/Co$_3$O$_4$ nanocomposites for supercapacitors, Mater. Chem. Phys. 103 (2007) 206–210.
[12] L. Yuan, X.-H. Lu, X. Xiao, T. Zhai, J. Dai, F. Zhang, et al., Flexible solid-state supercapacitors based on carbon nanoparticles/MnO2 nanorods hybrid structure, ACS Nano 6 (2012) 656–661, http://dx.doi.org/10.1021/nn2041279.
[13] X. Zang, X. Li, M. Zhu, X. Li, Z. Zhen, Y. He, et al., Graphene/polyaniline woven fabric composite films as flexible supercapacitor electrodes, Nanoscale 7 (2015) 7318–7322.
[14] W. Deng, X. Ji, Q. Chen, C.E. Banks, Electrochemical capacitors utilising transition metal oxides: an update of recent developments, RSC Adv. 1 (2011) 1171–1178.
[15] T.-F. Hsieh, C.-C. Chuang, W.-J. Chen, J.-H. Huang, W.-T. Chen, C.-M. Shu, Hydrous ruthenium dioxide/multi-walled carbon-nanotube/titanium electrodes for supercapacitors, Carbon 50 (2012) 1740–1747.
[16] P. Simon, Y. Gogotsi, Materials for electrochemical capacitors, Nat. Mater. 7 (2008) 845–854.
[17] Z. Zhao, F. Geng, J. Bai, H.-M. Cheng, Facile and controlled synthesis of 3D nanorods-based urchinlike and nanosheets-based flowerlike cobalt basic salt nanostructures, J. Phys. Chem. C 111 (2007) 3848–3852.
[18] W. Xing, S. Zhuo, H. Cui, H. Zhou, W. Si, X. Yuan, et al., Morphological control in synthesis of cobalt basic carbonate nanorods assembly, Mater. Lett. 62 (2008) 1396–1399.
[19] B. Li, Y. Xie, C. Wu, Z. Li, J. Zhang, Selective synthesis of cobalt hydroxide carbonate 3D architectures and their thermal conversion to cobalt spinel 3D superstructures, Mater. Chem. Phys. 99 (2006) 479–486.
[20] R. Xu, H.C. Zeng, Dimensional control of cobalt-hydroxide-carbonate nanorods and their thermal conversion to one-dimensional arrays of Co$_3$O$_4$ nanoparticles, J. Phys. Chem. B. 107 (2003) 12643–12649, http://dx.doi.org/10.1021/jp035751c.
[21] H. Zhang, J. Wu, C. Zhai, X. Ma, N. Du, J. Tu, et al., From cobalt nitrate carbonate hydroxide hydrate nanowires to porous Co(3)O(4) nanorods for high performance lithium-ion battery electrodes, Nanotechnology 19 (2008) 035711, http://dx.doi.org/10.1088/0957-4484/19/03/035711.
[22] S.L. Wang, LQ. Qian, H. Xu, G.L. Lü, W.J. Dong, W.H. Tang, Synthesis and structural characterization of cobalt hydroxide carbonate nanorods and nanosheets, J. Alloy. Compd. 476 (2009) 739–743.
[23] Z. Lu, W. Zhu, X. Lei, G.R. Williams, D. O'Hare, Z. Chang, et al., High pseudocapacitive cobalt carbonate hydroxide films derived from CoAl layered double hydroxides, Nanoscale 4 (2012) 3640–3643.
[24] T.M. Masikhwa, J.K. Dangbegnon, A. Bello, M.J. Madito, D. Momodu, N. Manyala, Preparation and electrochemical investigation of the cobalt hydroxide carbonate/activated carbon nanocomposite for supercapacitor applications, J. Phys. Chem. Solids 88 (2016) 60–67.
[25] X.-C. Dong, H. Xu, X.-W. Wang, Y.-X. Huang, M.B. Chan-Park, H. Zhang, et al., 3D graphene–cobalt oxide electrode for high-performance supercapacitor and enzymeless glucose detection, ACS Nano 6 (2012) 3206–3213.
[27] X. Yu, J. Lu, C. Zhan, R. Lv, Q. Liang, Z.-H. Huang, et al., Synthesis of activated carbon nanospheres with hierarchical porous structure for high volumetric performance supercapacitors, Electrochim. Acta (2015).

4.1.3   Conclude Remarks

Cobalt hydroxide carbonate nanorods were successfully synthesized using a hydrothermal method at a temperature of 120 °C with different synthesis times from 3 to12 h to adjust their morphological properties. The morphologies of cobalt hydroxide carbonate showed systematic improvements as function of reaction time. Cobalt hydroxide carbonate nanorods

synthesized with 12 h reaction time exhibited the highest specific capacitance of 466 F g^{-1} at current density of 1 A g^{-1} and capacity retention of 99 % after 2000 cycles at a current density of 10 A g^{-1} before the material transformed into cobalt oxide at high reaction time. These results suggest that cobalt hydroxide carbonate nanorods with the low cost and simple preparation process can be the promising electrode materials for supercapacitor application.

4.2 Preparation and Electrochemical Investigation of the Cobalt Hydroxide Carbonate/Activated Carbon Nanocomposite for Supercapacitor Applications.

4.2.1 Introduction

In section 4.1.1., cobalt hydroxide carbonate nanorods were successfully synthesized using a hydrothermal method at a temperature of 120 °C with different synthesis times from 3 to12 h to adjust their morphological properties. These section present results obtained when activated carbon (AC) was incorporated to cobalt hydroxide carbonate using a hydrothermal method at a temperature of 120 °C for 6 h to produce cobalt hydroxide carbonate/AC composites.

The reason for adding activated carbon is due to the fact that hydroxides normally suffer from poor electrical conductivity and low electrochemical stability, while carbon materials are known to have good electrical conductivity and electrochemical stability, so the synergy between the two materials should improve the electrochemical properties of the composite material. Therefore, the electrochemical performance of cobalt hydroxide carbonate can be improved by combining with three dimensional porous carbon materials to form a composite to increase the conductivity as well as the electrochemical properties of cobalt hydroxide carbonate. Porous carbon materials such as activated carbon (AC) have been used as electrode materials in the production of EDLCs due to their good electrical conductivities,

138

long cycle-life and large surface area. Based on this suggested concepts, hydrothermal method was used to synthesize cobalt hydroxide carbonate nanorods in the presence of activated carbon (AC) (from Polyvinyl alcohol PVA and graphene foam) denoted as AGF to obtained cobalt hydroxide carbonate/AC composites. This method showed that the synthesized cobalt hydroxide carbonates confirmations nanorods shape-like structure and that there is constant coverage of the AC by such nanorods. The morphological, structural and electrochemical properties of the synthesized cobalt hydroxide carbonate/AC composites were studied.

4.2.2   Results and Discussions

Detailed information on results obtained from this work is presented in the paper below.

Preparation and electrochemical investigation of the cobalt hydroxide carbonate/activated carbon nanocomposite for supercapacitor applications

CrossMark

Tshifhiwa M. Masikhwa, Julien K. Dangbegnon, Abdulhakeem Bello, Moshawe J. Madito, Damilola Momodu, Ncholu Manyala *

Department of Physics, Institute of Applied Materials, SARCHI Chair in Carbon Technology and Materials, University of Pretoria, Pretoria 0028, South Africa

ABSTRACT

Cobalt hydroxide carbonate/activated carbon (AC) composite was successfully synthesized by hydrothermal method. Morphological characterizations of cobalt hydroxide carbonate/AC composite were carried out by scanning electron microscopy (SEM) and transmission electron microscopy (TEM), and the results show that the cobalt hydroxide carbonate nanorods are well dispersed on the AC. Due to the synergistic effects arising from cobalt hydroxide carbonate nanorods and AC, the electrochemical performances of pure cobalt hydroxide carbonate material is significantly improved by the addition of AC. The composite shows a specific capacitance of 301.44 F g^{-1} at a current density of 1 A g^{-1} in 6 M KOH electrolyte and exhibits good cycling stability. Based on the above results, the cobalt hydroxide carbonate/AC composite shows a considerable promise as electrode for electrochemical applications.

Crown Copyright © 2015 Published by Elsevier Ltd. All rights reserved.

1. Introduction

In recent years, electrochemical capacitors (ECs) have attracted much more interests due to their distinctive properties like high power density, good reversibility, and wide energy storage applications [1–4]. ECs are novel power devices, which lie between batteries and conventional dielectric capacitors in terms of energy and power densities with applications in computer power backup, electric vehicles and power electronics. The major aim of developing ECs materials is to improve on the energy density of the device without sacrificing the high power density and long cycle life. Electrical double layer capacitor (EDLC) is a very attractive energy storage device because, besides its high power density, it is maintenance-free, has long-life operation, quick charge–discharge rate, and is environmentally friendly energy technology. In general, the performance of ECs strongly depends on the electrode materials used in its fabrication [5]. Carbon-based materials are ideal electrode materials for ECs owing to their low price, high charge/discharge rate, and quite stable physicochemical

properties. Typical electrode materials for EDLCs are activated carbon, graphene, carbon nanotubes, etc. [6]. In particular, carbon nanotubes have high electrical conductivity but a relatively low surface area, which causes a drastic drop in EDLC performance [7]. Graphene known for its high surface area and good surface exposure to electrolytes, has been recognized as an excellent component for supercapacitors. Nevertheless, other materials such as conductive polymers [8,9] and metal oxides [10,11] have been widely studied for ECs applications due to their unique properties such as high inherent capacitance [8,12].

Recently, three dimensional porous carbon materials have become attractive and are frequently used as electrode materials in the fabrication of EDLCs due to their good electrical conductivities and large surface area [13–17]. For examples Zhu et al. have produced carbon materials by microwave-assisted expansion of graphene oxide (a-MEGO) with exceptional properties. This material demonstrated excellent electrochemical properties in ionic electrolytes [2,18]. On the other hand faradaic materials utilize redox reaction to store charges at the surface or near surface region of the electrode materials [19]. Commonly used faradaic materials are transition metal oxides (TMOs) and conducting polymers (CPs) [20–25].

Cobalt hydroxide carbonate is considered as faradaic material and has attracted particular attention among researchers in recent years because of its unique properties such as easy synthesis route

* Corresponding author. Fax: +27 12 420 2516.
E-mail addresses: moureenmasikhwa@gmail.com (T.M. Masikhwa),
dangbegnon01@googlemail.com (J.K. Dangbegnon),
bellohakeem@gmail.com (A. Bello), jack.madito@gmail.com (M.J. Madito),
dymomodu@yahoo.com (D. Momodu), ncholu.manyala@up.ac.za (N. Manyala).

140

and various morphologies [26–28]. Recently, different morphologies of cobalt hydroxide nanostructures intercalated with carbonate anions have been synthesized using block copolymers or surfactants. Such structures include: nanorods and nanowires, sisal-like, dandelion-like, pinecone-like, urchin-like and flower-like nanostructures [26–31]. Cobalt hydroxide carbonate is considered to be a suitable candidate for ECs applications due to its good electrochemical activity, low cost raw material and environmental friendly amongst other faradaic materials [32]. However, the specific capacitance of pure cobalt hydroxide carbonate is still low compared with other TMOs [33–36].

In this work, pure cobalt hydroxide carbonate and cobalt hydroxide carbonate/AC composite are synthesized by hydrothermal method. The AC material was added to improve on the electrochemical performance of the pure cobalt hydroxide carbonate. The composite exhibited a specific capacitance of 301.44 $F\,g^{-1}$ at a current density of 1 $A\,g^{-1}$ in 6 M KOH electrolyte and showed excellent long cycle life of ~95.6% capacitance retention after 1000 cycles.

2. Experimental

2.1. Materials

Cobalt chloride hexahydrate ($CoCl_2.6H_2O$, purity > 99.99%), Hydrochloric acid (HCl, ≥ 32%) and Polyvinyl alcohol (PVA, 99+% hydrolyzed) were purchased from Sigma-Aldrich. Nickel Foam was purchased from (Alantum, Munich, Germany). Potassium hydroxide (KOH, min 85%) and urea (purity ≥ 98%) were purchased from Merck (South Africa).

2.2. Synthesis of cobalt hydroxide carbonate

$CoCl_2 \cdot 6H_2O$ (1.0 mmol) and urea (1.0 mmol) were added to 20 mL of water and stirred for 10 min. The homogeneous mixture was then transferred to a Teflon-lined stainless steel autoclave and kept at 120 °C for 6 h. After cooling to room temperature the light-pink powder was washed with deionized water and dried at 60 °C. The growth mechanism of this material involves a hydrolysis-precipitation process in which urea can slowly provide both carbonate and hydroxyl anions to form cobalt hydroxide carbonate [28]. The main reactions in the system can be expressed as follows:

$$H_2NCONH_2 + H_2O \rightarrow 2\ NH_3 + CO_2 \tag{1}$$

$$CO_2 + H_2O \rightarrow CO_3^{2-} + 2\ H^+ \tag{2}$$

$$NH_3 + H_2O \rightarrow NH_4^+ + OH^- \tag{3}$$

The formation of cobalt hydroxide carbonate can be formulated as:

$$2Co^{2+} + 2OH^- + CO_3^{2-} \leftrightarrow Co_2(OH)_2CO_3 \tag{4}$$

2.3. Synthesis of cobalt hydroxide carbonate/activated carbon

Activated carbon used for the production of the composite material was prepared as follows [37,38]: graphene foam (GF) and polyvinyl alcohol (PVA) were used as starting materials for the production of the hydrogel, which was subsequently used to produce porous carbon material after the activation process. GF was prepared by chemical vapor deposition (CVD) onto a catalytic nickel foam as reported in our previous work [39]. The three dimensional hydrogel was synthesized via a hydrothermal process.

Briefly, 100 mg of the GF was dispersed in 10 ml of polyvinyl alcohol (PVA) in a vial glass by ultrasonication followed by the addition of 1.5 ml of hydrochloric acid (HCl) as cross linker. The resultant mixture was transferred into a 150 ml Teflon-lined autoclave vessel and kept at 190 °C for 12 h [40]. After cooling to room temperature the hydrogel was washed several times with deionized water and dried for 6 h. The as-prepared hydrogel was then soaked in an aqueous KOH solution for 24 h. The KOH/hydrogel mass ratio was 7. The hydrogel was then placed in a horizontal tube furnace which was heated ramped from room temperature to 800 °C at a ramping rate of 10 °C/min under argon gas flow. The hydrogel was kept at this temperature for 1 h to complete simultaneously activation and carbonization processes. This procedure transforms the hydrogel into carbon material consisting of a continuous pore network distribution. The activated material was neutralized with 0.1 M HCl, washed with deionised water and dried at 120 °C for 12 h.

The cobalt hydroxide carbonate/activated carbon composites were prepared using a hydrothermal reduction technique. Typically, 15 mg of prepared AC was dispersed in 20 ml of water by ultrasonication for 12 h at room temperature. Then $CoCl_2 \cdot 6H_2O$ (1 mmol) and urea (1.0 mmol) was added to the AC dispersion and the mixture was stirred for 10 min. The obtained solution was then transferred to a Teflon-lined stainless steel autoclave and kept at 120 °C for 6 h. After naturally cooling to room temperature, the product was washed with deionized water and dried at 60 °C for 6 h.

2.4. Structure and morphology characterization

The morphology of the prepared cobalt hydroxide carbonate and cobalt hydroxide carbonate/AC was investigated using the high-resolution Zeiss Ultra plus 55 field emission scanning electron microscope (FESEM) operated at 2.0 kV. Transmission electron microscopy (TEM) was carried out with a JEOL JEM-2100F microscope operated at 200 kV (Akishima-shi, Japan). X-ray diffraction (XRD) patterns of prepared materials were collected using an XPERT-PRO diffractometer (PANalytical BV, Netherlands) with reflection geometry at 2θ values ranging from 30° to 90° with a step size of 0.01°. Co $K1\alpha$ radiation with a wavelength of 1.7890 Å was used as X-ray source and the X-ray tube was operated at 50 kV and 30 mA. The surface area of the synthesized materials was studied using Barrett–Joyner–Halenda (BJH) method from the desorption branch of the isotherm. Fourier transform infrared (FTIR) spectra of the cobalt hydroxide carbonate and cobalt hydroxide carbonate/AC were recorded using a Bruker Vertex 77v FTIR spectrometer.

2.5. Electrode preparation and electrochemical characterization

The electrochemical properties were investigated in a three-electrode configuration using a Bio-Logic VMP300 potentiostat (Knoxville TN 37930, USA) controlled by the EC-Lab® V10.37 software. The cobalt hydroxide carbonate and cobalt hydroxide carbonate/AC materials served as working electrodes in a 6 M KOH aqueous electrolyte, while glassy carbon plate was used as the counter electrode and Ag/AgCl (3 M KCl) as the reference electrode, respectively. The electrode materials were prepared according to the following steps: 85 wt% of the material was mixed with 10 wt% of carbon black and 5 wt% of polyvinylidene difluoride (PVdF) binder in an agate mortar. The mixture was then dissolved with 1-methyl-2-pyrrolidinone (NMP) to form a paste. The homogenous paste was coated onto a Ni foam current collector and dried at 60 °C in an electrical oven for 8 h to ensure complete evaporation of the NMP. The cyclic voltammetry tests were carried out in the potential range of 0 to 0.45 V (vs. Ag/AgCl)

141

at different scan rates ranging from 5 to 100 mV s^{-1}. The galvanostatic charge–discharge measurements were performed at various current densities from 1 to 15 A g^{-1} and the electrochemical impedance spectroscopy (EIS) measurements were performed in open circuit within the frequency range of 100 kHz to 10 mHz.

3. Results and discussion

XRD was used to analyze the crystal structure and phase composition of the products obtained. Fig. 1(a) shows the XRD patterns of the cobalt hydroxide carbonate and the composite material. Typical diffraction peaks observed are indexed to cobalt hydroxide carbonate phase using JCPDS card number 29-1416 (Sys.: Monoclinic, S.G.: P2$_1$/a, a: 9.368, b: 12.070 and c: 3.389) and JCPDS card number 48-0083 (Sys.: Orthorhombic, S.G.:, a: 8.792, b: 10.150 and c: 4.433). Both patterns are exactly the same which suggest that addition of AC does not alter the crystal structure of the cobalt hydroxide carbonate material composite. The XRD data suggest that cobalt hydroxide carbonate preferentially grows in the (110) and (001) low-index crystallographic direction. The data further suggests that the synthesized cobalt hydroxide carbonates are highly crystalline and have both monoclinic and orthorhombic crystal structure. Fig. 1(b) shows the FTIR spectra of cobalt hydroxide carbonate with and without activated carbon. The peaks at 3793, 3744 and 3513 cm^{-1} are due to the stretching vibration of the O–H group of molecular water and of hydrogen-bound O–H groups which indicates the presence of hydroxyl ions due to the metal –OH layer and/or water in the crystal [26]. A shoulder peak at around 2367 cm^{-1} is from hydrogen bonding in the interlayer indicating the presence of interlayer water molecules in cobalt hydroxide carbonate, but the cobalt hydroxide carbonate/activated carbon composite does not show this absorption [30]. This suggests that the presence of AC in cobalt hydroxide carbonate breaks the hydrogen bonding that carries the interlayer water molecules. The peak at 1620 cm^{-1} is due to the bending mode of water molecules [41]. The peak at 1527 and 1503 cm^{-1} are attributed to

CO$_3^{2-}$ ions, while the peak at 543 and 692 cm^{-1} corresponds to the Co–O vibrational modes, respectively [26,30]. Fig. 2 shows the morphology of the cobalt hydroxide carbonate with and without activated carbon. Fig. 2(a) and (b) display SEM images of cobalt hydroxide carbonate nanorods synthesized by hydrothermal at 120 °C for 6 h at different magnifications. The morphology of the cobalt hydroxide carbonate nanorods synthesized by the hydrothermal technique indicates that the product is homogenously composed of nanorods. Fig. 2(c) and (d) shows SEM images of cobalt hydroxide carbonate/AC composite at low and high magnifications, respectively. The micrographs show the successful mixture of the cobalt hydroxide carbonate nanorods with activated carbon to form the cobalt hydroxide carbonate/activated carbon composite. It can be seen that the rod-like structure of the cobalt hydroxide carbonate uniformly covers the irregular bulk porous cavities of the activated carbon showing the synergy of growth between both materials.

The morphology of the obtained cobalt hydroxide carbonates with and without activated carbon particles were also examined by TEM, as shown in Fig. 3. The results confirmed the SEM results from Fig. 2 that the synthesized cobalt hydroxide carbonate shows nanorod shape-like structure and that there is uniform coverage of the AC by such nanorods. In general, the surface area of a material is closely related to its morphology and since the capacity of the electrode material is significantly influenced by its surface area, the observed morphology of rods could be a key factor that could influence the electrochemical performance of the composite electrode material. The Brunauer–Emmett–Teller (BET) method was used to determine the surface area of both materials and their pore size distribution. Fig. 4 shows the N$_2$ gas isotherm and pore size distribution of both materials which were obtained using Barrett–Joyner–Halenda (BJH) method. The nitrogen adsorption–desorption isotherm of the cobalt hydroxide carbonate show a type III behavior (Fig. 4(a)), indicating a weak interaction between the N$_2$ adsorbent and the material. Furthermore, Fig. 4(b) shows a concentration of pore volume around 4 nm, suggesting that pores present in this material are predominantly mesopores. On the other hand, the N$_2$ adsorption–desorption isotherm of the cobalt

Fig. 1. (a) XRD patterns with standard JCPDS card numbers 48-0083 and 29-1416 be shown and (b) FTIR spectra of cobalt hydroxide carbonate and cobalt hydroxide carbonate/AC composite.

142

Fig. 2. (a) and (b) SEM images of cobalt hydroxide carbonate at low magnification and high magnification respectively; and (c) and (d) SEM images of cobalt hydroxide carbonate /AC composite at low magnification and high magnification respectively.

hydroxide carbonate/AC presents (Fig. 4(c)) a typical type II adsorption–desorption with H4 hysteresis isotherm that characterize complex materials containing micropores and mesopores. At high pressure, the inflection point occurs near completion of the first monolayer. The presence of micro- and mesopores in the composite material is supported by Fig. 4(d) where a concentration of pore volume is observed around 5 nm. Furthermore, the increased pore volume for diameter ($d < 2$ nm) indicates the presence of micropore in this material. The formation of micropore in the composite can be attributed to the addition of AC to the cobalt hydroxide carbonate material. The specific surface area (SSA) calculated for the cobalt hydroxide carbonate was $16.1 \, m^2 \, g^{-1}$ whereas the composite material exhibits a higher SSA value of $164.3 \, m^2 \, g^{-1}$. This value is one order of magnitude higher than that of cobalt hydroxide carbonate alone. The BET results indicate that cobalt hydroxide carbonate nanorods/AC possesses larger SSA than cobalt hydroxide carbonate nanorods alone and has additional micropores volume, which may favor a higher electrochemical performance.

Cyclic voltammetry (CV) measurements were used to understand the macroscopic electrochemical surface reactions at the electrode material during operation. Fig. 5(a) shows the CV curves

obtained in a three-electrode cell for the cobalt hydroxide carbonate and cobalt hydroxide carbonate/AC composite at scan rate of $50 \, mV \, s^{-1}$ in a potential range of 0.0–0.45 V. For the cobalt hydroxide carbonate nanorods, two redox peaks corresponding to anodic and cathodic at ~0.1 and ~0.3 V vs. Ag/AgCl are clearly observed indicating that the measured capacitance can be attributed to a redox mechanism [42,43]. Therefore the anodic peak is due to the oxidation of Co^{2+} to Co^{3+} whereas the cathodic peak is due to the reverse process. The composite also exhibits similar peaks which have shifted from the initial values when compared to the pure sample. This is attributed to the presence of the AC which might induce a shift in the peaks positions. Also the composite exhibits a better capacitive behavior as observed by the higher current response and hence the detailed measurements will be made on it. Fig. 5(b) shows the CV curves of the cobalt hydroxide carbonate/AC at the scan rates of 5, 10, 20, 50 and $100 \, mV \, s^{-1}$. No intrinsic shape change is observed from these CV curves as the scan rate increases from 5 to $100 \, mV \, s^{-1}$ implying a good high-current capability. The small shifts in both cathodic and anodic peak potentials are considered to have a direct relationship with internal resistance of the electrode.

The applicability of ECs electrode can be directly evaluated by

Fig. 3. TEM images of (a) cobalt hydroxide carbonate; (b) cobalt hydroxide carbonate/AC composite.

143

Fig. 4. (a) and (c) N$_2$ absorption/desorption isotherms; (b) and (d) pore size distribution of cobalt hydroxide carbonate and cobalt hydroxide carbonate/AC composite, respectively.

Fig. 5. (a) CV of cobalt hydroxide carbonate and cobalt hydroxide carbonate/AC composite at scan rate of 50 mV s^{-1}, (b) CV of cobalt hydroxide carbonate/AC composite at scan rates of 5–100 mV s^{-1}; (c) Galvanostatic charge–discharge of cobalt hydroxide carbonate/AC composite at current densities of 1–15 A g^{-1}; (d) specific capacitance of cobalt hydroxide carbonate and cobalt hydroxide carbonate/AC composite electrode versus current densities.

means of the galvanostatic charge–discharge method. Fig. 5 (c) shows the galvanostatic charge/discharge curves of cobalt hydroxide carbonate/AC electrode at different current densities within a potential range of 0–0.45 V. Each discharge curve includes two clear voltage steps: a fast potential drop from 0.45 V to 0.25 V and a voltage plateau from 0.25 V to 0.16 V. The voltage plateau at around 0.2 V suggests the typical faradic characteristic which is in good agreement with the CV curves in Fig. 5(b). Fig. 5(d) shows the

144

comparison of specific capacitance of hydroxide carbonate with and without AC as a function of current density. The composite shows superior specific capacitance as compared to pristine sample for all current densities measured which supports what is observed in Fig. 5(a). The specific capacitance decreases with increasing current density due to the increment of voltage drop, polarization effect and less utilization or insufficient access by the electrolyte ions to the active material during redox reaction under higher current densities [44].

The specific capacitance of the cobalt hydroxide carbonate with and without AC electrodes was calculated from charge–discharge using the Eq. (5).

$$C_{sp} = \frac{I \times t}{m \times \Delta V} \tag{5}$$

where I is the discharge current (A), t is the discharge time (s), m is the mass of active material (g), ΔV is the potential range of discharge (V), and C_{sp} (F/g) is the specific capacitance. A specific capacitance of 301 F g^{-1} is obtained for cobalt hydroxide carbonate/AC composite compared with a much lower specific capacitance value of 253 F g^{-1} for pristine cobalt hydroxide carbonate at a current density of 1 A g^{-1}. This represents a great improvement on the specific capacitance of cobalt hydroxide electrode material when compared with earlier studies [45,46]. In fact, Tan et al. reported a C_{sp} value of 166.7 F g^{-1} at a current density of 1 A g^{-1} for synthesized hierarchical sisal-like cobalt hydroxide [45]. Xu et al. synthesized triangle taper-like cobalt hydroxide and cobalt oxide and reported a C_{sp} value of 91.5 F g^{-1} at a scan rate of 5 mV s^{-1} [46]. This shows that the material presented in this work electrochemically outperforms those reported in previous works. This could be due to compact structure with less loosely nanorod density and also to the improved conductivity of the composite material when AC was added to the metal hydroxide material. Furthermore, C_{sp} value of 385 F g^{-1} at a high current density of 10 A g^{-1} was reported by Ji et al. [47], for hierarchical CoCO$_3$/CoO nanostructure. This excellent electrochemical performance was due to the ordered structure used in their work. Such a performance could be forseen for our material if an ordered structure is successfully synthesized.

In order to investigate the electrode/electrolyte interface behavior in detail, EIS measurements were employed at open circuit potentials to further evaluate the electrochemical behavior for the cobalt hydroxide carbonate and cobalt hydroxide carbonate/AC composite electrodes at a frequency range of 10 mHz to 100 kHz. Fig. 6(a) shows the Nyquist plots of the cobalt hydroxide carbonate with and without AC electrodes and the inset to the figure shows the equivalent series resistance (ESR – the combined resistance of electrolyte, intrinsic resistance of substrate and contact resistance at the active material/current collector interface) obtained at the

Table 1
The R_s and R_{CT} parameters of cobalt hydroxide carbonate and cobalt hydroxide carbonate/AC electrodes obtained from the Nyquist plot fitting.

Electrode	R_s (Ω)	R_{CT} (Ω)
Cobalt hydroxide carbonate	0.62	0.91
Cobalt hydroxide carbonate/AC	0.39	1.00

intercept of Z' axis (real part of the impedance) of 0.39 Ω for composite which is much smaller than that of the bare cobalt hydroxide carbonate electrode (0.62 Ω), indicating a lower diffusion resistance and charge-transfer resistance. However, slightly tilted vertical lines from the EIS of both materials are seen which indicate a deviation from pure capacitive behavior of the cobalt hydroxide carbonate and composite materials but also suggesting low diffusion resistance of ions within the structure of the material. Fig. 6(b) shows the data with the fitting curve obtained using the equivalent circuit shown as inset to the figure. The fitting was performed using a ZFIT software that applies the complex non-linear least-square (CNLS) method [48]. The corresponding fitting parameters are listed in Table 1 for both materials. In the circuit used for fitting the data, the equivalent series resistance, R_S is in series with the constant phase element Q, W, R_{CT} and C. The small semi-circular arcs in the high-mid frequency is modeled by a charge transfer resistance R_{CT} and Q the constant phase element which is responsible for the capacitance of the composite material and are connected in parallel to each other. C denotes the capacitance which arises as a result of the faradaic charge transfer process taking place during the electrochemical measurement and is in series with the charge transfer resistance R_{CT}. At these low frequencies, the current flowing through the composite electrode material has resistance and Warburg impedance characteristic element denoted by W which is expressed as $W = \frac{A}{j\omega^{0.5}}$ where A is the Warburg coefficient, ω is the angular frequency. In the Nyquist plots the inclined portion of the curve at the lower frequencies where the Warburg impedance, W, dominates, the phase angle is 45°. This is caused by the diffusion/transport of OH$^-$ ions within the pores or surface of cobalt hydroxide carbonate/AC electrode during the redox reaction.

The cyclic stability of the electrode materials is an essential and important parameter to rank the performance of the materials for energy storage applications. Fig. 7(a) shows the electrochemical stability and the life-cycle of the cobalt hydroxide carbonate/AC electrode at a high current density of 4 A g^{-1} for 1000 cycles The capacitance retention of the cobalt hydroxide carbonate/AC electrode material after 1000 cycles is 95.6%. This is an indication that the addition of activated carbon to the cobalt hydroxide carbonate matrix has a long-term electrochemical stability and a high degree

Fig. 6. (a) EIS plots of cobalt hydroxide carbonate and cobalt hydroxide carbonate/AC composite (the inset to the Figure is magnified high frequency region of the EIS), (b) EIS plot of cobalt hydroxide carbonate/AC composite fitted with the circuit shown in the inset to the Figure.

145

Fig. 7. (a) Capacitance retention of the cobalt hydroxide carbonate/AC for 1000 cycles at 4 A g^{-1} (the inset shows the 200 cyclic charge–discharge curves) and (b) Nyquist plots of the cobalt hydroxide carbonate/AC electrode before and after 1000 charge–discharge cycles.

of charge–discharge reversibility since it is known that oxide materials generally have low cycle stability. The capacitance retention upon electrochemical cycling could be strongly attributed to the nature of porous cobalt hydroxide carbonate/AC composite, having high surface area, pore volume, and complete utilization of electrode material. Fig. 7(b) shows the Nyquist plots of the cobalt hydroxide carbonate/AC before and after the last cycle recorded in the frequency range of 100 kHz to 10 mHz. Both plots show partial semi-circular arcs with R_s values of 0.39 and 0.44 Ω before and after cycling, respectively. These R_s values are quite similar and hence showing that the electrode material didn't deteriorate much during cycling.

4. Conclusion

In summary, electrodes of cobalt hydroxide carbonate with and without activated carbon (AC) were prepared by a facile and effective hydrothermal method. The incorporation of AC into the cobalt hydroxide carbonate clearly improved the electrochemical response of the composite electrode. This was indicated by the significant increase of both SSA and specific capacitance from 32.7 m^2 g^{-1} and 253 F g^{-1} (at 1 A g^{-1}) for cobalt hydroxide carbonate to 164.3 m^2 g^{-1} and 301.4 F g^{-1} (at 1 A g^{-1}) for cobalt hydroxide carbonate with AC coupled with very good capacitance retention of 95.6% over 1000 charge–discharge cycles of the composite. The good electrochemical performance coupled with the low cost and simple preparation process depicts cobalt hydroxide carbonate/AC as promising electrodes for ECs application.

Acknowledgments

References

[1] J. Chmiola, C. Largeot, P.-L. Taberna, P. Simon, Y. Gogotsi, Monolithic carbide-derived carbon films for micro-supercapacitors, Science 328 (2010) 480–483.
[2] Y. Zhu, S. Murali, M.D. Stoller, K.J. Ganesh, W. Cai, P.J. Ferreira, et al., Carbon-based supercapacitors produced by activation of graphene, Science (2011) 1537–1541.
[3] H. Jiang, J. Ma, C. Li, Mesoporous carbon incorporated metal oxide nanomaterials as supercapacitor electrodes, Adv. Mater. 24 (2012) 4197–4202.
[4] K.-J. Huang, J.-Z. Zhang, G.-W. Shi, Y.-M. Liu, Hydrothermal synthesis of molybdenum disulfide nanosheets as supercapacitors electrode material, Electrochim. Acta. 132 (2014) 397–403.
[5] J.P. Zheng, P.J. Cygan, T.R. Jow, Hydrous ruthenium oxide as an electrode material for electrochemical capacitors, J. Electrochem. Soc. 142 (1995) 2699–2703.
[6] E. Frackowiak, F. Beguin, F. Béguin, Carbon materials for the electrochemical storage of energy in capacitors, Carbon 39 (2001) 937–950.
[7] F. Chastel, E. Flahaut, A. Peigney, A. Rousset, Carbon nanotube-metal-oxide nanocomposites : microstructure, Electr. Conduct Acta Mater. 48 (2000) 3803–3812.
[8] L. Nyholm, G. Nyström, A. Mihranyan, M. Strømme, Toward flexible polymer and paper-based energy storage devices, Adv. Mater. 23 (2011) 3751–3769.
[9] J. Yin, D. Zhang, J. Zhao, X. Wang, H. Zhu, C. Wang, Meso-and micro-porous composite carbons derived from humic acid for supercapacitors, Electrochim. Acta. 136 (2014) 504–512.
[10] Z.-S. Wu, G. Zhou, L.-C. Yin, W. Ren, F. Li, H.-M. Cheng, Graphene/metal oxide composite electrode materials for energy storage, Nano Energy 1 (2012) 107–131.
[11] M. Zhi, C. Xiang, J. Li, M. Li, N. Wu, Nanostructured carbon-metal oxide composite electrodes for supercapacitors: a review, Nanoscale 5 (2013) 72–88.
[12] R.K. Sharma, A.C. Rastogi, S.B. Desu, Pulse polymerized polypyrrole electrodes for high energy density electrochemical supercapacitor, Electrochem. Commun. 10 (2008) 268–272.
[13] D. Hulicova-Jurcakova, X. Li, Z. Zhu, R. De Marco, G.Q. Lu, Graphitic carbon nanofibers synthesized by the chemical vapor deposition (CVD) method and their electrochemical performances in supercapacitors, Energy Fuels 22 (2008) 4139–4145.
[14] K. Hung, C. Masarapu, T. Ko, B. Wei, Wide-temperature range operation supercapacitors from nanostructured activated carbon fabric, J. Power Sources 193 (2009) 944–949.
[15] C. Portet, J. Chmiola, Y. Gogotsi, S. Park, K. Lian, Electrochemical characterizations of carbon nanomaterials by the cavity microelectrode technique, Electrochim. Acta. 53 (2008) 7675–7680.
[16] A. Celzard, F. Collas, J.F. Mareche, G. Furdin, I. Rey, Porous electrodes-based double-layer supercapacitors: pore structure versus series resistance, J. Power Sources 108 (2002) 153–162.
[17] T.-C. Weng, H. Teng, Characterization of high porosity carbon electrodes derived from mesophase pitch for electric double-layer capacitors, J. Electrochem. Soc. 148 (2001) A368.
[18] S. Murali, N. Quarles, L.L. Zhang, J.R. Potts, Z. Tan, Y. Lu, et al., Volumetric capacitance of compressed activated microwave-expanded graphite oxide (a-MEGO) electrodes, Nano Energy 2 (2013) 764–768.
[19] P. Simon, Y. Gogotsi, Materials for electrochemical capacitors, Nat. Mater. 7 (2008) 845–854.
[20] M. Ramani, B.S. Haran, R.E. White, B.N. Popov, Synthesis and characterization of hydrous ruthenium oxide-carbon supercapacitors, J. Electrochem. Soc. 148 (2001) A374–A380.
[21] D. Kalpana, K.S. Omkumar, S.S. Kumar, N.G. Renganathan, A novel high power symmetric ZnO/carbon aerogel composite electrode for electrochemical supercapacitor, Electrochim. Acta. 52 (2006) 1309–1315.
[22] Y. Tian, J. Yan, L. Huang, R. Xue, L. Hao, B. Yi, Effects of single electrodes of Ni (OH) 2 and activated carbon on electrochemical performance of Ni (OH) 2-activated carbon asymmetric supercapacitor, Mater. Chem. Phys. 143 (2014) 1164–1170.
[23] D. Rochefort, A.L. Pont, Pseudocapacitive behaviour of RuO$_2$ in a proton exchange ionic liquid, Electrochem. Commun. 8 (2006) 1539–1543.
[24] E. Frackowiak, V. Khomenko, K. Jurewicz, K. Lota, F. Beguin, Supercapacitors based on conducting polymers/nanotubes composites, J. Power Sources 153 (2006) 413–418.
[25] Y. Cheng, S. Lu, H. Zhang, C.V. Varanasi, J. Liu, Synergistic effects from graphene and carbon nanotubes enable flexible and robust electrodes for high-

performance supercapacitors, Nano Lett. 12 (2012) 4206–4211.

[26] R. Xu, H.C. Zeng, Dimensional control of cobalt-hydroxide-carbonate nanorods and their thermal conversion to one-dimensional arrays of Co₃O₄ nanoparticles, J. Phys. Chem. B 107 (2003) 12643–12649.

[27] B. Li, Y. Xie, C. Wu, Z. Li, J. Zhang, Selective synthesis of cobalt hydroxide carbonate 3D architectures and their thermal conversion to cobalt spinel 3D superstructures, Mater. Chem. Phys. 99 (2006) 479–486.

[28] S.L. Wang, L.Q. Qian, H. Xu, G.L. Lü, W.J. Dong, W.H. Tang, Synthesis and structural characterization of cobalt hydroxide carbonate nanorods and nanosheets, J. Alloy. Compd. 476 (2009) 739–743.

[29] H. Zhang, J. Wu, C. Zhai, X. Ma, N. Du, J. Tu, et al., From cobalt nitrate carbonate hydroxide hydrate nanowires to porous Co(3)O(4) nanorods for high performance lithium-ion battery electrodes, Nanotechnology 19 (2008) 035711.

[30] Z. Zhao, F. Geng, J. Bai, H.-M. Cheng, Facile and controlled synthesis of 3D nanorods-based urchinlike and nanosheets-based flowerlike cobalt basic salt nanostructures, J. Phys. Chem. C 111 (2007) 3848–3852.

[31] R. Xu, H.C. Zeng, Mechanistic investigation on self-redox decompositions of cobalt-hydroxide-nitrate compounds with different nitrate anion configurations in interlayer space, Chem. Mater. 15 (2003) 2040–2048.

[32] Y. Lin, N. Zhao, W. Nie, X. Ji, Synthesis of ruthenium dioxide nanoparticles by a two-phase route and their electrochemical properties, J. Phys. Chem. C 112 (2008) 16219–16224.

[33] A. Yuan, Q. Zhang, A novel hybrid manganese dioxide/activated carbon supercapacitor using lithium hydroxide electrolyte, Electrochem. Commun. 8 (2006) 1173–1178.

[34] S.X. Deng, D. Sun, C.H. Wu, H. Wang, J.B. Liu, Y.X. Sun, et al., Synthesis and electrochemical properties of MnO₂ nanorods/graphene composites for supercapacitor applications, Electrochim. Acta 111 (2013) 707–712.

[35] O. Ghodbane, J.L. Pascal, F. Favier, Microstructural effects on charge-storage properties in MnO₂-based electrochemical supercapacitors, ACS Appl. Mater. Interfaces 1 (2009) 1130–1139.

[36] J. Li, E. Liu, W. Li, X. Meng, S. Tan, Nickel/carbon nanofibers composite electrodes as supercapacitors prepared by electrospinning, J. Alloy. Compd. 478 (2009) 371–374.

[37] F. Barzegar, A. Bello, D.Y. Momodu, J.K. Dangbegnon, F. Taghizadeh, M. J. Madito, et al., Asymmetric supercapacitor based on an α-MoO₃ cathode and porous activated carbon anode materials, RSC Adv. 5 (2015) 37462–37468.

[38] A. Bello, F. Barzegar, D. Momodu, J. Dangbegnon, F. Taghizadeh, N. Manyala, Symmetric supercapacitors based on porous 3D interconnected carbon framework, Electrochim. Acta 151 (2015) 386–392.

[39] A. Bello, O.O. Fashedemi, J.N. Lekitima, M. Fabiane, D. Dodoo-Arhin, K. I. Ozoemena, et al., High-performance symmetric electrochemical capacitor based on graphene foam and nanostructured manganese oxide, AIP Adv. 3 (2013) 82118.

[40] L. Zhang, F. Zhang, X. Yang, G. Long, Y. Wu, T. Zhang, et al., Porous 3D graphene-based bulk materials with exceptional high surface area and excellent conductivity for supercapacitors, Sci. Rep. 3 (2013) 1408, http://dx.doi.org/10.1038/srep01408.

[41] B. Wang, T. Zhu, H. Bin Wu, R. Xu, J.S. Chen, X.W.D. Lou, Porous Co₃O₄ nanowires derived from long Co(CO₃)0.5(OH)0.11H₂O nanowires with improved supercapacitive properties, Nanoscale 4 (2012) 2145–2149.

[42] Y. Zhai, Y. Dou, D. Zhao, P.F. Fulvio, R.T. Mayes, S. Dai, Carbon materials for chemical capacitive energy storage, Adv. Mater. 23 (2011) 4828–4850.

[43] H. Li, R. Wang, R. Cao, Physical and electrochemical characterization of hydrous ruthenium oxide/ordered mesoporous carbon composites as supercapacitor, Microporous Mesoporous Mater. 111 (2008) 32–38.

[44] H. Teng, Y.-J. Chang, C.-T. Hsieh, Performance of electric double-layer capacitors using carbons prepared from phenol–formaldehyde resins by KOH etching, Carbon 39 (2001) 1981–1987.

[45] X. Tan, H. Gao, M. Yang, Y. Luan, W. Dong, Z. Jin, et al., Synthesize of hierarchical sisal-like cobalt hydroxide and its electrochemical applications, J. Alloy. Compd. 608 (2014) 278–282.

[46] C. Xu, J. Sun, L. Gao, Controllable synthesis of triangle taper-like cobalt hydroxide and cobalt oxide, CrystEngComm 13 (2011) 1586–1590.

[47] X. Ji, S. Cheng, L. Yang, Y. Jiang, Z. Jiang, C. Yang, H. Zhang, M. Liu, Phase transition–induced electrochemical performance enhancement of hierarchical CoCO₃/CoO nanostructure for pseudocapacitor electrode, Nano Energy 11 (2015) 736–745.

[48] B. Conway, Electrochemical Supercapacitors: Scientific Fundamentals and Technological Applications (POD), Kluwer Academic/Plenum, New York, 1999.

4.2.3 Conclude Remarks

Cobalt hydroxide carbonate/AC composite electrode was successfully synthesized by hydrothermal method. The result revealed that fabricating AC with the cobalt hydroxide carbonate clearly improved the surface area and electrochemical performance of the composite electrode. This was indicated by the increase of both SSA and specific capacitance from 32.7 m^2g^{-1} and 253.2 Fg^{-1} (at 1 Ag^{-1}) to 164.3 m^2g^{-1} and 301.4 Fg^{-1} (at 1 Ag^{-1}) for both pristine cobalt hydroxide carbonate and the composite with AC respectively accompanied by excellent constant coulombic efficiency of 95.6 % after 1000 charge-discharge cycles at current density of 4 A g^{-1}. These results showed that cobalt hydroxide carbonate/AC composite electrode could be the promising candidate as electrode material for high-performance supercapacitors.

147

4.3 High Performance Asymmetric Supercapacitor Based on CoAl-LDH/GF and Activated Carbon from Expanded Graphite

4.3.1 Introduction

Having established that the cobalt based hydroxides can be such good materials for electrochemical capacitors application, we then considered the synthesis of cobalt based double layered hydroxides (LDH) composite with carbon materials. This was motivated by the previous study that showed that the addition of carbon material into hydroxides indeed improved both their specific surface area and electrochemical performance. In this study the composite of CoAl-LDH with graphene foam (GF) was considered and the asymmetric supercacitor device was produced with CoAl-LDH/GF as the positive electrode and AC carbon synthesized from expanded graphite as negative electrode.

Asymmetric supercapacitors involving different materials as cathode and anode (such as faradic and EDLC materials) have been found to be an effective way of increasing the energy density of supercapacitor due to the fact that combines the properties from the faradic material cathode with that of the electric double layer anode which normally have different potential windows in the three electrode measurements. The importance of assembling an asymmetric cell is to use electrode materials which are stable in different potential windows in the same electrolyte in order to increase the full cell voltage. Therefore, this will enhance the device energy density because the energy density depends on potential window squared [4].

Layered double hydroxides (LDHs) containing transition metals have attracted remarkable attention because of their unique structural anisotropy, high specific capacitance, low cost and environmentally friendly nature, tunable composition, flexible ion-exchangeability [5,6]. CoAl-LDH ,with divalent Co^{2+} ion and trivalent Al^{3+} ion is one of the most commonly studied LDHs which could contribute to the faradaic redox reaction due to the conversion

148

Co^{2+} to Co^{3+} and vice versa [7]. Nevertheless, the relatively low conductivity restrains electron transfer, causing in poor high rate charge and discharge capability and therefore influences the performance of these electrode materials. Therefore, a hybrid electrode which incorporates LDH on high-surface conducting materials is alleged as a supreme method to enhance electrochemical performance of such material. Based on the above investigation, the graphene-composite can significantly improve the electrochemical properties due to its large surface area, high thermal/chemical stability and high electrical conductivity [7]. Previous study showed supercapacitor behavior of electrostatic self-assembly reduced graphene oxide/CoAl-LDH nanocomposites improved the capacitive performance of the electrodes due to the fact that electrostatic self-assemble behavior between CoAl-LDH-NS and RGO nanosheets can prevent the agglomeration of RGO [8].

In this section CoAl-LDH and CoAl-LDH/graphene foam (GF) were synthesized using a facile and environmentally friendly hydrothermal technique. The CoAl-LDH was well dispersed in the graphene foam matrix which is essential for providing the necessary surface area required for efficient charge transport and storage. An asymmetric supercapacitor was fabricated using CoAl-LDH/GF composite and activated carbon derived from expanded graphite (AEG) as cathode and anode electrodes respectively in a 6 M KOH aqueous electrolyte. The choice of the AEG as the anode material was informed by its extended potential window and its excellent electrochemical stability as reported in the study by Barzegar *et. al* [9].

4.3.2 Results and Discussion

The result of asymmetric cell made from CoAl-LDH/GF// AEG is presented in the paper below.

149

CrossMark
click for updates

High performance asymmetric supercapacitor based on CoAl-LDH/GF and activated carbon from expanded graphite

Tshifhiwa M. Masikhwa,[a] Moshawe J. Madito,[a] Damilola Y. Momodu,[a] Julien K. Dangbegnon,[a] Ouanassa Guellati,[b] Aicha Harat,[b] Mohamed Guerioune,[b] Farshad Barzegar[a] and Ncholu Manyala*[a]

An asymmetric supercapacitor fabricated with a CoAl-layered double hydroxide/graphene foam (LDH/GF) composite as the positive electrode and activated carbon derived from expanded graphite (AEG) as the negative electrode in aqueous 6 M KOH electrolyte is reported. This CoAl-LDH/GF//AEG cell achieved a specific capacitance of 101.4 F g^{-1} at a current density of 0.5 A g^{-1} with a maximum energy density as high as 28 W h kg^{-1} and a power density of 1420 W kg^{-1}. Furthermore, the supercapacitor also exhibited an excellent cycling stability with ~100% capacitance retention after 5000 charging–discharging cycles at a current density of 2 A g^{-1}. The results obtained show the potential use of the CoAl-LDH/GF//AEG material as a suitable electrode for enhanced energy storage in supercapacitors.

Introduction

Electrochemical capacitors (ECs), also called supercapacitors or ultracapacitors, have attracted much attention in the automotive and consumer electronics industry due to their high power density and long cycle life.[1–4] Recent efforts have been focused on supercapacitors due to their characteristic high specific power density, fast charge–discharge rates, longer cycle life, lower maintenance cost, safe operation, and environmental friendliness.[5,6] Such exciting properties make them suitable for a variety of applications such as in portable electronics, mobile communications, hybrid electric vehicles, memory backup systems, and military devices, where high power density, excellent reversibility and long cycle life are very much desirable.[7–12] Supercapacitors can be divided into three types depending on the charge storage mechanism namely; electrical double-layer capacitors (EDLCs), faradaic capacitors and hybrid capacitor systems. EDLCs store the charge electrostatically through the reversible adsorption of the electrolyte ions onto active materials. Faradaic capacitance arises from redox reaction at the electrode surfaces and hybrid capacitors combine the properties of the materials making up the two electrodes of different charge storage behaviour with one electrode being an EDLC and the other a faradaic material.[13,14] Based on the above classification by storage mechanism, common electrode

materials for supercapacitors include carbon-based materials, transition metal oxide/hydroxides and conducting polymers.[15] Carbon materials with unchanged physicochemical properties, low cost, good conductivity, and tuneable porous network, can provide a long cycle life but relatively low energy densities which are required for most important EDLCs applications. In contrast, faradic based on metal oxides/hydroxides and conducting polymer materials show higher capacitance than EDLCs due to their fast, reversible electrosorption and redox processes occurring at or near the solid electrode surface but are plagued with relatively low mechanical and cyclic stability. Thus, increasing research efforts have been focused on combining the unique merits of different capacitive materials in order to get devices with higher energy density along with an enhanced cyclic stability.[16]

Different scholars have explored numerous routes aimed at obtaining reliable materials for supercapacitors with improved performance. Carbon-based materials, (such as carbon nanotubes, carbon nanofibers and graphene) have been intensively studied in recent times as possible electrode materials for energy storage[17–21] due to their unique structural and morphological properties amongst other properties mentioned earlier. They have also been used with other faradic type materials as a means of improving device performance.[22–24]

Several faradic two dimensional (2D) materials like the transition metal oxides,[22,25,26] metal hydroxides,[23,27] layered double hydroxides (LDHs)[28–30] and metal chalcogenides[24,31,32] have been developed for energy storage applications. The morphology of these materials alongside their redox capability makes them ideal candidates for adoption in asymmetric ECs.

[a]*Department of Physics, Institute of Applied Materials, SARCHI Chair in Carbon Technology and Materials, University of Pretoria, Pretoria 0028, South Africa. E-mail: ncholu.manyala@up.ac.za; Fax: +27 12 420 2516; Tel: +27 12 420 3549*

[b]*LEREC Laboratory, Department of Physics, Badji Mokhtar University of Annaba, Annaba 23000, BP. 12, Algeria*

LDHs have been reported as an interesting and promising electrode materials for supercapacitor application due to their unique structural property, high specific capacitance, effective utilization of transition metal atoms, facile synthesis route and low synthesis cost.[33,34] However, the poor electric conductivity of LDHs affects their charge transfer ability resulting in a poor charge and discharge capability that affects their electrochemical performance when used as electrode materials.[28,35,36] It has been established that modifying the LDH with carbon materials to prepare composites is one of the most effective strategies to increase the conductivity as well as the electrochemical properties of LDH.[28,37–39] Carbon materials provide interconnecting meso-structured supports that can facilitate good nanoparticle dispersion and electron transport. For example Luojiang et al.[28] reported a facile synthesis of porous CoAl-layered double hydroxide/graphene composite with enhanced capacitive performance for supercapacitors. Shu et al.[37] also reported the immobilization of Co–Al layered double hydroxides on graphene oxide nanosheets, explaining the growth mechanism and final application as electrodes for electrochemical capacitors. Lei et al.[38] also reported a layered assembly of graphene oxide and Co–Al layered double hydroxide nanosheets as electrode materials for supercapacitor in which they showed an improved electrochemical performance as a result of the incorporation of graphene oxide nanosheets. In another report, Johong et al.[39] also provided a complete study of microwave-assisted synthesis of CoAl-layered double hydroxide/graphene oxide composite and its application in a supercapacitor which shows fabrication of graphene oxide and CoAl-LDH enhanced their contact area and functional electron transport between active materials and charge collector.

Furthermore, there are also detailed reports on the use of some other forms of carbon like activated carbon,[40–42] carbon aerogel[43,44] as suitable negative electrodes in asymmetric supercapacitor due to their high electrical conductivity, high surface area, high porosity and controllable pore structure. The asymmetric supercapacitor combines the properties from the faradic material cathode with that of the electric double layer anode to increase the overall cell voltage and thereby improve the energy density more effectively by providing a wider operating potential window.

Although numerous scientists have done detailed work involving the use of carbon materials in facilitating the electrochemical performance, very little studies have demonstrated the advantage of using different forms of carbon in improving both the conductivity of the faradic material as well as improving the overall device operating voltage. The present work therefore reports on the synthesis of CoAl-LDH and CoAl-LDH/graphene foam (GF) composite by a facile and environmentally friendly hydrothermal technique. The GF material was added to improve on the electrochemical performance of the pristine CoAl-LDH material. The composite exhibited a specific capacitance of 775.6 F g^{-1} at a current density of 0.5 A g^{-1} in KOH electrolyte as compared to a specific capacitance of 647.5 F g^{-1} for the CoAl LDH alone. To evaluate the practical application of the as-synthesized CoAL-LDH/GF composite, an asymmetric supercapacitor device was fabricated. The CoAl-LDH/GF//AEG asymmetric cell was found to perform reversibly at an extended and high cell voltage of 1.4 V in 6 M KOH. The CoAl-LDH/GF//AEG asymmetric exhibited a specific capacitance of 101.4 F g^{-1} at 0.5 A g^{-1} with a maximum energy density as high as 28 W h kg^{-1} and a power density of 1419.7 W kg^{-1}. Lastly, the supercapacitor also exhibited an excellent cycling stability with an approximately 100% capacitance retention after 5000 charge–discharge cycles at a current density of 2 A g^{-1}.

Experimental

Materials

Cobalt chloride hexahydrate ($CoCl_2 \cdot 6H_2O$, purity > 99.99%), aluminium chloride hexahydrate ($AlCl_3 \cdot 6H_2O$, purity $\geq$ 99.99%), hydrochloric acid (HCl, purity $\geq$ 32%) and polyvinyl alcohol (PVA, 99+% hydrolyzed) were purchased from Sigma-Aldrich. Nickel foam was purchased from (Alantum, Munich, Germany), graphite sample (grade ES 250 B5) was purchased from Qingdao Kropfmuehl Graphite, potassium hydroxide (KOH, purity $\geq$ 85%) and urea (purity $\geq$ 98%) were purchased from Merck (South Africa).

Synthesis of Co–Al LDH

$CoCl_2 \cdot 6H_2O$ (1.09 g), $AlCl_3 \cdot 6H_2O$ (1.2 g) and urea (1.2 g) were added to 40 mL of water and stirred for 10 minutes. The mixture was then carefully transferred into a sealed Teflon-lined stainless-steel autoclave and kept at a temperature of 120 °C for 18 h. After cooling to room temperature, the pinkish product was repeatedly washed with deionized water and ethanol several times to remove any unreacted precursor and residual. Thereafter, drying was done at 60 °C for 6 h to obtain the final product.

Synthesis of CoAl-LDH/GF

Graphene foam (GF) used for the production of the composite materials was prepared as reported in our earlier work.[45] Briefly, nickel foam (NF) template with an areal density of 420 g m^{-2} was placed in a quartz tube for the CVD growth of graphene. The nickel foam was first annealed at 1000 °C in the presence of Ar and H$_2$ gases for 60 minutes. Subsequently, CH$_4$ gas (acting as a carbon source) was introduced into the reaction chamber at 968 °C with the flow rate of the gases Ar : H$_2$: CH$_4$ set at 300 : 200 : 10 SCCM respectively. After 60 minutes growth time, the samples were quickly cooled by manually pushing the quartz tube to a lower temperature region. In order to get the graphene foam, the samples were further dipped in 3.0 M HCl and placed on a hot plate at 60 °C to ensure complete etching of the nickel supporting structure. After complete etching of the nickel, the remaining graphene foam was washed several times with deionized water and dried in an oven to obtain the final GF product.

The CoAl-LDH/GF composite was prepared using a hydrothermal reduction technique as shown in Scheme 1. Typically, 25 mg of the as-synthesized graphene foam (GF) was dispersed

151

Scheme 1 Preparation of CoAl-LDH/GF.

in 40 mL of water by ultrasonication for 12 h at room temperature. Then $CoCl_2 \cdot 6H_2O$ (1.09 g), $AlCl_3 \cdot 6H_2O$ (1.2 g) and urea (1.2 g) was added to the pre-sonicated GF solution and the entire mixture was stirred for 10 min. The resulting mixture was then transferred to a Teflon-lined stainless steel autoclave and kept at 120 °C for 18 h. After naturally cooling to room temperature the product CoAl-LDH/GF composite was washed with deionized water and ethanol, and dried at 60 °C for 6 h.

Synthesis of activated carbon from expanded graphite (AEG)

Activated carbon from expanded graphite designated as AEG used for the production of asymmetric device was prepared as reported in our earlier work.[46] Briefly expanded graphite and polyvinylpyrrolidonel (PVP) were used as starting material for the production of a hydrogel, which was then used to produce the AEG after the activation process. The activated material was neutralized with 1 M HCl, washed with deionised water and dried at 60 °C for 12 h.

Structure and morphology characterization

Here the characterization was done only for CoAl-LDH and the CoAl-LDH/GF composite since for the AEG sample, all these had already been done and reported in ref. 46 of our earlier work using the same sample. X-ray diffraction (XRD) patterns were collected using an XPERT-PRO diffractometer (PANalytical BV, Netherlands) with theta/2 theta geometry, operating with a cobalt tube at 50 kV and 30 mA. Fourier transform infrared (FTIR) spectra were recorded using a Bruker Vertex 77 v FTIR spectrometer. The morphology was studied using the high-resolution Zeiss Ultra plus 55 field emission scanning electron microscope (FE-SEM) operated at 2.0 kV. Transmission electron microscopy (TEM) micro-images, selected area electron diffraction (SAED) observations and energy dispersive X-ray (EDX) patterns were carried out with a (HRTEM) (Joel JEM-2100F Field Emission Electron Microscope, with a maximum analytical resolution of 200 kV and a probe size under 0.5 nm). The surface area was calculated by the Brunauer–Emmett–Teller (BET) method from the adsorption branch in the relative pressure range (P/P_0) of 0.01–1. The pore size distribution of the synthesized materials was studied using Barrett–Joyner–Halenda (BJH) method from the desorption branch of the isotherm nitrogen adsorption–desorption isotherms were measured at −196 °C using a Micromeritics ASAP 2020. All the samples were degassed at 180 °C for more than 12 h under vacuum conditions.

Electrode preparation and electrochemical characterization

The electrochemical measurements were carried out in both three and two electrodes configurations using a Biologic VMP-300 potentiostat (Knoxville TN 37930, USA) controlled by the EC-Lab® V10.37 software. The electrochemical measurements for CoAl-LDH, CoAl-LDH/GF and AEG were performed in a three-electrode configuration using a 6 M KOH electrolyte. The as prepared electrodes served as the working electrodes, Ag/AgCl (3 M KCl) served as the reference electrode and glassy carbon plate as the counter electrode. The AEG and polyvinylidene fluoride (PVDF) binder were mixed in a weight ratio of 9 : 1 which was homogenized and dispersed in *N*-methylpyrrolidone (NMP) solution to obtain the slurry, while for the other electrode materials (CoAl-LDH and CoAl-LDH/G), carbon black (CB) (to improve the conductivity) and polyvinylidene fluoride (PVDF) binder were mixed in a weight ratio of 8 : 1 : 1 and dispersed in *N*-methylpyrrolidone (NMP) solution to obtain a slurry. Both slurries from negative and positive electrodes were then uniformly coated on a nickel foam current collector and dried at 60 °C in an oven for 8 h.

The electrochemical test of the asymmetric cell was carried out in a two-electrode cell configuration by means of coin-type cells using a glass micro fiber filter paper as the separator in a 6 M KOH aqueous electrolyte solution with CoAl-LDH/GF and AEG as cathode and anode respectively.

Results and discussion

Fig. 1(a) shows the XRD patterns of the CoAl-LDH and CoAl-LDH/GF composite. The wavelength used for the XRD analysis was the 1.7890 Å line of a Co-K_α source. All diffraction peaks designated in the figure correspond to the pure hydrotalcite structure (JCPDS: 38-0487) with the characteristics peaks of (003), (006), (012), (015) and (018) planes.[47,48] The XRD data suggest that CoAl-LDH preferentially grows in the (003) crystallographic direction.

The interlayer spacing between the CoAl-LDH sheets was calculated to be 0.748 nm (d_{003}) indicating the presence of CO_3^{2-} ions and water molecules occupying the interlayer spaces.[49] The XRD peak of graphene was barely identifiable in the CoAl-LDH/GF as shown in the figure because the CoAl-LDH/GF crystals deposited on graphene can prevent graphene from

152

Fig. 1 (a) XRD patterns and (b) FTIR spectra of CoAl-LDH and CoAl-LDH/GF composite respectively.

Fig. 2 Low and high magnification SEM images of (a and b) CoAl-LDH and (c and d) CoAl-LDH/GF respectively.

stacking into multilayers leading to lesser crystalline intensity peak of graphene.[28] As a result, the weak graphene peak was enshrouded by the stronger CoAl-LDH peaks.

Fig. 1(b) shows the FTIR spectra of CoAl-LDH and CoAl-LDH/GF composite. The absorption peak at wavelength of 3421.6 cm^{-1} corresponds to the O–H stretching vibration of the interlayer water molecules,[48] but the CoAl-LDH/GF composite does not show this absorption peak and that suggest that a presence of graphene in CoAl-LDH breaks the hydrogen bonding that carries the interlayer water molecules. The peaks at 1343.14 and 781.4 cm^{-1} are due to the ν_3 vibration and the bending modes of CO$_3^{2-}$.[28] The peak below 800 cm^{-1} is associated with the metal–oxygen (M–O) stretching and bending modes.[28,37]

The morphology of the material significantly influences the suitability of the material for supercapacitor application. Fig. 2 shows the FESEM microstructures of the as-prepared samples. The morphology of the CoAl-LDH Fig. 2(a) and (b) indicates that the product is formed and mainly composed of thin irregular hexagonal flakes for low and high magnifications

respectively. However, in the presence of graphene foam, numerous CoAl-LDH nanosheets were observed to be densely anchored onto graphene as shown in Fig. 2(c) and (d) at low and high magnifications respectively. CoAl-LDH is well dispersed in the graphene matrix which is essential for providing the necessary surface required for efficient charge transport and storage.

Fig. 3(a) shows the TEM image of a typical nanosized CoAl-LDH. It can be clearly observed that the LDH samples are nearly hexagonal platelets with a lateral size. The TEM micrograph in Fig. 3(b) shows that the same CoAl-LDH sheets are well dispersed on the surface of graphene sheets. The crystallinity of the as-synthesized CoAl-LDH was further confirmed by selected-area electron diffraction (SAED) pattern as shown in Fig. 3(c), which shows the very high degree of crystallinity of the platelets with a net hexagonal symmetry revealing crystallographic nature of the sample. The corresponding EDX pattern in Fig. 3(d) confirms that a CoAl-LDH/GF composite is composed of three main elements of aluminium, cobalt and carbon atoms in the sample. The element Cu recorded in the spectra is depicted due to the copper grid sample holder for microscopy analysis.

A large surface area and favourable pore size distribution are known to be important factors to advance electrode materials for supercapacitor. The nitrogen adsorption–desorption isotherm of the CoAl-LDH and CoAl-LDH/GF composite show a type III behaviour with a very small H3 hysteresis loops indicating the existence of non-rigid aggregates of plate-like particles or assemblages of slit-shaped pores with no saturation (Fig. 4(a)). Corresponding specific surface areas (SSAs) of. 20.7 m^2 g^{-1} and 187 m^2 g^{-1} were recorded for the CoAl-LDH and CoAl-LDH/GF composite samples respectively. Fig. 4(b) shows the pore size distribution plot in which a concentration of pore volume ranging from 2–4 nm is observed. This suggests that the pores present in these materials are mainly mesopores. The BET results obtained for the CoAl-LDH/GF composite indicates that the sample possesses a larger SSA and micropore/mesopores volume than CoAl-LDH alone. It is clear that CoAl-LDH/GF composite will facilitate the electrolyte ion diffusion, improve the ion transport and provide more electroactive sites for fast

153

Fig. 3 TEM images of (a) CoAl-LDH, and (b) CoAl-LDH/GF, (c) SAED of CoAl-LDH and (d) EDX pattern of CoAl-LDH/GF respectively.

energy storage. These features in effect will lead to a correspondingly higher electrochemical performance for the CoAl-LDH/GF.

Electrochemical performance of CoAl-LDH and AEG

To evaluate the potential applications of the electrode materials for supercapacitor applications, the individual electrochemical properties of the CoAl-LDH, CoAl-LDH/GF composite and the AEG samples were first studied in a three-electrode system using 6 M KOH electrolyte. Cyclic voltammetry (CV), chronopotentiometry (CD) and electrochemical impedance spectroscopy (EIS) measurements were carried out for all samples. Fig. 5(a) shows the CV curves obtained in a three-electrode cell for the CoAl-LDH and CoAl-LDH/GF composite at scan rate of 50 mV s^{-1} in a potential range of 0.0 to 0.45 V. For the CoAl-LDH and CoAl-LDH/GF samples, two redox peaks corresponding to anodic and cathodic peaks at ∼0.20 V and ∼0.30 V *vs.* Ag/AgCl

are clearly observed showing that the measured capacitance can be attributed to a redox charge storage mechanism. Therefore, the pair of redox peaks were due to the faradic reaction of Co(ii)/Co(iii) (eqn (1)) and Co(iii)/Co(iv) (eqn (2)) respectively.[50] The COAl-LDH is denoted as LDH-Co (OH)$_2$ since the Al in this material is an electrochemically inert element.[50,51] The anodic/cathodic peaks show the faradic reaction of electrode occurred during the charge–discharge process which is, as a result of the redox reaction and can be written as follows:

$$LDH\text{-}Co(OH)_2 + OH^- \leftrightarrow LDH\text{-}CoOOH + H_2O + e^- \quad (1)$$

$$LDH\text{-}CoOOH + OH^- \leftrightarrow LDH\text{-}CoO_2 + H_2O + e^- \quad (2)$$

The CoAl-LDH/GF composite also shows similar peaks which have shifted from the initial values when compared to the pure

Fig. 4 (a) N$_2$ absorption/desorption isotherms and (b) pore size distribution of CoAl-LDH and CoAl-LDH/GF composite respectively.

154

Fig. 5 (a) Cyclic voltammetry comparison at scan rate of 50 mV s^{-1} and (b) cyclic voltammetry at scan rates of 5–100 mV s^{-1}; (c) galvanostatic charge–discharge comparison at current density of 1 A g^{-1}, (d) galvanostatic charge–discharge at current densities of 1–10 A g^{-1} and (e) specific capacitance *versus* current densities of the of CoAl-LDH, CoAl-LDH/GF composite and AEG respectively.

CoAl-LDH sample. This is attributed to the presence of the GF which might induce a shift in the peak positions. Also, the composite displays a better capacitive behaviour as observed by the higher current response. Fig. 5(b) shows the CV curves of the AEG electrodes at various scan rates ranging from 5 to 100 mV s^{-1}. These CV curves display relatively rectangular shapes without redox peaks which are the typical characteristic of electric double-layer capacitive sample behaviour.[9] Fig. 5(c) illustrates the overlaid galvanostatic charge–discharge (GCD) curves of the CoAl-LDH and the CoAl-LDH/GF composite at a current density of 1 A g^{-1} within a potential range of 0–0.45 V respectively. Each discharge curve includes two clear voltage steps: a fast potential drop from 0.40–0.30 V and a voltage plateau from 0.30–0.12 V. The voltage plateau at around 0.3 V suggests a typical faradic characteristic which is in good agreement with the CV curves reported in Fig. 5(a). It can also be clearly seen that the integral area of the cyclic voltammogram and discharge time of the CoAl-LDH/GF composite are large and longer respectively as compared to pristine sample which is the indication of the higher specific capacitance. Fig. 5(d) shows the

galvanostatic charge/discharge curves of the AEG electrode at different current densities within a potential range of −0.8 to 0 V. As can be seen from the figure, the shapes of the charge–discharge curves are all nearly symmetrical with a triangular shape which shows a typical electric double-layer capacitive behavior. This is also in agreement with the results from the CV curves in Fig. 5(b). The AEG electrode has a small amount of internal resistance (IR) voltage drop at a current density of 1 A g^{-1}, which is revealed by a rapid potential drop at the very beginning of the discharge process. Based on the galvanostatic charge–discharge (CD) curves, the specific capacitance of the electrode materials was evaluated from the galvanostatic charge–discharge (GCD) curves using eqn (3):

$$C_s = \frac{I \times t}{m \times \Delta v} \qquad (3)$$

where I is the discharge current (A), t is the discharge time (s), m is the mass of active material (g), Δv is the potential range of discharge (V), and C_s is the specific capacitance (F g^{-1}).

155

Fig. 6 (a) Cyclic voltammetry of CoAl-LDH/GF and AEG electrodes at scan rates of 50 mV s^{-1} for three-electrode setup; asymmetric CoAl-LDH/GF//AEG device (b) cyclic voltammetry at scan rates of 5–100 mV s^{-1}, (c) galvanostatic charge–discharge at current densities of 0.5–5 A g^{-1} and (d) the specific capacitance as function of the current density, (e) Ragone plot and (f) cycle stability at a constant current density of 0.5 A g^{-1} (inset shows charge–discharge curves after 200 circles) respectively.

The specific capacitances of the CoAl-LDH, CoAl-LDH/GF composite and the AEG were calculated at different current densities and the plot of the specific capacitance (F g^{-1}) as a function of current density (A g^{-1}) is shown in Fig. 5(e). The specific capacitance of pristine CoAl-LDH is lower than those of the CoAl-LDH/GF composite. An enhancement in the specific capacitance of the CoAl-LDH/GF composite is due to the addition of porous and conducting graphene foam to the CoAl-LDH matrix which provides an improved electron transfer rate and better structural support for the growth of CoAl-LDH flakes on the graphene sheets. The observed capacitive characteristic observed in the AEG sample is attributed to the presence of the microporous structure in carbon which facilitates rapid electrolyte transfer and relatively high degree of graphitization that provide good electrical conductivity to the electrode.[52]

Electrochemical properties of the asymmetric supercapacitor

To further assess the practical prospective application of the CoAl-LDH/GF composite with AEG in supercapacitors, an asymmetric device was assembled in which the positive electrode comprised of the CoAl-LDH/GF composite material and the AEG material was used as the negative electrode.

In order to obtain the optimal performance of the asymmetric full cell supercapacitor, the charge balance between the two electrodes should follow the relationship: $Q_+ = Q_-$, where Q_+ and Q_- are the charges stored in the positive and negative electrodes respectively. The charge stored by each electrode can be expressed as:[53]

$$Q = C_s \times m \times \Delta U \qquad (4)$$

where C_s is the specific capacitance of the active material, m is the mass of each active material and ΔU is the potential range during the charge–discharge process.

In order to get $Q_+ = Q_-$, the mass balancing between the negative and positive electrode could also be expressed as follows:

$$\frac{m_+}{m_-} = \frac{C_s - \Delta U_-}{C_s + \Delta U_+} \qquad (5)$$

156

Fig. 7 (a) EIS plot and fitting curve for the asymmetric cell, (b) EIS before and after cycling and (c) the real and imaginary part of the cells capacitance against frequency of asymmetric cell of CoAl-LDH/GF//AEG respectively.

For making two electrode cells, according to eqn (5), the mass ratio of the CoAl-LDH/GF (positive electrode) to the negative electrode was about 2.3 : 3.4. Fig. 6(a) shows the CV of the CoAl-LDH/GF and the AEG electrodes at a scan rate of 50 mV s^{-1} in a three electrode system. From Fig. 6(a), it is expected that the operating cell voltage could be extended up to about 1.4 V if the CoAl-LDH/GF electrode as a cathode and the AEG electrode as an anode are assembled into asymmetric devices in a 6 M KOH electrolyte solution. Fig. 6(b) shows the CV curves of the CoAl-LDH/GF//AEG asymmetric device measured at different scan rates from 5–100 mV s^{-1}. It indicates that the CV curves at different scan rates show an electric double layer capacitance and faradic behaviour which is a typical characteristic of hybrid asymmetric supercapacitors. The charge–discharge curves of the asymmetric supercapacitor at various current densities are shown in Fig. 6(c). It can be seen that the shapes of the charge–discharge curves show non-linearity indicating some contribution from the redox reaction of the CoAl-LDH/GF composite which is in good agreement with the CV curves reported in Fig. 6(b). The specific capacitance of the CoAl-LDH/GF//AEG can also be calculated from eqn (2). The specific capacitance of the asymmetric device decreases from 101 F g^{-1} to 42 F g^{-1} with an increase in current density from 0.5 to 5 A g^{-1} as shown in Fig. 6(d). The Ragone plot for energy density and power density presents two key parameters to characterize the performance of electrochemical supercapacitors. The corresponding energy and power densities of EC can be calculated from the specific capacitance, C_s according to the following equations:

$$E_d = \frac{1}{2}C_s\Delta U^2 = \frac{1000 \times C_s\Delta U^2}{2 \times 3600} = \frac{C_s\Delta U^2}{7.2} \quad (6)$$

$$P_d = \frac{3600 \times E_d}{\Delta t} \quad (7)$$

where E_d is the average energy density (W h kg^{-1}), C_s is the specific capacitance based on the electroactive material (F g^{-1}), ΔU is the potential window, P_d is the average power density (W kg^{-1}) and t is the discharge time (seconds).

The Ragone plot showing relationship between energy and power densities of the asymmetric device is shown in Fig. 6(e). The maximum energy density of the device was recorded as 28 W h kg^{-1} with a corresponding power density of 1420 W kg^{-1} at a current density of 0.5 A g^{-1} as shown in Fig. 6(e). The energy density in aqueous electrolyte solution is higher than reported asymmetric supercapacitor, such as Ni$_x$Co$_{1-x}$ LDH-ZTO//AC (23.7 W h kg^{-1} and 284.2 W kg^{-1} at 0.5 g^{-1}),[54] CoMn-LDH/Ni foam//AC (energy density of 4.4 W h kg^{-1} corresponding power density of 2500 W kg^{-1} at 0.5 A g^{-1})[55] and NiCo$_2$O$_4$-rGO//AC (23.32 W h kg^{-1} and 324.9 W kg^{-1} at 0.5 g^{-1})[56] but comparable or smaller than those reported for RGO/CoAl-LDH//AC (energy density of 35.5 W h kg^{-1} corresponding power density of 8.75 kW kg^{-1} at 1 A g^{-1})[57] and Ni–Al LDH/CNTs//AC (energy density of 52 W h kg^{-1} at 1 A g^{-1}).[58] However, our electrode material presents a higher and better stability compared to RGO/LDH//AC (90% after 6000 cycles at 4 A g^{-1}) and Ni–Al LDH/CNTs//AC (70.3% after 2000 cycles) materials. The latter already deteriorate after 500 cycles. The long-term stability of the CoAl-

157

LDH/GF//AEG asymmetric device was studied by continuous galvanostatic charge–discharge cycling at a current density of 0.5 A g^{-1} for 5000 cycles as shown in Fig. 6(f). The capacitance retention of the CoAl-LDH/GF//AEG asymmetric devices after 5000 cycles is 100%, indicating that the device shows good electrochemical stability. The electrode materials are selectively etched in the presence of KOH alkali solution and further activated electrochemically in the cycling process which aids in improving their wettability and these changes allow the trapped electrolyte ions to diffuse out.[59]

In order to investigate the impedance behaviour at the electrode/electrolyte interface in detail, EIS measurements were employed at an open circuit potential to further evaluate the electrochemical behaviour of the asymmetric device at a frequency range of 10 mHz to 100 kHz. The Nyquist plot for the asymmetric CoAl-LDH/GF//AEG device is shown in Fig. 7(a), with an intercept to x-axis of 0.89 Ω which corresponds to the solution resistance (R_S) and was calculated to be 1.2 Ω from the fit to the data using the circuit shown in the inset to the figure. In the circuit the equivalent series resistance, R_S is in series with the constant phase element (Q_1) representing double layer capacitance, which occur in the interface between material and the electrolyte, and Q_1 is connected in parallel with the charge transfer resistant R_{CT}. The leakage current R_L is connected in parallel to Q_2 element representing double-layer capacitance.

Fig. 7(b) shows the Nyquist plots for the CoAl-LDH/GF//AEG asymmetric devices before and after continuous cycling. From the x-axis intercept, R_S values of 0.89 Ω and 2.32 Ω were obtained before and after cycling. After 5000 cycles, the electrode shows a larger transfer resistance due to the decomposition of the electrolyte and decrease of electrical conductivity.[60]

The real ($C'(\omega)$) and imaginary ($C''(\omega)$) capacitances as a function of frequency are shown in Fig. 7(c). The capacitance of 0.016 F (from topmost part of the C') was observed which represents the deliverable capacitance as a function of frequency. Furthermore, it is observed that the imaginary capacitance passes through a maximum frequency f_0 (0.24 Hz), which is the transition frequency between a pure resistive behaviour and pure capacitive behaviour, and is related to the relaxation time $\tau = \dfrac{1}{f_0} = 4.3$ s. This time signifies that the cell could reach its maximum capacitance at a very fast recharging time of 4.3 s. The fast frequency response of 0.24 Hz was attributed to the porous structure of the electrode material which delivers full accessibility to the ions from the electrolyte leading to faster diffusion rates.

Conclusions

In summary, the CoAl-LDH/GF//AEG was investigated as a suitable material for an asymmetric supercapacitor cell based on AEG material as negative electrodes and CoAl-LDH/GF composite as positive electrode. The asymmetrical device exhibited high specific capacitance of 101.4 F g^{-1} at a current density of 0.5 A g^{-1} with a maximum energy density of 28 W h kg^{-1} and a corresponding power density of 1420 W kg^{-1} in aqueous electrolyte. In addition, an excellent stability with

~100% capacitance retention with no capacitance loss after 5000 cycles at a current density of 2 A g^{-1} is attained within an extended operating voltage of about 1.4 V in 6 M KOH aqueous electrolyte. These results demonstrate an optimized hybrid structure applicable in high performance supercapacitors. Finally, these findings offer a suitable and effective way to assemble asymmetric hybrid supercapacitors based on CoAl-LDH/GF composite and AEG with high energy density while sustaining the high power density property of supercapacitor.

Acknowledgements

References

1 L. L. Zhang and X. S. Zhao, *Chem. Soc. Rev.*, 2009, **38**, 2520–2531.

2 H. Wang, Y. Wang, Z. Hu and X. Wang, *ACS Appl. Mater. Interfaces*, 2012, **4**, 6827–6834.

3 L. Mei, T. Yang, C. Xu, M. Zhang, L. Chen, Q. Li and T. Wang, *Nano Energy*, 2014, **3**, 36–45.

4 H. Du, L. Jiao, K. Cao, Y. Wang and H. Yuan, *ACS Appl. Mater. Interfaces*, 2013, **5**, 6643–6648.

5 H. Chen, J. Jiang, L. Zhang, H. Wan, T. Qi and D. Xia, *Nanoscale*, 2013, **5**, 8879–8883.

6 M. Huang, F. Li, Y. X. Zhang, B. Li and X. Gao, *Ceram. Int.*, 2014, **40**, 5533–5538.

7 J. Zhang, X. Wang, J. Ma, S. Liu and X. Yi, *Electrochim. Acta*, 2013, **104**, 110–116.

8 W. Lu, P. Soukiassian and J. Boeckl, *MRS Bull.*, 2012, **37**, 1119–1124.

9 G. Wang, L. Zhang and J. Zhang, *Chem. Soc. Rev.*, 2012, **41**, 797.

10 Z. Gao, W. Yang, J. Wang, B. Wang, Z. Li, Q. Liu, M. Zhang and L. Liu, *Energy Fuels*, 2012, **27**, 568–575.

11 L. Huang, D. Chen, Y. Ding, S. Feng, Z. L. Wang and M. Liu, *Nano Lett.*, 2013, **13**, 3135–3139.

12 Q. Chen, H. Li, C. Cai, S. Yang, K. Huang, X. Wei and J. Zhong, *RSC Adv.*, 2013, **3**, 22922–22926.

13 Y. Li, X. Zhao, P. Yu and Q. Zhang, *Langmuir*, 2012, **29**, 493–500.

14 Y. Zhang, H. Feng, X. Wu, L. Wang, A. Zhang, T. Xia, H. Dong, X. Li and L. Zhang, *Int. J. Hydrogen Energy*, 2009, **34**, 4889–4899.

15 E. Frackowiak, *Phys. Chem. Chem. Phys.*, 2007, **9**, 1774–1785.

16 L. L. Zhang, R. Zhou and X. S. Zhao, *J. Mater. Chem.*, 2010, **20**, 5983.

158

17 J. P. C. Trigueiro, R. L. Lavall and G. G. Silva, *Electrochim. Acta*, 2016, **187**, 312–322.

18 Y. Jiang, J. Yan, X. Wu, D. Shan, Q. Zhou, L. Jiang, D. Yang and Z. Fan, *J. Power Sources*, 2016, **307**, 190–198.

19 J. Chen, Y. Cui, X. Wang, M. Zhi, M. Lavorgna, A. P. Baker and J. Wu, *Electrochim. Acta*, 2016, **188**, 704–709.

20 K. S. Novoselov, V. I. Fal, L. Colombo, P. R. Gellert, M. G. Schwab, K. Kim, *et al.*, *Nature*, 2012, **490**, 192–200.

21 A. K. Geim and K. S. Novoselov, *Nat. Mater.*, 2007, **6**, 183–191.

22 S. Bag and C. R. Raj, *J. Mater. Chem. A*, 2016, **4**, 587–595.

23 S. Gao, Y. Sun, F. Lei, L. Liang, J. Liu, W. Bi, B. Pan and Y. Xie, *Angew. Chem., Int. Ed.*, 2014, **53**, 12789–12793.

24 J. Feng, X. Sun, C. Wu, L. Peng, C. Lin, S. Hu, J. Yang and Y. Xie, *J. Am. Chem. Soc.*, 2011, **133**, 17832–17838.

25 S. Liu, K. S. Hui, K. N. Hui, V. V Jadhav, Q. X. Xia, J. M. Yun, Y. R. Cho, R. S. Mane and K. H. Kim, *Electrochim. Acta*, 2016, **188**, 898–908.

26 Y. Juan, Y. Chang, X. Fan, S. Liang, S. Li, H. Huang, Z. Ling, C. Hao and Q. Jieshan, *Energy Environ. Sci.*, 2016, **9**, 1299–1307.

27 Y. Zhu, C. Cao, S. Tao, W. Chu, Z. Wu and Y. Li, *Sci. Rep.*, 2014, **4**, 5787.

28 L. Zhang, K. N. Hui, K. San Hui and H. Lee, *Electrochim. Acta*, 2015, **186**, 522–529.

29 Y. Wimalasiri, R. Fan, X. S. Zhao and L. Zou, *Electrochim. Acta*, 2014, **134**, 127–135.

30 F. Lai, Y. Huang, Y.-E. Miao and T. Liu, *Electrochim. Acta*, 2015, **174**, 456–463.

31 K. Krishnamoorthy, G. K. Veerasubramani, S. Radhakrishnan and S. J. Kim, *Mater. Res. Bull.*, 2014, **50**, 499–502.

32 J. H. Han, S. Lee and J. Cheon, *Chem. Soc. Rev.*, 2013, **42**, 2581–2591.

33 W. Yang, Z. Gao, J. Wang, J. Ma, M. Zhang and L. Liu, *ACS Appl. Mater. Interfaces*, 2013, **5**, 5443–5454.

34 A. Zhang, C. Wang, Q. Xu, H. Liu, Y. Wang and Y. Xia, *RSC Adv.*, 2015, **5**, 26017–26026.

35 Y. Lin, L. Ruiyi, L. Zaijun, L. Junkang, F. Yinjun, W. Guangli and G. Zhiguo, *Electrochim. Acta*, 2013, **95**, 146–154.

36 L. Zhang, J. Wang, J. Zhu, X. Zhang, K. San Hui and K. N. Hui, *J. Mater. Chem. A*, 2013, **1**, 9046–9053.

37 S. Huang, G.-N. Zhu, C. Zhang, W. W. Tjiu, Y.-Y. Xia and T. Liu, *ACS Appl. Mater. Interfaces*, 2012, **4**, 2242–2249.

38 L. Wang, D. Wang, X. Y. Dong, Z. J. Zhang, X. F. Pei, X. J. Chen, B. Chen and J. Jin, *Chem. Commun.*, 2011, **47**, 3556–3558.

39 J. Fang, M. Li, Q. Li, W. Zhang, Q. Shou, F. Liu, X. Zhang and J. Cheng, *Electrochim. Acta*, 2012, **85**, 248–255.

40 Z. Lin, X. Yan, J. Lang, R. Wang and L.-B. Kong, *J. Power Sources*, 2015, **279**, 358–364.

41 S. Yang, K. Cheng, K. Ye, Y. Li, J. Qu, J. Yin, G. Wang and D. Cao, *J. Electroanal. Chem.*, 2015, **741**, 93–99.

42 J. Huang, P. Xu, D. Cao, X. Zhou, S. Yang, Y. Li and G. Wang, *J. Power Sources*, 2014, **246**, 371–376.

43 W. Liu, X. Li, M. Zhu and X. He, *J. Power Sources*, 2015, **282**, 179–186.

44 Z. Yu, M. McInnis, J. Calderon, S. Seal, L. Zhai and J. Thomas, *Nano Energy*, 2015, **11**, 611–620.

45 D. Y. Momodu, F. Barzegar, B. Abdulhakeem, J. Dangbegnon, T. Masikhwa, J. Madito, N. Manyala, A. Bello, J. Dangbegnon, T. Masikhwa, J. Madito and N. Manyala, *Electrochim. Acta*, 2015, **151**, 591–598.

46 F. Barzegar, A. Bello, D. Momodu, M. J. Madito, J. Dangbegnon and N. Manyala, *J. Power Sources*, 2016, **309**, 245–253.

47 L.-H. Su and X.-G. Zhang, *J. Power Sources*, 2007, **172**, 999–1006.

48 W. Lin, W. Yu, Z. Hu, W. Ouyang, X. Shao, R. Li and D. S. Yuan, *Electrochim. Acta*, 2014, **143**, 331–339.

49 L. Zhang, X. Zhang, L. Shen, B. Gao, L. Hao, X. Lu, F. Zhang, B. Ding and C. Yuan, *J. Power Sources*, 2012, **199**, 395–401.

50 J. Han, Y. Dou, J. Zhao, M. Wei, D. G. Evans and X. Duan, *Small*, 2013, **9**, 98–106.

51 E. Scavetta, B. Ballarin, M. Gazzano and D. Tonelli, *Electrochim. Acta*, 2009, **54**, 1027–1033.

52 K. Wang, N. Zhao, S. Lei, R. Yan, X. Tian, J. Wang, Y. Song, D. Xu, Q. Guo and L. Liu, *Electrochim. Acta*, 2015, **166**, 1–11.

53 A. Bello, F. Barzegar, D. Momodu, J. Dangbegnon, F. Taghizadeh, M. Fabiane and N. Manyala, *J. Power Sources*, 2015, **273**, 305–311.

54 X. Wang, A. Sumboja, M. Lin, J. Yan and P. S. Lee, *Nanoscale*, 2012, **4**, 7266–7272.

55 A. D. Jagadale, G. Guan, X. Li, X. Du, X. Ma, X. Hao and A. Abudula, *J. Power Sources*, 2016, **306**, 526–534.

56 X. Wang, W. S. Liu, X. Lu and P. S. Lee, *J. Mater. Chem.*, 2012, **22**, 23114–23119.

57 W. Zhang, C. Ma, J. Fang, J. Cheng, X. Zhang, S. Dong and L. Zhang, *RSC Adv.*, 2013, **3**, 2483–2490.

58 M. Li, F. Liu, J. P. Cheng, J. Ying and X. B. Zhang, *J. Alloys Compd.*, 2015, **635**, 225–232.

59 J. Yang, C. Yu, X. Fan and J. Qiu, *Adv. Energy Mater.*, 2014, **4**(18), DOI: 10.1002/aenm.201400761.

60 G. Huang, S. Xu, S. Lu, L. Li and H. Sun, *ACS Appl. Mater. Interfaces*, 2014, **6**, 7236–7243.

159

© University of Pretoria

4.3.3 Conclude Remarks

An asymmetric supercapacitor based on CoAl-LDH/GF and AEG material as positive and negative electrodes has been developed in 6M KOH aqueous electrolyte solution. This asymmetric device showed high specific capacitance of 101.4 F g^{-1} at a current density of 0.5 A g^{-1} with a maximum energy density of 28 Wh kg^{-1} and a corresponding power density of 1420 W kg^{-1}, with excellent stability of~ 100% capacitance retention with no capacitance loss after 5000 cycles. The most important aspect of this device is that it demonstrated a high energy density while retaining the high power density of the supercapacitor, unlike other supercapacitor devices that will show a high energy density but then a low power density. Such asymmetric device is anticipated to be an extremely promising candidate for application in high performance energy storage systems.

4.4 High Electrochemical Performance of Hybrid Cobalt Oxyhydroxide/Nickel Foam Graphene

4.4.1 Introduction

In section 4.3 CoAl-LDH was synthesized using a facile and environmentally friendly hydrothermal technique. In this section mesoporous nanosheets of cobalt oxyhydroxide (CoOOH) were synthesized on Ni foam graphene (Ni-FG) substrate by facile two-step processes, namely, hydrothermal reaction to produce CoAl-LDH nanosheets on Ni-FG which were converted to CoOOH nanosheets on Ni-FG by alkaline etching of the Al cations in CoAl-LDH using a NaOH solution. This is another simple route to produce a different phase of cobalt hydroxide material for electrochemical capacitors application. The in-sute synthesis of CoOOH on nickel foam graphene current collector was informed by our previous work which demonstrated that nickel foam electrical conductivity and the adhesion surface area can be improved by covering Ni-foam with graphene through CVD method [10].

160

4.4.2   Results and Discussion

The result of CoOOH on the Ni-FG substrate is presented in the paper below.

Regular Article

High electrochemical performance of hybrid cobalt oxyhydroxide/nickel foam graphene

Tshifhiwa M. Masikhwa, Moshawe J. Madito, Damilola Momodu, Abdulhakeem Bello, Julien K. Dangbegnon, Ncholu Manyala *

Department of Physics, Institute of Applied Materials, SARCHI Chair in Carbon Technology and Materials, University of Pretoria, Pretoria 0028, South Africa

GRAPHICAL ABSTRACT

A mesoporous nanosheets of cobalt oxyhydroxide (CoOOH) synthesized on nickel foam graphene (Ni-FG) substrate exhibited the specific capacity of 199 mA h g^{-1} at a current density of 0.5 A g^{-1}.

ARTICLE INFO

ABSTRACT

In this study, we report the in-situ hydrothermal synthesis of mesoporous nanosheets of cobalt oxyhydroxide (CoOOH) on nickel foam graphene (Ni-FG) substrate, obtained via atmospheric pressure chemical vapour deposition (AP-CVD). The produced composite were closely interlinked with Ni-FG, which enhances the synergistic effect between graphene and the metal hydroxide, CoOOH. It is motivating that the synthesized CoOOH on the Ni-FG substrate showed a homogenous coating of well-ordered intersected nanosheets with porous structure. The electrochemical properties of the material as electrode showed a maximum specific capacity of 199 mA h g^{-1} with a capacity retention of 98% after 1000 cycling in a three electrode measurements.

© 2016 Elsevier Inc. All rights reserved.

1. Introduction

Recently, research on electrode materials for supercapacitor applications has become one of the most important research topics

* Corresponding author.
  E-mail address: ncholu.manyala@up.ac.za (N. Manyala).

161

in energy storage materials. Supercapacitor has received much attention due to its advantages of long cycle life, moderate specific energy density ($\sim$10 W h kg^{-1}), high power density (>10 kW kg^{-1}) and short charging time [1–3]. These characteristics meet the increasing demand for power tools, hybrid electric vehicles and time-dependent electric power systems for portable electronics [4]. In the supercapacitor, the electrode material plays a significant role in the electrochemical capacitive performance. In the last decades, different types of electrode materials have been used in supercapacitor including carbonaceous materials, transitional metal hydroxides/oxide and conducting polymers [1,2,5,6]. Amongst these transitional metals, hydroxides/oxides have received much attention for high-performance due to their high specific capacitances, low costs, low toxicity, great flexibility in structure and morphology [7–14].

In addition, the cobalt oxyhdroxide is an improved charge storage material due to its morphology control nature of micrometer/-nanometer scale and reasonably lower material costs [15,16]. However cobalt oxyhdroxide practical capacitance is less than 200 F g^{-1} due to its low conductivity [17]. To improve the ionic transportation and electrical conductivity, various metal nanostructures and composites combined with carbon materials such as activated carbon, conducting polymers and graphene, with high surface area and high conductivity have been studied [18–22]. Among these materials, a porous and light-weight, graphene foam material (i.e. 3D structured graphene from nickel form templates) has been studied extensively as an ideal matrix for the growth of metal nanostructures because of its high conductivity [23–26]. Different kinds of nanostructured metal hydroxides/oxides have been deposited on graphene foam (GF) electrodes for supercapacitor applications [27,28]. For instance, Zhu et al. [9] considered Cobalt oxide (CoO) nanorods cluster on three-dimensional graphene (CoO-3DG) through a facile hydrothermal method followed by heat treatment which improved electrochemical capacitive performance, Dong et al. also produced 3D graphene/CO$_3$O$_4$ nanowire composites which demonstrated remarkable performance in supercapacitor [29], Zhao et al. synthesized Co(OH)$_2$/graphene/Ni foam nano electrodes with high cycling stability for supercapacitor [30], Shim et al. also reported 3D CO$_3$O$_4$/graphene/nickel foam with enhanced electrochemical performance for supercapacitor [31] and Deng et al. [32] synthesized CoO composited with 3D GF through a combination of hydrothermal method and thermal treatment which exhibited a high specific capacitance, excellent rate capability, and cycling stability as electrode material.

In this study, mesoporous nanosheets of cobalt oxyhydroxide (CoOOH) were synthesized on Ni foam graphene (Ni-FG) substrate by facile two-step processes, namely, hydrothermal reaction to produce CoAl-LDH nanosheets on Ni-FG which were converted to CoOOH nanosheets on Ni-FG by alkaline etching of the Al cations in CoAl-LDH using a NaOH solution. The CoOOH/Ni-FG electrode showed the specific capacity of 95 mA h g^{-1} at 10.0 A g^{-1} with 98 % capacity retention after 1000 cycles.

2. Experimental details

2.1. Graphene growth on nickel foam using AP-CVD

A Ni foam graphene substrate was synthesized by growing graphene sheets on the polycrystalline Ni foam (3D scaffold template with a macroporous structure) using atmospheric pressure chemical vapour deposition (AP-CVD). Polycrystalline Ni foam (Ni-F) (3D scaffold template with a macroporous structure) with an areal density of 420 g m^{-2} and 1.6 mm in thickness, was used as a substrate for graphene growth. A piece of Ni-F (2 cm $\times$ 3 cm) was treated with dilute hydrochloric acid, ethanol and distilled

water to clean the surface of the foam. A cleaned Ni-F was placed at a centre of a quartz tube for graphene growth and was annealed at 1000 °C under Ar and H$_2$ gases for 60 min and graphene was synthesized from a mixture of Ar:H$_2$:CH$_4$ (300:200:10 sccm respectively) gases at a temperature of 1000 °C for 10 min. Immediately after 10 min, the CH$_4$ flow was stopped and samples were rapidly cooled down (under Ar and H$_2$ gases) by pushing the quartz tube to the cooler region of the furnace. At less than 80 °C, Ni-F graphene was off loaded from AP-CVD quartz tube. A synthesized Ni foam graphene (Ni-FG) substrate was further used for growth of CoOOH nanosheets.

2.2. CoOOH growth on Ni foam graphene (Ni-FG) using hydrothermal method

CoOOH nanosheets supported on nickel foam graphene were deduced from in-situ hydrothermally prepared CoAl-LDH on Ni-FG substrate by alkaline etching in concentrated NaOH solution as reported in Ref. [33]. A solution (pink in colour) for hydrothermal reaction was prepared by adding Co(NO)$_3$6H$_2$O (2 mmol), Al (NO$_3$)$_3$6H$_2$O (2 mmol), NH$_4$F (8 mmol) and CO(NH$_2$)$_2$ (10 mmol) in 36 mL of deionized water and stirred for 10 min, as demonstrated in Fig. 1. Ni-FG substrate was immersed into the above solution and then carefully transferred into a sealed Teflon-lined stainless-steel autoclave and kept at a temperature of 100 °C for 24 h (Fig. 1). After cooling of the autoclave to room temperature, the obtained CoAl-LDH coated on Ni-FG was cleaned with deionized water. Then, the CoAl-LDH coated Ni-FG was immersed in 5 mol L^{-1} NaOH for 48 h and subsequently rinsed with deionized water, followed by ethanol for 5 min using ultrasonic bath, and dried at 60 °C for 6 h to obtain the final product CoOOH nanosheets (shown by micrograph image in the last step of Fig. 1) on Ni-FG substrate. The weight of the CoOOH film on Ni-FG substrate was measured by weighing the Ni-FG substrate before and after hydrothermal process, and a mass loading of $\sim$5 mg cm^{-2} was obtained.

3. Materials characterizations

The as-prepared Ni-FG and CoOOH film on Ni-FG were characterized by X-ray diffraction (XRD) using a XPERT-PRO diffractometer (PANalytical BV, Netherlands) with theta/2 theta geometry, operating with a Co Kα radiation source (λ = 1.789 Å). The XRD spectra were acquired at a scanning rate of 0.2 s^{-1} and 2θ range

Fig. 1. A schematic view of the hydrothermal growth of CoAL–LDH on graphene synthesized on Ni foam and alkaline etching in concentrated NaOH solution which produces a mesoporous structure of CoOOH on Ni foam graphene.

of 15–70°. Raman spectroscopy measurements were carried out using WITec Alpha 300 micro-Raman system with 532 nm excitation laser. Raman spectra were measured at room temperature with the laser power set below 5 mW in order to minimize heating effects. The SEM images were obtained on a Zeiss Ultra Plus 55 field emission scanning electron microscope (FE-SEM) operated at 2 kV beam and the working distance (WD) of 2.7 mm. The FE-SEM is equipped with an energy-dispersive X-ray spectrometer (EDX).

4. Electrode preparation and electrochemical characterization

The performance of Ni-FG and CoOOH film on Ni-FG were investigated using a Bio-Logic VMP300 potentiostat (Knoxville TN 37,930, USA) controlled by the EC-Lab® V10.40 software in a three-electrode configuration. The Ni-FG or CoOOH/Ni-FG (1 cm × 2 cm) served as the working electrode in a 6 M potassium hydroxide (KOH) electrolyte; glassy carbon plate was used as the counter electrode and Ag/AgCl (3 M KCl) as the reference electrode. The cyclic voltammetry (CV) tests were carried out in the potential range of 0–0.45 V (vs. Ag/AgCl) at different scan rates ranging from 5 to 50 mV s^{-1}. The galvanostatic charge-discharge (GCD) measurements were performed at various current densities from 0.5 to 10 A g^{-1} and the electrochemical impedance spectroscopy (EIS) measurements were performed in the frequency range of 10 mHz to 100 kHz.

5. Results and discussion

5.1. Morphology and structure

Fig. 2(a) and (b) shows the XRD patterns of the Ni-FG substrate and CoOOH on the Ni-FG substrate and the corresponding JCPDS files. The XRD patterns show poor intensities diffraction peaks (the intensities are embedded in the signal noise level) of CoOOH at diffraction angles of 23.5, 45.5 and 59.5 relative to the high intensities diffraction peaks of the Ni-FG substrate marked with "∗" (Fig. 2(b)).

The XRD patterns of the Ni-FG substrate and CoOOH on the Ni-FG substrate shown in Fig. 2(a) and (b) were indexed using the graphite JCPDS card: 75-1621 (Sys: hexagonal, S.G.: *P*63*mc* (186), *a*: 2.470 Å, *c*: 6.790 Å), Ni JCPDS card: 04-0850 (Sys: cubic, S.G.: *Fm*3*m* (225), *a*: 3.523 Å) and CoOOH JCPDS card: 07-0169 (Sys: hexagonal, S.G.: *R*3*m* (166), *a*: 2.855 Å, *c*: 13.15 Å). The XRD data suggest that CoOOH synthesized on Ni-FG substrate has a hexagonal crystal structure similar to that of graphene.

Fig. 3(a) shows the Raman spectra of the CoOOH/Ni-FG and Ni-FG and the peaks observed at 1587 and 2701 cm^{-1} corresponds to the G-band and 2D-band modes of graphene and the other peaks to CoOOH compound. The absence (low-intensity) of the disorder-induced D-band at ~1350 cm^{-1} confirms the high-quality of graphene sheet [34–36]. The synthesized graphene sheet has a non-uniform thickness (varying between 1 to few graphene layers) over

Fig. 2. (a) and (b) XRD patterns of the Ni-FG substrate and CoOOH on the Ni-FG substrate and the corresponding JCPDS files.

Fig. 3. (a) Raman spectra of the CoOOH synthesized on the Ni-FG substrate (CoOOH/Ni-FG) and that of the graphene sheet on the Ni foam (Ni-FG). (b) Lorentz fittings of peaks at 506, 572, 632, 700, 1033, 1068 and 1165 cm^{-1} assigned to the CoOOH compound.

163

Fig. 4. (a–c) SEM images of the graphene on nickel foam at low to high magnifications and graphene shows wrinkles and ripples. (d–f) SEM images of the CoOOH on Ni foam graphene (CoOOH/Ni-FG) at low to high magnifications with CoOOH showing intersected nanosheets.

Fig. 5. (a) Secondary electron beam image showing area 1 and 2 from which the (b) EDX data of the CoOOH synthesized on the Ni-FG substrate (CoOOH/Ni-FG) was obtained which shows the presence of C, O, Al, Co and Ni in the sample.

the entire Ni foam since polycrystalline Ni typically grows multi-layer graphene sheets with varying thickness due to non-uniform precipitation of carbon atoms from different grains surfaces and grain boundaries [37–39]. Fig. 3(b) shows peaks of CoOOH compound as shown in Fig. 3(a) and the peaks were fitted with peaks at 506, 572, 632, 700, 1033, 1068 and 1165 cm^{-1} assigned to the CoOOH crystalline compound. These peaks positions correspond to the values published by Yang et al. [40] and Pauporté et al. [41] for Raman spectra of the CoOOH compound. Bands fittings

were done using a Lorentz function and the fittings were carried out until reproducible fitting was obtained with squared correlation, r^2 of 0.99.

Fig. 4(a–c) shows typical SEM images at different magnifications of graphene synthesized on the Ni foam substrate showing a porous structure. The SEM images at a high magnification show wrinkles and ripples of graphene sheets which could be attributed to differences in thermal expansion coefficients between graphene and Ni substrate [42]. Fig. 4(d–f) shows SEM images at different

magnification of CoOOH synthesized on the Ni-FG substrate (CoOOH/Ni-FG). The images at low and high magnifications show homogenous coating of well-ordered intersected nanosheets forming a porous structure.

Fig. 5(a) shows a secondary electron beam image showing area 1 and 2 from which the EDX data of the CoOOH/Ni-FG was obtained as shown in Fig. 5(b). Fig. 5(b) shows the presence of C, O, Al, Co and Ni in the sample. Similar to the study of Xu et al. [43] and Abushrenta et al. [44], a ratio of Co to Al concentration is high and that confirms a successful alkaline etching of the Al cations in CoAl-LDH nanosheets using a NaOH solution for 48 h to give CoOOH nanosheets.

5.2. Electrochemical characterization

Fig. 6(a) shows CV curves of Ni-F, Ni-FG, and CoOOH/Ni-FG at a scan rate of 50 mV s^{-1} in a potential range of 0.0–0.45 V. CV curves of these electrode materials showing existence of reduction and oxidation peaks. For instance, CV curves of both Ni-F and Ni-FG show peaks that corresponds to the transformation reaction between Ni(OH)$_2$ and NiOOH [45], CV curve of a CoOOH/Ni-FG electrode shows a distinct difference in the current response (showing much higher current response which indicates high capacitance) compared to Ni-F and Ni-FG electrodes at the same potential of 0.45 V, indicating a better electrochemical response. Consequently, further investigation of the capacitive properties of CoOOH/Ni-FG electrode was made. Fig. 6(b) shows the CV curves of the CoOOH/Ni-FG electrode at different scan rates between

5 mV s^{-1} and 50 mV s^{-1}, but in the same potential window. These curves show the redox peaks which could be mainly due to electrochemical surface reactions on the CoOOH material corresponding to cathodic and anodic peaks at $\sim$0.1 and $\sim$0.37 V vs. Ag/AgCl respectively. These redox peaks can be explained by the reversible electrochemical oxidation and reduction (redox reaction) between Co^{2+} and Co^{3+} expressed as [15,46]

$$CoOOH + OH^- \Longleftrightarrow CoO_2 + H_2O + e^- \qquad (1)$$

From this redox equation, a theoretical specific value of 1747.9 mA h g^{-1} in 6 M KOH electrolyte is deduced. In Fig. 6(b), it can be seen that as the scan rate increases, the anodic peak shifts positively whereas the cathodic peak shifts negatively and this shift is attributed to the polarization of the electrodes due to the electrolyte ions diffusion in the porous structure of the electrode during redox reaction at the higher scan rates. The shapes of the curves (showing reduction and oxidation peaks) indicate that the predominant mechanism of charge storage in this material is based on Faradic characteristics [15].

Fig. 6(c) shows the charge-discharge (CD) curves of CoOOH/ Ni-FG electrode at current densities of 0.5–10 A g^{-1} in the potential window range of 0.0–0.45 V. The curves clearly show two voltage steps, specifically, a fast potential drop in the range of 0.41– 0.24 V and a slow potential drop in the range of 0.24-0.14 V. Similar to CV curves, these voltage drop regions of charge-discharge curves (0.24-0.14 V) show Faradic behaviour of the electrode resulting from the electrochemical redox reaction at an interface between electrode and electrolyte [47]. From the CD

Fig. 6. (a) Cyclic voltammetry (CV) of Ni-F, Ni-FG and CoOOH /Ni-FG at a scan rate of 50 mV s^{-1}. (b) CV of CoOOH/Ni-FG at scan rates ranging from 5 to 30 mV s^{-1}. (c) Galvanostatic charge–discharge of CoOOH/Ni-FG at current densities of 0.5–10 A g^{-1}. (d) Specific capacity of CoOOH/Ni-FG composite electrode versus current densities.

165

independent constant with dimensions of $(F\,cm^{-2})^n$ related to the roughness and pseudocapacitive kinetics of the electrode surface, the values for n range from -1 to 1 and can be calculated from the slope of the log Z versus log f. For values of $n = 0$, Q acts as a pure resistor and for $n = 1$, Q acts as a pure capacitor and for $n = -1$, Q acts as an inductor [51]. Furthermore, at the low frequency region, an ideal electrode yields a vertical line parallel to the imaginary axis with a mass capacitance given by Q. The deviation from this ideal behaviour is attributed to the leakage resistance R_L which is connected in parallel to the C_L in the equivalent circuit. C_L denotes the pseudocapacitance which arises due to the Faradaic charge transfer process [49]. The n-value obtained from the fitting of the Nyquist plot for the CoOOH/Ni-FG electrode was 0.91. Therefore, the fitting results for n show a capacitive behaviour of the electrode. A summary of the CNLS fitting parameters from the experimental impedance spectra (Fig. 7(a)) is presented in Table 1.

The cycling stability of the CoOOH/Ni-FG electrode was investigated at 10 A g^{-1} for 1000 cycles, as shown in Fig. 7(b). The CoOOH/ Ni-FG electrode shows the specific capacity of 95 mA h g^{-1} at 10.0 A g^{-1} with 98% capacity retention after 1000 cycles. Nyquist plots (Fig. 7(c)) of the CoOOH/Ni-FG electrode before and after 1000 charge–discharge cycles shows similar curves, suggesting good electrochemical stability of the active material.

5.3. Morphology and structure after electrochemical analysis

The structure of the electrode material after electrochemical measurement is presented to elucidate any structural change or degradation that might have occurred during the cycling process. Fig. 8(a) and (b) shows the SEM images (low and high magnifications) of the CoOOH/Ni-FG after electrochemical analysis. These images show a porous structure of nanosheets as seen before electrochemical analysis (Fig. 4(e) and (f)), however, with an effect of electrolyte and this suggest a good stability in the morphology of CoOOH electrode material. It is worth mentioning that these SEM images were acquired using 1 kV beam and the working distance (WD) of 2.5 mm compare to those in Fig. 4 which were acquired using 2 kV beam and the WD of 2.7 mm. As a result, SEM images in Fig. 8(a) and (b) appear larger than those in Fig. 4(e) and (f).

Fig. 9(a) shows a secondary electron beam image showing area from which the EDX data of the CoOOH/Ni-FG after electrochemical analysis was obtained (see Fig. 9(b)). Fig. 9(b) shows the presence of C, O, Al, Co and Ni in the sample and additional elements due to electrochemical analysis. A high concentration of K confirms the presence or the effect of electrolyte (i.e. KOH) as seen in Fig. 9 (b) after electrochemical analysis. A ratio of Co to Al concentration is still high (as observed before electrochemical analysis in Fig. 5 and that confirms structural stability of CoOOH compound. This is further supported by Raman spectra obtained before and after electrochemical analysis which shows similar spectra confirming a good stability in the structure of the CoOOH electrode material and the underlying graphene sheet (see Fig. 10(a)). In order to compare our results with other cobalt-based faradic materials, we recalculated the specific capacity from the estimated discharge time and current density from the articles that are being referred to in Fig. 10(b) in order to report the realistic values as suggested by Laheäär et al. [52]. Fig. 10(b) presents a comparison of specific

Fig. 8. (a) and (b) SEM images (low and high magnifications) of the CoOOH on Ni foam graphene (CoOOH/Ni-FG) after electrochemical analysis showing CoOOH intersected nanosheets covered with dried electrolyte which also filled the space between sheets (porous structure). These SEM images were acquired using 1 kV beam and the working distance of WD = 2.5 mm.

Fig. 9. (a) and (b) SEM image and EDX spectrum (from the region indicated by the yellow square in (a)) respectively of the CoOOH on Ni foam graphene (CoOOH/Ni-FG) after electrochemical analysis.

166

Fig. 10. (a) Raman spectra of the CoOOH synthesized on the Ni-FG substrate (CoOOH/Ni-FG) before and after electrochemical analysis. (b) A comparison of specific capacity at a current density of 0.5, 1.0 and 2.0 A g^{-1} obtained in this work and other previous published reports by Deng et al. [32], Zhu et al. [9], Nguyen et al. [10], Zhao et al. [30], Ghosh et al. [52] and SengáTan and MingáLi [12].

capacity at a current densities from 0.5 to 2.0 A g^{-1} obtained in this work and other previous published reports by Deng et al. [32], Zhu et al. [9], Nguyen et al. [10], Zhao et al. [30], Ghosh et al. [53] and SengáTan and MingáLi [12]. Our results are superior to the previously published Co-based electrode materials for supercapacitor applications.

6. Conclusion

The morphology of the synthesized CoOOH on the Ni-FG substrate showed a homogenous coating of well-ordered intersected nanosheets showing porous structure. The morphology of synthesized graphene sheet on the Ni foam showed wrinkles and ripples of graphene which retained the advantages of homogeneous adsorption and distribution of CoOOH intersected nanosheets on Ni-FG substrate. The morphology and structural analysis confirmed elemental composition and crystalline structure of the CoOOH compound before and after electrochemical analysis of the electrode. The electrochemical behaviour indicated that the CoOOH/Ni-FG electrode is a good Faradic electrode material exhibiting a high specific discharge capacity of 199 mA h g^{-1} at 0.5 A g^{-1} with a capacity retention of 98% after 1000 cycles. These results suggest that the CooOH/Ni-FG electrode material has great potential as a high capacity device and is further expected to contribute significantly to the ongoing scientific reports on Faradaic electrode materials for electrochemical applications.

Acknowledgements

References

[1] M. Winter, R.J. Brodd, What are batteries, fuel cells, and supercapacitors?, Chem Rev. 104 (2004) 4245–4270.
[2] A. Burke, Ultracapacitors: why, how, and where is the technology, J. Power Sources 91 (2000) 37–50.
[3] J.R. Miller, P. Simon, Fundamentals of electrochemical capacitor design and operation, Electrochem. Soc. Interf. c (2008) 31–32.
[4] K. Chen, D. Xue, Materials chemistry toward electrochemical energy storage, J. Mater. Chem. A 4 (2016) 7522–7537.
[5] J. Yan, T. Wei, W. Qiao, B. Shao, Q. Zhao, L. Zhang, et al., Rapid microwave-assisted synthesis of graphene nanosheet/Co₃O₄ composite for supercapacitors, Electrochim. Acta 55 (2010) 6973–6978.
[6] A.S. Arico, P. Bruce, B. Scrosati, J.-M. Tarascon, W. van Schalkwijk, Nanostructured materials for advanced energy conversion and storage devices, Nat. Mater. 4 (2005) 366–377.
[7] H. Wang, H.S. Casalongue, Y. Liang, H. Dai, Ni(OH)₂ nanoplates grown on graphene as advanced electrochemical pseudocapacitor materials, J. Am. Chem. Soc. 132 (2010) 7472–7477.
[8] J. Deng, L. Kang, G. Bai, Y. Li, P. Li, X. Liu, et al., Solution combustion synthesis of cobalt oxides (Co₃O₄ and Co₃O₄/CoO) nanoparticles as supercapacitor electrode materials, Electrochim. Acta 132 (2014) 127–135.
[9] Y.G. Zhu, Y. Wang, Y. Shi, Z.X. Huang, L. Fu, H.Y. Yang, Phase transformation induced capacitance activation for 3D graphene-CoO nanorod pseudocapacitor, Adv. Energy Mater. 4 (2014) 1301788.
[10] T.T. Nguyen, R.K. Deivasigamani, D. Kharismadewi, Y. Iwai, J.-J. Shim, et al., Facile synthesis of cobalt oxide/reduced graphene oxide composites for electrochemical capacitor and sensor applications, Solid State Sci. 53 (2016) 71–77.
[11] M.Q. Zhao, Q. Zhang, J.Q. Huang, F. Wei, Hierarchical nanocomposites derived from nanocarbons and layered double hydroxides - properties, synthesis, and applications, Adv. Funct. Mater. 22 (2012) 675–694.
[12] K. SengáTan, C. MingáLi, et al., Fabrication of Co₃O₄-reduced graphene oxide scrolls for high-performance supercapacitor electrodes, Phys. Chem. Chem. Phys. 13 (2011) 14462–14465.
[13] K. Chen, C. Sun, D. Xue, Morphology engineering of high performance binary oxide electrodes, Phys. Chem. Chem. Phys. 17 (2015) 732–750.
[14] P. Lu, F. Liu, D. Xue, H. Yang, Y. Liu, Phase selective route to Ni(OH)₂ with enhanced supercapacitance: performance dependent hydrolysis of Ni(Ac)₂ at hydrothermal conditions, Electrochim. Acta 78 (2012) 1–10.
[15] L. Zhu, W. Wu, Y. Zhu, W. Tang, Y. Wu, Composite of CoOOH nanoplates with multiwalled carbon nanotubes as superior cathode material for supercapacitors, J. Phys. Chem. C 119 (2015) 7069–7075.
[16] A.D. Jagadale, D.P. Dubal, C.D. Lokhande, Electrochemical behavior of potentiodynamically deposited cobalt oxyhydroxide (CoOOH) thin films for supercapacitor application, Mater. Res. Bull. 47 (2012) 672–676.
[17] M. Wang, W. Ren, Y. Zhao, H. Cui, Synthesis of nanostructured CoOOH film with high electrochemical performance for application in supercapacitor, J. Nanoparticle Res. 16 (2014) 1–7.
[18] A. Davies, A. Yu, Material advancements in supercapacitors: from activated carbon to carbon nanotube and graphene, Can. J. Chem. Eng. 89 (2011) 1342–1357.
[19] D. Antiohos, M. Romano, J. Chen, J.M. Razal, Carbon nanotubes for energy applications. http://dx.doi.org/10.5772/51784.
[20] M. Zhi, C. Xiang, J. Li, M. Li, N. Wu, Nanostructured carbon-metal oxide composite electrodes for supercapacitors: review, Nanoscale 5 (2012) 72–88.
[21] H. Jiang, J. Ma, C. Li, Mesoporous carbon incorporated metal oxide nanomaterials as supercapacitor electrodes, Adv. Mater. 24 (2012) 4197–4202.
[22] K. Chen, D. Xue, In-situ electrochemical route to aerogel electrode materials of graphene and hexagonal CeO₂, J. Colloid Interface Sci. 446 (2015) 77–83.
[23] Z. Yang, S. Chabi, Y. Xia, Y. Zhu, Preparation of 3D graphene-based architectures and their applications in supercapacitors, Prog. Nat. Sci. Mater. Int. 25 (2015) 1–9.
[24] X. Fan, X. Chen, L. Dai, 3D graphene based materials for energy storage, Curr. Opin. Colloid Interface Sci. 20 (2015) 429–438.

167

[25] A. Bello, K. Makgopa, M. Fabiane, D. Dodoo-Ahrin, K.I. Ozoemena, N. Manyala, Chemical adsorption of NiO nanostructures on nickel foam-graphene for supercapacitor applications, J. Mater. Sci. 48 (2013) 6707–6712.
[26] M.T. Pettes, H. Ji, R.S. Ruoff, L. Shi, Thermal transport in three-dimensional foam architectures of few-layer graphene and ultrathin graphite, Nano Lett. 12 (2012) 2959–2964.
[27] K. Chen, D. Xue, Rare earth and transitional metal colloidal supercapacitors, Sci. China Technol. Sci. 58 (2015) 1768–1778.
[28] K. Chen, Y. Yang, K. Li, Z. Ma, Y. Zhou, D. Xue, CoCl₂ designed as excellent pseudocapacitor electrode materials, ACS Sust. Chem. Eng. 2 (2013) 440–444.
[29] X.C. Dong, H. Xu, X.W. Wang, Y.X. Huang, M.B. Chan-Park, H. Zhang, et al., 3D graphene-cobalt oxide electrode for high-performance supercapacitor and enzymeless glucose detection, ACS Nano 6 (2012) 3206–3213.
[30] C. Zhao, X. Wang, S. Wang, Y. Wang, Y. Zhao, W. Zheng, Synthesis of Co(OH)₂/graphene/Ni foam nano-electrodes with excellent pseudocapacitive behavior and high cycling stability for supercapacitors, Int. J. Hydrogen Energy. 37 (2012) 11846–11852.
[31] J.-J. Shim et al., The 3DCo₃O₄/graphene/nickel foam electrode with enhanced electrochemical performance for supercapacitors, Mater. Lett. 139 (2015) 377–381.
[32] W. Deng, Y. Sun, Q. Su, E. Xie, W. Lan, Porous CoO nanobundles composited with 3D graphene foams for supercapacitors electrodes, Mater. Lett. 137 (2014) 124–127.
[33] Z. Lu, W. Zhu, X. Lei, G.R. Williams, D. O'Hare, Z. Chang, et al., High pseudocapacitive cobalt carbonate hydroxide films derived from CoAl layered double hydroxides, Nanoscale 4 (2012) 3640.
[34] L.M. Malard, M.a. Pimenta, G. Dresselhaus, M.S. Dresselhaus, Raman spectroscopy in graphene, Phys. Rep. 473 (2009) 51–87.
[35] A.C. Ferrari, J.C. Meyer, V. Scardaci, C. Casiraghi, M. Lazzeri, F. Mauri, et al., Raman spectrum of graphene and graphene layers, Phys. Rev. Lett. 97 (2006) 187401.
[36] M.J. Madito, A. Bello, J.K. Dangbegnon, C.J. Oliphant, W.A. Jordaan, T.M. Masikhwa, et al., Raman analysis of bilayer graphene film prepared on commercial Cu(0.5 at% Ni) foil, J. Raman Spectroc. 47 (2016) 553–559.
[37] A. Reina, S. Thiele, X. Jia, S. Bhaviripudi, M.S. Dresselhaus, J.A. Schaefer, et al., Growth of large-area single- and Bi-layer graphene by controlled carbon precipitation on polycrystalline Ni surfaces, Nano Res. 2 (2009) 509–516.
[38] W. Liu, S. Kraemer, D. Sarkar, H. Li, P.M. Ajayan, K. Banerjee, Controllable and rapid synthesis of high-quality and large-area bernal stacked bilayer graphene using chemical vapor deposition, Chem. Mater. 26 (2014) 907–915.
[39] N. Liu, L. Fu, B. Dai, K. Yan, X. Liu, R. Zhao, et al., Universal segregation growth approach to wafer-size graphene from non-noble metals, Nano Lett. 11 (2011) 297–303.
[40] J. Yang, H. Liu, W.N. Martens, R.L. Frost, Synthesis and characterization of cobalt hydroxide, cobalt oxyhydroxide, and cobalt oxide nanodiscs, J. Phys. Chem. C 114 (2010) 111–119.
[41] T. Pauporté, L. Mendoza, M. Cassir, M.C. Bernard, J. Chivot, Direct low-temperature deposition of crystallized CoOOH films by potentiostatic electrolysis, J. Electrochem. Soc. 152 (2005) C49, http://dx.doi.org/10.1149/1.1842044.
[42] C. Mattevi, H. Kim, M. Chhowalla, A review of chemical vapour deposition of graphene on copper, J. Mater. Chem. 21 (2011) 3324.
[43] T. Xu, X. Wu, Y. Li, W. Xu, Z. Lu, Y. Li, et al., Morphology and phase evolution of CoAl layered double hydroxides in an alkaline environment with enhanced pseudocapacitive performance, ChemElectroChem 2 (2015) 679–683.
[44] N. Abushrenta, X. Wu, J. Wang, J. Liu, X. Sun, Hierarchical co-based porous layered double hydroxide arrays derived via alkali etching for high-performance supercapacitors, Sci. Rep. 5 (2015) 13082.
[45] L. Zhang, J. Wang, J. Zhu, X. Zhang, K. San Hui, K.N. Hui, 3D porous layered double hydroxides grown on graphene as advanced electrochemical pseudocapacitive materials, J. Mater. Chem. A 1 (2013) 9046–9053.
[46] K.K. Lee, W.S. Chin, C.H. Sow, Cobalt-based compounds and composites as electrode materials for high-performance electrochemical capacitors, J. Mater. Chem. A 2 (2014) 17212–17248.
[47] D.-D. Zhao, S.-J. Bao, W.-J. Zhou, H.-L. Li, Preparation of hexagonal nanoporous nickel hydroxide film and its application for electrochemical capacitor, Electrochem. Commun. 9 (2007) 869–874.
[48] T.M. Masikhwa, J.K. Dangbegnon, A. Bello, M.J. Madito, D. Momodu, N. Manyala, Preparation and electrochemical investigation of the cobalt hydroxide carbonate/activated carbon nanocomposite for supercapacitor applications, J. Phys. Chem. Solids 88 (2016) 60–67.
[49] Y. Zhou, H. Xu, N. Lachman, M. Ghaffari, S. Wu, Y. Liu, et al., Advanced asymmetric supercapacitor based on conducting polymer and aligned carbon nanotubes with controlled nanomorphology, Nano Energy 9 (2014) 176–185.
[50] F. Tao, Y.Q. Zhao, G.Q. Zhang, H.L. Li, Electrochemical characterization on cobalt sulfide for electrochemical supercapacitors, Electrochem. Commun. 9 (2007) 1282–1287.
[51] B.E. Conway, Electrochemical Supercapacitors: Scientific Fundamentals and Technological Applications, Kluwer Academic/ Plenum, New York, 1999.
[52] A. Laheäär, P. Przygocki, Q. Abbas, F. Béguin, Appropriate methods for evaluating the efficiency and capacitive behavior of different types of supercapacitors, Electrochem. Commun. 60 (2015) 21–25.
[53] D. Ghosh, S. Giri, C.K. Das, Preparation of CTAB-assisted hexagonal platelet Co(OH)₂/graphene hybrid composite as efficient supercapacitor electrode material, ACS Sust. Chem. Eng. 1 (2013) 1135–1142.

4.4.3   Conclude Remarks

The morphology of the synthesized CoOOH on the Ni-FG substrate showed a homogenous coating of well-ordered intersected nanosheets showing porous structure. The morphology of synthesized graphene sheet on the Ni foam showed wrinkles and ripples of graphene which retained the advantages of homogeneous adsorption and distribution of CoOOH intersected nanosheets on Ni-FG substrate. The morphology and structural analysis confirmed elemental composition and crystalline structure of the CoOOH compound before and after electrochemical analysis of the electrode. The electrochemical behavior indicated that the CoOOH/Ni-FG electrode is a good Faradic electrode material exhibiting a high specific discharge capacity of 199 mAh g^{-1} at a current density of 0.5 A g^{-1}. In addition ,the supercapacitor also exhibit good cycle stability with a 98 % capacity retention after 1000 cycles. These results suggest that the CooOH/Ni-FG electrode material has great potential as

a high capacitiy device and is further expected to contribute significantly to the ongoing scientific reports on Faradaic electrode materials for electrochemical applications.

4.5 Asymmetric Supercapacitor Based on VS$_2$ Nanosheets and Activated Carbon Materials.

4.5.1 Introduction

As much as we considered the cobalt based faradic materials for electrochemical capacitor applications because of their excellent redox reaction of which making hybrid materials with EDLC materials was found to be the best way of improving electrochemical performance, we then extended our work to include the transition metal chalcogenides. The main reason to consider these faradic materials was that they have similar 2D structure like graphene but still suffer low electrical conductivity and poor electrochemical stability because of redox reaction. Hence like other faradic materials their composite with carbon materials like graphene should be able to improve their electrical conductivity, electrochemical stability and prevent restacking so that a large surface area can be realized. In this study we considered the VS$_2$ nanomaterial that was synthesized through solvothermal approach as cathode and AEG as anode materials respectively for asymmetric supercapacitor for the same reason that this kind of approach has a potential of increasing the energy density of the supercapacitor. Vanadium sulphides have been investigated as low-cost electroactive material ,with good mechanical properties and high electrochemical performance [11,12].

4.5.2 Results and Discussion

The results obtained from this work are presented in detail in the paper below.

CrossMark
click for updates

Asymmetric supercapacitor based on VS$_2$ nanosheets and activated carbon materials

Tshifhiwa M. Masikhwa, Farshad Barzegar, Julien K. Dangbegnon, Abdulhakeem Bello, Moshawe J. Madito, Damilola Momodu and Ncholu Manyala*

An asymmetric supercapacitor was fabricated using VS$_2$ nanosheets as the positive electrode and activated carbon (AC) as the negative electrode, with a 6 M KOH solution as electrolyte. These materials were combined to maximize the specific capacitance and enlarge the potential window, therefore improving the energy density of the device. A specific capacitance of 155 F g^{-1} at 1 A g^{-1} with a maximum energy density as high as 42 W h kg^{-1} and a power density of 700 W kg^{-1} was obtained for the asymmetric supercapacitor within the voltage range of 0–1.4 V. The supercapacitor also exhibited good stability, with ~99% capacitance retention and no capacitance loss after 5000 cycles at a current density of 2 A g^{-1}.

Introduction

Recently, supercapacitors, which are advanced electrochemical energy storage systems, have been a hot topic due to their numerous advantages in power source applications such as short-term power sources for mobile electronic devices and auxiliary power sources for hybrid electric vehicles (HEV).[1–3] Supercapacitors, also known as ultracapacitors or electrochemical capacitors, are energy storage devices that exhibit high power density but relatively low energy density as compared to rechargeable batteries. Thus, there has been a massive focus by researchers to improve on supercapacitor technology in order to enhance the energy density to at least the level of rechargeable battery systems. Besides high power density, supercapacitors also show excellent properties such as long cycle life, rapid energy delivery and long stability as compared to rechargeable batteries. The performance of supercapacitors depends, to a large extent, on the nature of the electrode material.[4,5]

Typically, supercapacitors are categorized into three types based on their charge-storage mechanism, namely, the electrical double-layer capacitors (EDLCs) and the faradaic and hybrid capacitors.[2] The storage mechanism in EDLCs arises from the accumulation of charges at the electrode/electrolyte interface that results in a non-faradaic reaction, whereas the faradaic storage mechanism results from the fast redox reaction (faradaic reaction).[6]

Hybrid capacitors are obtained from either making composites of two materials with different charge storage mechanisms, or using the two materials as positive and negative electrodes to form an asymmetric cell. An example could be

the use of an EDLC-type material as negative electrode and a faradaic-type material as positive electrode. This offers the possibility of synergizing the advantages of both electrodes, such as the high electrical conductivity and stability of EDLC materials and the high specific capacitance of faradic or pseudo-capacitance materials. The properties of the resulting hybrid device lie between those of a supercapacitor and a battery.[7] Asymmetric supercapacitors are a special type of hybrid capacitors obtained by mounting an EDLC carbon material electrode with a faradaic-type material electrode in order to increase the energy density by utilizing the resulting wide operating voltage window. This should not be detrimental to the cyclic stability attributed to carbon-based materials and the excellent power density from the higher capacitance of the faradaic-type material.[7–10]

Carbon-based nanomaterials, such as activated carbon (AC), carbon nanotubes (CNTs), and graphene,[11–15] are frequently used as the negative electrodes of asymmetric supercapacitors due to their stability in the negative potential region, good electronic conductivity, large surface area and relatively low cost.[16–18] Activated carbon (AC) is the most suitable negative electrode material that has been adopted for hybrid capacitors, not only due to the numerous merits listed above but also its facile preparation process.[19,20]

Various transition metal oxides and conductive polymers[21–25] are mostly used as positive electrodes due to their fast and reversible electron-exchange reactions at the electrode interface, which contribute to the high power densities and high capacitance of asymmetric supercapacitors.[26–34]

In recent years, metal chalcogenide materials have been considered for electrochemical energy storage applications due to their diverse chemical and physical properties.[35] For example, two-dimensional (2D) layered transition-metal dichalcogenides (TMDs) such as MoS$_2$, CoS$_2$, VS$_2$ and NiS$_2$ have been extensively

Department of Physics, Institute of Applied Materials, SARCHI Chair in Carbon Technology and Materials, University of Pretoria, Pretoria 0028, South Africa. E-mail: ncholu.manyala@up.ac.za; Fax: +27 (0)12 420 2516; Tel: +27 (0)12 420 3549

170

Paper

studied for applications in electrochemical supercapacitors due to their promising electrochemical performance.[36–38] Numerous studies involving vanadium sulfides have been reported for various applications.[37,39–42] Pandurangan *et al.* reported the synthesis of VS_2/rGO nanosheets by an rGO-assisted phase transformation *via* annealing of VS_4/rGO sheets at 350 °C for the electrocatalysis of hydrogen evolution reaction.[43] Similarly, Satyajit *et al.* also provided a detailed study of VS_4/rGO sheets synthesized by a facile, one-step hydrothermal route and with the enhanced supercapacitor performance of VS_4/rGO.[39] The experimental results were further confirmed by computational simulations to further provide useful insights into the design of efficient energy storage devices. However, there have been little or no reports on the fabrication of an asymmetric capacitor with activated carbon from polymer-based materials as the anode and VS_2 as the cathode in an aqueous electrolyte.

In this work, we report on the design of an asymmetric capacitor based on 3D interconnected activated carbon as negative electrode and mesoporous VS_2 nanosheets as positive electrode material. The hybrid material showed high rate capability compared with a pure VS_2 nanosheet electrode. The VS_2//AC asymmetric supercapacitor performed reversibly at a high cell voltage of 1.4 V in 6 M KOH. It exhibited a specific capacitance of 155 F g^{-1} at 1 A g^{-1} with a maximum energy density as high as 42 W h kg^{-1} and a power density of 700 W kg^{-1}. Furthermore, the supercapacitor also exhibited good stability with ~99% capacitance retention and no capacitance loss after 5000 cycles at a current density of 2 A g^{-1}.

Experimental

Materials

Ammonium vanadate (NH_4VO_3, purity > 99.99%), thioacetamide (CH_3CSNH_2, Sigma-Aldrich, ≥ 99%), ammonia (NH_3, ≥ 99.95%) and polyvinyl alcohol (PVA, 99+% hydrolyzed) were purchased from Sigma-Aldrich. Nickel foam was purchased from Alantum (Munich, Germany); potassium hydroxide (KOH, min 85%) and urea (purity ≥ 98%) were purchased from Merck (South Africa).

Synthesis of VS_2 nanosheets

Scheme 1 shows the schematic method used to prepare the VS_2 nanosheets in this study. Ammonium metavanadate (NH_4VO_3, 2 mmol) was added to an 18 ml mixture of 15 ml deionized

water and 3 ml ammonia, accompanied by vigorous stirring to completely dissolve the ammonium vanadate. Subsequently, thioacetamide (CH_3CSNH_2, 10 mmol) was added to the above solution under vigorous stirring. The final homogeneous solution was transferred into a sealed, Teflon-lined, stainless-steel autoclave and kept at a temperature of 180 °C for 20 h. After cooling to room temperature, the black powder was washed with deionized water and dried at 60 °C. The formation of the nanosheet morphology of the VS_2 electrode includes two steps: an initial nucleating stage and a crystal growth stage including an Ostwald ripening process, which is known for the development of nanosheet metal sulfide structures.[44] In the early stage, various functional groups present in the reaction vessel such as $-NH_2$, $-COOH$, and $-SH$ react with V^{4+} ions to form V–S complexes, which then decay to form VS_2 nuclei in the last stage of the synthesis mechanism.[45] In the second stage, nanosheet structures form as a result of the Ostwald ripening and self-assembly of the VS_2 sheets. Throughout the reaction, the hydrolysis of thioacetamide produces HS^-, which decreases V^{5+} to V^{4+}, and layered VS_2 structures are formed.[46]

Synthesis of activated carbon

Activated carbon used for the production of the composite materials was prepared as reported in our earlier work.[47,48] Briefly, graphene foam (GF) and polyvinyl alcohol (PVA) were used as starting material for the production of a hydrogel, which was then used to produce porous carbon materials after the activation process. The activated material was neutralized with 0.1 M HCl, washed with deionised water and dried at 120 °C for 12 h, after which samples were characterized.

Structure and morphology characterization

The morphology of the prepared VS_2 and activated carbon electrodes was studied using the high-resolution Zeiss Ultra Plus 55 field emission scanning electron microscope (FE-SEM) operated at 2.0 kV. Energy-dispersive X-ray (EDX) patterns were taken with a JEOL 5800LV microscope equipped with an energy-dispersive X-ray spectrometer operated at 20 kV, and they were used to estimate the elemental composition of the produced materials. Transmission electron microscopy (TEM) micro-images and selected area electron diffraction (SAED) observations were carried out with a JEOL JEM-2100F microscope operated at 200 kV (Akishima-shi, Japan). X-ray diffraction (XRD) patterns of the prepared

Scheme 1 Preparation procedure of VS_2 nanosheets.

171

Fig. 1   X-ray diffraction of (a) VS_2 and (b) AC electrodes.

materials were collected using an XPERT-PRO diffractometer (PANalytical BV, Netherlands) with theta/2theta geometry, operating with a cobalt tube at 50 kV and 30 mA and with reflection geometry at 2θ values ranging from 30–90° with a step size of 0.01°. The Raman spectra were recorded using a WITEC-Alpha 300R Plus confocal Raman spectrometer (WITEC GmbH, Ulm, Germany) with a 532 nm laser. X-ray photoelectron spectroscopy (XPS, K-alpha, Thermo Fisher) with monochromatic Al Kα radiation as the X-ray source was used to irradiate the sample surface and determine the chemistry of the samples synthesized in powder form. Nitrogen adsorption–desorption isotherms were measured at −196 °C using a Micromeritics ASAP 2020. All the samples were degassed at 180 °C for more than 12 h under vacuum conditions. The surface area was calculated by the Brunauer–Emmett–Teller (BET) method from the adsorption branch in the relative pressure range (P/P_0) of 0.01–1.

Electrode preparation and electrochemical characterization

All electrochemical measurements were carried out using a Biologic VMP-300 potentiostat (Knoxville, TN, USA) controlled by the EC-Lab® V10.37 software. Three-electrode measurements were performed for both AC and VS_2 serving as the working electrodes, Ag/AgCl (3 M KCl) serving as the reference electrode and glassy carbon plate as the counter electrode. The negative electrode was prepared by mixing the active material of activated carbon (AC) with polyvinylidene fluoride (PVDF) binder in

a weight ratio of 9 : 1, which was then homogenized and dispersed in N-methylpyrrolidone (NMP) solution. The slurry was then uniformly pasted on a nickel foam current collector and dried at 60 °C in an oven for 8 h to ensure complete evaporation of the NMP. The positive electrode was prepared by mixing the active material (VS_2), carbon black (CB) and polyvinylidene fluoride (PVDF) binder, which helped to improve the conductivity of material, in a weight ratio of 8 : 1 : 1 and then dispersing in N-methylpyrrolidone (NMP) solution. The slurry was then uniformly pasted on a nickel foam current collector and dried at 60 °C in an oven for 8 h.

The electrochemical test of the asymmetric cell was carried out in a two-electrode cell configuration by means of coin-type cells with thickness of 0.2 mm and diameter of 16 mm, using a glass micro-fibre filter paper as the separator in a 6 M KOH aqueous electrolyte solution. The mass loading of VS_2 (positive electrode) was within 2–3 mg and that of AC (negative electrode) within 6–9 mg.

Results and discussion

Fig. 1(a) shows the XRD patterns of the VS_2 powder sample. The wavelength used for the XRD analysis was the 1.7890 Å line of a Co-K_α source. All diffraction peaks designated in the figure correspond to the pure hexagonal phase of VS_2 (JCPDS 36-1139) with lattice constants of $a = b = 0.322$ Å and $c = 0.576$ Å. The XRD data suggest that VS_2 preferentially grows in the (001) low-index crystallographic direction, hence leading to nanosheet formation.

Fig. 2   Raman pattern of (a) VS_2 and (b) AC electrodes, respectively.

172

Fig. 3 Low- and high-magnification SEM images of (a) and (b) VS_2, (c) and (d) AC electrodes.

Fig. 1(b) presents the XRD patterns of AC powder. The wavelength used for the XRD analysis was Cu-Kα, 1.5405 Å. All the peaks are identified to those of graphite (COD: 96-900-8570), which crystallizes in the hexagonal structure with space group $P6_3mc$(186), and lattice parameters $a = 2.4560$ Å and $c = 6.6960$ Å.[48]

Fig. 2(a) shows the Raman spectrum of the VS_2 electrode. The characteristic peak positions of 278 cm^{-1} and 404 cm^{-1} due to the in-plane E_{2g}^1 and the out-of-plane A_{1g} vibration modes show the presence of VS_2.[49] The A_{1g} mode was due to the out-of-plane vibration of only the S atoms in opposite directions, while the

Fig. 4 (a) HRTEM image of VS_2 nanosheets with the inset to the figure showing d spacing (upper), (b) SAED pattern of VS_2 nanosheets, and (c) TEM image of the AC sample.

173

Fig. 5 EDX pattern of (a) VS_2 and (b) AC electrodes.

in-plane E_{2g}^1 mode formed from the opposite vibration of the two S atoms with respect to the V atom.[49]

Fig. 2(b) shows two prominent D and G peaks, signifying that the produced AC is composed of highly disordered graphitic structures. It shows two distinct peaks at 1344 cm^{-1} (D-band) and 1603 cm^{-1} (G-band). These bands correspond to the disordered carbon/structural defects and graphitic layers (sp^2-bonded carbon atoms) of the carbon material.[50] The intensity ratio of the D-band to that of G-band ($R = I_D/I_G$) is 0.8, and this shows a low degree of graphitic crystalline structure.[51]

Fig. 3(a) and (b) show the low- and high-magnification SEM micrographs of the VS_2 sample. It can be seen from the figure that the sample is composed of a large number of nanosheets. Fig. 3(c) and (d) present the low and high magnification SEM of the AC sample. As observed in the micrograph, the sample is composed of large, interconnected macropores that provide a large ion-accessible surface for fast ion transport in high-performance supercapacitors.[48]

The high-resolution TEM (HRTEM) image of the VS_2 nano-sheets in Fig. 4(a) shows layered VS_2 sheets with an interlayer

Fig. 6 (a) VS_2 XPS survey spectra and high-resolution scans of (b) V 2p and (c) S 2p.

174

Paper

spacing of 0.26 nm (upper inset to the figure), which corresponds to the (001) plane of the hexagonal phase of VS_2. Fig. 4(b) shows the selected area electron diffraction (SAED) pattern of a single nanosheet, which is well indexed to the single-crystalline hexagonal phase of VS_2. Fig. 4(c) shows the TEM image of activated carbon with large particles.

The corresponding EDX pattern in Fig. 5(a) confirms that the synthesized VS_2 composite is composed of the elements vanadium and sulfur in the sample.

Fig. 5(b) confirms that activated carbon is composed of carbon. The element Al is present due to signals from the copper grid used as a sample holder for microscopy.

The chemical composition of VS_2 was also confirmed by XPS, as shown in Fig. 6. Before ion sputtering, C, O, V and S elements are detected in the survey; however, after ion sputtering for 30 minutes, only V and S elements are detected, which suggests that the appearance of C and O in the initial survey could be due to surface-adsorbed CO_2 and O_2 (see Fig. 6(a)). Fig. 6(b) and (c) show high-resolution scans of V 2p and S 2p, respectively. The energy positions of the V-peaks, which correspond to 513.5 eV and 521.1 eV (V $2p_{3/2}$ and V $2p_{1/2}$), indicate a V valence of +4.[52,53] The S peaks corresponding to S 2p at 161.4 eV energy are comprised by S $2p_{1/2}$ (160.5 eV) and S $2p_{3/2}$ (161.9 eV) peaks, which are orbitals of divalent sulfide ions. Therefore, the survey after ion sputtering (showing only V and S elements) corresponds to a pure VS_2 phase.

Fig. 7(a) and (b) represent the BET results from the surface area and porosimetry analysis carried out on the VS_2 and the AC samples, respectively. The nitrogen adsorption–desorption isotherm of VS_2 shows a type III behaviour with H3 hysteresis isotherm (Fig. 4(a)), indicating a weak interaction between the N_2 adsorbent and the material. On the other hand, the N_2 adsorption–desorption isotherm of the AC (Fig. 4(b)) presents a typical type I adsorption–desorption that characterizes complex materials containing micropores. The samples have a corresponding specific surface area (SSA) of 5.5 m^2 g^{-1} and 1040 m^2 g^{-1} for the VS_2 and AC samples, respectively. In addition, the nature of the pore structure present in the VS_2 nanosheets are mainly mesoporous with a broad pore size distribution of 2–7 nm (inset to Fig. 7(a)), while a microporous structure is recorded in the AC samples with an average pore size of 2.7 nm (inset to Fig. 7(b)).

Electrochemical performance of VS_2 nanosheets and activated carbon

To evaluate the potential of the electrode materials for supercapacitor applications, the individual electrochemical properties of the VS_2 and AC electrodes were firstly studied in a three-electrode system using 6 M KOH electrolyte. Cyclic voltammetry (CV), chronopotentiometry (CD) and electrochemical impedance spectroscopy (EIS) measurements were carried out for both samples. Fig. 8(a) shows the CV curves of the VS_2 electrode at scan rates of 5, 10, 20, 50 and 100 mV s^{-1}, respectively. A pair of redox peaks corresponding to the anodic peak at ~0.25 V and cathodic peak at ~0.34 V is visible in all the CV curves, revealing distinct faradic characteristics. Therefore, the anodic peak is due to the oxidation of V^{3+} to V^{4+}, whereas the cathodic peak is due to the reverse process. With an increase in scan rates, the small shifts in both cathodic and anodic peak potentials are considered to have a direct relationship with the internal resistance of the electrode, indicating that the fast redox reactions occur at the electroactive material/electrolyte interface. Fig. 8(b) shows the CV curves of the AC electrode at various scan rates ranging from 5 to 100 mV s^{-1}. These CV curves show relatively rectangular shapes without redox peaks, which is a typical electric double-layer capacitive sample behaviour.

Fig. 8(c) shows the galvanostatic charge/discharge curves of the VS_2 electrode at different current densities within a potential range of 0–0.5 V. Each discharge curve includes two clear voltage steps: a fast potential drop from 0.50 V to 0.35 V and a voltage plateau from 0.35 V to 0.22 V. The voltage plateau at around 0.3 V suggests a typical faradic characteristic that is in good agreement with the CV curves reported in Fig. 8(a). Fig. 8(d) shows the galvanostatic charge/discharge curves of the AC electrode at different current densities within a potential range of −0.8 to 0.0 V. As can be seen from Fig. 8(d), the shapes of the charge and discharge curves are very similar to each other and show a typical electric double-layer capacitive property, characterized by a nearly symmetrical triangular shape. This is in agreement with the results from CV curves in Fig. 8(b). Based on the galvanostatic charge–discharge (CD) curves, the specific capacitance of the VS_2 and AC electrodes were calculated using eqn (1):

Fig. 7 The N_2 adsorption–desorption isotherm of the (a) VS_2 nanosheets and (b) AC, insets show pore size distribution.

175

Fig. 8 Cyclic voltammetry at scan rates of 5–100 mV s^{-1} for (a) VS$_2$ and (b) AC electrodes; galvanostatic charge–discharge at current densities of 1–15 A g^{-1} for (c) VS$_2$ and (d) AC electrodes; (e) specific capacitance *versus* current densities of the VS$_2$ and AC electrodes.

$$C_m = \frac{I \times t}{m \times \Delta V} \qquad (1)$$

where I is the discharge current (A), t is the discharge time (s), m is the mass of active material (g), ΔV is the potential range of discharge (V), and C_m is the specific capacitance (F g^{-1}). The specific capacitance of VS$_2$ and AC electrodes was calculated at different current densities, and the plot of the specific capacitance (F g^{-1}) of the VS$_4$ nanosheets and AC electrodes as a function of current density (A g^{-1}) is shown in Fig. 8(e). The good performance of VS$_2$ nanosheets can be attributed to the open structure of the VS$_2$ electrode, which can facilitate the penetration of electrolyte ions into the inner part and shorten the ionic diffusion path, therefore improving the dynamic

electrochemical performance. The activated carbon has been shown to have interconnected porous cavities that are in sizes of several micrometres, with a substantial amount of macropores, offering enough reservoirs for the electrolyte, which is highly required for improved supercapacitor electrode performance.[47]

Electrochemical properties of the asymmetric supercapacitor

To further assess the potential application of the VS$_2$ nanosheet array electrode in supercapacitors, an asymmetric super-capacitor was fabricated in which the positive electrode comprised of the VS$_2$ material and the activated carbon material was used as the negative electrode. In order to obtain the optimal performance of the asymmetric full cell supercapacitor,

176

Fig. 9 (a) Cyclic voltammetry of the VS_2 nanosheet and activated carbon electrodes at a scan rate of 50 mV s^{-1} for the three-electrode setup. For the asymmetric VS_2//AC device: (b) cyclic voltammetry at scan rates of 50–200 mV s^{-1}, (c) galvanostatic charge–discharge at current densities of 1–10 A g^{-1}, (d) Ragone plot and the specific capacitance as a function of the current density, and (e) cycle stability at a constant current density of 2 A g^{-1}.

a charge balance $Q_+ = Q_-$ between the two electrodes was done, where Q_+ and Q_- are the charges stored in the positive and negative electrodes, respectively. The charge can be expressed by:[54]

$$Q = C_s \times m\Delta U \qquad (2)$$

where C_s is the specific capacitance of the active material, m is the mass of each active material, and ΔU is the potential range during the charge–discharge process.

In order to get $Q_+ = Q_-$, the mass balancing follows the equation.

$$\frac{m_+}{m_-} = \frac{C_{s-}\Delta U_-}{C_{s+}\Delta U_+} \qquad (3)$$

To make two-electrode cells, according to eqn (3), the mass of the VS_2 electrode should be two times mass of the AC electrode.

From Fig. 9(a), it is expected that the operating cell voltage could be extended to about 1.4 V in 6 M KOH solution as electrolyte if the VS_2 electrode as cathode and the AC electrode as anode are assembled into asymmetric ECs.

Fig. 9(b) shows the CV curves of the VS_2//AC asymmetric device measured at different scan rates from 5 to 200 mV s^{-1}. It indicates that the CV curves simultaneously express the faradic and electric double-layer capacitive behaviour, which are the typical characteristics of hybrid asymmetric supercapacitors. An asymmetric charge–discharge curve was observed showing the existence of both faradic behaviour (0.55–0.15 V) and electric double-layer behaviour (0.55 V–1.4 V) at all current densities (Fig. 9(c)).

The energy density (E, in W h kg^{-1}) and power density (P, in W kg^{-1}) of ECs can be calculated from the specific capacitance, C_s according to the following equations:

$$E = \frac{1}{2}C_s\Delta U^2 = \frac{1000 \times C_s \times \Delta U^2}{2 \times 3600} = \frac{C_s \times \Delta U^2}{7.2} \quad (4)$$

$$P = \frac{E}{t} = \frac{3600 \times E}{1000 \times \Delta t} = \frac{3.6 \times E}{\Delta t} \quad (5)$$

where U is the voltage window of the full cell, and Δt is the discharge time.

The Ragone plot and the specific capacitance as a function of the current density of the asymmetric device are shown in Fig. 9(d). The specific capacitance of the VS$_2$//AC can reach 155 F g^{-1} at a current density of 1 A g^{-1} as calculated from eqn (2).

The maximum energy density of the device was recorded as 42 W h kg^{-1} with a corresponding power density of 700 W Kg^{-1} at a current density of 1 A g^{-1}, as shown in Fig. 9(d). The asymmetric VS$_2$//AC shows a much improved energy density at high power density in comparison with other asymmetric devices involving AC as negative electrode, such as AC//Ni(OH)$_2$/XC-72 (energy density of 36 W h kg^{-1} and corresponding power density of 490 W kg^{-1} at 0.5 A g^{-1}),[55] Ni(OH)$_2$@3D Ni-AC (energy density of 21.8 W h kg^{-1} and corresponding power density of 660 W kg^{-1} at 1 A g^{-1})[56] and CuS//AC (energy density of 15.06 W h kg^{-1} and corresponding power density of 392.9 W kg^{-1} at 0.5 A g^{-1}).[57]

The stability of the electrode material is also a very important characteristic for its application as energy storage device. In order to understand the stability of the VS$_2$//AC asymmetric device, the samples were subjected to 5000 cycles at the high current density of 2 A g^{-1} as shown in Fig. 9(e). The coulombic efficiency of VS$_2$//AC after 5000 cycles is ~99%, thus exhibiting its excellent electrochemical stability.

Fig. 10(a) presents the Nyquist plot of the asymmetric device with an R_s value of 2.97 Ω obtained from the fitted plot using the circuit shown in the inset to the figure. The Nyquist plot before and after cycling is shown in Fig. 10(b). From this, an R_s-intercept value of 2.97 Ω before cycling and 4.10 Ω after cycling was obtained.

The frequency response of porous carbon electrodes has been modelled with a single series resistor–capacitor (RC) circuit.[58] Based on this model, the real and imaginary part of the capacitance as a function of the frequency can be calculated using the equations below:

$$C = \frac{-1}{(\omega Z'')} \quad (6)$$

$$C(\omega) = C'(\omega) - jC''(\omega) \quad (7)$$

$$C' = \frac{Z''(\omega)}{\omega|Z(\omega)|^2} \quad (8)$$

$$C'' = \frac{Z'(\omega)}{\omega|z(\omega)|^2} \quad (9)$$

where Z is the complex impedance written as $Z(\omega) = Z'(\omega) + Z''(\omega)$, $\omega = 2\pi f$; $C'(\omega)$ represents the real accessible capacitance

Fig. 10 (a) EIS plot and fitting curve for the asymmetric VS$_2$//AC cell, (b) EIS before and after cycling, (c) the real and the imaginary parts of the asymmetric cell's capacitance against frequency.

178

of the cell at the corresponding frequency, which signifies the deliverable capacitance; $C''(\omega)$ represents the energy loss due to the irreversible process of the electrodes; and Z' and Z'' represent the real and imaginary parts of the Nyquist plot, respectively.[58] Based on the above formulae, the capacitance (C') of the cell is 0.035 F (from the topmost part of the C' graph as shown in Fig. 10(b)), and C'' defines the transition frequency between a purely resistive and purely capacitive behaviour of the asymmetric capacitor with a relaxation time of 0.6 s, achieved by taking the reciprocal of the maximum frequency in the C'' graph in Fig. 10(c). This value shows that the cell can be fully charged within a very short time.

Conclusions

We have successfully fabricated an asymmetric supercapacitor cell based on porous activated carbon material as negative electrode and VS_2 as positive electrode. The asymmetrical device displays a high specific capacitance of 155 F g^{-1} at 1 A g^{-1} with a maximum energy density of 42 W h kg^{-1} and power density of 700 W kg^{-1}. In addition, its great stability record, with ~99% capacitance retention and no capacitance loss after 5000 cycles at a current density of 2 A g^{-1} and an operating voltage of about 1.4 V in 6 M KOH aqueous electrolytes, shows that pairing such hybrid materials could be an excellent method to produce supercapacitors with high energy and power densities. These results offer a convenient and effective way to fabricate asymmetric hybrid supercapacitors based on VS_2 and AC with high energy density while maintaining the high power density property of supercapacitors.

Acknowledgements

References

1 A. S. Arico, P. Bruce, B. Scrosati, J.-M. Tarascon and W. van Schalkwijk, *Nat. Mater.*, 2005, **4**, 366–377.
2 B. E. Conway, *Electrochemical Supercapacitors: Scientific Fundamentals and Technological Applications*, Kluwer Academic/Plenum, New York, 1999.
3 W. Van Schalkwijk and B. Scrosati, *Advances in lithium-ion batteries*, Springer Science & Business Media, 2002.
4 L. Zhang, F. Zhang, X. Yang, G. Long, Y. Wu, T. Zhang, K. Leng, Y. Huang, Y. Ma, A. Yu and Y. Chen, *Sci. Rep.*, 2013, **3**, 1408.
5 L. L. Zhang and X. S. Zhao, *Chem. Soc. Rev.*, 2009, **38**, 2520–2531.
6 J. W. Long, B. Dunn, D. R. Rolison and H. S. White, *Chem. Rev.*, 2004, **104**, 4463–4492.
7 Y.-G. Wang, L. Cheng and Y.-Y. Xia, *J. Power Sources*, 2006, **153**, 191–196.
8 S.-B. Ma, K.-W. Nam, W.-S. Yoon, X.-Q. Yang, K.-Y. Ahn, K.-H. Oh and K.-B. Kim, *Electrochem. Commun.*, 2007, **9**, 2807–2811.
9 V. Ganesh, S. Pitchumani and V. Lakshminarayanan, *J. Power Sources*, 2006, **158**, 1523–1532.
10 H. Inoue, T. Morimoto and S. Nohara, *Electrochem. Solid-State Lett.*, 2007, **10**, A261–A263.
11 T.-W. Lin, C.-S. Dai, T.-T. Tasi, S.-W. Chou, J.-Y. Lin and H.-H. Shen, *Chem. Eng. J.*, 2015, **279**, 241–249.
12 W. Lin, W. Yu, Z. Hu, W. Ouyang, X. Shao, R. Li and D. S. Yuan, *Electrochim. Acta*, 2014, **143**, 331–339.
13 T. Peng, H. Wang, H. Yi, Y. Jing, P. Sun and X. Wang, *Electrochim. Acta*, 2015, **176**, 77–85.
14 J.-W. Lang, L.-B. Kong, M. Liu, Y.-C. Luo and L. Kang, *J. Solid State Electrochem.*, 2010, **14**, 1533–1539.
15 Q. T. Qu, Y. Shi, L. L. Li, W. L. Guo, Y. P. Wu, H. P. Zhang, S. Y. Guan and R. Holze, *Electrochem. Commun.*, 2009, **11**, 1325–1328.
16 D. Xuan, W. Chengyang, C. Mingming, J. Yang and W. Jin, *J. Phys. Chem. C*, 2009, **113**, 2643–2646.
17 B. G. Choi, S.-J. Chang, H.-W. Kang, C. P. Park, H. J. Kim, W. H. Hong, S. Lee and Y. S. Huh, *Nanoscale*, 2012, **4**, 4983–4988.
18 P. Tang, L. Han and L. Zhang, *ACS Appl. Mater. Interfaces*, 2014, **6**, 10506–10515.
19 P. Simon and Y. Gogotsi, *Acc. Chem. Res.*, 2012, **46**, 1094–1103.
20 Y.-G. Wang, Z.-D. Wang and Y.-Y. Xia, *Electrochim. Acta*, 2005, **50**, 5641–5646.
21 M. Kumar, A. Subramania and K. Balakrishnan, *Electrochim. Acta*, 2014, **149**, 152–158.
22 S. J. Zhu, J. Zhang, J. J. Ma, Y. X. Zhang and K. X. Yao, *J. Power Sources*, 2015, **278**, 555–561.
23 Y. Xiao, Y. Cao, Y. Gong, A. Zhang, J. Zhao, S. Fang, D. Jia and F. Li, *J. Power Sources*, 2014, **246**, 926–933.
24 H. R. Ghenaatian, M. F. Mousavi and M. S. Rahmanifar, *Electrochim. Acta*, 2012, **78**, 212–222.
25 Y. Zhou, N. Lachman, M. Ghaffari, H. Xu, D. Bhattacharya, P. Fattahi, M. R. Abidian, S. Wu, K. K. Gleason and B. L. Wardle, *J. Mater. Chem. A*, 2014, **2**, 9964–9969.
26 M.-Y. Cho, S.-M. Park, J.-W. Lee and K.-C. Roh, *J. Electrochem. Sci. Technol.*, 2011, **2**, 152–156.
27 Y. Wang, L. Yu and Y. Xia, *J. Electrochem. Soc.*, 2006, **153**, A743–A748.
28 T. Brousse, P.-L. Taberna, O. Crosnier, R. Dugas, P. Guillemet, Y. Scudeller, F. Favier, Y. Zhou, P. Simon and D. Blanger, in *Meeting Abstracts*, 2006, p. 125.
29 L.-M. Chen, Q.-Y. Lai, Y.-J. Hao, Y. Zhao and X.-Y. Ji, *J. Alloys Compd.*, 2009, **467**, 465–471.
30 S. W. Lee, J. Kim, S. Chen, P. T. Hammond and Y. Shao-Horn, *ACS Nano*, 2010, **4**, 3889–3896.
31 M. A. Bissett, I. A. Kinloch and R. A. W. Dryfe, *ACS Appl. Mater. Interfaces*, 2015, **7**, 17388–17398.

32 S. Nohara, T. Asahina, H. Wada, N. Furukawa, H. Inoue, N. Sugoh, H. Iwasaki and C. Iwakura, *J. Power Sources*, 2006, **157**, 605–609.

33 D. P. Dubal, G. S. Gund, C. D. Lokhande and R. Holze, *Energy Technol.*, 2014, **2**, 401–408.

34 W. Tang, L. Liu, S. Tian, L. Li, Y. Yue, Y. Wu and K. Zhu, *Chem. Commun.*, 2011, **47**, 10058–10060.

35 S. Surendran, K. V. Sankar, L. J. Berchmans and R. K. Selvan, *Mater. Sci. Semicond. Process.*, 2015, **33**, 16–23.

36 K. Krishnamoorthy, G. K. Veerasubramani, S. Radhakrishnan and S. J. Kim, *Mater. Res. Bull.*, 2014, **50**, 499–502.

37 J. Feng, X. Sun, C. Wu, L. Peng, C. Lin, S. Hu, J. Yang and Y. Xie, *J. Am. Chem. Soc.*, 2011, **133**, 17832–17838.

38 P. Justin and G. R. Rao, *Int. J. Hydrogen Energy*, 2010, **35**, 9709–9715.

39 S. Ratha, S. R. Marri, N. A. Lanzillo, S. Moshkalev, S. K. Nayak, J. N. Behera and C. S. Rout, *J. Mater. Chem. A*, 2015, **3**, 18874–18881.

40 L. Li, S. Kim, W. Wang, M. Vijayakumar, Z. Nie, B. Chen, J. Zhang, G. Xia, J. Hu and G. Graff, *Adv. Energy Mater.*, 2011, **1**, 394–400.

41 H. A. Therese, F. Rocker, A. Reiber, J. Li, M. Stepputat, G. Glasser, U. Kolb and W. Tremel, *Angew. Chem., Int. Ed.*, 2005, **44**, 262–265.

42 J. Feng, L. Peng, C. Wu, X. Sun, S. Hu, C. Lin, J. Dai, J. Yang and Y. Xie, *Adv. Mater.*, 2012, **24**, 1969–1974.

43 P. Mohan, J. Yang, A. Jena and H. Suk Shin, *J. Solid State Chem.*, 2015, **224**, 82–87.

44 F. Cao, W. Hu, L. Zhou, W. Shi, S. Song, Y. Lei, S. Wang and H. Zhang, *Dalton Trans.*, 2009, 9246–9252.

45 C. Song, K. Yu, H. Yin, H. Fu, Z. Zhang, N. Zhang and Z. Zhu, *J. Mater. Chem. C*, 2014, **2**, 4196–4202.

46 C. S. Rout, R. Khare, R. V. Kashid, D. S. Joag, M. A. More, N. A. Lanzillo, M. Washington, S. K. Nayak and D. J. Late, *Eur. J. Inorg. Chem.*, 2014, **2014**, 5331–5336.

47 A. Bello, F. Barzegar, D. Momodu, J. Dangbegnon, F. Taghizadeh and N. Manyala, *Electrochim. Acta*, 2015, **151**, 386–392.

48 F. Barzegar, A. Bello, D. Y. Momodu, J. K. Dangbegnon, F. Taghizadeh, M. J. Madito, T. M. Masikhwa and N. Manyala, *RSC Adv.*, 2015, **5**, 37462–37468.

49 X. Liu, H.-L. Shuai and K.-J. Huang, *Anal. Methods*, 2015, **7**, 8277–8284.

50 G. Ma, D. Guo, K. Sun, H. Peng, Q. Yang, X. Zhou, X. Zhao and Z. Lei, *RSC Adv.*, 2015, **5**, 64704–64710.

51 W. Gao, L. B. Alemany, L. Ci and P. M. Ajayan, *Nat. Chem.*, 2009, **1**, 403–408.

52 J. Mendialdua, R. Casanova and Y. Barbaux, *J. Electron Spectrosc. Relat. Phenom.*, 1995, **71**, 249–261.

53 T.-H. Yang, S. Nori, H. Zhou and J. Narayan, *Appl. Phys. Lett.*, 2009, **95**, 2506.

54 A. Bello, F. Barzegar, D. Momodu, J. Dangbegnon, F. Taghizadeh, M. Fabiane and N. Manyala, *J. Power Sources*, 2015, **273**, 305–311.

55 L. Sui, S. Tang, Z. Dai, Z. Zhu, H. Huangfu, X. Qin, Y. Deng and G. M. Haarberg, *New J. Chem.*, 2015, **39**, 9363–9371.

56 Y.-Z. Su, K. Xiao, N. Li, Z.-Q. Liu and S.-Z. Qiao, *J. Mater. Chem. A*, 2014, **2**, 13845–13853.

57 J. Zhang, H. Feng, J. Yang, Q. Qin, H. Fan, C. Wei and W. Zheng, *ACS Appl. Mater. Interfaces*, 2015, **7**, 21735–21744.

58 P. L. Taberna, P. Simon and J.-F. Fauvarque, *J. Electrochem. Soc.*, 2003, **150**, A292–A300.

180

4.5.3 Conclude Remarks

Asymmetric supercapacitor based on VS$_2$//AC electrode demonstrated a high capacity of 155 F g^{-1} and high energy and power densities of 42 Wh kg^{-1} and 700 W kg^{-1} respectively at 1 A g^{-1}.The device also displayed a good stability with ~ 99% capacitance retention and no capacitance loss after 5000 cycles at a current density of 2 Ag^{-1} at an extended operating voltage of about 1.4 V .Therefore, these above results showed that pairing such hybrid materials could be an excellent method for tailoring high-performance supercapacitor electrodes.

4.6 High Performance Asymmetric Supercapacitor Based on MoS$_2$/GF and Activated Carbon from Expanded Graphite

4.6.1 Introduction

One of the mostly studied transition metal chalcogenides material for electrochemical capacitance is molybdenum disulphide (MoS$_2$) due to its excellent mechanical and electrochemical properties and unique morphology [13].

Molybdenum disulphide comprises of covalently bonded S-Mo-S atoms which are held together by weak van der Waals forces [14,15] just like few layer graphene. It has been established that modifying the MoS$_2$ with carbon materials to obtain a composite material is one of the most effective ways of increasing the conductivity as well as its electrochemical properties [16–21]. In this study hybrid composite materials consisting of MoS$_2$ and different graphene foam mass loading were synthesized through hydrothermal synthesis. The composites were characterized through different techniques and the electrochemical measurements were studied as a function of graphene foam mass loading in three electrode configuration. The best performing composite was used to make asymmetric device where such composite was used as cathode and AEG as anode electrodes respectively.

181

4.6.2 Results and Discussion

The results obtained from this work are presented in detail in the paper below.

Regular Article

High performance asymmetric supercapacitor based on molybdenum disulphide/graphene foam and activated carbon from expanded graphite

Tshifhiwa M. Masikhwa, Moshawe J. Madito, Abdulhakeem Bello, Julien K. Dangbegnon, Ncholu Manyala *

Department of Physics, Institute of Applied Materials, SARCHI Chair in Carbon Technology and Materials, University of Pretoria, Pretoria 0028, South Africa

GRAPHICAL ABSTRACT

MoS$_2$ with 150 mg of graphene shows the highest current response

MoS$_2$ 150 mg graphene shows the highest specific capacitance

ABSTRACT

Molybdenum disulphide which has a graphene-like single layer structure has excellent mechanical and electrical properties and unique morphology, which might be used with graphene foam as composite in supercapacitor applications. In this work, Molybdenum disulphide (MoS$_2$)/graphene foam (GF) composites with different graphene foam loading were synthesized by the hydrothermal process to improve on specific capacitance of the composites. Asymmetric supercapacitor device was fabricated using the best performing MoS$_2$/GF composite and activated carbon derived from expanded graphite (AEG) as positive and negative electrodes, respectively, in 6 M KOH electrolyte. The asymmetric MoS$_2$/GF//AEG device exhibited a maximum specific capacitance of 59 F g^{-1} at a current density of 1 A g^{-1} with maximum energy and power densities of 16 W h kg^{-1} and 758 W kg^{-1}, respectively. The supercapacitor also exhibited a good cyclic stability with 95% capacitance retention over 2000 constant charge-discharge cycles. The results obtained demonstrate the potential of MoS$_2$/GF//AEG as a promising material for electrochemical energy storage application.

© 2016 Elsevier Inc. All rights reserved.

1. Introduction

The increasing demand for novel energy storage systems to meet today's technological advancement has inspired the need to design and develop efficient energy storage devices. Supercapacitors, also known as electrochemical capacitors, have now been revealed to be suitable candidates for next-generation energy storage devices due to their fast charge-discharge rate, high power density as well as excellent cycle stability compared with electrolytic capacitors and conventional batteries [1–4]. Supercapacitors are being used in power backup systems, portable electronics, hybrid electrical vehicles, pacemakers and various

182

devices where long cycle life and high power density are needed [5,6]. Although the energy density of commercially accessible supercapacitor is quite low, a great deal of research determination has remained engaged in order to improve the energy density of supercapacitor while retaining its high power density [6].

On the basis of their energy storage mechanism, supercapacitors can be classified into three categories such as the electric double-layer capacitors (EDLCs) that apply the capacitance arising from charge separation at an electrode/electrolyte interface, pseudocapacitors or redox supercapacitors which use the charge-transfer arising from redox reactions occurring on the surface of the electrode and hybrid capacitors which combine both the supercapacitors properties with a battery-type characteristic to form asymmetric supercapacitors [7]. The formation of asymmetric supercapacitors has been found to be an actual alternative method to improve the energy density by either increasing the overall device specific capacitance with different electrode materials or increasing the operating voltage window up to about 2.5 V by using organic and ionic liquids electrolytes because of their broader cell potential windows than those of aqueous electrolytes [8,9]. However, both types of electrolytes are plagued with drawbacks when adopted for practical application because organic electrolytes have poor electrical conductivity and are not environmentally friendly, while ionic liquids are cost ineffective.

The electrode material plays a key role in improving the overall device performance and this remains a great challenge in finding unique and efficient electrode materials for this purpose. In general, electrode materials including conducting polymers and transition metal oxides and their composites with carbon materials have been used as positive electrodes [10–12]. Designing hybrid supercapacitors composed of carbon materials with electric double layer capacitance and pseudo-capacitive materials with faradic capacitance in the same cell to form an asymmetric supercapacitor has been established as a promising approach to increase the cell voltage window up to 2.0 V in aqueous or neutral electrolytes [13,14]. The importance of assembling an asymmetric cell is to use electrode materials which are stable in different potential windows in the same electrolyte in order to increase the full cell voltage. As a result, this will increase the device energy density because it depends on potential window squared [6].

Carbonaceous materials, like carbon nanotubes, graphene and activated carbon are generally being used as a negative electrode due to their good rate capacity, high surface area, low cost and facile synthesis procedure [15,16]. Transition metal chalcogenides such as Cobalt disulphide [17–19], molybdenum disulphide (MoS_2) [20–22], Nickel disulphide [23–25] and copper disulphide [26] are potential electrode materials for supercapacitor applications because they are known to be electrochemically active with good electrochemical performance. Molybdenum disulphide which has a graphene-like single layer structure has attracted great attention in phototransistors, catalysis, lithium ion batteries and supercapacitor applications due to its excellent mechanical and electrical properties and unique morphology [27–31]. Molybdenum disulphide comprises of covalently bonded S—Mo—S atoms which are held together by weak van der Waals forces [32,33]. It has been established that modifying the MoS_2 with carbon materials to obtain a composite material is one of the most effective ways of increasing the conductivity as well as its electrochemical properties [22,34–38]. Graphene with its excellent electrical conductivity and good stability can provide interconnecting mesostructured supports that can facilitate good nanoparticle dispersion and electron transport for MoS_2. For example, Huang et al. [39] produced layered MoS_2-graphene composites for supercapacitor applications with improved capacitive performance, Patil et al. [40] reported MoS_2/graphene oxide hybrid for supercapacitor application, da Silveira Firmiano et al. [35] also reported MoS_2 deposited by micro-

wave heating on a reduced graphene oxide, Huang et al. [36] produced MoS_2/multi-walled carbon nanotube composites for enhanced performance supercapacitor, Hu et al. [37] also demonstrated the preparation of porous tubular C/MoS_2 nanocomposite for supercapacitor application, Bissett et al. [41] also reported characterization of MoS_2-graphene composites for high performance coin cell supercapacitors, Fan et al. [22] also demonstrated flower-like MoS_2/C composite for supercapacitor application and Ji et al. [38] also produced MoS_2/C hybrid composites for supercapacitor performance.

In this work pure MoS_2 and MoS_2/graphene foam (GF) with different graphene foam mass loading were synthesized by the hydrothermal process to improve on the specific capacitance of the composites. An asymmetric supercapacitor was fabricated using the best performing MoS_2/GF composite and activated carbon derived from expanded graphite (AEG) as positive and negative electrodes respectively in an aqueous electrolyte. The hybrid material composite demonstrated a high rate capability when compared with a pure MoS_2 electrode. The MoS_2/GF//AEG asymmetric supercapacitor could perform reversibly at a high cell voltage of 1.4 V in 6 M KOH delivering high energy and power densities of 16 W h kg^{-1} and 758 W kg^{-1} at a current density of 1 A g^{-1}, respectively. The supercapacitor also displayed a good cyclic stability with 95% capacitance retention over 2000 constant charge-discharge cycles.

2. Experimental

2.1. Materials

Ammonium molybdate $(NH_4)_2MoO_4$, purity 99.98%), hydrochloric acid (HCl, purity $\geqslant$ 32%), thiourea (CH_4N_2S, purity $\geqslant$ 99%) and polyvinylpyrrolidonel (PVP) were purchased from Sigma-Aldrich. Nickel foam (NF) with areal density of 420 g m^{-2} was purchased from Alantum, (Munich, Germany) while potassium hydroxide (KOH, purity $\geqslant$ 85%) was purchased from Merck Stores (South Africa).

2.2. Synthesis of MoS_2

1 mmol of ammonium molybdate was dissolved in 30 ml of deionized water under vigorous stirring for 20 min, 5 mmol of thiourea (CH_4N_2S) was then added to this solution and stirring of the mixture was further continued for 30 min. The mixture was then carefully transferred into a 120 mL sealed Teflon-lined stainless-steel autoclave and kept at a temperature of 150 °C for 20 h. After cooling to room temperature, the black powder samples were repeatedly washed with deionized water and ethanol several times and finally dried at 60 °C for 6 h. During the hydrothermal reaction, ammonium molybdate releases the MoO_4^- and ammonium ions, with thiourea acting as the sulphur source. A layered structure, MoO_4^- ions react with the sulphur ions to form the molybdenum disulphide (MoS_2) and the residual ammonia intercalation inhibits the stacking of MoS_2 nanostructures and basically self-assembles into a sphere like morphology [42]. The reaction of the synthesis of MoS_2 can be expressed as [43]:

$$CSN_2H_4 + 2H_2O \rightarrow 2NH_3 + CO_2 + H_2S \tag{1}$$

$$4((NH_4)_2MoO_4) + 9H_2S + 6HCl \rightarrow 4MoS_2 + (NH_4)_2SO_4 + 12H_2O + 6NH_4Cl \tag{2}$$

2.3. Synthesis of MoS_2/GF

Schematic 1 shows the method used to prepare the MoS_2/GF composite in this study. In order to obtain the MoS_2/graphene foam (MoS_2/GF) composite, the GF was initially synthesized by

Schematic 1. Preparation of MoS$_2$/GF.

atmospheric chemical vapor deposition (APCVD) technique [44]. Briefly, a known mass of compressed nickel foam template (Alantum, Munich, Germany), with an areal density of $420 \, g \, m^{-2}$ was positioned in a quartz tube for the APCVD graphene growth. The nickel foam was first annealed at 800 °C in the presence of Ar and H$_2$ gas for 60 min, prior to the introduction of the carbon source (CH$_4$ gas) at 1000 °C. The flow rates of the gasses Ar:H$_2$: CH$_4$ were 300:200:10 sccm, respectively. After 60 min period of deposition, the samples were quickly cooled by horizontally pushing the quartz tube to a lower temperature section to attain the nickel foam-graphene. In order to get the final GF product, the sample was subsequently submerged in a 3.0 M HCl solution and placed on a hot plate at 60 °C for 16 h to ensure complete etching of the nickel template structure. After complete etching of the nickel, the remaining GF was washed several times with deionized water and dried in the oven to get the GF. The MoS$_2$/GF composites were prepared using a hydrothermal reduction technique. Typically, 50, 100, 150 and 200 mg of laboratory synthesized GF samples were dispersed in 30 mL of water by ultrasonication for 12 h at room temperature. Then 1 mmol of ammonium molybdate and 5 mmol thiourea was added to the different GF solutions and the mixtures were all stirred for 10 min. The obtained solutions were then transferred to a Teflon-lined stainless steel autoclave system and kept at 150 °C for 20 h. After naturally cooling to room temperature, the final MoS$_2$/GF product containing different amounts of GF was washed with deionized water and dried at 60 °C for 6 h. For comparison, MoS$_2$ and GF were also mixed after synthesis to investigate the effect of the hydrothermal synthesis. Different masses of laboratory synthesized GF and 40 mg of MoS$_2$ samples were dispersed in 30 mL of water by ultrasonication for 12 h at room temperature. The final mixture of MoS$_2$ and GF product was washed with deionized water and dried at 60 °C for 6 h.

2.4. Synthesis of activated carbon from expanded graphite

Activated carbon from expanded graphite used as anode material for our asymmetric supercapacitor was prepared as reported in our earlier work [45]. Briefly, expanded graphite and polyvinylpyrrolidonel (PVP) were used as an initial material for the production of a hydrogel, which was then used to produce activated carbon denoted as AEG after the activation process. The activated material was neutralized with 1 M HCl, washed with deionized water and dried at 60 °C for 12 h for further samples characterization.

2.5. Structural and morphology characterization

X-ray diffraction (XRD) spectra of the prepared materials were collected using an XPERT-PRO diffractometer (PANalytical BV, Netherlands) with theta/2theta geometry, operating with a cobalt tube at 50 kV and 30 mA and reflection geometry at 2θ values rang-

ing from 30 to 90° with a step size of 0.01°. The morphology of the prepared MoS$_2$, MoS$_2$/GF and AEG was studied using a high-resolution Zeiss Ultra plus 55 field emission scanning electron microscope (FE-SEM) operated at a voltage of 2.0 kV. Transmission electron microscopy (TEM) micro-images was carried out with a JEOL JEM-2100F microscope operated at 200 kV (Akishima-shi, Japan). X-ray photoelectron spectroscopy (XPS, K-alpha, Thermo Fisher) with monochromatic Al Kα radiation as the X-ray source was used to irradiate the sample surface and determine the chemistry of the samples synthesized in powder form. Nitrogen adsorption–desorption isotherms were measured at -196 °C using a Micromeritics ASAP 2020. All the samples were degassed at 180 °C for more than 12 h under vacuum conditions. The surface area was calculated by the Brunauer–Emmett–Teller (BET) method from the adsorption branch in the relative pressure range (P/P$_0$) of 0.01–1.0.

2.6. Electrode preparation and electrochemical characterization

All electrochemical measurements were carried out using a Biologic VMP-300 potentiostat (Knoxville TN 37,930, USA) controlled by the EC-Lab$^®$ V10.37 software. The three electrode measurements were performed for MoS$_2$, MoS$_2$/GF and AEG serving as the working electrodes, glassy carbon plate as the counter electrode and Ag/AgCl (3 M KCl) serving as the reference electrode. The negative electrode was made by mixing the active material of AEG with polyvinylidene fluoride (PVDF) binder in a weight ratio of 9:1 which was homogenized and dispersed in N-methylpyrrolidone (NMP) solution. The slurry was then homogeneously pasted on a nickel foam current collector and dried at 60 °C in an oven for 8 h to make sure complete evaporation of the NMP. The positive electrode was prepared by mixing the active material MoS$_2$/GF, polyvinylidene fluoride (PVDF) binder and carbon black (CB) which served to increase the conductivity of the material in a weight ratio of 8:1:1 and dispersed in N-methylpyrrolidone (NMP) solution. The slurry was then uniformly pasted on a nickel foam current collector and also dried at 60 °C in an oven for 8 h. In this experiment, the active material loading was ranging from 1.2 to 3.0 mg.

The electrochemical test of the asymmetric cell was carried out in a two-electrode cell configuration by means of coin-type cells with a thickness of 0.2 mm and diameter of 16 mm, using a glass microfiber filter paper as the separator in a 6 M KOH aqueous electrolyte solution.

3. Results and discussion

3.1. Structural and morphological characterization

Fig. 1(a) shows the measured XRD patterns for as-prepared MoS$_2$ and MoS$_2$ with GF at different mass loading while Fig. 1(b) shows the XRD pattern for a mixture of 40 mg MoS$_2$ and 150 mg

184

Fig. 1. X-ray diffraction of (a) MoS₂ and MoS₂/GF, (b) 40 mg MoS₂/150 mg GF mixture (obtained using a cobalt tube) and (c) AEG (obtained using a copper tube) with standard ICSD, respectively.

GF with other GF foam mass loading showing similar behaviour. Typical diffraction peaks which were observed for MoS_2 phase are indexed using the MoS_2 ICSD card number 84180 (Sys: hexagonal, S.G.: $P63/mmc$ (194), a: 3.1600 Å, c: 12.2900 Å, a/b = 1.0000, b/c = 0.2571 and c/a = 3.8892) and for GF phase are indexed using the graphite ICSD card 31170 (Sys.: hexagonal, S.G: $P63mc$ (186) a: 2.4700 Å, c: 6.7900 Å, a/b: 1.0000, b/c: 0.3638 and c/a: 2.7490). It can be seen that as-prepared MoS_2 has a preferential wide peak at $2\theta = 40°$ which could be due to disorder in the material and/or overlap peaks that should be at $2\theta = 38°$, 39° and 44°.

Except for 150 mg GF, the addition of 50 and 100 mg GF to the MoS_2 shows similar diffraction patterns as that of pristine MoS_2. Interestingly, an addition of 150 mg GF (which has a preferential (0 0 2) texture) to the MoS_2 causes this material to have a dominating (0 0 2) texture similar to that of GF.

We suggest that the increased mass loading of graphene during the hydrothermal synthesis may favour the growth of MoS_2 in the (0 0 2) direction (see the spectrum for 150 mg GF mass loading). Though, GF influences the texture of the MoS_2, it does not alter the hexagonal crystal structure of the material except the fact that the material could be disordered. The XRD for material which was produced through MoS_2 and GF mixing does not exhibit striking difference as compared to the hydrothermally grown samples which just shows the presence of carbon (GF) and MoS_2 (Fig. 1(b)).

Fig. 1(c) represents the XRD patterns of AEG powder. The wavelength used for the XRD analysis was Cu-Kα, 1.5405 Å. All the peaks are identified to graphite peaks (COD:96-900-0047) which crystallizes in the orthorhombic structure with space group Fmmm(69), lattice parameters $a = 2.4560$ Å and $c = 6.6960$ Å [46]. Fig. 2 shows the FESEM microstructures of the as-prepared samples. The morphology of the MoS_2 (Fig. 2(a and b)) at different magnifications indicating a cauliflower morphology constructed by MoS_2 nanowalls. However, in the presence of GF acting as a growth support, numerous MoS_2 nanosheets are densely attached on graphene as shown in Fig. 2(c)–(h) for low and high magnifications respectively. The graphene forms an interconnected conducting network and assists in fast electronic transport in the electrode. Fig. 2(i and j) show the FESEM microstructures of the mixed MoS_2 and GF at low and high magnifications, respectively. The flower-like MoS_2 and the graphene sheets are clearly distinguishable from these images. No homogeneous deposition of the MoS_2 on the sheet of carbon is noticed. Fig. 2(k) and (l) presents the low and high magnification SEM of the AEG sample. As observed in the micrographs, the sample is composed of a sheet-like material which provides a large ion-accessible surface for fast ion transport in high-performance supercapacitors.

Fig. 3(a) and (b) shows high-resolution TEM (HRTEM) images of both MoS_2 and MoS₂/GF (150 mg GF) composite respectively. In both figures, a number of lattice fringes in different directions are observed suggesting polycrystalline nature of the material which is in agreement with the observed XRD spectra (Fig. 1(a)) which shows diffraction peaks with different crystallographic directions.

The bonding characteristics and the composition of the MoS_2 nanosheets were obtained by XPS as shown in Fig. 4. Besides the element of C and O, the unsputtered and sputtered XPS spectra of the MoS_2 nanosheets (Fig. 4(a)) show only signals from Mo and S elements. The presence of some O and C elements may be due to the surface-adsorbed CO_2 and O_2 along with oxides of Mo and/or S elements. The curve-fitting analysis of the Mo 3d

185

Fig. 2. Low and high magnification SEM images of (a, b) MoS_2; (c, d) MoS_2_50 mg GF; (e, f) MoS_2_100 mg GF; (g, h) MoS_2_150 mg GF and (i, j) 40 mg $MoS_2/150$ mg GF mixture and (k, l) AEG, respectively.

spectrum after sputtering for 30 min (Fig. 4(b)) shows the doublet Mo $3d_{5/2}$ and Mo $3d_{3/2}$ which shows that Mo atoms are bonded with chemically different bonds. Similarly, the curve-fitting analysis of the S 2p spectrum (Fig. 4(c)) shows that sulphur atoms are bonded with chemically different bonds and the two peaks in S 2p peak correspond to the S $2p_{1/2}$ and S $2p_{3/2}$ orbital of divalent sulphide ions (S^{2-}) respectively.

The Brunauer–Emmett–Teller (BET) method was used to determine the surface area of the composite and its pore size distribution. Fig. 5(a) and (b) shows the BET isotherm and pore size distribution of the pristine MoS_2 and MoS_2/GF with different GF mass loading indicated in the figures. Fig. 5(a) shows the nitrogen adsorption–desorption isotherm of the MoS_2 with and without GF to be of type-III with H3 hysteresis loops indicating the presence of

186

Fig. 3. (a) and (b) low and high TEM images of MoS_2/GF (150 mg GF), respectively.

Fig. 4. (a) XPS survey spectrum, and high resolution scans of (b) Mo 3d, (c) S 2p for MoS_2 sample.

non-rigid aggregates of plate-like particles or collections of slit-shaped pores with no saturation. The specific surface area (SSA) calculated for all five samples listed in Fig. 5(a) above is presented in the exact order: 9.28, 10.31, 15.04, 26.07 and 13.28 $m^2\,g^{-1}$ for pristine MoS_2 and MoS_2/GF composites with 50 mg, 100 mg, 150 mg and 200 mg of GF, respectively. The results obtained suggest that the specific surface area increases with increase in the amount of GF added up to 150 mg, and thereafter decreases with increasing mass of GF (to 200 mg). Fig. 5(b) shows a concentration of pore volume around 3 nm, suggesting that pores present in this material are predominantly mesopores. BET results indicate that

MoS_2/GF with 150 mg GF possesses larger SSA and high pore volume which provide the probability of efficient transport of electrons and ions, which may favour a higher electrochemical performance of this material.

3.2. Electrochemical performances of MoS$_2$ and AEG

To evaluate the potential applications of the electrode materials for supercapacitor applications, the individual electrochemical properties of the MoS_2, MoS_2/GF composites, mixed MoS_2 and GF and AEG samples which include cyclic voltammetry (CV) and

Fig. 5. (a) N$_2$ absorption/desorption isotherms; and (b) pore size distribution of MoS$_2$ and MoS$_2$/GF composites.

galvanostatic charge-discharge (CD) were firstly studied in a three-electrode system using 6 M KOH electrolyte and the results are shown in Fig. 6. Fig. 6(a) shows the CV curves of AEG electrodes at various scan rates ranging from 5 to 100 mV s^{-1}. These CV curves display relatively rectangular shapes without redox peaks which are typical electric double-layer capacitive sample behaviour. Fig. 6(b) shows the galvanostatic charge/discharge curves of the AEG electrode at different current densities within a potential range of −0.8 to 0.0 V. As can be seen from Fig. 6(b), the charge and discharge curves are highly symmetrical and linear at increased current densities from 1 to 10 A g^{-1} which is a typical characteristic of an electric double-layer capacitor. This is also in agreement with the results recorded from the CV curves in Fig. 6 (a). Fig.6(c) illustrates the overlaid cyclic voltammograms (CV) obtained in a three-electrode cell comparing the MoS$_2$, MoS$_2$/GF composites, MoS$_2$/GF mixture with mass loading of GF being indicated at scan rate of 50 mV s^{-1} in a potential window range of 0.0–0.5 V. A pair of redox peaks corresponding to anodic peak at ∼0.22 V and cathodic peak ∼0.40 V is visible in all the CV curves, suggesting the presence of faradic properties. During the redox process, there occurs intercalation of alkali metal K$^+$ in the MoS$_2$ and MoS$_2$/GF composites interlayers upon reduction, followed by the de-intercalation upon oxidation [21] represented by Eq. (3).

$$MoS_2 + K^+ + e^- \leftrightarrow MoS\text{-}SK^+ \tag{3}$$

It can also be obviously seen that the integral area of the cyclic voltammogram of MoS$_2$_150 mg GF is the largest implying the highest specific capacitance as per Eq. (4).

Fig. 6(d) illustrates the overlaid galvanostatic charge-discharge (GCD) curves comparing pristine MoS$_2$ with those of MoS$_2$/GF and MoS$_2$/GF mixture composites at a current density of 1 A g^{-1} within a potential range of 0–0.45 V respectively. The discharge time of the MoS$_2$_150 mg GF is significantly longer than the other composites suggesting the better rate of discharge and this is in agreement with the CV reported in Fig. 6(c). We also carried out cyclic voltammogram and galvanostatic charge–discharge (GCD) measurements of all samples at different scan rates and current densities respectively. Then the specific capacitance of the MoS$_2$ nanosheets, MoS$_2$/GF composites, MoS$_2$/GF mixture and AEG electrodes can be calculated using both Eqs. (4) and (5):

$$C_s = \frac{\int I(V)dV}{vm\Delta V} \tag{4}$$

$$C_s = \frac{I \times t}{m \times \Delta V} \tag{5}$$

where $\int I(V)$ is the integrated area under CV plot, v is the scan rate, m is the mass of the electrode, ΔV is the potential window, I is the discharge current (A), t is the discharge time (s), and C_s is the specific capacitance (F g^{-1}).

The plot of the specific capacitance as a function of scan rate and current density for all samples is shown in Fig. 6(e) and (f) respectively, while Fig. 6(g) shows the specific capacitance of MoS$_2$/GF composites as a function of GF mass loading. From all the results of MoS$_2$/GF composites including the pristine MoS$_2$ and MoS$_2$/GF mixture (where we only presented mixture with 150 mg GF loading), the sample with 150 mg GF mass loading is showing the highest specific capacitance. The excellent capacitive performance of MoS$_2$_150 mg GF composite electrode can be attributed to the synergetic effect of the graphene and the faradic contribution of MoS$_2$ which can facilitate the penetration of electrolyte ions into the inner part and reduce the ionic diffusion length during the charge-discharge process. These results show that when increasing the mass loading GF up to 150 mg the specific capacitance increases, and thereafter decreases with increasing mass of GF (to 200 mg). Electrochemical measurements also show that the hydrothermally synthesized samples out-perform the mixed material which indicates that the material produced through the hydrothermal process is different from just mixing the two materials. This could be due to the good interaction between both materials during the synthesis process. In other words, MoS$_2$ will nucleate and grow on the surface of the graphene foam, reducing the interface resistance unlike in the case of the mixed sample. Our results show improvement on the specific capacitance of MoS$_2$ electrode material with added carbon composites compared with earlier studies. In fact, Hu et al. reported the synthesis of porous tubular C/MoS$_2$ nanocomposites with a specific capacitance of 210 F g^{-1} at current density of 1 A g^{-1} [37]. Fan et al. also reported a facile one-step hydrothermal of MoS$_2$/C composite with a specific capacitance of 201 F g^{-1} at much lower current density of 0.1 A g^{-1} [22]. Yang produced three-dimensional MoS$_2$/graphene aerogel composites with a specific capacitance of 268 F g^{-1} at a current density of 0.5 A g^{-1} [47]. Wang et al. also produced MoS$_2$/PANI with a specific capacitance of 390 F g^{-1} at a current density of 0.8 A g^{-1} [48].

From both BET and electrochemical results show consistent improvement with SSA and specific capacitance respectively of the MoS$_2$/GF composites with the increase in GF mass loading up to 150 mg beyond which both SSA and specific capacitance decreases. This is the clear indication that 150 mg GF mass loading in MoS$_2$ is the optimum for improvement of MoS$_2$/GF composites.

Fig. 6. (a) and (b) CV at 5–100 mV s^{-1}, and GCD at 1–10 A g^{-1} of AEG respectively, (c) and (d) comparison of CV at 50 mV s^{-1} and GCD at 1 A g^{-1} for MoS$_2$, MoS$_2$/GF composites and MoS$_2$/GF mixture respectively, (e) and (f) specific capacitance versus current density and scan rate respectively of MoS$_2$, MoS$_2$/GF, MoS$_2$/GF mixture and AEG respectively and (g) the specific capacitance of MoS$_2$/GF as function of GF mass loading calculated from CV at scan rate of 5 mV s^{-1}.

3.3. Electrochemical properties of the asymmetric supercapacitor

Impressed by the three electrode measurements performance of MoS$_2$_150 mg GF sample as compared to the rest of the MoS$_2$ based samples, we additionally evaluate the potential application of the MoS$_2$ array electrode in supercapacitors, by fabricating an asymmetric supercapacitor in which the positive electrode comprised of the MoS$_2$_150 mg GF composite and the AEG material was used

as the negative electrode. In order to acquire the optimal performance of the asymmetric full cell supercapacitors, a charge balance $Q_+ = Q_-$ between the two electrodes was done; where Q_+ and Q_- are the charges stored in the positive and negative electrodes, respectively. The charge can be expressed by [49]:

$$Q = C_s \times m\Delta U \tag{6}$$

189

where C_S is the specific capacitance, m is the mass of active material and ΔU is the potential range during the charge-discharge process.

In order to get $Q_+ = Q_-$, the mass balancing follows the equation

$$\frac{m_+}{m_-} = \frac{C_{s-}\Delta U_-}{C_{s+}\Delta U_+} \tag{7}$$

From these calculations, the active material loading in the positive electrode and the negative electrode were 2.0 mg and 2.4 mg respectively.

From the CV curve (Fig. 7(a)) of AEG electrode, no peaks of oxidation and reduction are observed, indicating a typical characteristic of EDL capacitor behaviour over the potential window of −0.8 V to 0.0 V, while the CV shape of the MoS$_2$_150 mg GF electrode in the potential range of 0.0–0.5 V is of faradic type showing oxidation and reduction peaks (Fig. 7(a)). On the basis of these results, the operating cell voltage was extended to about 1.4 V in 6 M KOH electrolyte solution with the MoS$_2$_150 mg GF positive electrode as a cathode and the AEG negative electrode as an anode assembled into asymmetric device. Fig. 7(b) shows the CV curves of the MoS$_2$_150 - mg GF//AEG asymmetric device measured at different scan rates from 5 to 100 mV s^{-1} in 6 M KOH electrolyte solution. The MoS$_2$_150 mg GF//AEG asymmetric supercapacitor presents pseu-

docapacitance behaviour with relatively rectangular CV curves even at the high scan rate up to 100 mV s^{-1}. This portrays a fast ion charge transport at the interface between the electrolyte and electrode surface for an efficient double layer capacitor. Fig. 7(c) shows the galvanostatic charge-discharge curves of the asymmetric cell at varying current density ranging from 0.5 to 10 A g^{-1} showing close to typical triangular shapes corresponding to pseudocapacitance characteristics of the cell as confirmed from the CV curves, except for lower current density. The specific capacitances of these asymmetric cells were calculated from the charge-discharge curves as compared to using CV curves at different scan rates because the CD measurements are a true reflection of the supercapacitor device performance. The realistic specific capacitance of the asymmetric device decreases from 59 F g^{-1} to 14 F g^{-1} with an increase in current density from 1 to 10 A g^{-1} as shown in Fig. 7(d).

The energy density (E, in W h kg^{-1}) and power density (P, in W kg^{-1}) of ECs can be calculated from specific capacitance, C_s according to the following equations:

$$E_d = \frac{1}{2}C_s\Delta U^2 = \frac{1000 \times C_s \times \Delta U^2}{2 \times 3600} = \frac{C_s \times \Delta U^2}{7.2} \tag{8}$$

$$P_d = \frac{3600 \times E_d}{\Delta t} \tag{9}$$

Fig. 7. (a) CV of MoS$_2$ 20 h_150 mg composites and AEG electrodes at 50 mV s^{-1} for three-electrode setup; asymmetric cell of MoS$_2$ 20 h_150 mg//AEG, (b) CV at 5–100 mV s^{-1}, (c) GCD at 0.5–10 A g^{-1}, (d) the specific capacitance as function of the current density, (e) Ragone plot and (f) cycle stability at 2 A g^{-1} respectively.

190

Fig. 8. (a) EIS plot and fitting curve for the asymmetric cell, and (b) EIS before and after cycling.

where E_d is the average energy density (W h kg^{-1}), C_S is the specific capacitance based on the electroactive material (F g^{-1}), ΔU is the cell potential window, P_d is the average power density (W kg^{-1}) and Δt is the discharge time (seconds).

The Ragone plot showing the relationship between energy and power densities of the asymmetric device is shown in Fig. 7(e). The maximum energy density of the device was recorded as 16 W h kg^{-1} with a corresponding power density of 758 W kg^{-1} at a current density of 1 A g^{-1} for aqueous based electrolyte. The energy density obtained here is higher than that found in the previous reports where MoS_2 formed composites with carbon materials and tested in aqueous electrolyte. For example, symmetric pseudocapacitors based on s-MoS_2/CNS exhibited an energy density of 7.4 W h kg^{-1} with a corresponding power density of 3700 W kg^{-1} at 0.1 A g^{-1} [50]. The values obtained here are also comparable to MoS_2 nanosphere electrode which exhibited 17 W h kg^{-1} for a corresponding power density of 204 W kg^{-1} at a current density of 0.5 A g^{-1} [20]. However, these values were obtained in a three-electrode configuration and recent a paper by Patil et al. on MoS_2/GO//GO showed the energy density of 23 W h kg^{-1} and power density of 17 kW kg^{-1} at 25 mV s^{-1} [40]. Since the scan rate was used for the calculation of the specific capacitance and hence the energy density, it is not easy to compare our results with this results but all in all our energy density results are still quite comparable to the reported result having used much more practical approach of calculating specific capacitance which is the CD, not scan rate.

Cycle performance of the electrode is very important for practical application of supercapacitor. Fig. 7(f) shows the capacitance retention of MoS_2_150 mg GF//AEG charge-discharge as a function of cycle number which showed a higher and promising electrochemical behaviour with about 95% retention after 2000 cycles. It is worthy to note that the capacitance retention increases slightly after a few number of cycles, and this is attributed to the improvement of electrode surface wettability during the charge-discharge process [51].

EIS measurements of the MoS_2_150 mg GF//AEG were further carried out so as to characterize in detail this sample. Fig. 8(a) presents the experimental data and fitting data of the MoS_2_150 mg GF//AEG asymmetric device with the equivalent circuit diagram shown in the inset to the figure. The circuit consists of different parameters such as solution resistance R_S, charge transfer resistance R_{CT}, constant phase angle representing double layer capacitance leakage current R_L and Warburg parameter (W). The intercept on the real axis of the Nyquist plot in the high-frequency region provide information about the combined resistance of the electrolyte also known as the equivalent series resistance (ESR) or solution resistance denoted by R_S and this value was found to be 12.95 Ω and 14.2 Ω from both data and the fitting

to the data. The semicircle is a result of the charging of the double layer which appeared in the medium frequency region. This is accredited to the interfacial charge transfer resistance and mass transport through the porous structure of the material and is denoted by R_{CT} and the smaller the value of this parameter the better the device. The Nyquist plot before and after cycling is shown in Fig. 8(b) and R_S values of 12.95 Ω and 16.97 Ω and R_{CT} values of 56 Ω and 59 Ω were obtained for before and after cycling respectively as labelled in the figure. After 2000 cycles, the device shows a slight increase in both solution and transfer resistances which could be due to the decay of the electrolyte and decrease of electrical conductivity of the electrode materials.

4. Conclusion

Graphene foam was demonstrated to improve systematically the physical and electrochemical properties of MoS_2 material as the graphene mass loading was increased from 50 mg to 200 mg with 150 mg found to be the optimum mass of graphene foam for such improvement to be observed. We then successfully fabricated an asymmetric supercapacitor cell based on porous activated carbon derived from expanded graphite material as negative electrodes and MoS_2_150 mg as the positive electrode. The asymmetrical device displays high specific capacitance of 59 F g^{-1} at a current density of 1 A g^{-1} with maximum energy and power densities of 16 W h kg^{-1} and 758 W kg^{-1}, respectively. In addition, the supercapacitor also exhibits good cycle stability with 95% Columbic efficiency over 2000 charge-discharge cycles at a current density of 2 A g^{-1} in addition to an extended operating voltage of about 1.4 V in 6 M KOH aqueous electrolyte. The stability of the cell is a breakthrough since it shows the chemical stability of the MoS_2 unlike in Mo oxides material. This is due to the addition of the highly conductive graphene which will allow fast charge transfer without deteriorating the electrode material. Furthermore, the energy density obtained in this study is higher than that found in the previous reports where MoS_2 formed composites with carbon materials and tested in aqueous electrolyte. The results of this study offer a useful and realistic way to fabricate asymmetric hybrid supercapacitors based on MoS_2/GF and AEG with high energy density and power densities. The performance of such device can be enhanced by finding proper way to exfoliate the 2D MoS_2 material, exposing more active surface area on a very thin material.

191

References

[1] Q. Wang, Z. Wen, J. Li, Carbon nanotubes/TiO$_2$ nanotubes hybrid supercapacitor, J. Nanosci. Nanotechnol. 7 (2007) 3328–3331.

[2] M. Liu, Y. Fu, H. Ma, T. Wang, C. Guan, K. Hu, Flower-like manganese-cobalt oxysulfide supported on Ni foam as a novel faradaic electrode with commendable performance, Electrochim. Acta (2016) 916–922.

[3] A.K. Mondal, H. Liu, Z.-F. Li, G. Wang, Multiwall carbon nanotube-nickel cobalt oxide hybrid structure as high performance electrodes for supercapacitors and lithium ion batteries, Electrochim. Acta 190 (2016) 346–353.

[4] X. Lu, M. Yu, G. Wang, Y. Tong, Y. Li, Flexible solid-state supercapacitors: design, fabrication and applications, Energy Environ. Sci. 7 (2014) 2160–2181.

[5] J. Yan, Z. Fan, W. Sun, G. Ning, T. Wei, Q. Zhang, et al., Advanced asymmetric supercapacitors based on Ni (OH)$_2$/graphene and porous graphene electrodes with high energy density, Adv. Funct. Mater. 22 (2012) 2632–2641.

[6] J. Zhang, J. Jiang, H. Li, X.S. Zhao, A high-performance asymmetric supercapacitor fabricated with graphene-based electrodes, Energy Environ. Sci. 4 (2011) 4009–4015.

[7] P. Simon, Y. Gogotsi, Materials for electrochemical capacitors, Nat. Mater. 7 (2008) 845–854.

[8] E. Frackowiak, Carbon materials for supercapacitor application, Phys. Chem. Chem. Phys. 9 (2007) 1774–1785.

[9] C. Liu, F. Li, L.-P. Ma, H.-M. Cheng, Advanced materials for energy storage, Adv. Mater. 22 (2010) E28–E62.

[10] G. Wang, L. Zhang, J. Zhang, A review of electrode materials for electrochemical supercapacitors, Chem. Soc. Rev. 41 (2012) 797.

[11] F. Wang, S. Xiao, Y. Hou, C. Hu, L. Liu, Y. Wu, Electrode materials for aqueous asymmetric supercapacitors, RSC Adv. 3 (2013) 13059–13084.

[12] Z. Wu, X. Pu, X. Ji, Y. Zhu, M. Jing, Q. Chen, et al., High energy density asymmetric supercapacitors from mesoporous NiCo$_2$S$_4$ nanosheets, Electrochim. Acta 174 (2015) 238–245.

[13] L. Zhang, F. Zhang, X. Yang, G. Long, Y. Wu, T. Zhang, et al., Porous 3D graphene-based bulk materials with exceptional high surface area and excellent conductivity for supercapacitors, Sci. Rep. 3 (2013) 1408.

[14] V. Khomenko, E. Raymundo-Pinero, F. Béguin, Optimisation of an asymmetric manganese oxide/activated carbon capacitor working at 2 V in aqueous medium, J. Power Sources 153 (2006) 183–190.

[15] L. Sui, S. Tang, Y. Chen, Z. Dai, H. Huangfu, Z. Zhu, et al., An asymmetric supercapacitor with good electrochemical performances based on Ni (OH)$_2$/AC/CNT and AC, Electrochim. Acta 182 (2015) 1159–1165.

[16] M. Jana, J.S. Kumar, P. Khanra, P. Samanta, H. Koo, N.C. Murmu, et al., Superior performance of asymmetric supercapacitor based on reduced graphene oxide-manganese carbonate as positive and sono-chemically reduced graphene oxide as negative electrode materials, J. Power Sources 303 (2016) 222–233.

[17] L. Zhang, H. Bin Wu, X.W. (David) Lou, Unusual CoS$_2$ ellipsoids with anisotropic tube-like cavities and their application in supercapacitors, Chem. Commun. 48 (2012) 6912.

[18] F. Luo, J. Li, H. Yuan, D. Xiao, Rapid synthesis of three-dimensional flower-like cobalt sulfide hierarchitectures by microwave assisted heating method for high-performance supercapacitors, Electrochim. Acta 123 (2014) 183–189.

[19] Q. Wang, L. Jiao, H. Du, J. Yang, Q. Huan, W. Peng, et al., Facile synthesis and superior supercapacitor performances of three-dimensional cobalt sulfide hierarchitectures, Cryst. Eng. Comm. 13 (2011) 6960–6963.

[20] P. Ilanchezhiyan, G. Mohan Kumar, T.W. Kang, Electrochemical studies of spherically clustered MoS$_2$ nanostructures for electrode applications, J. Alloys Compd. 634 (2015) 104–108.

[21] A. Ramadoss, T. Kim, G.-S. Kim, S.J. Kim, Enhanced activity of a hydrothermally synthesized mesoporous MoS$_2$ nanostructure for high performance supercapacitor applications, New J. Chem. 38 (2014) 2379.

[22] L.-Q. Fan, G.-J. Liu, C.-Y. Zhang, J.-H. Wu, Y.-L. Wei, Facile one-step hydrothermal preparation of molybdenum disulfide/carbon composite for use in supercapacitor, Int. J. Hydrogen Energy 40 (2015) 10150–10157.

[23] H. Pang, C. Wei, X. Li, G. Li, Y. Ma, S. Li, et al., Microwave-assisted synthesis of NiS$_2$ nanostructures for supercapacitors and cocatalytic enhancing photocatalytic H$_2$ production, Sci. Rep. 4 (2014) 3577.

[24] T. Zhu, Z. Wang, S. Ding, J.S. Chen, X.W.D. Lou, Hierarchical nickel sulfide hollow spheres for high performance supercapacitors, RSC Adv. 1 (2011) 397–400.

[25] A. Wang, H. Wang, S. Zhang, C. Mao, J. Song, H. Niu, et al., Controlled synthesis of nickel sulfide/graphene oxide nanocomposite for high-performance supercapacitor, Appl. Surf. Sci. 282 (2013) 704–708.

[26] C.J. Raj, B.C. Kim, W.-J. Cho, W.-G. Lee, Y. Seo, K.-H. Yu, Electrochemical capacitor behavior of copper sulfide (CuS) nanoplatelets, J. Alloys Compd. 586 (2014) 191–196.

[27] D. Merki, X. Hu, Recent developments of molybdenum and tungsten sulfides as hydrogen evolution catalysts, Energy Environ. Sci. 4 (2011) 3878–3888.

[28] K. Chang, W. Chen, In situ synthesis of MoS$_2$/graphene nanosheet composites with extraordinarily high electrochemical performance for lithium ion batteries, Chem. Commun. 47 (2011) 4252–4254.

[29] Y. Li, H. Wang, L. Xie, Y. Liang, G. Hong, H. Dai, MoS$_2$ nanoparticles grown on graphene: an advanced catalyst for the hydrogen evolution reaction, J. Am. Chem. Soc. 133 (2011) 7296–7299.

[30] Z. Yin, H. Li, H. Li, L. Jiang, Y. Shi, Y. Sun, et al., Single-layer MoS$_2$ phototransistors, ACS Nano 6 (2011) 74–80.

[31] J.M. Soon, K.P. Loh, Electrochemical double-layer capacitance of MoS$_2$ nanowall films, Electrochem. Solid-State Lett. 10 (2007) A250–A254.

[32] C. Sha, B. Lu, H. Mao, J. Cheng, X. Pan, J. Lu, et al., 3D ternary nanocomposites of molybdenum disulfide/polyaniline/reduced graphene oxide aerogel for high performance supercapacitors, Carbon 99 (2016) 26–34.

[33] X. Huang, Z. Zeng, H. Zhang, Metal dichalcogenide nanosheets: preparation, properties and applications, Chem. Soc. Rev. 42 (2013) 1934–1946.

[34] L. Zhang, F. Zhang, X. Yang, G. Long, Y. Wu, T. Zhang, et al., Porous 3D graphene-based bulk materials with exceptional high surface area and excellent conductivity for supercapacitors, Sci. Rep. 3 (2013).

[35] E.G. da Silveira Firmiano, A.C. Rabelo, C.J. Dalmaschio, A.N. Pinheiro, E.C. Pereira, W.H. Schreiner, et al., Supercapacitor electrodes obtained by directly bonding 2D MoS$_2$ on reduced graphene oxide, Adv. Energy Mater. 4 (2014).

[36] K.-J. Huang, L. Wang, J.-Z. Zhang, L.-L. Wang, Y.-P. Mo, One-step preparation of layered molybdenum disulfide/multi-walled carbon nanotube composites for enhanced performance supercapacitor, Energy 67 (2014) 234–240.

[37] B. Hu, X. Qin, A.M. Asiri, K.A. Alamry, A.O. Al-Youbi, X. Sun, Synthesis of porous tubular C/MoS$_2$ nanocomposites and their application as a novel electrode material for supercapacitors with excellent cycling stability, Electrochim. Acta 100 (2013) 24–28.

[38] H. Ji, C. Liu, T. Wang, J. Chen, Z. Mao, J. Zhao, et al., Porous hybrid composites of few-layer MoS$_2$ nanosheets embedded in a carbon matrix with an excellent supercapacitor electrode performance, Small 11 (2015) 6480–6490.

[39] K.-J. Huang, L. Wang, Y.-J. Liu, Y.-M. Liu, H.-B. Wang, T. Gan, et al., Layered MoS$_2$-graphene composites for supercapacitor applications with enhanced capacitive performance, Int. J. Hydrogen Energy 38 (2013) 14027–14034.

[40] U.M. Patil, M.S. Nam, S. Kang, J.S. Sohn, H.B. Sim, S. Kang, et al., Fabrication of ultra-high energy and power asymmetric supercapacitors based on hybrid 2D MoS$_2$/graphene oxide composite electrodes: a binder-free approach, RSC Adv. 6 (2016) 43261–43271.

[41] M.A. Bissett, I.A. Kinloch, R.A.W. Dryfe, Characterization of MoS$_2$–graphene composites for high-performance coin cell supercapacitors, ACS Appl. Mater. Interfaces 7 (2015) 17388–17398.

[42] K. Krishnamoorthy, G.K. Veerasubramani, S. Radhakrishnan, S.J. Kim, Supercapacitive properties of hydrothermally synthesized sphere like MoS$_2$ nanostructures, Mater. Res. Bull. 50 (2014) 499–502.

[43] L.-Q. Fan, G.-J. Liu, C.-Y. Zhang, J.-H. Wu, Y.-L. Wei, Facile one-step hydrothermal preparation of molybdenum disulfide/carbon composite for use in supercapacitor, Int. J. Hydrogen Energy 40 (2015) 10150–10157.

[44] D.Y. Momodu, F. Barzegar, B. Abdulhakeem, J. Dangbegnon, T. Masikhwa, J. Madito, et al., Simonkolleite-graphene foam composites and their superior electrochemical performance, Electrochim. Acta 151 (2015) 591–598.

[45] F. Barzegar, A. Bello, D. Momodu, M.J. Madito, J. Dangbegnon, N. Manyala, Preparation and characterization of porous carbon from expanded graphite for high energy density supercapacitor in aqueous electrolyte, J. Power Sources 309 (2016) 245–253.

[46] F. Barzegar, A. Bello, D.Y. Momodu, J.K. Dangbegnon, F. Taghizadeh, M.J. Madito, et al., Asymmetric supercapacitor based on an α-MoO$_3$ cathode and porous activated carbon anode materials, RSC Adv. 5 (2015) 37462–37468.

[47] M. Yang, J.-M. Jeong, Y.S. Huh, B.G. Choi, High-performance supercapacitor based on three-dimensional MoS$_2$/graphene aerogel composites, Compos. Sci. Technol. 121 (2015) 123–128.

[48] J. Wang, Z. Wu, K. Hu, X. Chen, H. Yin, High conductivity graphene-like MoS$_2$/polyaniline nanocomposites and its application in supercapacitor, J. Alloys Compd. 619 (2015) 38–43.

[49] A. Bello, F. Barzegar, D. Momodu, J. Dangbegnon, F. Taghizadeh, M. Fabiane, et al., Asymmetric supercapacitor based on nanostructured graphene foam/polyvinyl alcohol/formaldehyde and activated carbon electrodes, J. Power Sources 273 (2015) 305–311.

[50] T.N.Y. Khawula, K. Raju, P.J. Franklyn, I. Sigalas, K.I. Ozoemena, Symmetric pseudocapacitors based on molybdenum disulfide (MoS$_2$)-modified carbon nanospheres: correlating physicochemistry and synergistic interaction on energy storage, J. Mater. Chem. A. 4 (2016) 6411–6425.

[51] B. Fang, L. Binder, A novel carbon electrode material for highly improved EDLC performance, J. Phys. Chem. B. 110 (2006) 7877–7882.

192

4.6.3 Conclude Remarks

Graphene foam was demonstrated to improve systematically the physical and electrochemical properties of MoS_2 material as the mass load was increased from 50 mg to 150 mg with 150mg found to be the optimum mass for such improvement to be observed. We then successfully fabricated an asymmetric supercapacitor cell based on porous activated carbon derived from expanded graphite material as negative electrodes and MoS_2_150 mg as positive electrode. The asymmetrical device displays high specific capacitance of 59 F g^{-1} at a current density of 1 A g^{-1} with maximum energy and power densities of 16 Wh kg^{-1} and 758 W kg^{-1}, respectively. In addition, the supercapacitor also exhibit a good cycle stability with 95 % coulombic efficiency over 2000 charge-discharge cycles at a current density of 2 A g^{-1} with an extended operating voltage of about 1.4 V in 6 M KOH aqueous electrolyte. This study illustrated the merit of combining such hybrid materials as an exceptional method to produce supercapacitors with high energy and power densities. These results offer a useful and realistic way to fabricate asymmetric hybrid supercapacitors based on MoS_2/GF and AEG with high energy density while retaining the high power density property of supercapacitor.

Bibliography

[1] Z. Zhao, F. Geng, J. Bai, H.M. Cheng, Facile and controlled synthesis of 3D nanorods-based urchinlike and nanosheets-based flowerlike cobalt basic salt nanostructures, J. Phys. Chem. C. 111 (2007) 3848–3852.

[2] W. Xing, S. Zhuo, H. Cui, H. Zhou, W. Si, X. Yuan, et al., Morphological control in synthesis of cobalt basic carbonate nanorods assembly, Mater. Lett. 62 (2008) 1396–1399.

[3] B. Li, Y. Xie, C. Wu, Z. Li, J. Zhang, Selective synthesis of cobalt hydroxide carbonate 3D architectures and their thermal conversion to cobalt spinel 3D superstructures, Mater. Chem. Phys. 99 (2006) 479–486.

[4] J. Zhang, J. Jiang, H. Li, X.S. Zhao, A high-performance asymmetric supercapacitor fabricated with graphene-based electrodes, Energy Environ. Sci. 4 (2011) 4009–4015.

[5] L. Yu, N. Shi, Q. Liu, J. Wang, B. Yang, B. Wang, et al., Facile synthesis of exfoliated Co–Al LDH–carbon nanotube composites with high performance as supercapacitor electrodes, Phys. Chem. Chem. Phys. 16 (2014) 17936.

[6] A. Zhang, C. Wang, Q. Xu, H. Liu, Y. Wang, Y. Xia, A hybrid aerogel of Co-Al layered double hydroxide/graphene with three-dimensional porous structure as a novel electrode material for supercapacitors., RSC Adv. 5 (2015) 26017–26026.

[7] L. Zhang, K.N. Hui, K.S. Hui, H. Lee, Facile synthesis of porous CoAl-layered double hydroxide/graphene composite with enhanced capacitive performance for supercapacitors, Electrochim. Acta. 186 (2015) 522–529.

[8] Y. Zhong, Y. Liao, A. Gao, J. Hao, D. Shu, Y. Huang, et al., Supercapacitive behavior of electrostatic self-assembly reduced graphene oxide/CoAl-layered double hydroxides nanocomposites, J. Alloys Compd. 669 (2016) 146–155.

[9] F. Barzegar, A. Bello, D. Momodu, M.J. Madito, J. Dangbegnon, N. Manyala,

Preparation and characterization of porous carbon from expanded graphite for high energy density supercapacitor in aqueous electrolyte, J. Power Sources. 309 (2016) 245–253.

[10] D. Momodu, A. Bello, J. Dangbegnon, F. Barzeger, F. Taghizadeh, M. Fabiane, et al., Solvothermal synthesis of NiAl double hydroxide microspheres on a nickel foam-graphene as an electrode material for pseudo-capacitors, AIP Adv. 4 (2014) 097122.

[11] W. Fang, H. Zhao, Y. Xie, J. Fang, J. Xu, Z. Chen, Facile hydrothermal synthesis of VS2/graphene nanocomposites with superior high-rate capability as Lithium-ion battery cathodes, ACS Appl. Mater. Interfaces. (2015) 150528080807004.

[12] P. Mohan, J. Yang, A. Jena, H.S. Shin, VS$_2$/rGO hybrid nanosheets prepared by annealing of VS$_4$/rGO, J. Solid State Chem. 224 (2015) 82–87.

[13] M.-R. Gao, Y.-F. Xu, J. Jiang, S.-H. Yu, Nanostructured metal chalcogenides: synthesis, modification, and applications in energy conversion and storage devices., Chem. Soc. Rev. 42 (2013) 2986–3017. doi:10.1039/c2cs35310e.

[14] C. Sha, B. Lu, H. Mao, J. Cheng, X. Pan, J. Lu, et al., 3D ternary nanocomposites of molybdenum disulfide/polyaniline/reduced graphene oxide aerogel for high performance supercapacitors, Carbon N. Y. 99 (2016) 26–34.

[15] X. Huang, Z. Zeng, H. Zhang, Metal dichalcogenide nanosheets: preparation, properties and applications, Chem. Soc. Rev. 42 (2013) 1934–1946.

[16] L. Zhang, F. Zhang, X. Yang, G. Long, Y. Wu, T. Zhang, et al., Porous 3D graphene-based bulk materials with exceptional high surface area and excellent conductivity for supercapacitors, Sci. Rep. 3 (2013).

[17] E.G. da Silveira Firmiano, A.C. Rabelo, C.J. Dalmaschio, A.N. Pinheiro, E.C. Pereira, W.H. Schreiner, et al., Supercapacitor electrodes obtained by directly bonding 2D MoS$_2$ on reduced graphene oxide, Adv. Energy Mater. 4 (2014).

195

[18] K.-J. Huang, L. Wang, J.-Z. Zhang, L.-L. Wang, Y.-P. Mo, One-step preparation of layered molybdenum disulfide/multi-walled carbon nanotube composites for enhanced performance supercapacitor, Energy. 67 (2014) 234–240.

[19] B. Hu, X. Qin, A.M. Asiri, K.A. Alamry, A.O. Al-Youbi, X. Sun, Synthesis of porous tubular C/MoS_2 nanocomposites and their application as a novel electrode material for supercapacitors with excellent cycling stability, Electrochim. Acta. 100 (2013) 24–28.

[20] L.-Q. Fan, G.-J. Liu, C.-Y. Zhang, J.-H. Wu, Y.-L. Wei, Facile one-step hydrothermal preparation of molybdenum disulfide/carbon composite for use in supercapacitor, Int. J. Hydrogen Energy. 40 (2015) 10150–10157.

[21] H. Ji, C. Liu, T. Wang, J. Chen, Z. Mao, J. Zhao, et al., Porous Hybrid Composites of Few-Layer MoS_2 Nanosheets Embedded in a Carbon Matrix with an Excellent Supercapacitor Electrode Performance, Small. 11 (2015) 6480–6490.

CHAPTER 5

5.1 General conclusions and future works

In this chapter, the main results reported and discussed in chapter 4 are summarized below. This chapter includes a brief discussion on the possible future work of this study.

Cobalt-based hydroxides and transitional metal dichalcogenides with carbon materials were synthesized using a hydrothermal technique. Two types of activated carbon (from Polyvinyl alcohol PVA and graphene foam denoted as AGF and from expanded graphite donated as AEG) were produced using the hydrothermal technique. The activated carbon from Polyvinyl alcohol PVA and graphene foam was used to make the composite and the expanded graphite was used as the negative electrode for the asymmetric devices. Three-dimensional graphene foam (GF) has been synthesized successfully by AP-CVD using nickel foam as a growth substrate. Because faradaic materials suffer from poor electrical conductivity and low electrochemical stability, while carbon materials are known to have good electrical conductivity and electrochemical stability, therefore the faradaic materials were incorporated with carbon materials to improve the electrochemical properties of the composite materials. Based on this suggested concepts, hydrothermal method was used to synthesize cobalt hydroxide carbonate nanorods in the presence of activated carbon (AC) (from Polyvinyl alcohol PVA and graphene foam) denoted as AGF to obtained cobalt hydroxide carbonate/AC composites. Faradaic materials were also synthesized using various routes in order to make graphene-based composites materials. The CoAl-LDH and MoS_2 have been synthesized using hydrothermal technique in order to enhance both the electrical double layer properties from graphene with faradaic properties from CoAl-LDH and MoS_2 component. Graphene was also involved in the growth of a thin film of few-layer graphene on the NF current collector to form a cobalt oxyhydroxide/nickel foam graphene.

Each of the produced materials was characterized by scanning electron microscopy (SEM), transmission electron microscopy (TEM), X-ray diffraction (XRD), X-ray photoelectron spectroscopy (XPS), N_2 adsorption-desorption isotherm (BET), Fourier transformation infrared spectroscopy (FTIR) and Raman spectroscopy. All produced materials were also analysed in the electrochemical system as electrodes for supercapacitors both in the two and three electrode configurations.

In section 4.1. Cobalt hydroxide carbonate nanorods were successfully synthesized using a hydrothermal method at a temperature of 120 °C with different synthesis times from 3 to 12 h for transformation of phases and morphologies. The results from XRD characterization and scanning electron microscopy with the morphology of nanorods exhibited the crystal structure consisting of the mixture of both monoclinic and orthorhombic phases. Different measurements that have been done on these samples show systematic improvements of the specific capacitance as function of increasing reaction time. Cobalt hydroxide carbonate nanorods synthesized with 12 h reaction time, which is the reaction time just before the materials transforms into cobalt oxide under the same synthesis conditions exhibited the highest specific capacitance of 466 F g^{-1} at a current density of 1 A g^{-1} in 6M KOH electrolyte and also showed excellent stability with ~99 % capacitance retention after 2000 cycles at a current density of 10 A g^{-1}. These results suggest that cobalt hydroxide carbonate nanorods with the low cost and simple preparation process can be promising electrode materials for supercapacitor application.

Activated carbon (AC) was incorporated to cobalt hydroxide carbonate using a hydrothermal method at a temperature of 120 °C for 6 h reaction time sample to produce cobalt hydroxide carbonate/AC composites. The reason for adding activated carbon to growth time of 6 h is due to the fact that the synergy between the two materials should improve the electrochemical

properties of the composite material since the carbon will add the electrical conductivity and stability, while cobalt hydroxide carbonate will contribute high specific capacitance. The results are discussed in section 4.2 where activated carbon was incorporated into cobalt hydroxide carbonate. The result revealed that fabricating AC with the cobalt hydroxide carbonate clearly improved the surface area and electrochemical performance of the composite electrode. This was indicated by the increase of both SSA and specific capacitance from 32.7 $m^2 g^{-1}$ and 253.2 F g^{-1} (at 1 A g^{-1}) to 164.3 $m^2 g^{-1}$ and 301.4 F g^{-1} (at 1 Ag^{-1}) for both pristine cobalt hydroxide carbonate and the composite respectively accompanied by excellent constant coulombic efficiency of 95.6 % after 1000 charge-discharge cycles at current density of 4 A g^{-1}. This demonstrated that cobalt hydroxide carbonate/AC composite electrode could be promising candidate as electrode material for high performance supercapacitors.

Having established that the cobalt based hydroxides could be good materials for electrochemical capacitors application; another approach was to synthesis cobalt based double layered hydroxides (LDH) composite with carbon materials. In section 4.3 The cobalt based double layered hydroxides (LDH) composite with graphene foam (GF) synthesized via hydrothermal method synthesis as electrode material for supercapacitor application had been discussed. The asymmetric supercacitor device was also produced with CoAl-LDH/GF as the positive electrode and AC carbon synthesized from expanded graphite as negative electrode to increasing the energy density of supercapacitor. This asymmetric device showed high specific capacitance of 101.4 F g^{-1} at a current density of 0.5 A g^{-1} with a maximum energy density of 28 Wh kg^{-1} and a corresponding power density of 1420 W kg^{-1}, with excellent stability of ∼100 % capacitance retention with no capacitance loss after 5000 cycles. These promising results show the potential of these asymmetric device for high energy and power densities supercapacitor devices.

199

In section 4.4 mesoporous nanosheets of cobalt oxyhydroxide (CoOOH) were synthesized on Ni foam graphene (Ni-FG) substrate by facile two-step processes, namely, hydrothermal reaction to produce CoAl-LDH nanosheets on Ni-FG which were converted to CoOOH nanosheets on Ni-FG by alkaline etching of the Al cations in CoAl-LDH using a NaOH solution. The electrochemical behavior showed that the CoOOH/Ni-FG electrode exhibit a high specific capacity of of 199 mAh g^{-1} at a current density of 0.5 A g^{-1} accompanied by excellent constant coulombic efficiency of 98 % after 1000 charge-discharge cycles at current density of 10.0 A g^{-1} after 1000 cycles .

As stated before the transition metal chalcogenides have similar 2D structure like graphene, but still suffer low electrical conductivity and poor electrochemical stability because of redox reaction. Hence like other faradic materials their composite with carbon materials like graphene should be able to improve their electrical conductivity, electrochemical stability and prevent restacking so that a large surface area can be realized

In section 4.5 the VS_2 nanomaterial synthesized through solvothermal approach as cathode and AEG as anode materials respectively for asymmetric supercapacitor to increasing the energy density of the supercapacitor was discussed. The asymmetric devices showed a specific capacitance of 155 F g^{-1} at 1 A g^{-1} with a maximum energy density as high as 42 Wh kg^{-1} and a power density of 700 W kg^{-1} with good stability after 5000 cycles at a current density of 2 A g^{-1} at an extended operating voltage of about 1.4 V. These results showed that asymmetric hybrid supercapacitors constructed on VS_2 and AC has a great potential as a high-performance energy storage device.

In section 4.6 pure MoS_2 and MoS_2/graphene foam (GF) with different graphene foam mass loading synthesized by hydrothermal process to improve on the specific capacitance of the composites were reported. An asymmetric supercapacitor were fabricated using the best performing Mos_2/GF composite and activated carbon derived from expanded graphite (AEG)

200

as positive and negative electrodes respectively in an aqueous electrolyte. The asymmetrical device exhibited high specific capacitance of 189 F g^{-1} at 0.5 A g^{-1} with a maximum energy density of 51 Wh kg^{-1} and power density of 1765 W kg^{-1}. In addition, the supercapacitor also exhibited a good cycle stability with 95 % coulombic efficiency over 2000 charge discharge cycles at a current density of 2 A g^{-1} in addition to an extended operating voltage of about 1.4 V in 6 M KOH aqueous electrolyte. These results offer a convenient and effective way to fabricate asymmetric hybrid supercapacitors based on MoS_2/GF and AEG with high energy density while maintaining the high power density property of supercapacitor.

In summary, the results clearly showed the great potential of incorporating carbon materials into the cobalt based hydroxide and transition metal chalcogenides to obtain carbon-based composites for energy storage device electrodes. The improvement of the electrochemical properties could also be achieved by mounting ACs produced as negative electrode and faradaic-type materials such as cobalt-based materials and transition metal chalcogenides as positive electrodes in order to increase the energy density by utilizing the resulting wide operating voltage window.

Future work could be further exploration of the effects of different carbon materials such as activated carbon, carbon nanotubes on the electrochemical performance of transition metal chalcogenides composite materials as supercapacitor electrodes. This could be achieved by optimization of composite materials which will give high energy and power densities by fabricating asymmetric supercapacitor by using different electrolytes of the supercapacitor device.